RMIT
UNIVERSITY

Modelling and Verification of doses delivered to deformable moving targets in radiotherapy

THIS THESIS SUBMITTED IN FULFILMENT OF THE REQUIREMENTS FOR THE DEGREE OF PHILOSOPHIE DOCTOR

UNJIN ADAM YEO

MASTER OF SCIENCE (MSC) APPLIED PHYSICS

BACHELOR OF SCIENCE (BSC) PHYSICS, WITH HONOURS

BACHELOR OF SOCIAL SCIENCE (BSOSC) COGNITIVE SCIENCE

SCHOOL OF APPLIED SCIENCES

COLLEGE OF SCIENCE, ENGINEERING AND HEALTH

RMIT UNIVERSITY

OCTOBER 2015

DECLARATION OF AUTHENTICITY

"Self-trust is the first secret of success."

Ralph Waldo Emerson

Declaration

I certify that except where due acknowledgement has been made, the work is that of the author alone; the work has not been submitted previously, in whole or in part, to qualify for any other academic award; the content of the thesis is the result of work which has been carried out since the official commencement date of the approved research program(Program code: DR230, Doctor of Philosophy, RMIT University); any editorial work, paid or unpaid, carried out by a third party is acknowledged; and, ethics procedures and guidelines have been followed.

Unjin Adam Yeo, October 2015

SUPERVISORS

"To ask when you already know is politeness, to ask when you do not know is the rule and necessary."

General Yamamoto Jin'emon

Primary supervisors

Assoc. Prof. Rick Franich

 Associate Professor, Medical Physics,

 School of Applied Sciences and Health Innovations Research Institute,

 College of Science, Engineering and Health,

 RMIT University (Melbourne, Australia).

Prof. Tomas Kron

 Principle Research Physicist,

 Department of Physical Sciences,

 Peter MacCallum Cancer Centre (Melbourne, Australia).

 Adjunct Professor, Medical Physics,

 School of Applied Sciences and Health Innovations Research Institute,

 College of Science, Engineering and Health,

 RMIT University (Melbourne, Australia).

Dr. Michael Taylor

 Postdoctoral Research Fellow, Medical Physics

 School of Applied Sciences, College of Science, Engineering and Health

 RMIT University (Melbourne, Australia)

Further supervisor

Mr. Ryan Smith

 Senior Medical Physicist

 William Buckland Radiotherapy Centre

 The Alfred Hospital (Melbourne, Australia)

ACKNOWLEDGEMENTS

"It's my experience that the people who gain trust, loyalty, excitement, and energy fast are the ones who pass on the credit to the people who have really done the work. A leader doesn't need any credit, he's getting more credit than he deserves anyway."

Robert Townsend, *former CEO of AVIS*

The author's confession

I lift up my eyes to the mountains – where does my help come from?

My help comes from the LORD the Maker of heaven and earth.

He will not let your foot slip – he who watches over you will not slumber;

indeed he who watches over Israel will neither slumber no sleep.

The LORD watches over you – the LORD is your shade at your right hand;

the sun will not harm you by day, nor the moon by night.

The LORD will keep you from all harm – he will watch over your life;

the LORD will watch over your coming and going both now and forevermore.

(Psalm 121, NIV version)

Benevolent lectors   This thesis describes a range of well-aligned work in each chapter that has taken several years to complete. In the author's personal opinion, I feel I am so blessed to happen to have the project comprised of several bodies that are linearly followed one after another. I started with enrolling in the Master's program in Medical & Health Physics in 2010. I have since converted the Masters to a PhD to maximise my research training and fully realise potential outcomes from this research project. Although I have been involved in several other studies and teaching at RMIT along the way, I can certify that I have been most concentrated in this present work and as such, this has been both a large and a unique part of my personal journey. The work undertaken for this thesis involved both intense academic and research trainings in which I have fully committed with a great enthusiasm. This work has therefore shaped and defined my life style and I have experienced many moments of both jubilance and frustration over the years. Despite the fact that I am not a talkative person, I should not just make short comments saying 'thanks' since I am heavily indebted to the many that have helped and encouraged me throughout my candidature. I apologise in advance for the following acknowledgment part if it is boring to read.

First of all, I declare that many parts of the work have been published, and that these sections have had the benefit of much polishing by co-authors and through the peer-review process. However, all papers were written and drafted by me in the first instance. The most contributed three people I must thank are Assoc Prof Rick Franich, Prof Tomas Kron and Dr Michael Taylor. I am immeasurably indebted to them for their invaluable guidance and support throughout the period of my PhD candidature, since this work is the result of a whole-hearted effort rather than of my own art to be done. I am incredibly privileged to have these genuine and at same time brilliant guys as my supervisors. I greatly admire both the humility and experience of these guys, there is absolutely no doubt that their striking insights have driven

me to be who I am as a medical physicist. I would not hesitate to say that this thesis would not have been possible without these guys' contribution and invaluable supervision.

At this moment I would like to put an important message that I have always wanted to thank until now, regarding a massive help and assistance of improving my English skill as well as communication skill. I look back the period of this PhD candidature and the time after deciding to immigrate to Australia to be closer with my immediate family members in 2009. Although my English skill is still not perfect, it was much more immature in both verbal and writing manner at the first moment when I anxiously met Rick and Michael. I think it was the first step to becoming a medical physicist. I remember when I made the first manuscript regarding deformable gel dosimetry. To be honest it was such a heavy frustration when I saw countless track changes and full of comments they made in every single page of the manuscript, that I could not even read the whole text! I cannot describe the amount of joy that I felt when the paper was published in *Medial Physics* journal after numerous rounds of the editing process and correspondence with the associate editors. Since then, Rick and Michael's correction/comments as well as communication with them have accelerated my English speaking and writing skill (still in-progress), which was something like that a dedicated artist that erases the existing picture then draws a new picture on the blank white paper. I have always deeply appreciated their dedicated work of art. I also feel that this journey with the many collaborations involved in this work has strengthened my academic growth as well as my personal character and provided many valuable lessons in interacting with others. This research has been extremely fulfilling for me both personally and in practicality. In this context, I am indebted *again* to my supervisors for their invaluable guidance and support throughout the years. I look forward to many more years of working with Prof Franich, Prof Kron and Dr Taylor!

This work has been based primarily at RMIT, however, it would not be even feasible to write a single chapter of this thesis without connections to MacCallum Cancer Centre (Melbourne, Australia) and the Alfred Hospital (Victoria, Australia), where numerous irradiations and 3D/4D CT scans of dosimeters have been conducted. Mr Ryan Smith, Senior Medical Physicist at Alfred Hospital also held the role of supervisor and consultant in the clinical aspect of my research project. It is also thanks to Mr Smith because not only have we had many heated discussions about the world of brachytherapy where he has kindly enlightened me, but he has spent many late nights and early mornings generously advising me and assisting me with both the external beam radiotherapy and brachytherapy procedures, the results of which are set out in this present thesis. Without his assistance, it would not have

TABLE OF CONTENTS

Table of contents

ABSTRACT

"Everything should be made as simple as possible, but not simpler."

Albert Einstein

Scientific abstract

During the last two decades, advanced treatment techniques have been developed in radiotherapy to achieve more conformal beam targeting of cancerous lesions. The advent of these techniques, such as intensity modulated radiotherapy (IMRT), volumetric modulated arc radiothreapy (VMAT), Tomotherapy etc., allows more precise localisation of higher doses to complex-shaped target volumes, thereby sparing more healthy tissue. In this context, motion management is a critical issue in contemporary radiotherapy (RT). That anatomic structures move during respiration is well known and much research is presently being devoted to strategies to contend with organ motion. However, moving structures are typically regarded as rigid bodies. The fact that many structures *deform* as a result of motion makes their resultant dose distributions difficult to measure and calculate, and has not been fully accounted for. The potential for ineffective treatments that do not take into account motion and anatomic deformation is self-evident.

This thesis addresses the pressing need to investigate dose distributions in targets that deform during and/or between treatments, to ensure robust calculations for dose accumulation and delivery, thus providing the most positive outcomes for patients. This involves the direct measurement of complex and re-distributed dose in deforming objects (*an experimental model*), as well as calculations of the deformed dose distribution (*a mathematical model*). The comparison thereof aims to validate the dose deformation technique, thereby to apply the method to a clinical example such as liver stereotactic body radiotherapy.

To facilitate four-dimensional deformable dosimetry for both external beam radiotherapy and brachytherapy, methodologies for three-dimensional deformed dose measurements were developed and employed using radiosensitive polymer gel combined with a cone beam optical computed tomography (CT) scanner. This includes the development of a novel prototype deformable target volume using a tissue-equivalent, deformable gel dosimetric phantom, dubbed "DEFGEL". This can reproducibly simulate targets subject to a range of mass- and density-conserving deformations representative of those observable in anatomical targets. This novel tool was characterised in terms of its suitability for the measurement of dose in deforming geometries. It was demonstrated that planned doses could be delivered to the deformable gel dosimeter in the *presence* of different deformations and complex spatial re-distributions of dose in all three dimensions could be quantified.

For estimating the cumulative dose in different deformed states, deformable image registration (DIR) algorithms were implemented to 'morph' a dose distribution calculated by

a treatment planning system. To investigate the performance of DIR and dose-warping technique, two key studies were undertaken. The first was to systematically assess the accuracy of a range of different DIR algorithms available in the public domain and quantitatively examine, in particular, *low-contrast regions*, where accuracy had not previously been established. This work investigates DIR algorithms in 3D *via* a systematic evaluation process using DEFGEL suitable for verification of mass- and density-conserving deformations. The second study was a full three-dimensional experimental validation of the dose-warping technique using the evaluated DIR algorithm and comparing it to directly measured deformed dose distributions from DEFGEL. It was shown that the dose-warping can be accurate, i.e. over 95% passing rate of 3D-gamma analysis with 3%/3mm criteria for given extents of deformation up to 20 mm

For the application of evaluating patient treatment planning involving tumour motion/deformation, two key studies were undertaken in the context of liver stereotactic body radiotherapy. The first was a 4D evaluation of conventional 3D treatment planning, combined with 4D computed tomography, in order to investigate the extent of dosimetric differences between conventional 3D-static and path-integrated 4D-cumulative dose calculation. This study showed that the 3D planning approach overestimated doses to targets by $\leq 9\%$ and underestimated dose to normal liver by $\leq 8\%$, compared to the 4D methodology. The second study was to assess a consequent reduction of healthy tissue sparing, which may increase risk for surrounding healthy tissues. Estimates for normal tissue complications probabilities (NTCP) based on the two dose calculation schemes are provided. While all NTCP were low for the employed fractionation scheme, analysis of common alternative schemes suggests potentially larger uncertainties exist in the estimation of NTCP for healthy liver and that substantial differences in these values may exist across the different fractionation schemes.

These bodies of work have shown the potential to quantify such issues of under- and/or over-dosages which are quite patient dependent in RT. Studies presented in this work consolidate gel dosimetry, image guidance, DIR, dose-warping and consequent dose accumulation calculation to investigate the dosimetric impact and make more accurate evaluation of conventional 3D treatment plans. While liver stereotactic body radiotherapy (SBRT) was primarily concerned for immediate clinical application, the findings of this thesis are also applicable to other organs with various RT techniques. Most importantly, however, it is hoped that the outcomes of this thesis will help to improve treatment plan accuracy. By considering both computation and measurement, it is also hoped that this work will open new windows for future work and hence provide building blocks to further enhance the benefit of radiotherapy treatment.

CHAPTER ONE

: Introduction

"The man who removes a mountain begins by carrying away small stones."[*]

William Faulkner

---

[*] Carrying away small stones?

: Describing the questions which should first be discussed, with a view to the physical science
the author is investigating.

1.1 Motivation

This thesis addresses one of major challenges in contemporary radiotherapy – anatomic variation due to organ motion and deformation, particularly when implementing highly conformal fields with high-dose delivery. Organ deformation inherent in intra- and inter-fractional motion makes their resultant dose distributions difficult to measure and calculate. This has an effect not only on tumour control (i.e. *has the tumour been given enough dose?*) but also on the potential risk for adjacent healthy tissues (i.e. *have local organs-at-risk been given too much radiation dose?*). Whether by under-dosage to targeted tumours or over-irradiation of surrounding healthy tissues, poor clinical outcomes may result. Such dosimetric discrepancies are investigated in this work with the development of a novel deformable dosimeters, and recommendations are provided on improved means of dosimetry, image-registration, dose reconstruction and treatment planning for more accurate dose delivery.

1.2 Context

Radiation treatment has evolved over the past 20 years from two dimensional (2D) therapy to three-dimensional (3D) conformal treatment aimed at delivering lethal dose of radiation to a complex-shaped target whilst minimising damage to surrounding healthy tissues (normal tissue sparing). To facilitate this, it is necessary to spatially restrict the high dose to a volume of tissue that incorporates only the tumour, and a small margin to ensure elimination of microscopic tumour extensions and account for any error in setup (ICRU, 1999). During the last two decades, a number of advanced treatment techniques have been developed to achieve more conformal radiation beam delivery. These new and emergent techniques allow more precise localisation of higher doses to the target volume while sparing more healthy tissues. However, the fact that anatomic structures move during respiration has been a well-known key challenge facing physicists and clinicians in contemporary radiotherapy and much research is presently being devoted to strategies to contend with organ motion. In this context, many strategies for motion management have been addressed and investigated over the past few decades.

The existence of organ deformation associated with anatomic motion adds a further layer of complexity to the problem of inter- and intra-fractional variation in anatomic structures; the resultant dosimetric consequences have not been explicitly investigated in current routine clinical practice. The variations could result from filling and emptying of bladder, rectum, stomach, etc., as well as respiratory and cardiac motion. The organ deformation inherent to inter- and intra-fractional anatomic motion complicates the measurement and calculation of

dose distribution. Any inaccuracy in dose prediction or delivery may have detrimental consequences for patients as a result of under-dosage of the tumour if improper margins are employed or over-irradiation of healthy tissues in the immediate periphery of a targeted lesion, which is not accurately known. Such doses can result in reduced tumour control and an increased relative risk of radio-carcinogenesis and other health complications as a consequence of the treatment.

There is a pressing need to investigate dosimetry in deforming targets during and/or between treatments so as to ensure accurate calculations for dose accumulation and delivery. This has consequently driven the research and development of four-dimensional (4D) treatment planning in order to deliver the most positive outcome for patients. The techniques and results discussed in this thesis are applicable to a range of fields within radiotherapy such as complex 3D dosimetry, deformable medical image registration, dose-warping, and adaptive 4D treatment planning. These have extensions to patient specific dose delivery.

1.3 The objective and scope of this thesis

The objective of this thesis is to model and verify doses delivered to deformable moving targets. This incorporates two key components: a tumour surrogate that enables 3D integrating measurement of complex and re-distributed dose in deforming objects (*an experimental model*); and calculation techniques that enable deformed dose distributions to be estimated (*a mathematical model*). The development of the novel deforming dosimeter is important for validation of the model. Such work is utilisable for the evaluation of conventional treatment planning, which does not take organ deformation into account in the treatment optimisation process. This is to improve the prediction and delivery of conformal-field dose distributions and thereby reduce the probability of potential detriment to the patient.

In this work, the most promising methods of experimental dosimetry and mathematical image processing are implemented for the verification of dose deformation: gel dosimetry and deformable image registration. The studies described in this thesis not only involve the application of these methods, but build on them fundamentally. In addition to the complexities of the dose distributions in deformable moving objects, is the issue of the lack of tools to predict dose deformations and of limitations of computation power and time consumption. In this context, the immediate clinical relevance of this work is application of the evaluated calculation method to patient treatment planning. To illustrate this capability,

this work investigates dosimetric discrepancies between planned and delivered doses in linac-based stereotactic body radiotherapy for liver cancer. Furthermore, this work provides estimates of tumor control and normal tissue complications. Such complexities are not considered in current treatment optimisation processes, and limitations of current commercial planning systems do not allow accurate dose calculations on deformable moving anatomy.

In summary, the structure of this thesis, titled *'Modelling and verification of doses delivered to deformable moving targets'*, and topics of each chapter are concisely described here:

- Background of challenges/difficulties dealing with deformable moving targets (Chapter 2):

    Interfraction and intrafraction variation in anatomic structures is a significant challenge in contemporary radiotherapy. Understanding the cumulative dose distribution in deforming anatomy can be difficult due to complex dose redistribution and lack of measurement tools in order to verify computation of dose redistribution and its accumulation;

- Developing a deformable dosimeter (Chapter 3):

  - The study in Chapter 3 develops and introduces a novel, tissue-equivalent 3D deformable gel dosimetric phantom, DEFGEL, which can be subject to deformation and relaxation followed by CT imaging and planning for irradiation of a certain field. This enables direct measurement of redistributed dose distribution and its accumulation in different state of deformation, i.e. 4D deformable dosimetry;

- Assessing deformable image registration (Chapter 4):

  - One proposed strategy for calculating deformed dose distributions uses DIR. This approach is constrained by the accuracy of the results of the DIR calculation. In this chapter, the performance of 11 algorithms, which are available in the public domain, is assessed for deformations of the new deformable dosimeters, particularly in low-contrast region.

- Validating dose deformation calculation (Chapter 5):

  - Having tools for i) direction measurements of dose redistribution in deforming geometry and ii) its corresponding caluclations *via* DIR, this chapter presents a novel approach to experimentally validate DIR based dose-warping technique. This study trials 11 DIR algorithms, of which accuracies have been evaluated in the previous chapter, for different complexities of beam geometry/deformation combinations;

- Applying these to evaluate patient treatment planning (Chapter 6):

  - The straightforward application of the validated dose-warping method is to implement 4D dose accumulation into the evaluation of conventional 3D plans that feature step dose gradients and respiratory movement as well as the associated deformation. In this chapter, the 4D method is applied to several liver SBRT plans in order to give a better dose estimate for target as well as OARs and compare to the 3D planning results; and

- Conclusion and recommendations (Chapter 7).

1.4 Scientific publications and presentations arising from this work

The present work has yielded 6 publications in international peer-reviewed journals (including 5 full journal articles and 1 correspondence letter to a point-counterpoint paper), 3 publications in international peer-reviewed conference series, 15 international and local conference presentations and 5 invited seminars.

1.4.1 Publications in international peer-reviewed journals

(1) **UJ Yeo**, ML Taylor, L Dunn, RL Smith, T Kron and RD Franich (2012)
A novel methodology for 3D deformable dosimetry
Medical Physics, **39** (4), 2203-2213. doi: 10.1118/1.3694107

(2) **UJ Yeo**, ML Taylor, RL Smith, JR Supple, L Dunn,T Kron and RD Franich (2012)
Is it sensible to 'deform' dose? 3D experimental validation of dose-warping
Medical Physics, **39** (8), 5065-5072. doi: 10.1118/1.4736534

(3) ML Taylor, **UJ Yeo**, T Kron, JR Supple, S Siva, D Pham and RD Franich (2013)
Comment on "It is not appropriate to 'deform' dose along with deformable image registration in adaptive radiotherapy"
Medical Physics, **40** (1), 0171011-0171013. doi: 10.1118/1.4771962

(4) **UJ Yeo**, ML Taylor, RL Smith, JR Supple, L Dunn,T Kron and RD Franich (2013)
Performance of 12 DIR algorithms in low-contrast regionsfor mass and density conserving deformation
Medical Physics, **40** (10), 101701-101711. doi: 10.1118/1.4819945

(5) **UJ Yeo**, ML Taylor, T Kron, D Pham, S Siva and RD Franich (2014)
Evaluation of dosimetric misrepresentations from 3D conventional planning of liver SBRT using 4D deformable dose integration
Journal of Applied Clinical Medical Physics, **15** (6), 188-203. doi: 10.1120/jacmp.v15i6.4978

(6) M Taylor, **UJ Yeo,** J Supple, S Siva, T Kron, D Pham, A Haworth and RD Franich (2015)
The importance of quasi-4D path-integrated dose accumulation for more accurate risk estimation in stereotactic liver radiotherapy
Technology in Cancer Research and Treatment, **14**, 1533-0346 doi: 10.1177/1533034615584120

1.4.2 Publications in international peer-reviewed conference series

(1) **UJ Yeo**, ML Taylor, JR SuppleL, RL Smith, T Kron and RD Franich (2013)
Deformable gel dosimetry I : Application to external beam radiotherapy and brachytherapy
Journal of Physics: Conference Series, **444**, 012032. doi:10.1088/1742-6596/444/1/012032

(2) **UJ Yeo**, ML Taylor, JR SuppleL, RL Smith, T Kron and RD Franich (2013)
Deformable gel dosimetry II : Experimental validation of DIR-based dose-warping
Journal of Physics: Conference Series, **444**, 012107. doi:10.1088/1742-6596/444/1/012107

(3) **UJ Yeo**, ML Taylor, JR SuppleL, RL Smith, T Kron and RD Franich (2013)
Potential dosimetric benefit of dose-warping based 4D planning compared to conventional 3D planning in liver stereotactic body radiotherapy (SBRT)
Journal of Physics: Conference Series, **444**, 012071. doi:10.1088/1742-6596/444/1/012071

1.4.3 Conference presentations

(1) UJ Yeo, ML Taylor, JR Supple, RL Smith, T Kron and RD Franich
3-D experimental validation of deformation-based dose accumulation
Engineering and Physical Sciences in Medicine (EPSM) 2 – 6 Dec 2012, Melbourne, Australia
(Oral)

(2) UJ Yeo, ML Taylor, T Kron, D Pham, S Siva, RD Franich
Dosimetric differences between conventional 3D-treatment planning and 4D dose-warping cumulative treatment planning: Patient study in the case of liver SBRT
Engineering and Physical Sciences in Medicine (EPSM) 2 – 6 Dec 2012, Melbourne, Australia
(Oral)

(3) JR Supple, UJ Yeo, ML Taylor, RL Smith, T Kron and RD Franich
Experimental assessment of intensity-based DIR accuracy in low-contrast regions
Engineering and Physical Sciences in Medicine (EPSM) 2 – 6 Dec 2012, Melbourne, Australia
(Oral)

(4) ML Taylor, UJ Yeo, J Supple, S Keehan, T Kron, D Pham, S Siva and RD Franich
Normal tissue complications and latent stochastic effects following liver SBRT: Quantitative differences between 3D and 4D planning methodologies
Engineering and Physical Sciences in Medicine (EPSM) 2 – 6 Dec 2012, Melbourne, Australia
(Poster)

(5) UJ Yeo, ML Taylor, RL Smith, T Kron and RD Franich
Deformable gel dosimetry I: Application in external beam radiotherapy and brachytherapy
7th International Conference on 3D Radiation Dosimetry (IC3DDose) 4 – 8 Nov 2012, Sydney, Australia (Oral)

(6) UJ Yeo, ML Taylor, JR Supple, RL Smith, T Kron and RD Franich
Deformable gel dosimetry II: Experimental validation of DIR-based dose-warping technique
7th International Conference on 3D Radiation Dosimetry (IC3DDose) 4 – 8 Nov 2012, Sydney, Australia (Oral)

(7) UJ Yeo, ML Taylor, T Kron, D Pham, S Siva, RD Franich
Potential dosimetric benefit of dose-warping based 4D planning compared to conventional 3D planning in the case of liver SBRT
7th International Conference on 3D Radiation Dosimetry (IC3DDose) 4 – 8 Nov 2012, Sydney, Australia (Oral)

(8) UJ Yeo, JR Supple, ML Taylor, RL Smith, T Kron and RD Franich
Experimental quantification of errors in low contrast regions during deformable image registration
World Congress on Medical Physics and Biomedical Engineering (WC) 26 – 31 May 2012, Beijing, China (Oral)

(9) UJ Yeo, ML Taylor, JR Supple, RL Smith, L Dunn, T Kron and RD Franich
3D Experimental validation of DIR-based dose warping for interfraction deformation of soft tissue
World Congress on Medical Physics and Biomedical Engineering (WC) 26 – 31 May 2012, Beijing, China (Oral)

(10)   UJ Yeo, ML Taylor, L Dunn, RL Smith, T Kron and RD Franich
Dose integration with the first deformable tissue-equivalent gel phantom

World Congress on Medical Physics and Biomedical Engineering (WC) 26 – 31 May 2012, Beijing, China (Poster)

(11) L Priestley, UJ Yeo, D Pham, T Kron, A Thompson, F Foroudi and S Siva
Renal Stereotactic Ablative Body Radiotherapy Treatment: Dosimetric impact of deep and shallow breathing
10th Annual Scientific Meeting of Medical Imaging and Radiation Therapy (ASMMIRT) 8 – 10 Mar 2013, Hobart, Australia (Oral)

(12) UJ Yeo, ML Taylor, L Dunn, RL Smith, T Kron and RD Franich
A novel methodology for 3D deformable dosimetry
Engineering and Physical Sciences in Medicine (EPSM) 14 – 18 Aug 2011, Darwin, Australia (Oral)

(13) UJ Yeo, ML Taylor, RL Smith, JR Supple, T Kron and RD Franich
Is it sensible to 'deform' calculated doses? Experimental validation of 'dose warping' with the first 3D deformable dosimeter
Engineering and Physical Sciences in Medicine (EPSM) 14 – 18 Aug 2011, Darwin, Australia (Oral)

(14) UJ Yeo, ML Taylor, JR Supple, RL Smith, L Dunn, T Kron and RD Franich
Validation of common deformable image registration (DIR) algorithms with a novel deformable phantom
Engineering and Physical Sciences in Medicine (EPSM) 14 – 18 Aug 2011, Darwin, Australia (Poster)

(15) RL Smith, UJ Yeo, ML Taylor, L Dunn, T Kron and RD Franich
3D Deformable Dosimetry in High Dose Rate Prostate Brachytherapy
Engineering and Physical Sciences in Medicine (EPSM) 14 – 18 Aug 2011, Darwin, Australia (Poster)

1.4.4 Invited seminars

(1) *Modelling and verification of delivered dose on deformable moving targets in radiotherapy*
RMIT University, Melbourne, Dec 2012

(2) *Complexities in computational modelling and verification of radiation beam delivery*
Victorian Life Sciences Computation Initiative (VLSCI), Melbourne, Nov 2012

(3) *Use of the first tissue-equivalent 3D deformable gel dosimetry (DEFGEL) to validate dose-warping technique*
Australasian College of Physical Scientists and Engineers in Medicine (ACPSEM), VIC/TAS Branch Seminar, Jun 2012

(4) *Quantitative assessment of intensity-based DIR accuracy in low-contrast regions using a tissue equivalent deformable gel phantom*
Australasian College of Physical Scientists and Engineers in Medicine (ACPSEM), VIC/TAS Branch Seminar, Jun 2012

(5) *A deformable gel 'DEFGEL' and its used in dose mapping: 4D dose calculation*
Urology Group, Peter MacCallum Cancer Insititute, Melbourne, Oct 2011

CHAPTER TWO

: Dosimetric challenges in radiotherapy of moving and deforming targets

"Nothing's ever easy."

  Rick Franich's 1st Law, the author's primary supervisor

2.1 Overview of chapter

In this chapter, the literature is reviewed to demonstrate that motion and deformation are important issues in contemporary RT. The nature of dose prescription, conformal treatment planning and its delivery mean that uncertainties in the position and shape of targets can result in under-dosage of the target, over-dosage of neighbouring healthy tissues. Consequent miscalculation of cumulative doses from multi-fraction treatments is self-evident. Strategies for dealing with motion and deformation are described, together with a proposed strategy for modelling accumulated dose (dose-warping). Lastly, three dimensional dosimetry tools are presented, which provide the basis for experimental validation of deformable dosimetry and dose warping, enabling clinical application of deformable dose accumulation to evaluate patient treatment plans.

2.2 The therapeutic cell killing mechanism through radiotherapy

When ionising radiation is incident upon a human body, the radiation interacts with matter – tissues, in more depth cells, and ultimately with deoxyribonucleic acid (DNA). The desired outcome in the context of radiotherapy is the resultant biological damage from the cell-killing mechanism through the interaction of ionising radiation with the tissues.

From a radio-biological perspective, DNA is recognised to be the primary target for cell inactivation by ionising radiation that causes chromosomes to break, exposing part of the DNA of rapidly dividing cells, including tumour cells. Cell death (i.e. cytotoxic effect) induced by radiation is most likely the result of lack of repair or misrepair of complex lesions in DNA (Goodhead, 1994, Hüttermann et al., 1978, Todd, 1983, Olive, 1998).

From a radio-biochemical perspective, there is scientific consensus that the cytotoxic effect of ionising radiation is caused by the interaction of the DNA molecule with free radicals generated from a cascade of radiolysis products (mainly with hydroxyl free radicals), resulting in direct or indirect breaks of DNA strands (Gordon, 1957, Hagen, 1989, Hüttermann et al., 1978). The direct DNA breaks results in ionisation that can occur within DNA, while the indirect breaks occur via the interaction with the free radical(s) generated from the radiolysis of water molecules (Alpen, 1997), which is the predominant molecule existing in all living organisms.

From a radiological physics perspective, the incident high-energy photons or electrons interact (either directly or indirectly) with surrounding tissues producing a cascade of high-speed electrons that are able to split water molecules. It is these electrons that deliver a 'dose' to tissues, and in more depth that cause DNA breaks.

From a clinical or physiological perspective, the DNA of a cell is vulnerable to breakage during all stages of the mitotic process (Barendsen, 1982). Normal cells do not experience as much of a deadly result as cancerous cells do because normal cells are not dividing as rapidly and normal cells have the ability to repair the damaged DNA while the cancerous cells cannot repair themselves after the DNA breaks. (Wolfson, 1999). Such relatively different radiosensitivities yield the concept of '*therapeutic ratio*' that effectively works throught a probabilistic process (see Figure 2-1).
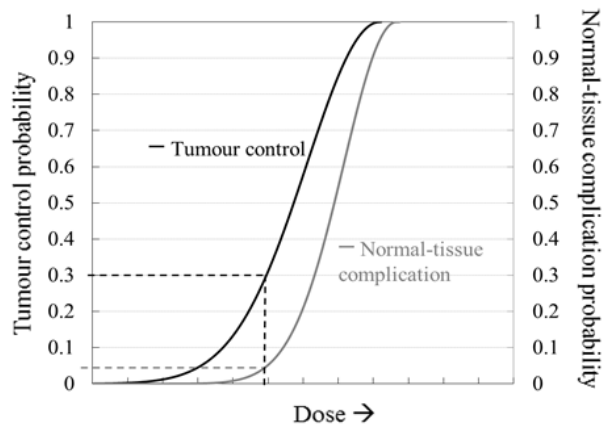
Figure 2-1 An example of idealistic dose-response curve illustrating the concept of therapeutic ratio. Note in this example, about 30 % tumour control can be achieved for a 5% incidence of normal tissue damage or complication probability (NTCP).

In this context, the basis for multiple fractionations was conceptualised in radiotherapy (Arcangeli et al., 1979) in order to deliver a lethal dose to the cancerous cells whilst sparing adjacent (healthy) tissues by delivering a sub-lethal dose However, different healthy tissues/organs also have relatively different sensitivities to ionising radiation, thus different parameters are used to estimate tumour control probability (TCP) and normal tissue complication probability (NTCP) of different organs (Thames et al., 1983). The conventionally standardised fractionation scheme, used by most radiation oncologists use today, administrates 1.8 - 2.0 Gray (Gy) once daily prescriptions for up to six weeks; this has developed over many years as a result of both radiobiological experiments and clinical experience (Strauss et al., 1981, Peracchia and Salti, 1981, Lyman, 1985, Lee et al., 1995, Yamada et al., 1999). There are also *many* variations outside (either less or more) of the standard fractionation scheme in modern treatment techniques.

2.3 Advanced treatment techniques and dose-to-volume specification

With the emergence of advanced computer power and reliability in the late 20th century, it was a natural consequence that these advances would greatly impact the medical radiation physics era to develop new techniques. Such development does not only include medical volumetric (3D) imaging modalities, such as CT, Magnetic Resonance Imaging (MRI), Positron Emissioin Tomography (PET), ultrasound etc., but also accurate volumetric (3D) treatment planning and delivery.

With the turn of the 21st century, a number of new techniques dealing with the 'dynamic (temporal variation)' paradigm for both imaging and dose delivery became clinically available. For examples, new imaging techniques such as four-dimensional CT (4DCT) and its fusion with PET/MRI are now routinely implemented in clinical practice; this yields the concept of 4D treatment planning and delivery (Keall et al., 2005). Cone-beam CT and MV imaging also allow more precise localization of target volumes. Consequently, dose-to-volume specification has been evolved, which is briefly described below.

For a dose prescription, volumes of interest (VOI) must be specified to deliver the prescribed dose to a target while sparing specific volumes of organs-at-risk (OAR). The International Commission on Radiation Units and Measurements (ICRU) Reports (ICRU, 1978, ICRU, 1993, ICRU, 1999). provided the radiation oncology community a consistent language and a methodology, in terms of prescribing, recording and reporting for image-based volumetric treatment planning, in which the physician specifies the VOI, such as tumour or target as well as OARs. A summary of the ICRU volume nomenclature per report is shown in Figure 2-2.
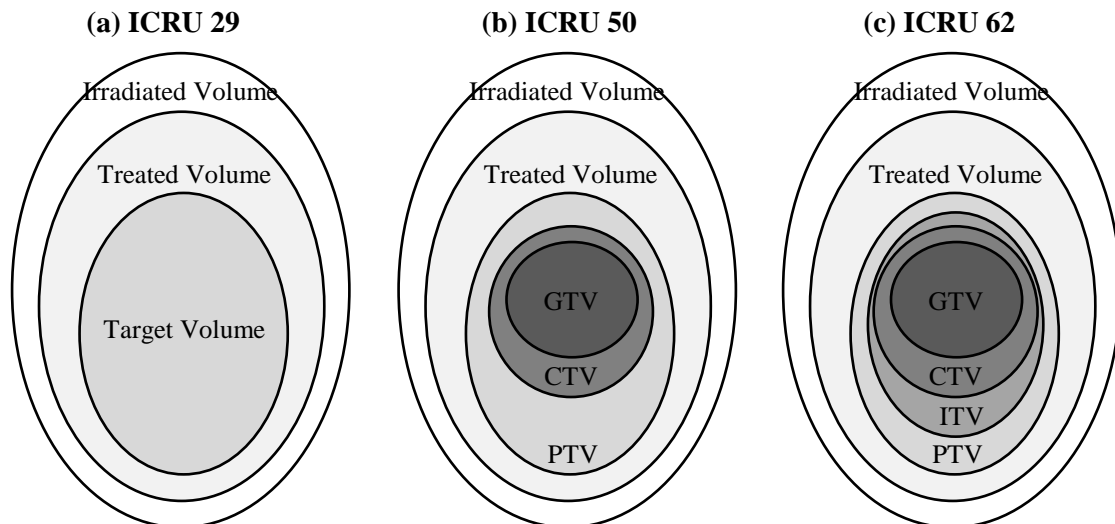
Figure 2-2 Schematic illustration of the volumes defined by ICRU reports: (a) ICRU Report 29, (b) ICRU Report 50, and (c) ICRU Report 62, illustrating different concepts of dose prescription.

Two dose volumes (irradiated volume and treated volume) are consistent throughout the history of ICRU publications; Report 29 defined two dose volumes:

(i)   *the treatment volume* that is enclosed by the isodose surface representing the minimal target dose; and

(ii)   *the irradiated volume* that receives a dose considered significant in relation to normal tissue tolerance (e.g. 50% isodose surface).

These volumes were not based on anatomy but instead were based on the dose distribution. The volumes of *organs at risk (OARs)* are defined for especially radiosensitive organs in or near the target volume whose presence influences treatment planning and/or prescribed dose.

The definition of target volumes has been evolved to take into account spatial/temporal uncertainties stemming from inter- and intra-fractional anatomic changes due to organ motion/deformation. ICRU Report 62 (a supplement to the report 50) refined the definition of PTV by introducing the additional margin concepts as follows:

(i) Internal margin (IM) – taking into account variations in size, shape, and position of the CTV referenced to patient anatomic coordinate system;

(ii) Setup margin (SM) – taking into account all uncertainties in patient-beam positioning referenced to the treatment machine coordinate system; and

As such, the definition of the target volume is separated into four distinct boundaries:

(i)   Gross target volume (GTV) – visible or palpable (via clinical examination) tumour region i.e. the volume of known tumour;

(ii)   Clinical target volume (CTV) – a region to account for uncertainties in microscopic tumour spread or subclinical extension;

(iii) Internal target volume (ITV) – formed by the CTV and the IM, representing the excursion of the CTV due to internal organ motions (e.g. breathing motion or filling and emptying of rectum, bladder, stomach etc.).

(iv) Planning target volume (PTV) – formed by the ITV and the SM to account for geometric uncertainties.

The GTV and CTV are anatomic-clinical concepts that are defined before a choice of treatment modality and irradiation technique, while the ITV and PTV are static-geometrical concepts defined by specifying the IM and SM margins. Using the analogy to the ITV, the supplementary report also introduced the concept of the planning organ at risk volume (PRV), in which a margin is added around the OAR to compensate for that organ's geometric uncertainties.

The implementation of spatial and/or temporal modulation of radiation beams with high-dose and steep dose-gradient has been necessitated for conformal treatment of cancerous lesions. The development of such delivery techniques could implement highly conformal and dynamic fields (e.g. IMRT/VMAT), and may include specific alterations to the conventional fractionation scheme, such as stereotactic body radiotherapy (SBRT) or streotactic radiosurgery (SRS). Consequently, in conjunction with precise imaging techniques, these treatment techniques could yield 3D dose distributions that are tightly conformed to the specific target volume (e.g. PTV). Such evolution enabled the advanced RT to increase its treatment quality, so as to achieve the fundamental goal of RT – 'precise localisation of lethal dose to tumours while sparing surrounding organs'. In particular, dose escalated radiotherapy, at more extreme high-dose per fraction courses, for instance, 6 – 10 Gy per fraction) is the treatment standard for some locally advanced disease and is also viable treatment option for early stages (Peeters et al., 2005, Pollack et al., 2000, Kupelian et al., 2008). As such, accurate localisation is critical as the consequences for complications in irradiated tissues may be more significant, e.g. acute side effects may present a number of days after the treatment is complete.

The treatment of a deformable moving target results in a 'blurred' dose distribution around the periphery occupying a large fraction of the field volume. This necessitates accurate knowledge of dosimetry and clear understanding of dose prediction that is difficult to measure and calculate in the case of implementing conformal small-fields. Such issues are discussed in the following section. The focus of the current work is to address issues associated with the accuracy of current dose measurement and calculation methodologies as applied to treatment planning and its delivery in the presence of deformation, which, if inaccurate, can lead to complications for the patient.

2.4 The challenge of anatomic motion and deformation

2.4.1 Overview: why/how is it challenging?

The human anatomy is subject to motion and deformation. Clinically, inter- and intra-fractional uncertainties due to this fact lead to the systematic exposure of larger volumes of healthy tissue in the vicinity of the targeted tumour and a miscalculation of dose volume histograms, tumour control and normal tissue complication probabilities. Consequently, any inaccuracy in calculation or measurement of dose delivery can lead not only to over-dosage of healthy tissues, but also to tumour under-dosage if motion is not properly managed or accounted for and/or margins are not adequate. Unfortunately, the latency and stochastic nature of the potentially detrimental outcomes means that errors are often neither identified immediately nor estimated later as a long term risk. This renders clinicians less confident than when employing broader-beam treatment in 1990's RT history. In this context, the use of conformal fields is often considered to add a level of uncertainty to radiation beam delivery for both targets and surrounding organs that are subject to motion and deformation. This fact challenges i) verification of dose delivery and ii) prediction of delivered dose through treatment planning; the former is the dose measurement and the latter is the dose calculation. In particular, inaccuracies in both components are more pronounced when implementing spatial and/or temporal modulations of radiation beams, compared to 'stationary' beams and targets.

Many factors induce anatomic variations. Organ motion during patient breathing (intrafraction motion) causes the greatest variation; in addition, filling and emptying of bladder, rectum and stomach between treatments (interfraction motion) also results in significant variations. In such cases, there is a potential for the interplay between organ motion and dose delivery. Such interplay may occur within a treatment session called '*intrafraction effect*' or even between treatment sessions, referred to as '*interfraction effect*'. Hence, dose accumulation over the period of treatment is not a trivial practice at all. This implies a need for using image guidance and fixing devices such as a stereotactic localiser or abdominal pressure plate, to achieve precise localisation of the fields to the target. On the other hand, there is the lack of tools for *3D measurements* necessary to verify the beam delivery when any volumes in the field move and/or deform. Dose-measurement-based verification, coupled with their greater dose distribution complexity and the temporal nature

of dose delivery, is complicated by loss of lateral electronic equilibrium and detector volume effect.

All these issues make the resultant 'blurred' dose distribution difficult to measure and/or calculate. Such difficulty limits not only radiation dose delivery but also image acquisition and treatment planning. The aim of this chapter is to provide an overview of such issues that cause the difficulty, with the objective of giving the reader an understanding of the complexities and challenges with the use of advanced RT techniques. Such issues are mainly:

(i)   organ motion/deformation management due to breathing and emptying/filling of organs in advanced RT;

(ii)   various dosimeters that are subject to 'volume averaging effect' caused by the finite size of the detectors;

(iii)   limitation of dose calculation and associated treatment planning that implements a 'snap-shot' of anatomic image which cannot adapt inter- and intra-fraction effects;

(iv)   lack of measurement tools such as 3D dosimetry that can verify/quantify discrepancies between dose estimate and actual delivery in the presense of organ motion and deformation.

2.4.2 Management of anatomic variations: inter-fraction motion

A number of studies have established strategies for motion management that are currently being used in clinics worldwide; much research is still increasingly being devoted to strategies to contend with organ motion. These strategies encompass the image acquisition through to treatment planning to radiation dose delivery. Interfraction motion occurs when the tumour position changes on a day-to-day level or between treatment sessions (i.e. fractionation). Various lesions are subject to interfraction motion including stomach, bladder, rectum, prostate, and gynaecological lesions, which are associated with organs that are part of or adjacent to the digestive system (Langen and Jones, 2001). In addition, the loss or gain of patient weight as well as organ atrophy can also affect the relative tumour position. The extent of interfraction motion for these lesions was investigated in numerous studies; some examples of interfraction motion are described below:

-   Wysocka et al. quantified the interfraction motion of gastric lesions (*stomach*) relative to point of interest (POIs; splenic hilum that is the point of attachment of the gastro-splenic ligament on the surface of the spleen) for 22 patients. A median displacement of ~6mm was seen in superior-inferior (SI) direction and ~2 mm in other directions (Wysocka et al., 2010).

- Turner et al. investigated *bladder* movement for 30 patients with invasive bladder carcinoma. A transversal bladder wall displacement over 15 mm was found in 60 % of the patients with the maximum displacement of 27 mm. The variation in rectal diameter ranged from 3 to 46 mm with median of 13 mm (Turner et al., 1997).
- Ten Haken et al. evaluated interfraction motion in *prostate* position in response to variations in bladder and rectum filling. Prostate movement > 5mm was observed in 31 of 50 patients with dominant directions of displacement being anterior and/or superior (Ten Haken et al., 1991).
- Buchali et al. assessed the mobility of *gynaecological lesions* (i.e. cervical and endometrial tumours) for 29 patients in response to bladder and rectum filling levels. Superior-inferior (SI) direction movements were ~4 mm and ~7 mm for both the cervix and the corpus uteri respectively, without a significant AP direction movement (Buchali et al., 1999).

Image guidance is a key technique to deal with interfraction changes. Image guidance is not only to improve patient setup but allows to 'adapt' to anatomic changes before or during the treatment sessions, which is often referred to as *adaptive radiotherapy (ART)*. In the non-adaptive case, the treatment is not altered, but daily images are used for patient set-up correction, referred to as image-guided radiotherapy (IGRT). There are various modalities used as image guidance to detect the variation via internal implanted fiducials or external markers; such are kilovoltage (kV) and/or megavoltage (MV) imaging, MRI, ultrasound, PET and so on.

ART emcompasses a wide range of processes including image acquisitions from different imaging modalities, automated segmentation of planning CT images, dose reconstruction using the CT image set, deformable registration of the acquired images, and re-optimisation. One example of ART (e.g. bladder treatment) is to take one and/or multiple CT scans (up to 3) in different phases of bladder filling/emptying and use to generate treatment plans. Daily CT imaging may indicate any subsequent changes since the original CT scan(s) and plan(s). According to the change in anatomy evident in the image, the best plan can be chosen. Treatments may not be adapted if the variation due to interfraction motion is under a certain *action-level* that is protocol-specific, depending on lesion site, size, motion, position relative to surrounding organs etc., which may vary in different hospitals. As such, the nature of the resultant dose distribution is less readily calculated than the one with the *absence* of anatomic changes and *static* dose distribution.

2.4.3 Management of anatomic variations: intrafraction motion

Intrafraction motion mainly occurs due to respiration of the patient during a treatment session. Various lesions are subject to this issue, such as lung, liver, kidney and pancreatic lesions. Intrafraction motion can yield different degrees of extent of movement for tumours in these organs; a concise overview of such motion reported in the literature is described here:

- Seppenwoolde et al. quantified three-dimensional motions of lung tumours using fluoroscopy in 20 patients whose tumours were located in different regions of the lungs, such as the lower, middle, and upper lobes. The mean peak-to-peak displacement was ~ 2 mm (with a range of 0.2 – 2.8 mm), ~ 2 mm (with a range of 0.2 – 8.2 mm), and ~ 12 mm (with a range of 0.2 – 24.6 mm) for the lateral, AP, and SI, respectively (Seppenwoolde et al., 2002).
- Suramo et al. measured *liver* movements in 50 patients using ultrasound. The mean peak-to-peak displacement observed was 25 mm (with a range of 10 – 40 mm) and 55 mm (with a range of 30 – 80 mm) under normal- and deep-breathing, respectively (Suramo et al., 1984).
- Weiss et al. assessed *diaphragm* movements in 30 patients using fluoroscopy. Under shallow breathing, the mean peak-to-peak diaphragm movement was found to be 13 mm and 8 mm for supine patients and standing patients respectively. During deep-breathing, the movement ranged from 12 to 75 mm for all patient positions (Weiss et al., 1972).
- Moerland et al. studied *kidney* movements in 14 volunteers using MRI. The mean peak-to-peak displacement ranged 2 – 35 mm and 10 – 86 mm under normal-breathing condition (for 25 kidneys) and deep-breathing condition (for 22 kidneys), respectively (Moerland et al., 1994).
- Bryan et al. investigated *pancreas* movements in 35 patients using ultrasonography. The mean peak-to-peak displacement of 18 mm, 19 mm, and 22 mm were measured for supine, prone, and lateral decubitus patient positions respectively, with a range of 0 – 35 measured over all patient positions (Bryan et al., 1984).

Various strategies were investigated to manage intrafractional breathing motion. This issue was comprehensively reviewed by the American Association of Physicists in Medicine (AAPM) Task Group 76 report (Keall et al., 2006), which advised on various forms of motion management, such as motion-encompassing CT, breath-holding, beam-gating technique and real-time tracking.

A. Motion-encompassing CT scanning

Accurately estimating the mean position and range of motion during CT imaging is important because tumour motion induced by respiration will be present during radiation delivery (which is referred to ICRU Report 62, as mentioned in Section 2.). There are several CT scanning techniques in existence that account for the entire range of tumour motion during respiration, such as slow CT (Lagerwaard et al., 2001, van Sörnsen et al., 2001), inhalation and exhalation breath-hold CT (Keall et al., 2006), and respiration-correlated 4DCT (Vedam et al., 2002, Keall, 2004). These approaches are effective in obtaining a tumour-encompassing volume for the patient's breathing, but limitations of such techniques exist.

In the slow CT scanning, the limitation is the loss of resolution due to motion blurring from free-breathing for the slow scan, thus, additional margins are required to account for these variations (Lagerwaard et al., 2001, van Sörnsen et al., 2001). Although the blurring artefact is not caused in inhalation and exhalation breath-hold CT scanning, taking two CT scans at the both endphases takes longer, almost twice the time and it relies on the patients' ability to reproduce their breath holding. Respiration correlated 4DCT is a promising solution for obtaining high quality CT data in the presence of respiratory motion (Vedam et al., 2002, Keall, 2004). The four-dimensional dataset provides the mean tumour position as well as the range of motion with the relation of tumour trajectory to the other organs. However, the AAPM report 76 provided an important note that the radiation dose to the patient from these imaging procedures can be greater than standard CT simulation procedures by a factor of 2–15 if no efforts are made to reduce the dose delivered, and tumour motion may change between simulation sessions and treatment sessions (Keall et al., 2006)

B. Beam-gating technique

Beam 'gating' refers to the administration (switching on/off) of the radiation beam during both imaging and treatment delivery within a particular portion of the patient's breathing cycle, e.g. both ends of respiratory phases (inhalation and exhalation).The duty cycle (the fraction of time a radiation beam is active during the delivery of a respiratory gated treatment field) can be determined by monitoring the breathing cycle by using different means. Examples are the use of an external respiration signal using an infrared light source from the camera attached to ceiling (or wall), being reflected from a IR reflector placed on the chest wall, e.g. the Real-time Position Management (RPM) system (Varian Medical Systems, Palo Alto, CA), or internal fiducial markers with image-guidance, e.g. gold spheres or rod implants monitored via digitally reconstructed radiograph (DRR) (Shirato et al., 2000, Shirato et al., 2003). Respiratory-gated IMRT was demonstrated and evaluated for its clinical use by a number of studies (Kubo and Wang, 2000, Hugo et al., 2002, Duan et al., 2003). Mageras et

al investigated the gating technique by comparing it with deep-inspiration breath hold (DIBH) approach for reducing organ motion. It is noted that treatment session times with gated operation are increased relative to standard treatments by 2–10 min depending on patient compliance. Consequent considerations with increased delivery time are the increased likelihood of patient movement and decreased patient throughput as well as patient comfort (Mageras and Yorke, 2004).

C. Controlled breathing methods

There are several variations of breath-holding method depending on the location of lesion and patients' ability to reproduce the desired holding patterns. Such variations are the deep-inspiration breath hold (DIBH), active-breathing control (ABC) with the facilitation of a control device, self-held breath hold with or without respiratory monitoring and forced shallow breathing with abdominal compression. These controlled breathing methods have been favourably implemented in thoracic and abdominal cancer radiotherapy (e.g. lung, breast, liver etc.), because the methods are fairly simple and substantially reduce respiratory tumour motion. Consequently the breath-hold methods can significantly reduce doses in surrounding normal tissues such as breast (Remouchamps et al., 2003a, Korreman et al., 2005), heart and lung (Sixel et al., 2000, Remouchamps et al., 2003b, Pedersen et al., 2004, Duggan et al., 2007) and liver and spinal cord (Lax et al., 1994, Blomgren et al., 1995, Lohr et al., 1999, Timmerman et al., 2005). These studies, including a study by Berson et al that reported on 108 patients treated with either a free-breathing gating technique or the breath-hold technique (Berson et al., 2004), found several advantages of implementing the breath-hold technique. Advantages cited are the reduction of time for a single-slice CT scan as well as treatment delivery by a factor of two relative to the free-breath gating; the elimination of a possible time delay between the tumour motion and the motion of external marker or internal fiducials; and improved diaphragm positional reproducibility.

D. Real time tumour tracking methods

Another approach to contend with intrafraction breathing motion, which can be differentiated from the other respiratory 'compensation' methods, is 'real-time tumour tracking'. This refers to synchronising the position of radiation beam dynamically following the tumour's changing position. The conceptual thought for this approach has been in existence for a long time but the first systematic implementation was consolidated by Keall et al (Keall et al., 2005). They addressed that the real-time tumour tracking can eliminate the need for a tumour-motion margin in the dose distribution, while maintaining a 100% duty cycle for dose delivery. This method can be performed using dynamic multi-leaf collimators (DMLC) for temporal/spatial beam modulations and various means of detecting/monitoring tumour position. Examples are

imaging of the tumour itself via e.g., fluoroscopy, implanted fiducial markers or surrogate breathing signals from an external device. Detecting the tumour position is the most important and challenging task in real-time tracking (Keall et al., 2005). In addition, since some tumour motion (e.g. lung lesion) can follow a complex 3D trajectory (Seppenwoolde et al., 2002), it requires heavy computational power to feed accurate information concerning the tumour position in real-time to DMLC, which changes its shape corresponding to the tumour position. A more detailed discussion is available in to the AAPM report 76 which provides a comprehensive review and recommendation of implementing this approach (Keall et al., 2006). Recent studies from Keall's group demonstrated the first clinical implementation of i) a real-time image guidance with kV intrafraction monitoring (Keall et al., 2015) and ii) DMLC tracking and gating deliveries into prostate treatment using VMAT modality (Colvill et al., 2014), which can improve target (CTV/PTV) converages while reducing the maximum doses to rectum and bladder.

2.4.4 Management of anatomic variations: inter- and intra-fraction deformation

Strategies dealing with motion, described in the two previous sections, do not necessarily also deal with deformation. IGRT approaches can help with improving conformality of beam shaping, but not with dosimetry associated non-rigid anatomic changes. There is clinical awareness of and interest in anatomic deformation and the dosimetric consequences thereof, and in adapting deformation to better simulate temporal/spatial anatomic changes compared to a model that linearly moves an organ as a rigid body.

Most organs will deform to some extent, typically in the millimetre-centimetre range. The potential for under-dosage of the target, over-dosage of neighbouring healthy tissues, and miscalculation of cumulative doses from multi-fraction treatments, is self-evident. This issue is related to both (i) intra-fractional effect and (ii) inter-fractional effect. A particular example of the former is the case of dose-escalated treatment for a small brain (or neck) lesions (e.g. SRS) or treatment for a mobile lung or liver lesion (e.g. SBRT) using multiple conformal beams. The latter becomes a more significant challenge than the former since various multi-fractionation schemes have been implemented in RT. A typical example is the case of treatment for a prostate that is subject to motion and deformation due to filling and emptying of the bladder and/or rectum. In such situations, it is a non-trivial practice not only to accurately deliver fractionated dose to changing anatomy, but also to calculate consequent dose accumulation in moving and/or deforming targets and the surrounding organs. The nature of the resultant dose distribution is less readily calculated than the one with the *absence* of anatomic changes and *static* dose distribution. For this reason, hypo-fractionated

treatment schemes (e.g. SBRT) that implement high doses per fraction with small number of total fractions may need strategies to adapt for non-rigid anatomy changes within the context of adaptive RT.

As a non-rigid anatomy change makes the accurate merging of dose distributions difficult, strategies for dose accumulation in deforming anatomy are of interest in radiotherapy. A proposed solution is dose-warping *via* deformable registration of images and corresponding dose distributions. Algorithms exist for the deformation of dose based on patient image sets. The warped distribution can then be added to previous fractions in order to interpret the accumulated dose. The deformation of dose distribution via the resultant vector map associated with deformable image registration (DIR) calculation is so called 'dose-warping via DIR' or 'DIR based dose-warping technique'. This technique is an existing process, proposed to accumulate doses from multiple image sets taken in different time frames. What is not well known, is the degree to which this approach is acceptable. As observed by the recent Point-Counterpoint article in Medical Physics (Schultheiss and Tomé, 2012), entitled 'It is not appropriate to "deform" dose along with deformable image registration in adaptive radiotherapy', "the ultimate problem with deformed dose is our inability to measure it".

Next, we describe tools and techniques for the complicated business of dose measurement, and ultimately demonstrate a new approach to measuring dose in a deforming target and the application to validation of dose-warping.

2.5 The difficulty of volumetric measurement of conformal fields using various dosimeters

The implementation of highly modulated small fields pose challenges for properly measuring delivered dose, i.e. quality assurance (QA) of radiation dose distributions for the verification of treatment planning systems (TPS). For the accurate measurement of dose distribution, a detector with a high degree of spatial resolution is required and should not perturb the radiation field (i.e. media-matched dectector). In the dosimetry of small fields and of steep dose gradient regions (e.g. IMRT), a well-known source of error which can occur during cross beam profile measurement, is the artificial broadening of profile penumbra caused by the finite size of the measuring detectors (dosimeters). This phenomenon is called the 'volume averaging effect'. If the size of the field approaches that of the active volume of the detector, this volume averaging effect may yield significant errors. Dose escalated radiotherapy using high dose and small field (e.g. stereotactic radiosurgery) is the particular case of possibly

having a negative impact on the measurement accuracy. Consequent detriment can be inaccurate prediction of tumour control and normal tissue complication probability thereby decreasing treatment quality.

A number of established studies have investigated this issue both theoretically and experimentally (Attix, 1986, Higgins et al., 1995, Metcalfe et al., 1997, Low et al., 2003, Laub and Wong, 2003, Bucciolini et al., 2003, Yan et al., 2008, Low et al., 2011). Referring to these references, various conventional measurement techniques (i.e. dosimeters) and potential limitations thereof are briefly discussed in this section.

2.5.1 Point-dose measurements

A. *Ionisation chamber*

Cylindrical ionisation chambers are the standard dosimeter for point-dose measurements of high energy (megavoltage, MV) photon radiation in a clinical medical physics department. This is because the ionisation chambers have high stability, a linear response to absorbed dose, small directional dependency, response independency to beam-quality, and traceability to a primary calibration standard. However, all ionisation chambers clinically used exhibit detector volume averaging effect, since the collected ions are created throughout the active chamber volume (Low et al., 2003). Significant perturbations in measurements of dose distribution caused by the volume effect will occur, in particular, in the steep dose-gradient regions of highly conformal beam delivery. Rice et al (2000) found that the finite size of an ionisation chamber introduces a volume averaging effect which can lead to overestimation of penumbras (Rice et al., 2000), implying substantial dose measurement errors for IMRT beams.

B. *Solid state (semiconductor) dosimeters*

When using detectors of smaller size, such as p-type silicon diode detector or metal oxide semiconductors transistor (MOSFET), there are various advantages for small-field measurements of MV photon radiation. Some examples include very small active volumes and high sensitivity to radiation, high stability, and *in vivo* real-time readout. However, these dosimeters introduce other problems. The relatively high atomic number of silicon in the diode detector will lead to a greater sensitivity to low-energy scattered photons (i.e. photo-electric effect), thus, diode detectors are usually used only for relative dosimetry (Higgins et al., 2003). The response of solid state dosimeters also exhibits orientation dependency, resulting in its variation up to 15% (Westermark et al., 2000). Furthermore, this detector

exhibits a couple of other dependences including dose rate dependence (Wilkins et al., 1997) and temperature dependence (Grusell and Rikner, 2000).

C. Solid state (diamond) dosimeters

In contrast to silicon diode detectors, diamond detectors are almost soft-tissue equivalent in terms of atomic composition (i.e. comprised of carbon), although they have a physical density much greater than water at 3.5 g cm^{-3}. Laub et al provided a good overview of the advantages of diamond detectors, highlighting that diamond detectors can produce clinically identical results to *p*-type silicon diodes for conformal small-field treatment (Laub et al., 1999). Diamond detectors also exhibit a small directional dependence and good mechanical stability. The most apparent problem is dose rate dependence that is attributed to the reduction in recombination time as dose rate increases, necessitating the use of correction factors. (Hoban et al., 1999). The diamond detector is less user friendly, since it requires a pre-irradiation dose before daily use to obtain sufficient response stability (Bucciolini et al., 2003).

D. Thermoluminescent detectors (TLD)

Another type of small-field dosimeter that has been routinely used in clinical environments is the thermoluminescence dosimeter (TLD), which is an integrating dosimeter formed in different shapes of small sizes, often a cubic or cylindrical chip with a typical physical density of 2.6 g cm^{-3}. Kron provided a great overview of TLDs and their application in medicine, detailing both physical and radiological aspects (Kron, 1994). Taylor calculated effective atomic numbers (Z_{eff}) for commonly used types of TLDs over 1 keV to 100 MeV, showing that Z_{eff} of TLDs is approximately 1.8 times greater than Z_{eff} of water (Taylor, 2011). The most prominent difference in the Z_{eff} is due to the relatively high atomic number of metal components. Supra-linearity of dose response is a well-known issue along with some energy response variations (Troncalli and Chapman, 2003), so that it must be evaluated and corrected for before use. TLD implementation is laborious and it requires a routine QA of the TLD reader and annealing oven temperature control, (Low et al., 2011).

2.5.2 Two-dimensional (2D) measurements

A. Radiographic film (Silver halide film)

The use of silver halide based radiographic film was until relatively recently standard practice in a clinical environment and is one of the earliest applied methods to detect x-rays (Trevert, 1896). Radiographic film, is not reusable but relatively cheaper than the other dosimeters, and provides an attractive measurement technique considering the trade-off between the

information obtained (two dimensional map of complex dose distribution) and experimental complexity and labour. Despite this, there are many potential disadvantages when using this technique. Bogucki et al listed these factors, including variations in film sensitivity caused by film batch, processor conditions, densitometry artefacts, and deviation from water throughout photon beam spectrum resulting from the high atomic number of the active material (Bogucki et al., 1997). Of these variables, the factor of the greatest potential for causing dosimetry errors is the variation in optical density with film processor developer temperature.

B. Radiochromic film

In contrast to radiographic film, radiochromic film is nearly tissue-equivalent and does not require a processor for generating the optical density response to ionising radiation, as it is self-developing (Blackwell et al., 1998). This thin film is easy to handle and has very high spatial resolution, but underexposure at low-energy range may occur with radiochromic films (Muench et al., 1991). With all the advantages of film dosimetry, Cheng and Das addressed the several difficulties associated with conformal field measurement, such as energy dependence, film orientation, inter- and intra-film density variation, sensitometric nonlinearity and inhomogeneity due to trapped air pockets inside the film jacket (Cheng and Das, 1996). In general, radiochromic film should not be used for absolute dose measurements and to verify output measurement by ionisation chamber. The obvious limitation of radiochromic film is the restriction of 2D planar dosimetry, in particular for verification of irregular 3D dose distributions.

C. Electronic Potal Imaging Device (EPID) dosimetry

The use of electronic portal imaging devices (EPIDs) can be an efficient option as a pre-treatment dosimetric measurement tool for patient-specific QA of modulated treatment plans. It is because of its properties such as high contrast, high spatial/temporal resolutions, large detecting surfaces, linear response to radiation dose, and efficient online capabilities. Consequently, various commercial vendors and clinical institutions have produced algorithms to convert calibrated EPID response into a simulated dose plane, in order to utilise EPID images as a verification tool for delivery of modulated fields (Luchka and Pistorius, 2001, Greer and Popescu, 2003, Greer, 2007, Bailey et al., 2010). At the same time, however, high-Z component materials and large detector density render EPIDs far from water-equivalent. Another obvious limitation of using EPID dosimetry is associated with rotational delivery technique (e.g. performing VMAT QA). It is because EPID is mounted to the rotating gantry, that is, the lack of independent verification of gantry motion and the possibility of angle-

dependent detector sag due to gravitational force, which is also machine dependent. In addition, EPID dosimetry is often restricted 2D plane.

D. Array detectors

A recent and popular new tool available for routine clinical quality assurance (QA) of conformal beam radiotherapy is a planar array of point dosimeters calibrated to yield multiple cumulative readings of absorbed dose (Low et al., 2011). Planar arrays have been used for QA of IMRT (Jursinic and Nelms, 2003) and helical tomotherapy (Langen et al., 2005). These studies implemented two-dimensional *n*-type diode array, which was the only commercially available product until recently and is called MapCheck (Sun Nuclear, Melbourne, FL). Ionisation chamber array detectors are also commercially available, e.g. IC-profiler (Sun Nuclear, Melbourne, FL). Low et al. addressed the several limitations regarding dosimetry tools and techniques for IMRT in their review paper (Low et al., 2011). Limitations include the fact that existing array detectors have low spatial resolution (typically ~ 10 mm of detector spacing). This limits their role in routine QA for hypo-fractionated small fields delivery (e.g. SRS/SBRT), since initial commissioning should be performed with a higher resolution system (e.g. film) enabling thorough evaluation of the fine dose distribution structure. In addition, 2D array detectors cannot provide the composite 3D dose distribution from the superposition of all beams although each beam can be independently verified. In other words, both individual beam errors and the accumulation of all errors in the 3D distribution are unknown. 3D structured array detectors are now available, e.g. Octavius and ArcCHECK; however, these are still in limited use mainly due its low resolution and planar dose measurement (i.e. virtual 3D dose reconstruction from 2D measurements for Octavius and 2D measurements along the surface of 3D structure for ArcCHECK).

2.5.3 Ideal dosimeter for measurements and verifications

To be considered as the ideal dosimeter for measurements and verifications of the conformal fields, it would need to possess (i) a 'volumetric' property to act as a dosimeter as well as a volumetric phantom material, so as not to be subject to volume averaging issues and (ii) water or tissue equivalency (i.e. 'media-matched' properties), so as not to perturb the radiation field. Radiosensitive gel dosimeter is a tissue equivalent 3D dosimetric phantom, that is, a 3D version of radiosensitive film. Hence, gel can act as a moving tissue surrogate while enabling 3D measurement of integrated dose in the volume. Consequently, gel dosimeters are a very promising tool to enable the measurement of highly conformal field(s) in moving objects. Following sections briefly describe the history of 3D gel dosimetry and discuss its radiochemical processes upon irradiation. In addition, use of different types of gels in radiotherapy is provided in greater details based on a comprehensive review of scientific

literature. Subsequently, the next chapter (Chapter 3) will discuss another unique potential of gel, that is, a new development of deformable gel dosimetry that has the capacity to be a dose-integrating deformable tissue surrogate.

2.6 A review of fundamentals in 3D dosimetry: Radiosensitive gels

2.6.1 An overview of 3D dosimetry

Radiosensitive gels are material that can *map* the absorbed radiation dose in three dimensions (3D) via chemical processes upon irradiation, i.e. ionic conversion or polymerisation, as a function of the dose delivered. 3D gel dosimetry in radiotherapy has the potential to play an important role in commissioning new advanced treatment protocols, to help prevent potentially significant inaccuracies in test treatments at a variety of institutions (Doran and Krstaji, 2006, Venning et al., 2005a).

In early studies, Day and Stein in 1950 first suggested the use of radiosensitive polymer gels for the purposes of radiation dosimetry. They investigated radiation-induced colour changes in gel matrices containing radiosensitive dyes, such as methylene blue (Fong et al., 2001). Spectrophotometry and a pH probe were also used to measure depth doses in the irradiated gels (De Deene et al., 2002). The feasibility of using radiosensitive gels for the dosimetry purpose, however, was founded by Gore et al in 1984. They initially demonstrated that changes due to ionising radiation in the ferrous sulphate chemical dosimeter, called the Fricke dosimeter (Gore and Kang, 1984), could be evaluated by nuclear magnetic relaxometry (NMR) signals, hence by magnetic resonance imaging (MRI) for dose readout (De Deene et al., 2006).

Since then, numerous studies have been undertaken investigating the following:
- new formulations of radiochromic gels using various gel matrices such as gelatin (protein), agarose (polysaccacharide), and PVA (polyvinyl alcohol) (TRCR, 2006, Xu et al., 2004, Hilts and Duzenli, 2004, Xu et al., 2003, ICRP, 2007);
- various radiosensitive chemical reactants such as xylenol orange, leuco-malachite green and potassium ferricyanide (Turnbull blue) as radiochromic dyes (Rutqvist et al., 2003, Adamovics and Maryanski, 2004, Bomford and Kunkler, 2003, Zackrisson et al., 2003);
- new types of polymer-based gel using radiation-induced polymerising monomers and/or crosslinker such as polymethylmethacrylate, polyacrylamide acrylamide

(AAm) and/or *N,N'*-methylene-bis-acrylamide (Bis) (Bleehen and Stenning, 1991, Gowda et al., 2003, Baldock et al., 1999);

- spatial and temporal stabilities affected by ion diffusion for radiochromic gels and by oxygen diffusion for polymer based gels (De Deene et al., 2000, Schultheiss et al., 2012, McAleese et al., 2003);

- addition of diffusion suppressing chemicals for radiochromic gels such as anionic micelle (Bomford and Kunkler, 2003, Zhong et al., 2012) or genipin crosslinker (Mi et al., 2003, Zhong et al., 2010, Schultheiss and Tome, 2013);

- addition of antioxidant such as tetrakis (hydroxymethyl) phosphonium chloride (THPC) for polymer-based gels (De Deene et al., 2002, Karim et al., 1996, Jirasek et al., 2006);

- new types of radiochromic plastic dosimeter using polyurethane and leuco-malachite green dye (Mather and Baldock, 2003, Adamovics and Maryanski, 2004);

- characterisation of radiological properties in 3D dosimeters fabricated using various formulations/compositions of materials (Salazar et al., 1979, McAleese et al., 2003, Venning et al., 2005a, González et al., 1994) and;

- characterisation of different dose readout systems and development of new reading devices (Nilsson et al., 2004, Gore et al., 1999, Hilts et al., 2000, Oldham et al., 2001, Mather et al., 2002, Islam et al., 2003).

Fundamental principles most of 3D dosimeters (except radiochromic plastic dosimeter) are governed by the interaction of ionising radiation with water, i.e. water radiolysis. Contemporary gel dosimetry is broadly categorised into three types depending on its composition: radiochromic gel, radiochromic (polyurethane) plastics, and polymer-based gels. For evaluation purposes, this gel dosimetry typically employs the following readout systems: magnetic resonance imaging (MRI), optical-computed tomography (optical-CT), x-ray CT imaging, or ultrasound imaging. This section discusses the advantages of gels (Section 2.6.2), the fundamentals of water radiolysis (Section 2.6.3), then basic chemical processes of individual gel types (Section 2.7) and the usage of each imaging modality (Section 2.8).

2.6.2 Advantages of 3D gel dosimetry

Gels have many inherent advantages over other more 'standard' dosimeters. Examples of the more standard *point* dosimeters include ion chambers or thermo-luminescent dosimeters (TLD). The use of gel dosimeters may also be preferred over the use of two-dimensional dosimeters, such as film or array detectors. Such detectors are unable to obtain three dimensional (3D) dose information and can only provide dose information at a limited number of points or two dimensional planes. The use of these detectors may perturb dose

information (e.g. volume averaging effect, angular dependence or media-mismatch). Gel dosimeters, on the other hand, contain not only radiological and physical properties similar to that of water and soft-tissue but are also capable of integrating dose distributions independent of the incident directions of beams. As such, gels possess the *dual* capacity to act as a 3D dosimeter and also as a tissue-equivalent phantom. Gels are not subject to the aforementioned perturbing factors, yielding dose information over a three dimensional volume through multiple beamlets during irradiation or multiple fractionations.

These advantages are particularly significant in investigating the dosimetric impact on moving and/or deforming targets with advanced treatment techniques that implement steep dose gradients, high dose and beam modulation, such as in IMRT, VMAT or stereotactic therapy. There is *no substitute* for the 3D measurement of dose delivered to the deformable moving targets, i.e. 4D deformable dosimetry which has not previously been demonstrated, such application is the aim of the next chapter. Gel dosimeters also have specific advantages for brachytherapy dosimetry, which requires volumetric dose measurement with a high degree of spatial resolution. Further potential dosimetry applications (though not explicitly discussed in this thesis) include the use of gels for low-energy x-rays, high linear energy transfer (LET) particle and proton therapy, radionuclide and boron capture neutron therapy dosimetry (Venning et al., 2005a).

2.6.3 Water radiolysis: the fundamentals of interaction of radiation with gels/tissues

Water radiolysis refers to decomposition of water molecules by ionisation when ionising radiation deposits its dose (energy per mass, J/kg) into water. This phenomenon has been well-studied in various eras and industries since radiation was actively studied from isotope decays until now (Baldock et al., 1999, Senden et al., 2006, Wu et al., 2002b, Kirby et al., 2013, Lepage et al., 2001a). In the radiotherapy field, this is particularly important to understand the consequence of irradiating the human body and gels, matter mainly composed of water, 60-70% for the former and 80-90% for the latter.

Water radiolysis is commonly described in three distinct stages after incident radiation: (i) the physical stage has time scale in the order of 10^{-14}s, (ii) the physicochemical stage in the order of 10^{-12}s, and (iii) chemical stage in the order of 10^{-7}s (Kirby et al., 2013, Lepage et al., 2001a). When incident ionising radiation deposits its energy into the human body, ionised water molecules mainly form H_2O^+ + e^- pairs and partially excited (H_2O^*), which is decomposed into $H\bullet$ + $OH\bullet$ (or H_2 + O) pairs in the body. These decompositions take place in localised spots where the energy deposition occurs in a time scale of 10^{-14}s (i.e. physical

stage). The resultant ions readily react with surrounding water molecules to form hydrogen radicals (H•) and hydroxyl radicals (OH•). A cascade of radiolysis products are sequentially generated as forms of e^-_{eq} (a hydrated electron), H•, OH•, H^+, H_2 within 1 ps (10^{-12}s) after the energy deposition. Initial inhomogeneous distributions of these radiolysis products are called 'initial yields' (i.e. the physicochemical stage). Sequential homogeneous distribution of the initial yields occurs along simultaneous reactions with each other due to their high-reactivity and high local concentration. As a result, other cascades of radiolysis products are formed (e.g. e^-_{eq}, H•, OH•, H^+, H_2 H_2O_2) and distributed homogeneously further beyond the local spots 0.1 μs (10^{-7}s) after the energy deposition occurs. The homogeneous distributions of these radiolysis products are called 'primary yields', which are involved in homogeneous reactions with each other (i.e. chemical stage). A schematic diagram of these processes is shown below:

$Radiation + H_2O$ ➔ H_2O^* ➔ $H• + OH•$ or $H_2 + O$ or H_2O (excitation)

$Radiation + H_2O$ ➔ $H_2O^+ + e^-$ (ionisation) ➔ $H^+ + OH + e^-_{eq}$

$e^- + H_2O$ ➔ H_2O^- $\quad$ $H^+ + e^-$ ➔ $H•$

H_2O^+ ➔ $H^+ + OH•$ $\qquad\qquad\qquad$ $e^-_{eq} + H_2O +$ ➔ H_2O^-

H_2O^- ➔ $H• + OH^-$ $\qquad$ *Physicochemical stage (~ 1 ps)*

$OH• + OH•$ ➔ H_2O_2 $\qquad\qquad$ *Chemical stage (~ 0.1 μs)*

$H• + OH•$ ➔ H_2O

$H^+ + OH^-$ ➔ H_2O

$H^+ + O_2$ ➔ $HO_2•$
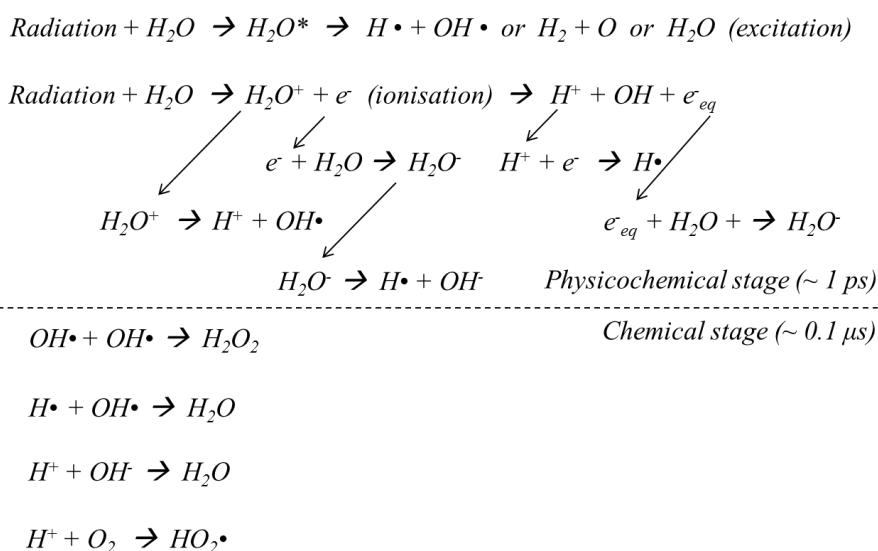
Figure 2-3 A schematic diagram of water radiolysis processes.

Although most highly reactive free radicals formed in these reactions recombine to form oxygen and water in a time scale of ~10 μs (10^{-5}s), some may interact with other chemical compounds in either tissues or gels irradiated. In terms of damage to DNA during treatment, the hydroxyl (OH•) radical (an oxidising species) is the most important radical of the products in water radiolysis, resulting in detrimental biological effects in tissues (Kirby et al., 2013). In the context of gel dosimetry, the most important products are H_2O_2 and the radicals e^-_{eq}, OH•, and H^+ in the absence of oxygen, resulting in readable changes in gels (e.g. colour or opacity) (Trapp et al., 2002).

2.7 Polymer-based gel and other 3D dosimeters

This section primarily sets out fundamental characteristics and practical considerations for polymer gel dosimeters which are used in the next chapter; other types of 3D dosimeters such as radiochromic gel and radiochromic polymer plastic are also brifely described. There are a series of excellent review articles regarding 3D gel dosimetry, all with different perspectives. The fundamental chemistry of radiochromic gels (Schreiner, 2004) and that of polymer gels (McAuley, 2007), and concisely summarised fundamentals of both gels and plastic dosimeters (Lepage and Jordan, 2010) have been previously published in International Conference in 3D Dosimetry proceedings (IC3DDose), formerly called DOSGEL. Members of the conference committee established a comprehensive review article that overlooks a full range of 3D polymer gel dosimetry (Venning et al., 2005a).

2.7.1 Polymer gels

In 3D gel dosimetry, a major stream to address the ionic diffusion problem has been the development and implementation of polymer gel dosimeters (Venning et al., 2005a). Polymer gels are predominantly water (~ 90 %), with a gelling agent (such as gelatine or agarose) and monomers (organic hydrocarbons). The monomers are readily involved in a chemical reaction, i.e. polymerisation, due to its relatively small molecule size characterised by a carbon-carbon double. The gelling agent forms a three dimensional matrix into which the polymer chain formed can hardly diffuse; this preserves the spatial integrity of the radiation dose distribution. The currently used formulation was initially proposed in 1993, which was based on the polymerisation of acrylamide and N,N'-methylene-bis-acrylamide monomers (referred to as Bis which also acts as a cross-linker) infused in an aqueous agarose matrix (Nilsson et al., 2004).

Since the inception of the polymer-based gel, many different variations on the gel composition have been investigated, examined and used. Fundamental processes of polymerisation in response to the irradiation have been thoroughly studied, yielding a rigorous understanding of the factors that affect important properties of the polymer gels, such as the radiation dose sensitivity, dose response linearity, water equivalency, spatial and temporal stability, and dose integrity (Keall and Baldock, 1999, De Deene et al., 2000, De Deene et al., 2002, Senden et al., 2006, Venning et al., 2005b, Taylor et al., 2007a, Taylor et al., 2009c).

2.7.2 Polymerisation process

Under irradiation, the monomers undergo a polymerisation process via a chemical interaction with highly reactive free radicals generated from the dissociation of water molecules i.e. water radiolysis (Section 2.6.3). These radicals are readily bound to the electron double-bond of a monomer, forming a monomer radical that initiates polymerisation by reacting with another monomer. The resultant polymer radical does not only contain a reactive site consisting of electron double-bonds but the loose ends of polymer chains that propagate the reaction with another radical and/or radical monomers and/or radical polymers exist nearby the polymer (i.e. successive polymerisation). This propagation progressively forms a larger polymer chain (i.e. macromolecules), resulting in the modification of the physical properties in the dosimeter, such as opacity (optical density), water molecule mobility and electron density. Such changes can be then probed using different techniques such as optical CT, MRI, x-ray CT, and ultrasound.

Termination of polymerization occurs through various reaction processes of polymer radical with other chemicals; examples of reactions are the polymer radical–polymer radical reaction, polymer radical–gelatin reaction, and polymer radical–water free radical reaction. This terminating process is an important step in polymer gel chemistry because full polymerisation of the monomers only occurs after a significant radiation dose with an absence of termination. Following a cascade of the polymerisation process, approximately 10^4 monomers form a polymer chain before terminating the propagation (Lepage et al., 2000).

The gelling agent (e.g. gelatin), which mainly plays a role of the three dimensional matrix, is also involved throughout the polymerisation process. Due to its porous structure (albeit microscopic level), small molecules such as monomers may diffuse from the unirradiated region to the irradiated region; a direct consequence of the diffusion is the smearing effect of dose profiles/distributions, which does not reflect what happens in reality. However, gelatin is also known for its role as a 'scavenger' of water free radicals in acrylamide-based polymer gel dosimeter. In other words, a higher concentration of gelatin in the dosimeter implies that relatively fewer water free radicals become available for reaction with polymers, resulting in a decreased dose sensitivity with an increased stability both temporally and spatially (Lepage et al., 2001b).

Oxygen is very reactive and it quickly reacts with water free radicals, yielding peroxide radicals. These peroxide radicals react rapidly with other radicals (e.g. monomer radicals or polymer radicals), inhibiting or terminating the polymerisation process. As such, polymer gels should be prepared in an oxygen-free environment to avoid exposure to oxygen, i.e.

preparation should occur in an inert gas atmosphere using a nitrogen-purged glove-box, requiring a more laborious manufacturing process.

2.7.3 Normoxic polymer gel

In 2001, Fong et al introduced an innovative strategy of adding an antioxidant that scavenges oxygen molecules present in the gel solution during manufacture, facilitating normal atmosphere (normoxic) condition throughout the gel manufacture process (Fong et al., 2001). This new type of polymer gel dosimeter, known as MAGIC, consists of methacrylic acid, ascorbic acid, gelatin and copper. Free oxygen present in the aqueous gelatin matrix can be bound to ascorbic acid, commonly known as vitamin C, forming metallo-organic complexes in a process initiated by copper sulfate.

Subsequently, another oxygen scavenger, tetrakis hydroxymethyl phosphonium chloride (THPC) has been well-studied and incorporated to polyacrylamide-gelatin based polymer gel (hypoxic or anoxic gel dosimeters); such formulations include not only a patented commercial gel product such as BANG$^{®}$ (Maryanski et al., 1994) but also in-house gels such as polyacrylamide-gelatin based polymer gel (PAG) (Baldock et al., 1999). A full understanding of the effect of its addition in gels has been acquired before its practical use via many studies (Fong et al., 2001, De Deene et al., 2002, Venning et al., 2005a, Brindha et al., 2004, De Deene et al., 2006).

These types of polymer gel dosimeters became known as the new class of *normoxic* gel dosimeters, which are mainly used in current systems. Numerous studies have investigated different compositions and formulations of normoxic polymer gel dosimeters, which have been well-summarised by (Senden et al., 2006) and comprehensively reviewed by (Baldock et al., 2010)

2.7.4 Different types of 3D polymer dosimeters

Radiochromic gels present colour changes as a function of absorbed radiation dose, for example, via ionic conversion of ferrous (Fe^{2+}) ions into ferric (Fe^{3+}) ions in Fricke xylenol gels. There are different types of radiochromic gels depending on the aqueous solutions, gelling matrices and initiator dyes used.

Ferrous-sulphate doped gels are an aqueous ferrous solution integrated into a gelling matrix, often referred to as the Fricke dosimeter. Gore et al initially demonstrated that 3D dose distributions could be mapped with the Fricke gels and probed with MRI (Gore and Kang, 1984) . Although these Fricke dosimeters will continue to be important for fundamental radiochemistry studies (Lepage and Jordan, 2010), the diffusion of ferrous and ferric ions in Fricke gels presents a fundamental problem in terms of time constraints for post-irradiation imaging. This issue becomes more significant for dose delivery involving fields of very high dose gradients. As such, other variations of radiochromic gels have been developed with different strategies for diffusion suppression.

Gupta and Nilekani thoroughly investigated the infusion of xylenol orange (i.e. radiosensitive dye) into gelling matrix of Fricke solution, which allowed sensitive and reproducible measurement of the concentration change of ferric ions with visible light (Gupta and Nilekani, 1998). Appleby initially demonstrated the feasibility of adding xylenol orange into ferrous agarose gels (Rutqvist et al., 2003), this is often referred to as ferrous xylenol orange gels (FX gels or FXG). Jordan's group introduced these new gel types providing thorough examination of their radiological and mechanical properties in practical aspects (Bomford and Kunkler, 2003, Zhong et al., 2012). These authors integrated water-insoluble leuco malachite green (LMG) with nonionic surfactants to create micelles in an aqueous gelling matrix. This is often referred to as radiochromic micelle gels (Lepage and Jordan, 2010).

Another strategy of developing non-diffusing radiochromic gels is to use a crosslinking agent such as genipin that crosslinks gelatin to form a blue hydrogel (Mi et al., 2003). These gels are radiosensitive at low pH (i.e. low oxidisation of ions) and the blue crosslinked gels become opaque as a function of absorbed dose. Baldock's group demonstrated that the genipin gels are stable at room temperature and the crosslinking provides stable gels with lower concentrations of gelatin (Baldock et al., 2010). This type of gel is referred to as radiochromic crosslinked (Genipin-gelatin) gels.

A major challenge in gel dosimetry is an artefact at the boundary between the gel and the container wall (e.g. plastic material) due to the optical refractive index mismatch between gel, container, and surrounding medium, which can readily interfere with readout signal. In order to eliminate any interference, a promising material for routine clinical 3D dosimetry is the radiochromic plastic based on clear polyurethane as the host plastic, combined with leuco-malachite green (LMG); thereby eliminating the need for the container to retain a certain shape. This plastic polymer dosimeter was initially proposed by Adamovics's group, its commercial product name is PRESAGE^{TM} (Adamovics and Maryanski, 2006). There has been

a continuous improvement in optical quality and tissue equivalence from different formulations (González et al., 1994, Sakhalkar et al., 2009, Guo et al., 2006, Gorjiara et al., 2010, Mostaar et al., 2010, Alqathami et al., 2012a, Alqathami et al., 2012b)

2.8 Readout modalities of 3D gel dosimeters

Various imaging techniques have been implemented as readout modalities to evaluate 3D gel dosimeters including MRI, x-ray CT, optical CT, and ultrasound (Doran and Krstaji, 2006). A review of these readout systems can be found in literature – MRI (De Deene, 2004) , optical CT (Oldham, 2007), x-ray CT (Hilts et al., 2000), and ultrasound scanning (Mather et al., 2002). Their principles, use and limitations are concisely summarised in this section.

2.8.1 Magnetic resonance imaging (MRI)

Nuclear magnetic resonance was the earliest preceptor to evaluate radiosensitive gel dosimeter, which was firstly implemented by Gore (1984). As ferrous (Fe^{2+}) and ferric (Fe^{3+}) ions possess different magnetic moments, the oxidation of Fe^{2+} to ferric Fe^{3+} after irradiation of a Fricke dosimeter results in radiation induced changes in nuclear magnetic resonance (NMR) relaxation. The concentration of the different ions, proportional to the delivered dose, affect the spin-lattice relaxation time (T2) and the spin-spin relaxation time (T1) of the hydrogen nuclei in the gel, implying that dose-dependency of NMR signal can be quantified then calibrated. Commonly the relaxation rate, either R1 (= 1/T1) or R2 (= 1/T2), can be determined in the gel, which can be reconstructed in 3D via magnetic resonance imaging (MRI).

Similar in principle, polymer gels can be evaluated via NMR relaxation measurement, as radiation induced polymerisation of gel dosimeters results in the mobility change of protons within the gel. There are three different circumstances surrounding protons (Lepage *et al,* 2001b):

i)   protons associated with free water and monomer molecules,

ii) protons associated with the polymeric chains and

iii) protons bound to the gel matrix

The mobility of the protons within these circumstances differs, consequently the thermal motion of the molecules containing those protons changes between before and after irradiation. Therefore, the extent of polymerisation, proportional to the delivered dose, influences the spin-spin interaction of protons in the gel, implying that dose-dependency of

NMR signal can be quantified then calibrated. For further details regarding MRI scanning of polymer gels refer to (De Deene, 2004), as MRI imaging is a large field of research area itself.

Accessibility is a major limitation on the use of MRI for gel dosimetry, mainly due to its high cost, which would not apply to a research centre having access to a MRI facility. Even when MRI is available for use, substantial time is required for proper setup and parameter optimisation, equalising the temperature of the gel to the MRI room etc. These factors highlight the limitations of using MRI, as patient diagnostics generally take precedence over research. Consequently, research is highly likely to be undertaken out of hours, which may be prohibited by the administering department.

In order for alternative 3D gel dosimetry imaging systems to be attractive, they need to be easily accessible, fast reading, and low cost, such as x-ray computed tomography or optical tomography systems.

2.8.2 X-ray computed tomography imaging

An alternative read-out system of polymer gel dosimeters to MRI is x-ray computed tomography (CT) scanning, which is the most commonly employed imaging modality in clinics today. Hence, new equipment is not required nor is there any additional time consumption for training and familiarisation with the system at the same time being easily accessible as well as fast-reading. Hilts et al (2000) initially demonstrated the idea of employing CT for read-out of polymer gel dosimeters, in which the underlying principle is that a density change associated with radiation-induced polymerisation of polymer gels results in different photon attenuation. Although a dose-dependent change in Hounsfield unit (CT number) can be achieved, CT implementation as a read-out system for gels is significantly limited due to its very low dose sensitivity and high noise level, i.e. a poor contrast-to-noise ratio (CNR) or signal-to-noise ratio. For example, a change in CT number is less than 1 Hounsfield unit per Gy for PAG dosimeters (Trapp et al., 2002). Even a further reduction of the dose sensitivity to > 0.4 HU per Gy has been reported for normoxic gel formulations (i.e. adding antioxidants), compared to the anoxic gel formulations (Jirasek et al., 2006).

Nonetheless, a dose related image with a sufficiently high SNR in CT can be achieved through image averaging from a number of images acquisitions (in the order of 100 scans), and by applying an image post-processing technique such as image filtering correction (Hilts and Duzenli, 2004). The additional high dose delivered to gel dosimeters through multiple scans (on the order of 100) is problematic as well as the low sensitivity with x-ray CT as a

readout system for gel dosimetry. These limitations preclude the image averaging strategy from many scans while increasing dosimetric uncertainty (Hilts et al., 2000).

Another imaging modality that may overcome some of the limitations of x-ray CT is optical computed tomography (OCT) discussed below.

2.8.3 Optical computed tomography (OCT) imaging

Optical computed tomography (OCT) has particularly driven a strong interest in gel dosimetry because of its attractiveness as an easy-access, fast-reading, and low-cost imaging modality (Gore et al., 1999). With MRI increasingly being seen as an expensive option, optical CT scanning, using either charge coupled devices (CCDs) (Krstajic and Doran, 2007a, b, 2006; Doran et al., 2001; Wolodzko et al., 1999; Jordan et al., 2001) or laser-based instruments (Gore et al., 1996; Kelly et al., 1998), have been rapidly developed and considered to play a significant role as a cost-effective and efficient readout system in 3D gel dosimetry.

Optical CT uses the same principles as the more conventional x-ray CT, except that a visible light source is used instead of an x-ray source. The source is used to acquire 2D projections of the volumetric object through full 360^0 degree views and reconstruct an attenuation map in the corresponding scanned volume using the 2D information. The main difference in the geometric setup of OCT is that an object rotates during the scan with a fixed or translating optical source and detector pair in optical CT (analogous to first generation x-ray CT). In contrast, conventional x-ray CT possesses an x-ray source aligned with a fully distributed 'fan' detector array that rotates around a fixed object. Because of the nature of optical beam (visible light), gels must be (semi-) transparent, so that the optical beam can partially penetrate the object to allow the partial transparency of gel to be measured. Beer's law relates the measured signal intensity I to the signal in the absence of the sample I_0 as below,

$$I = I_0 \, exp \, [-\textstyle\int_{ray-path} \mu(r) \, dr] = I_0 \, exp(-\mu \cdot r), \text{ (in the case of linear ray-path)} \qquad (2\text{-}1)$$

where $\mu(\mathbf{r})$ is the optical linear attenuation coefficient for each voxel, and $\mathbf{r}$ is a distance along the selected ray-path through the sample. The integrated optical density (OD), also called absorbance (A), is defined as

$$A = \log_{10}(1/T) = \log_{10}(I_0/I) \qquad (2\text{-}2)$$

where T is the transmittance (I/I_0). The optical density is related to the linear attenuation coefficient μ in the following manner, using Eq.(2-1):

$$A = \log_{10}(I_0 / I) = -\mu \cdot r / \ln(10) \qquad (2\text{-}3)$$

Often the integrated OD is seen as a whole and defined as Eq.(2-2), in that case, OD has no units. However, in this work the definition:

$$OD = A / r = \log_{10}(1/T) / r = -\mu / ln(10) \approx -\mu / 2.3026 \qquad (2\text{-}4)$$

is used, in which case OD does have units and these may be expressed in terms of distance (cm^{-1}). OD then becomes an integral property of the sample that is imaged on a voxel-by-voxel basis.

$\Delta\mu$, changes in optical density, can be mapped in the 3D volume of object, which are proportional to the absorbed dose (or can at least be related by a calibration curve). Optical density may be composed of either an absorption term (μ_{abs}) or a scattering term (μ_{scat}), depending on which term dominates the attenuation mechanism of optical beam through object (i.e. colour changes for μ_{abs}, opacity changes for μ_{scat}).

For radiochromic gels or radiochromic plastics, the ionic conversion of dye element upon irradiation causes a shift in its absorption peak, and then the change in μ_{abs} can be measured throughout the volume of objects. Depending on the reactant, the absorption peak is in different wavelength regions (e.g. the ultraviolet or visible regions – yellow and green) and the dose sensitivity can be varied (i.e. the slope of the optical density vs. dose relation can be increased or decreased) (Doran and Krstaji, 2006). The issue of ion diffusion not only smears out the edge of radiation field but also deviates the optical density in the volume irradiated.

For polymer based gel, radiation-induced-polymerisation leads the gels to turn cloudy, a feature which is immediately apparent when polymer gels are irradiated, i.e. the gels become more opaque white with higher dose. When the gel is scanned, the incident optical beam is scattered off by the particles (polymer chains) of polymer created by the irradiation. The increase in μ_{scat} can be measured for each voxel in the irradiated volume and the dose sensitivity can be optimized by adjusting polymer, co-polymer and gel composition depending on its use. Polymer gel is minimally subject to the ion diffusion due to a relatively large size of polymer-chain comparing to its matrix, however, it should be noted that deviations from Beer's Law of attenuation occur for high concentrations of scattering particles.

Despite the challenge of optical artefacts, the field of 3D gel dosimetry by optical CT has recently become more accessible through commercially available optical CT systems such as OCTOPUS[TM] laser scanner (MGS Research Inc., Madison, Connecticut, USA) and Vista[TM] cone-beam scanner (Modus Medical devices Inc., London, Ontario, Canada). Different types of optical CT scanner are summarized in (Baldock et al., 2010). Several groups have reported

very successful 3D dosimetry verifications with the characterisation of systems for the laser scanner (Xu et al., 2003, Xu et al., 2004, Lopatiuk-Tirpak et al., 2008b) and for cone-beam scanner (Bosi et al., 2009, Olding et al., 2010, Olding and Schreiner, 2011), indicating that workable low-scatter regimes are feasible.

2.8.4 Ultrasound imaging

The change in acoustic properties of polymer gel dosimeters, associated with radiation-induced polarization, has been also investigated, including the acoustic speed of propagation, ultrasonic absorption and ultrasonic attenuation. Such changes following irradiation of gels can be reconstructed with ultrasound imaging (Mather et al., 2002). This system was developed to evaluate irradiated dose distributions in 3D (Mather and Baldock, 2003). Although relatively easy-access, fast and low-cost, the source of contrast (i.e. change in elastic modulus and density) is very small thus a high SNR is hardly achievable. In addition, the inherent low resolution of the imaging modality (for normal ultrasound image being used in clinics) makes the merit of 3D ultrasound dosimetry a less preferred option.

Although significant artifacts have been observed in the transmission image, which is mainly due to an acoustic impedance mismatch between water and gels, this evaluation method is still in early stages and there is still much room for improvement of image quality (Baldock et al., 2010).

2.9 Final comments

The discussion in this chapter has aimed to provide some challenges and complexities in contemporary radiotherapy and an understanding of the fundamental principles of 3D dosimetry. The existence of organ deformation associated with anatomic motion adds a further layer of complexity to the problem of inter- and intra-fractional variation in anatomic structures, which have not been fully investigated in current clinical practice. Organ deformation inherent in intra- and inter-fractional motion makes their resultant dose distributions difficult to measure and calculate. Consequent dosimetric uncertainties and inaccuracies in dose delivery may have detrimental outcomes for patients as a result of under-dosage of the tumour or over-irradiation of healthy tissues in the immediate periphery of a targeted lesion.

Accurate volumetric dosimetry to deformable moving objects is therefore critical for the verification of advanced delivery techniques. Robust calculation methods for the prediction of radiation dose distribution in deformable moving objects is therefore crucial in order to improve treatment planning accuracy. Once both components are available, then appropriate evaluation of conventional 3D planning can be performed to determine the degree of error associated with the assumption of static geometry.

3D dosimetry has been used for 3D complex dose verification as well as studying motion compensation techniques. Each variant of 3D dosimeter has its own specific features that make them preferred for certain applications. Currently Presage™ (Heuris Pharma LLC, USA) and BANG (MGS Research, USA) are commercially available and all other formulations require preparation by the users. Other considerations for material development for clinical usage include: ease of preparation and disposal, reproducibility, toxicity and raw material costs. Of possible readout modalities for gels, MRI was previously the most popular option, its use as routine dosimetry system in medical physics department is likely limited by time, expense and accessibility. Optical CT has been favoured in the research field for 3D dosimetry as dedicated instruments can be built at a cost several orders of magnitude less than that of an MRI scanner. Numerous conference papers highlight the advantages of optical CT gel dosimetry over other modalities (IC3DDose 2010 and IC3DDose 2012).

In the next chapter, we show how normoxic polymer gel dosimetery was employed to develop a novel deformable dosimeter, with the ability to map dose in three dimensions and accumulate the dose delivered in multiple different states of deformation. Optical CT (OCT) was used as the readout modality, principally due to advantages associated with availability. A procedure for reproducible exposure and readout is described.

In Chapter 5, it is shown how this deformable dosimeter can be used to experimentally verify dose deformation computation (i.e dose-warping). Because the results from dose-warping are critically dependant upon DIR performance, we first show in Chapter 4 a technique for quantitatively assessing the accuracy of DIR algorithm, in particular, in low-contrast regions.

Lastly, the validated dose warping technique is applied in Chapter 6 to the case of liver stereotactic body radiotherapy, where the consequences of the redistribution of dose due to deformation are quantified for target and OAR doses respectively.

CHAPTER THREE

: A novel 4D deformable dosimetry system

The measurement of complex re-distribution of dose in deforming and moving targets

"Retention rather than deterioration is the opposite of innovation."

Stephen M.R. Covey, the speed of trust

3.1 Overview of chapter

The objective of this chapter is to demonstrate a novel methodology for 3D deformable dosimetry using the first fully deformable dosimetric gel phantom. This allows experimental measurement of dose delivered to volumetric deformable moving targets; thereby the dosimetric impact of deformation on the targets is investigated according to the geometry changing in time (i.e. *4D*).

To establish the utility of 4D deformable dosimetric gel phantoms, a series of studies is presented in this chapter. These relate to the characterisation of both physical and radiological properties, calibration of dose response of gels, robust structural integrity and reproducibility of deformation. This measurement tool is then used to perform quantitative analysis of the complex dose redistribution in 3D and dose accumulation upon consecutive irradiations in different states of deformation, to demonstrate the cumulative effect of deformation on the dose distribution of a clinically relevant composite field.

3.2 A novel 4D deformable dosimetry system: Intro

Image guidance is a key technique to develop more conformal approaches to restrict the treatment beam to the shape and location of the tumour being targeted. Image guidance not only improves patient setup but allows for adaptive radiotherapy (ART) to improve conformity. In either case, deformation of anatomy presents challenges to interpretation of the cumulative effect of fractionated delivery of dose. In the non-adaptive case, the treatment is not altered, but the target organ and surrounding tissue may deform during treatment, or between fractions. One can then be interested to know what the cumulative dose distribution is both within the target volume and nearby organs at risk. In the case of adaptive radiotherapy, subsequent treatment beams may be made more conformal (Wu et al., 2002a) but the distribution and re-distribution of dose as the organ changes shape, or even size, is critical to controlling the prescription dose for local tumour control (Kron et al., 2010). The integration of subsequent dose delivered, with a non-identical fraction, is the goal.

Mathematical algorithms which perform "dose warping" have been described (Janssens et al., 2009b, Zhong et al., 2008). For the most part, these algorithms apply a deformation vector field, derived from non-rigid image registration, to a dose distribution. Deformable image registration (DIR) is performed between images of the anatomy in different states of deformation. The vector field that describes the "destination" co-ordinates of each pixel of the "before" image, is applied to the first TPS calculated dose distribution to predict the distribution in the "after" geometry. A number of studies have developed and validated methods for deformable image registration (Horn and Schunck, 1981b, Barron et al., 1994, Lu et al., 2004c, Thirion, 1998b, Rogelj and Kovačič, 2006) and dose calculations on deforming geometries (Schaly et al., 2004b, Rosu et al., 2005, Flampouri et al., 2006, Guerrero et

al., 2005, Velec et al., 2015). However, thus far no experimental means of validating three-dimensional dose distributions delivered to deforming structures have been presented.

Deforming phantoms have been developed for testing DIR algorithms, by being able to independently verify the position of specific features/points in each image (Serban et al., 2008, Kashani et al., 2007a). Moving and deforming phantoms have had point dosimeters included for monitoring single dose reference points (Seco et al., 2010). Two and three dimensional dosimeters (e.g. film and gel) have been incorporated into moving phantoms to assess "dose smearing" effects due to *rigid* motion only, but not deformation (Duan et al., 2006, Ceberg et al., 2008, Lopatiuk-Tirpak et al., 2008a).

The novel deformable gel dosimeter (DEFGEL) described in this work enables, for the first time, the full 3-D experimental validation of both of these approaches: dose integration in a deforming target, and verification of dose warping calculations. The high resolution 3-D dosimetry provided by radiochromic gels has been shown to be extremely valuable, particularly in small field dosimetry (Baldock et al., 2010, Taylor et al., 2011b). Several shortcomings of other detectors can be overcome, such as detector volume averaging and coarse spatial sampling.

The DEFGEL phantom can also provide an additional tool for validation of DIR to supplement the several published approaches (Kashani et al., 2007a, Kashani et al., 2008c, Wang et al., 2005c, Wang et al., 2005a). With DEFGEL, the particular case of a mass and density conserving deformation of a tissue-equivalent material is provided for. This is likely to be relevant to a variety of anatomical cases. The deformation-relaxation-deformation cycle is shown to be highly reproducible, and therefore useful for confirmation and validation of changes relative to known geometry.

In this work, a modified version of the nPAG (Deene et al., 2006) polymer gel has been used as a 3D deformable phantom and dosimeter to investigate doses delivered to a deforming tissue-equivalent geometry. The deformable gel dosimeter/phantom is comprised of polymer gel in a latex membrane, moulded (in this case) into a cylindrical geometry and deformed with an acrylic compressor. Irradiations were performed coaxial and orthogonal to the axis of compression and resultant dose distributions were evaluated with the Vista™ optical cone beam scanner (Modus Medical Devices, London, Canada). Reproducibility of deformation was determined via fiducial marker implantation and x-ray CT imaging. The effect of deformation on absorbed dose distributions was investigated by applying beams to deformed and undeformed phantoms. Deformed phantoms were scanned before and after being released from compression and allowed to return to their undeformed states, for direct comparison with undeformed samples. Exposure of a single dosimeter in both deformed and undeformed states demonstrates the utility of the DEFGEL phantom as a dose fraction integrator accounting for organ/target deformation.

3.3 A novel 4D deformable dosimetry system: Method

This section describes a modified nPAG formulation designed to be suitable for use in an elastic latex membrane container, and compatible for readout using OCT. The calibration procedure and radiological response properties of the gel are described. The deformation reproducibility of the gel is demonstrated before using the system to evaluate the dosimetric impact of deformations.

3.3.1 Manufacture of DEFGEL

The gel consists of a hydrogel matrix of 6 wt% (w/w) gelatine (from the porcine skin Type A, Sigma Aldrich Ltd, Oakville, Canada) in which 3 wt% (w/w) N,N'-methylene-bis-acrylamide (Bis) cross-linking monomer and 3 wt% (w/w) acrylamide (AAm) monomer are dissolved (both monomers were obtained from Sigma Aldrich and are of electrophoresis grade). Bis [tetrakis (hydroxymethyl-phosphonium)] sulphate (THP) as an antioxidant was added to the mixture in a concentration of 5 mM. These polymer gels are henceforth identified according to literature convention as 6 % total monomers, 50 % cross-linker nPAG. Hydroquinone (HQ), a polymerization inhibitor, was added at a concentration of 0.01 mM, to compensate for oxygen permeation through the latex membrane which may occur to a greater extent than for nPAG in conventional polyethylene terephthalate (PET) containers. The monomers and gelatine were each pre-dissolved in DI water, which is 88% (w/w) of the total mass. The monomer solution was heated to 45 °C for 2 hours until all components were dissolved. The gelatine was soaked in water at room temperature for 15 min and allowed to swell. The solution was then heated to 45 °C, at which the gelatine dissolves. Subsequently, both solutions were cooled to 30 °C before mixing to prevent heat-induced polymerization. After mixing, the THP and HQ were added and the solution thoroughly stirred before pouring into the container. For calibration, 900 ml of gel was transferred into a PET jar (Modus Medical Devices Inc, London, ON, Canada). For the deformation experiments, 110 ml of gel was transferred into the latex membrane. A cellulose-acetate film cast was used to mould the DEFGEL into a cylindrical shape of 46 mm diameter. After the gel was poured into containers, it was refrigerated at 4 °C for ~12 hours before irradiation.

3.3.2 Dose readout: Optical computed tomography

A cone beam optical CT (OCT) scanner (Vista^{TM} Optical Scanner by Modus Medical Devices Inc.) was employed in this study as a dose readout system. A brief description of OCT is provided here:

The optical-CT consists of a light source and detector, placed on either side of the object to be imaged. The Vista OCT consists of a panel of LEDs shining through a translucent diffusing screen, illuminating (in transmission) a polyethylene terephthalate (PETE) screw-top jar (Modus Medical

Devices, London, Canada) which contains the medium to be imaged. The jar is mounted in an aquarium filled with refractive index matching liquid (12 wt% glycerol in deionised water), which acts as a refractive index matching medium to minimize the refraction of the transmitted light at the jar surface. A CCD camera takes snapshots of the transmitted image of the jar through a selectable wavelength filter. The scans are made with the program VistaScan (VistaScan Application © 2004 Modus Medical Devices Inc.). These snapshots are used for the 2D measurements and as projections for the 3D reconstruction (see Figure 3-1). The program VistaRecon (VistaScan Application © 2004 Modus Medical Devices Inc.) reconstructs the geometry of the image object according to Beers law).
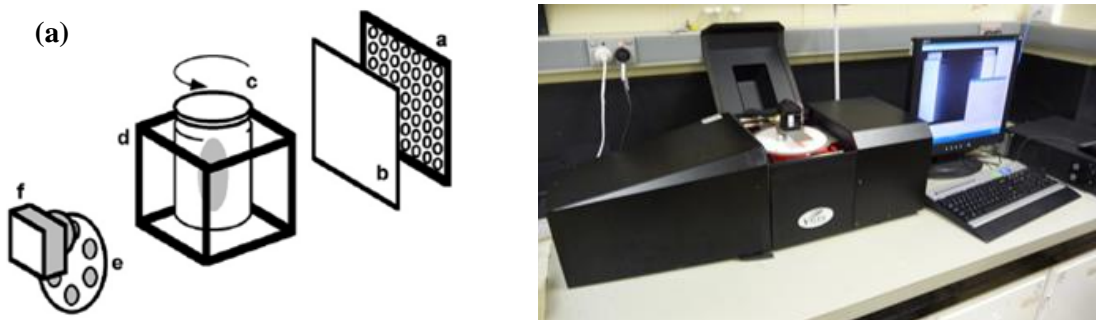
Figure 3-1 a) The schematic of cone-beam OCT scanner (Bosi et al., 2007), b) The cone beam scanner.

The red LED light source (wavelength: ~633 nm) and bandpass filter pair were used. Camera gain was set to minimum, and shutter speed and frame rate were adjusted to 50 mps and 5.0 fps, respectively. Reconstruction using Feldkamp filtered back projection with high resolution mode (512 projections) generated a CT array of 256 x 256 x 256 elements in 15 minutes using a dual processor 3MHz PC. The reconstructed voxel size was approximately 0.86 x 0.86 x 0.86 mm^3. The DEFGEL phantom was scanned within a PET jar filled with refractive index matching liquid (12 wt% glycerol in deionised water). Sample motion during scanning was eliminated by immobilising the DEFGEL via fixation of the cylindrical mould to the rotating jar. As the dosimeter reacts over a period of several hours after irradiation, a post-irradiation time of ~12h was chosen to ensure that the polymerization reaction was near completion at the time of imaging.

3.3.3 Radiological properties and calibration of DEFGEL

The radiological properties of gels have been well-studied, and they are generally considered to be 'water-equivalent' (Venning et al., 2005c, Keall and Baldock, 1999). Here, the water equivalence of the new gel formulation is demonstrated using the energy-dependent effective atomic number method (Taylor et al., 2008, Taylor et al., 2009b) (see Section 3.4.1 DEFGEL: Calibration and properties). Irradiations were performed using a clinical linear accelerator (Varian 21EX). Each calibration PET jar was irradiated in a water tank with 6 MV photons at a source-to-surface distance (SSD) of 100cm

and a dose rate of 600 cGy/min. The surface of gel in the container was perpendicular to the axis of the beam. Three 4 x 4 cm^2 square fields were aligned on quarters of the jar with one quarter left unirradiated for the background dose calculation to account for cross talk (see Figure 3-2). Calibration using a large tub of gel with multiple fields has been shown to accurately represent dose to water to better than 1 % (Taylor et al., 2007b, Taylor et al., 2009a). Background radiation scatter was assumed to be linearly correlated with beam fluence and the weighted background-subtraction radiation scattering factor was calculated for each beam. Field edges were separated by 1 cm such that at D_{max} the centre of each field was well beyond the range of secondary electrons from the adjacent fields, and the centre of each field was contained in the 90 % inner area of the PET jar. Using this method, irradiation doses of 0 cGy to 1889 cGy were delivered. Six vessels were used for this purpose and Figure 3-2 shows an example of the calibration arrangement.
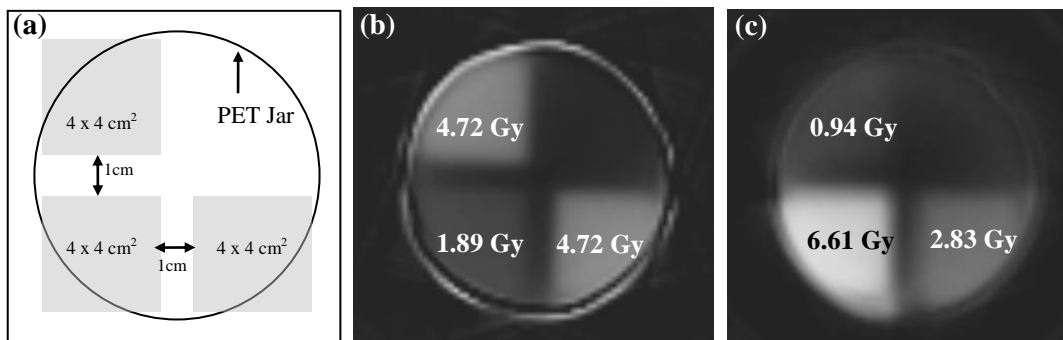
Figure 3-2 (a) Schematic of irradiations for calibration. (b) and (c) are examples of transverse planes of calibration samples: (b) irradiated with one 189 cGy field and two 472 cGy fields (i.e. the average of multiple measurements was used for each field to plot dose calibration curve, see Section 3.4.1), (c) irradiated with three different fields: 94, 283, 661 cGy.

3.3.4 Reproducibility of deformation

The reproducibility of the deformation state and the return to the rest state are important for the use of DEFGEL for applications involving DIR and dose integration. This is mainly because of two reasons: firstly, this is to correctly read out dose distribution from DEFGEL, i.e. the shape of DEFGEL should be identical between pre- and post- irradiation, so as to accurately measure dose integration between different deformation states; secondly, this is to use the same deformation for imaging and irradiation steps – particularly in the case for multiple irradiations or accumulation so that it enables to appropriately validate dose-warping calculation using DIR. To investigate possible displacement of the gel structure within the DEFGEL after deformation, phantoms were manufactured with Aluminium (Al) fiducial markers (FM) implanted into them and scanned with x-ray CT. Fifteen markers approximately 1-2 mm in diameter were implanted into the dosimeter during the gel setting phase (Figure 3-2 (a)). Marker sizes differed to aid in distinguishing them from each other. The phantom was scanned using a GE LightSpeed RT 4 slice, wide-bore CT scanner (GE Medical

Systems, USA). The slice thickness and spacing were both 1.25 mm and a 150 mA/100 kV source was used.

For a given deformation, the DEFGEL phantom (4.6 cm diameter) was compressed by 2.3 cm (a significant deformation) using an acrylic compressor, held for one second in that state, and then released. The pressure applied to each side was about 5.4 kPa (in atmospheric pressure condition). Using the in-room lasers and physical reference lines on the surface of the mould, the phantom position was replicated between scans; see
Figure 3-3(b) and (c).

A number of methods employing CT were used to establish reproducibility. Several DEFGEL phantoms with fiducial markers were deformed and CT scanned between deformations. Between CT scans the deformation was conducted 1, 10, 20, 30, 40, and 50 times (i.e. 151 in total). For the first set, all scans were undertaken with the DEFGEL in the undeformed state to examine the reproducibility of the return to the undeformed state. The procedure was repeated with another set, with the DEFGEL scanned in the deformed state each time to confirm the reproducibility of the compressions. A series of control scans were also undertaken. In the latter case, DEFGEL phantoms that had undergone *no* deformations were scanned and analysed in the same fashion to quantify the set-up error contribution to any observed shift. FM locations were evaluated by identifying the position of maximum intensity of all fifteen FMs in each scan (relative to an absolute reference position) using DoseLab version 4 (created by Nathan Childress, Ph.D., and Isaac Rosen, Ph.D., University of Texas, M.D. Anderson Cancer Center, Houston, TX) and Image J (National Institute of Health, Bethesda, Maryland, USA). FM locations were also determined relative to each other to isolate set-up error.
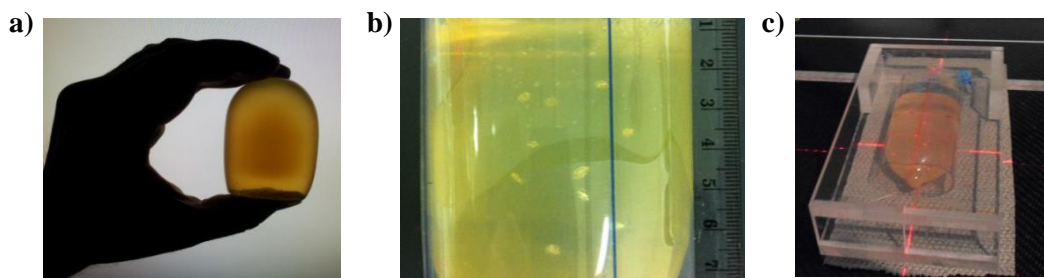
Figure 3-3 (a) DEFGEL phantom (b) DEFGEL with fiducial markers and (c) setup for CT scanning of the DEFGEL with deformation using the acrylic compressor.

3.3.5 Deformation and irradiation

DEFGEL samples were deformed in a controlled manner with the use of a parallel-plate acrylic compressor. The cylindrical samples were deformed such that their circular cross section became ellipsoidal.

Two sets of irradiations are presented here. The first set of 3 samples was irradiated with a simple 1 x 1 cm square field to illustrate the re-distribution of dose in a regular field (representative of a single beamlet) arising from the change in state of deformation. The beam was incident coaxial with the cylindrical samples and perpendicular to the direction of compression as illustrated in Figure 3-4. To observe pronounced effects of deformation, the distance between the two plates was set to 2.3 cm (half of the phantom's diameter). DEFGEL phantoms were irradiated in three scenarios: (1) without deformation, (2) with deformation and (3) irradiated twice: first in the deformed state, then after release of the compression, in the undeformed state to integrate the cumulative dose.

A second pair of samples was irradiated with a small stereotactic plan of three dynamic arcs adapted from a patient plan, to demonstrate the ability of DEFGEL to quantify severe under- and over-dosage associated with target deformation. 8.97 Gy was delivered to isocentre – half of the clinically prescribed dose, to remain near the centre of the calibration range. The treatment was delivered to an undeformed DEFGEL and also to a deformed sample. The sample deformation in this case was a compression from 46 mm to 30 mm.

Samples were irradiated within a water bath to remove dosimetric effects of surface curvature. All doses were delivered with a Varian 21EX (VARIAN Medical Systems, Palo Alto, CA, USA) clinical linear accelerator, using 6MV photons at 600 cGy/min at an SSD of 100 cm. Figure 3-4 indicates the three scenarios described for the first set of 3 samples. For the second set of 2 samples, only the first two scenarios apply.

(a) Scenario 1: *Undeformed. Irradiate and read out.*
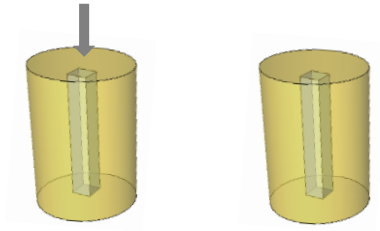
(b) Scenario 2: *Irradiate deformed. Read out undeformed.*
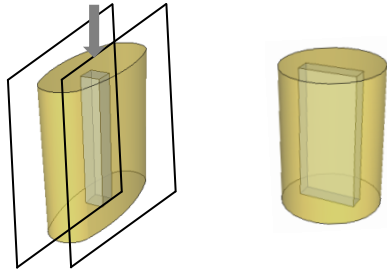
(c) Scenario 3: *Irradiate deformed. Irradiate undeformed. Read out undeformed.*
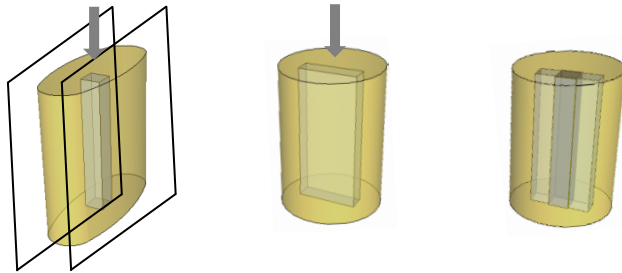
Figure 3-4 Arrangements of DEFGEL irradiation coaxial with the axis of the DEFGEL (and perpendicular to the direction of compression). The beam direction is indicated by the gray arrow. The gray hexahedrons in each figure represent the simplified dose distribution in the DEFGEL after irradiation. (a) and (b) correspond to irradiation of an undeformed DEFGEL (Scenario 1) and the deformed DEFGEL (Scenario 2), respectively. (c) corresponds to Scenario 3 - irradiation with and without deformation, resulting in an accumulated dose distribution.

3.4 A novel 4D deformable dosimetry system: Results

3.4.1 DEFGEL: Calibration and properties

The radiological properties of DEFGEL closely represent that of water, as indicated in Figure 3-5. The energy-dependent effective atomic number is calculated for both electron and photon interactions between 10 keV and 10 MeV. The maximum discrepancy between DEFGEL and water is roughly 1.5 % (in the low energy regime), indicating good water equivalence. The mass density of the gel is 0.969 $\pm$ 0.024 gcm^{-3}.
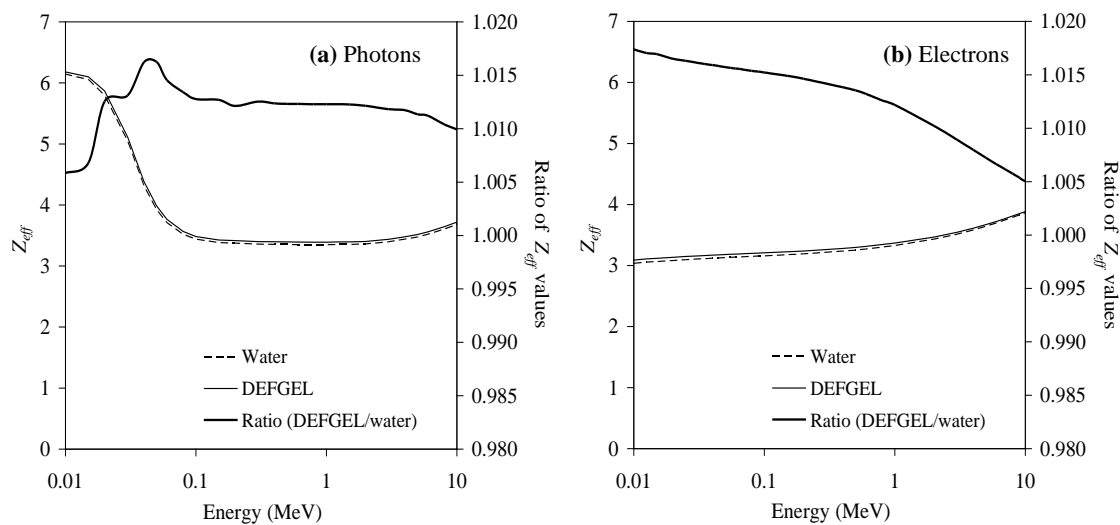
Figure 3-5 The energy-dependent effective atomic number (Z_{eff}) of DEFGEL, plotted with water for comparison, and the ratio of the two (presented on the right axis) for (a) photon interactions and (b) electron interactions. Calculations were performed using the method of Taylor *et al*(Taylor et al., 2008, Taylor et al., 2009b). The greatest discrepancy in both cases is ~1.5 %, indicating good water-equivalence.

The dose response curve is plotted in Figure 3-6. The optical density at D_{max} (~1.6 cm) was chosen for the plot, consistent with the requirements for minimal systematic error (Taylor et al., 2007b). The detection limit is approximately 30 cGy and dose sensitivity is 0.02 cm^{-1}Gy^{-1}. The R^2 value is 0.9994 implying a desirable linear dose response up to the maximum measured dose of 1889 cGy. The high degree of linearity although having a somewhat lower dose sensitivity coefficient compared with other gel formulations (Oldham et al., 2001, Wuu and Xu, 2006), indicates that the addition of HQ leads to an overall reduction of dose sensitivity due to scavenging of free radicals generated during water radiolysis while not resulting in an increase in threshold dose before polymerisation response. The optical density for 0 cGy was acquired by scanning an unirradiated dosimeter and averaging the value throughout the effective volume. For doses up to 500 cGy, the values plotted represent the average of multiple measurements. The error bars in Figure 3-6, ($\pm1\sigma$ of two to three measurements per each point) are smaller than the symbol size.
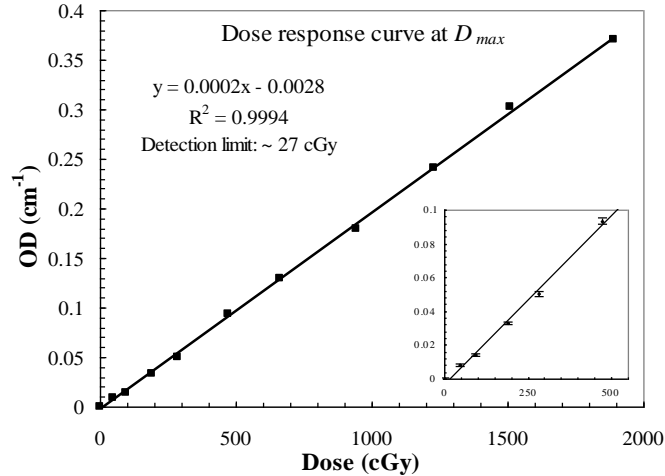
Figure 3-6 The optical density (cm^{-1}) as a function of dose for DEFGEL is plotted. The detection limit is approximately 27 cGy and dose sensitivity is 0.02 cm^{-1}Gy^{-1}. The R^2 value is 0.9994 indicating a strong linear relationship. The error bars ($\pm 1\sigma$ of two to three measurements per each point) are smaller than the symbol size. The inset depicts the 0-500 cGy region with error bars.

Dose distributions in exposed DEFGEL phantoms are highly stable. Repeated scans after 3 months and 6 months show no change in OD or penumbra sharpness in dosimeters stored at low temperatures (refrigerated at ~4 °C).

3.4.2 Reproducibility of deformation

Figure 3-7(a) and (b) show a 3D rendering of CT data of a DEFGEL phantom (containing Al FMs) in a non-deformed state (without compressor) and deformed state (with compressor), respectively.
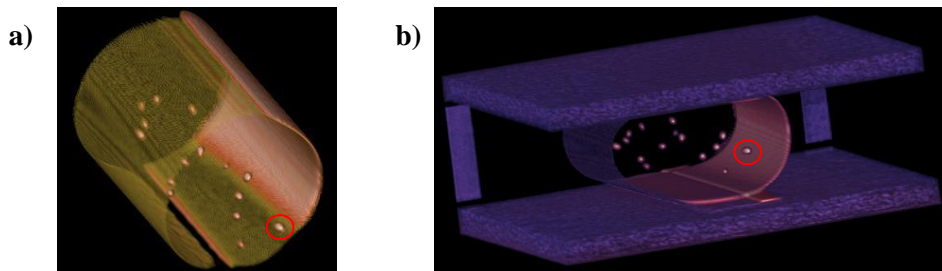
Figure 3-7 This figure shows the volume rendering of the DEFGEL phantom with fiducial markers implanted (a) without deformation and (b) with deformation. For reference, the same fiducial marker is encircled in red in both images.

Two methods were employed for CT data analysis, as described in the Methods section. In the first instance, a comparison of the position of each FM relative to a reference point was undertaken. An illustration of this idea is shown for an example case in Figure 3-8. Figure 3-8 (a) and (b) show the DEFGEL before (left image) and after (middle image) 50 deformations, respectively, and the

difference (right image) indicates very good agreement. Example line profiles through the FMs of Figure 3-8(a) are provided in Figure 3-9 for both directions: (a) vertical and (b) horizontal. These show excellent agreement between maximum intensity peaks corresponding to fiducial marker locations before and after deformation (i.e. the two curves are almost perfectly overlapped). The pixel resolution of each image was 0.488 mm derived from image size/pixels (= 250 mm / 512).
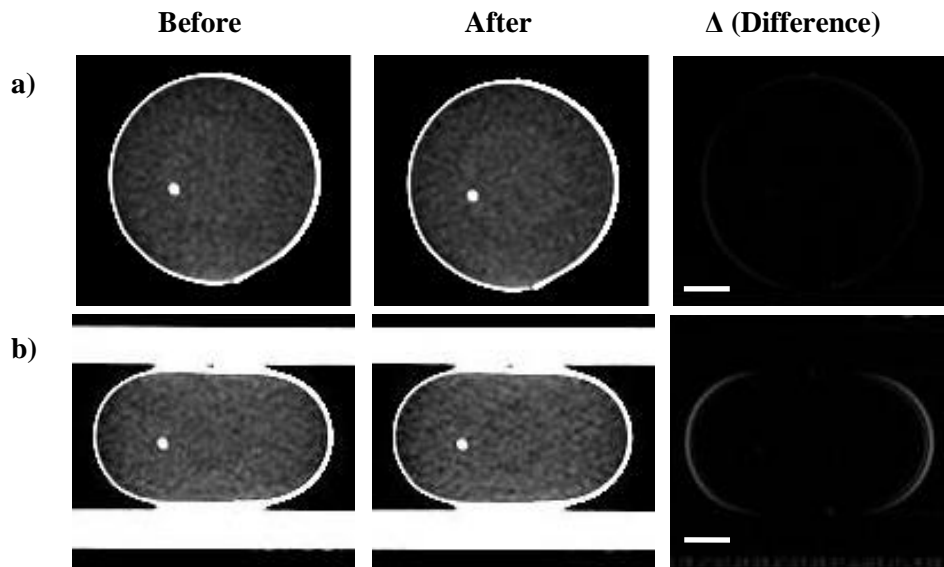
Figure 3-8 An example of fiducial marker location agreement (a) without compression and (b) with compression. The left column corresponds to the CT image before deformation, the middle column after 50 deformations and the right column represents the difference between the two images. The scale bar is 10 mm.
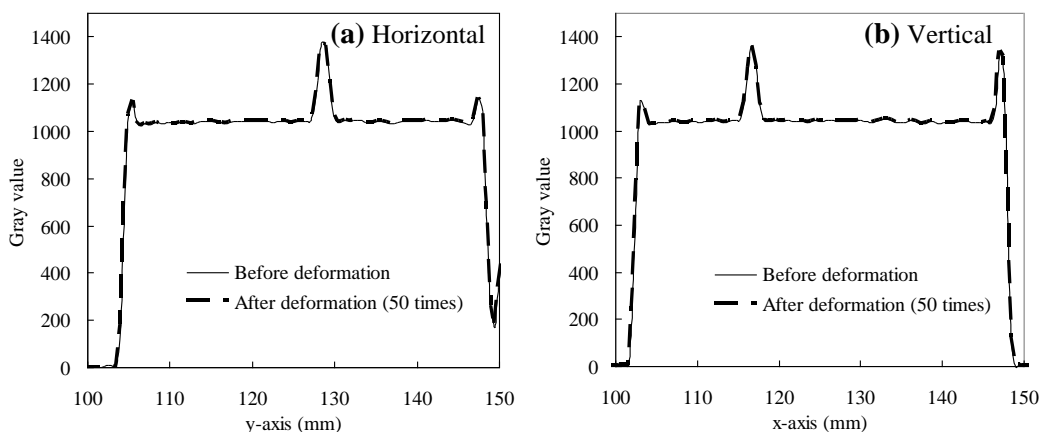
Figure 3-9 (a) horizontal and (b) vertical line profiles through the marker locations of Figure 7(a). The solid and dashed lines indicate the line profile before and after 50 cycles of deformation, respectively. The nearly identical line profile before and after deformation implies the deformation cycle was highly reproducible. The centroid of each peak was used as position coordinates to identify the location of each marker.

The centroids of the peaks were used as the x, y and z coordinates of each marker. The z coordinates were obtained by rotating the sample 90° and repeating the CT scan to give the same resolution as for

the x and y coordinates. The shift of each marker was calculated after 1, 10, 20, 30, 40 and 50 repetitions of the compression described in Section 3.3.4 Reproducibility of deformation. The mean absolute displacement of all markers is shown in Table 3-1. There is clear indication that all markers returned to their initial locations to within 0.15 mm ($\sigma = 0.22$ mm, maximum shift = 0.98 mm, the latter corresponding to two pixels). The control group shown in Table 1 was *not* deformed between repeated imaging, showing that the variations observed for the deformed cases are due only to setup error associated with aligning the samples with the CT alignment lasers. This illustrates that the DEFGEL returns to its initial undeformed state reproducibly, even after many compressions. Rows 3 and 4 of Table 1 show analogous data for the sample in its compressed state. This shows the reproducibility of the compressed state.

It is important to note that *absolute values* are shown in Table 3-1, i.e. the difference is not systematically higher. If positive and negative values are compared, the mean position differences are zero. The reason that the mean shifts are invariably less than the resolution is that the majority (77 %) of markers exhibited zero shift, 22 % exhibited a shift of one pixel, and in one case two pixels. The table indicates perfect deformation reproducibility, with all differences clearly being attributable to typical CT set-up error.

Table 3-1 This table indicates the reproducibility of deformation of the DEFGEL. $\Delta d_{absolute}$ refers to the shift (in mm) of 'peak position', i.e. the shift in fiducial marker location relative to a fixed reference point. $\Delta d_{relative}$ refers to the difference in the relative separation of fiducial markers. The DEFGEL phantoms were CT scanned in either deformed (*Def.*) or undeformed (*Undef.*) states as indicated. Control DEFGEL phantoms (that had undergone no deformations) were also evaluated for comparison.

DEFGEL	Scanned in state:		$|\Delta d_{absolute}|$ (mm)			$|\Delta d_{relative}|$ (mm)		
	Def.	*Undef.*	Mean	Max.	σ	Mean	Max.	σ
Post-deformation		✓	0.154	0.691	0.216	0.064	0.369	0.089
Control (no def.)		✓	0.226	0.988	0.242	0.061	0.280	0.107
Post-deformation	✓		0.251	0.691	0.233	0.065	0.450	0.081
Control (no def.)	✓		0.233	0.988	0.262	0.082	0.369	0.096

To isolate the effect of setup error, the positions of all markers were also assessed relative to an arbitrarily chosen reference marker within the sample. Mean shifts were less than 0.1 mm with a standard deviation in the order of 0.1 mm. This confirms the reproducibility of the deformation/relaxation cycle, and that observed variations are due to setup effects.

3.4.3 Deformed dose distribution

In the first irradiation scheme, the beam was incident upon the end of the cylindrical DEFGEL phantom. The cylinder was laterally compressed orthogonal to the cylinder and beam axes. Isodose contours are shown in Figure 3-10 for a plane through the depth of maximum dose for each of the 3 deformation scenarios. Figure 3-11 shows line profiles through the same plane at the locations indicated by dashed lines in Figure 3-10, labeled A-A', B-B', and C-C' respectively.

The dose distributions corresponding to the undeformed (Scenario 1) and deformed (Scenario 2) states of the DEFGEL phantom were compared. A third arrangement involved irradiation of a DEFGEL in both deformed and undeformed states (Scenario 3). This demonstrates the capacity for integrative dosimetry over different states of deformation.
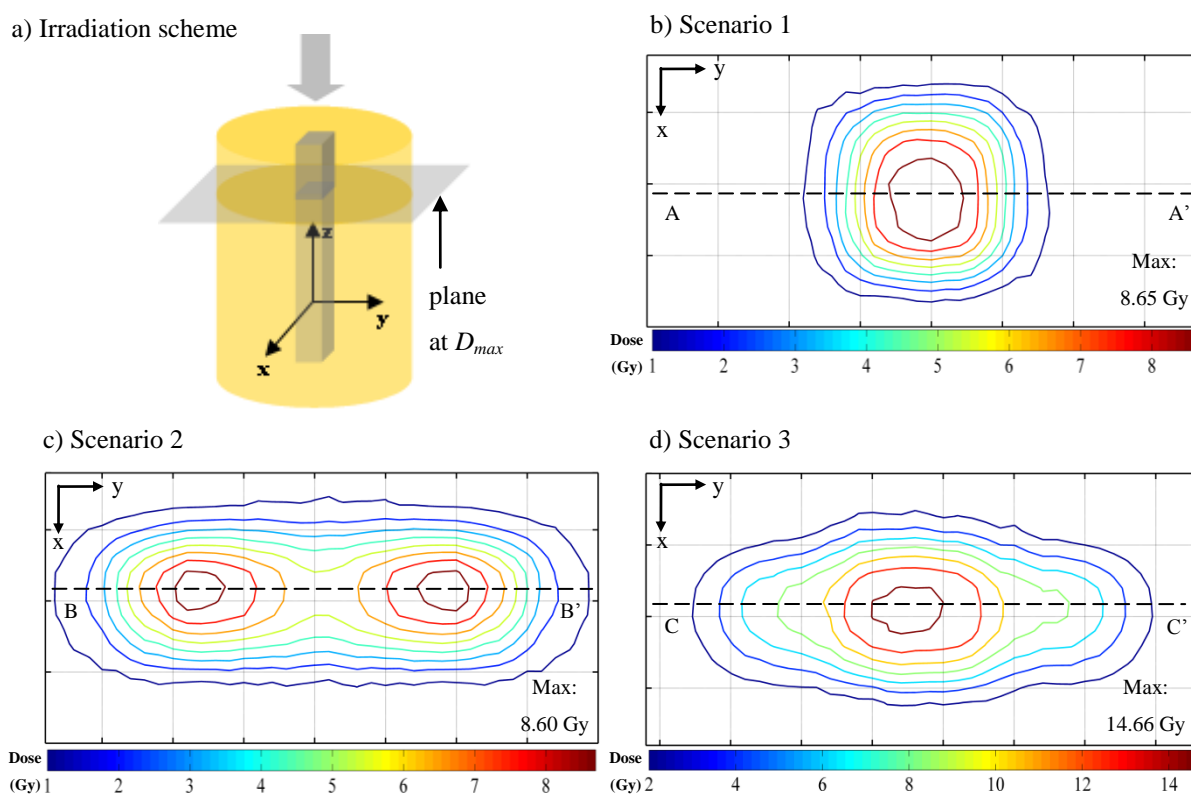
Figure 3-10 Dose distributions for *coaxial* irradiation. (a) represents the schematic of irradiation. The gray arrow indicates the direction of the beam applied. Plane at D_{max} was chosen for all cases. Three different scenarios are shown: (b), (c) and (d) correspond to scenarios 1, 2 and 3 respectively. Deformation/relaxation was applied along the y-direction for scenarios 2 and 3. Accumulated absorbed dose distribution in the DEFGEL phantom of scenario 3 is shown in figure (d). Isodose curves at 10% increments of maximum dose are displayed (10 to 90%). The grid spacing is 4.28 mm. Dashed lines along the y direction A-A', B-B' and C-C' are plotted as line profiles in Figure 3-11.
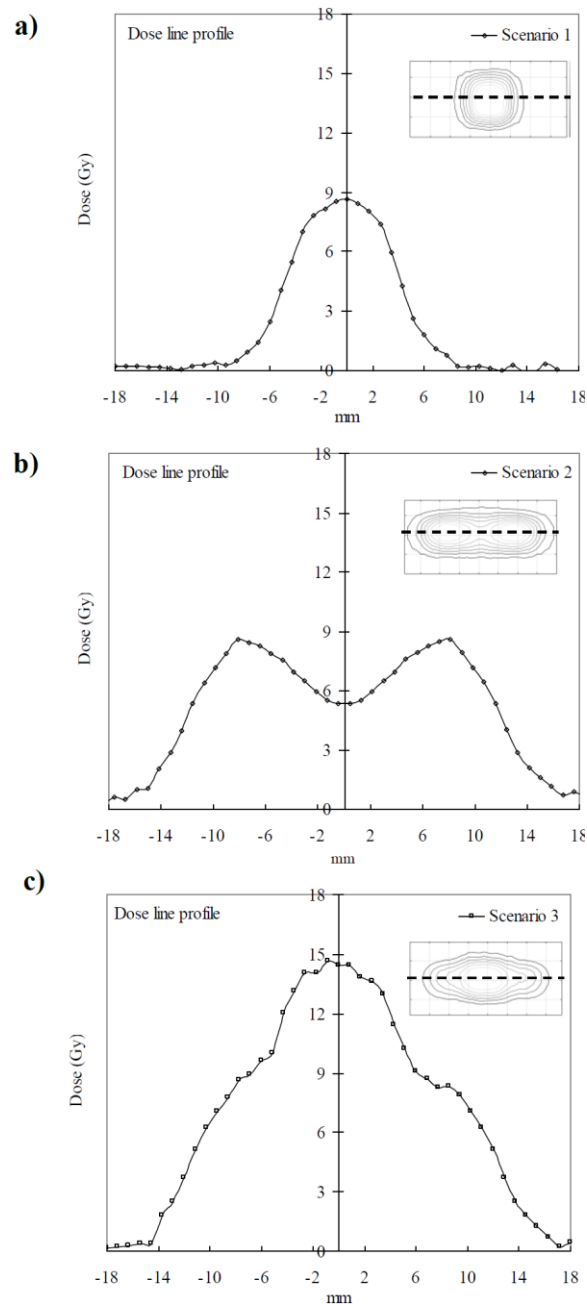
Figure 3-11 Dose profiles corresponding to the dashed lines along the y direction A-A', B-B' and C-C' in Figure 3-10. (a) shows the expected profile for this simple field in a sample without deformation (b) shows the significant dose redistribution that occurs as a result of the change in deformation state. (c) A line profile across the twice-irradiated DEFGEL shows the non-trivial profile arising from the integration of the 2 fields.

When the sample is deformed, mass also moves in directions other than that of the applied compression. Dose redistribution in the z-direction is illustrated by depth dose (DD) plots in Figure 3-12. Curve A (dotted line) is the 'normal' DD curve on the central axis (CAX) of the undeformed sample. Curve B (solid line) shows an off-axis DD curve through the point of maximum dose of the deformed sample. Curve C (dashed line) shows the resulting DD curve on the central axis of the deformed sample, which no longer contains the point of maximum dose.
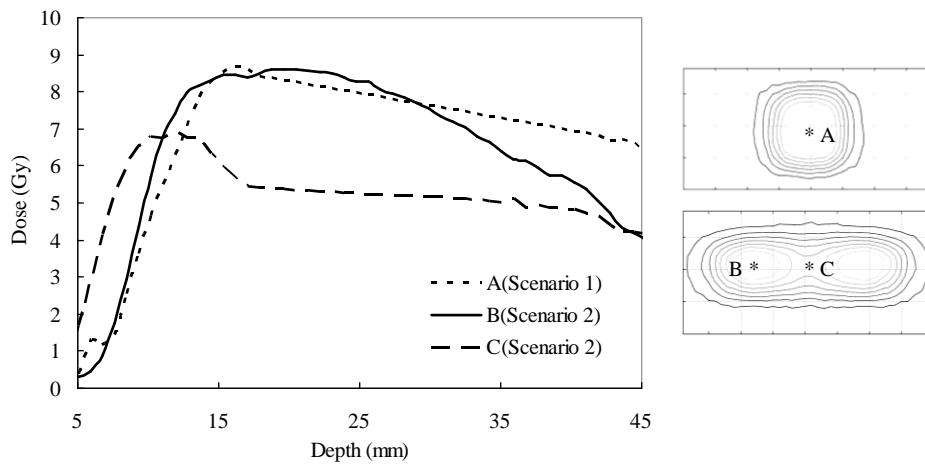
Figure 3-12 Depth Dose profiles for several different cases: (A) on the central axis of the sample without deformation (B) off axis through the point of maximum dose in the deformed sample. (C) on the central axis of the deformed sample.
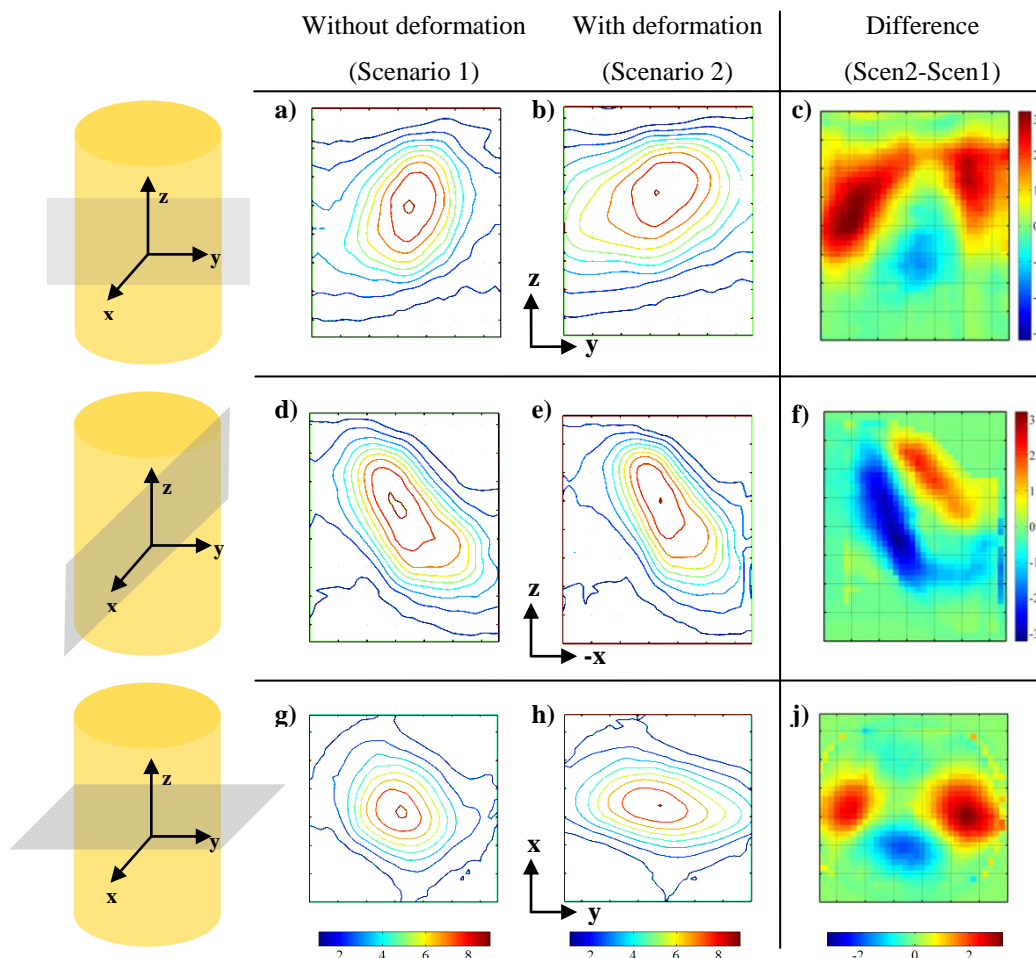
Figure 3-13 Dose distributions of three orthogonal planes for the stereotactic field irradiation. a), b) and c) show coronal plane dose distributions of Scenario 1, Scenario 2 and the difference of Scenario 1 and 2, respectively. d), e), and f) correspond to the sagittal plane, and g), h) and i) to the transverse plane. Compression & release was applied in the y-direction as indicated in Figure 3-4. Maximum doses were 9.17 and 9.03 Gy for Scenario 1 and Scenario 2, respectively, the difference being due to attenuation by the compressor used for Scenario 2. All doses are in Gy and the grid spacing is 5 mm.

Results for the second irradiation, the adapted patient plan, are shown in Figure 3-13. Three orthogonal planes through isocentre are shown for each of the deformed and undeformed samples. A dose difference map is also shown for each plane to demonstrate the ability to quantify the discrepancies arising due to deformation.

3.5. A novel 4D deformable dosimetry system: Discussion

The investigations of reproducibility have confirmed not only that there is no shift or displacement of in-structure geometry of the phantom resulting from the deformation, but also that the employed deformation method is highly reproducible. This validates the use of the released sample as equivalent geometry to an uncompressed sample. As only the two endpoint states of the compression cycle were of interest, hysteresis effects were not explored. These might be of interest in dynamic or multi-phase studies where intermediate states are important.

Scattering effects, which have been associated with OCT scanning of polymer gels, are much lower in DEFGEL than we have encountered with other gel formulations. This is mainly attributable to the lower sensitivity of DEFGEL (due to lower monomer concentrations used) and the consequent lower total optical density of small field samples. Thus, light transmission dominates scattered light intensity – these are the conditions identified by Bosi et al (Bosi et al., 2007) as criteria for avoiding cupping artefacts. Fields of a few cm width in DEFGEL yield optical path length products (geometric path length x OD) in the order of 0.1. This is approximately a factor of 5 below the value at which Olding et al (Olding et al., 2010, Olding and Schreiner, 2011) have identified the onset of discernible cupping (9 cm x ~0.05 cm^{-1}). 'Doming', attributable to scattering in the medium surrounding the field, illuminating the distal interface of a high OD region (also described by Bosi et al (Bosi et al., 2009)) is not seen in DEFGEL measurements of small fields. Small DEFGEL samples are scanned while suspended in the commonly used PETE jars (supplied by Modus Medical for use with Vista OCT) which are filled with the same RI matching fluid as outside the jar in the tank. Thus the vast majority of surrounding material is optically clear, and the scattering contribution is negligible. In summary, neither cupping nor doming artefacts, were observed in either calibration fields or sample measurements. However, the calibration jar (irradiated with 4x4 cm^2 field) and the measured 1x1 cm^2 field in the DEFGEL phantom have similar scatter perturbation in the measurements that somewhat cancel out one another but not perfectly.

Hence, there is still an inherent uncertainty present in the absolute dose measurement due to a non-linear scatter perturbation with its reasonable expectation of 2-3% that will affect uniformly across the overall dose distribution. This may limit deformable polymer gel dosimetry to achieve an accurate absolute dose measurement within 3% uncertainty. In any future work this can be improved by correcting background scatter perturbation in calibrated measurement data. With larger fields measurements, the simplest approaches to reduce scatter-sourced stray light perturbation could be increasing the scanner light source wavelength into the infrared but also developing a new gel formulation and/or modifying the current formulation to reduce the dose contrast sensitivity as well as scatter attenuation background. However, both options will result in lower signal-to-noise ratio that is an inevitable trade-off to supress stray light perturbation. Alternatively, laser scanning method can be also used for larger fields.

A preliminary examination of 2x2 cm^2 field irradiation on undeformed DEFGEL shows that dose profiles of 2x2 cm^2 field are well agreed with the corresponding TPS profiles, demonstrating there were no more confounding scatter effects present on 2x2 cm^2 case compared to 1x1cm. It is also recommended that for the study of larger field sizes (therefore requiring larger phantoms than those used in this work) one should scale the doses delivered to maintain a pathlength-OD product below 0.45 (corresponding to a pathlength-*dose* product of 22.5 cm·Gy). For such larger phantoms, the presence of doming is not easily predicted and should be explicitly tested for. One strategy for reducing its influence would be to work with phantoms no larger than needed for the fields to be used taking into account a margin of approximately 1 cm to avoid the usual optical artefacts associated with container walls.

Figure 3-10 and Figure 3-11 show dose distributions and profiles from irradiation with the beam coaxial to the cylindrical phantom and perpendicular to the applied compression. Panel (b) of Figure 3-10 depicts the plane through D$_{max}$ for the undeformed case. Note the rounding of the expected square field. This illustrates the deficiency of the TPS at accurately estimating the lateral electron disequilibrium and collimator scatter for these small fields (of which results shown in Chapter 5) (Yeo et al., 2012). This has been confirmed in the study performed by our research group with Monte Carlo simulations which agree better with the gel results than with TPS calculations In the study, the Monte Carlo simulation of the treatment delivered to the phantom containing the gel was run on a 608-core high-performance computing cluster, using the BEAMnrc and DOSXYZnrc codes with a model of the Varian iX linear accelerator and BrainLab m3 micro-MLC. A comparisons was performed between TPS (iPlan i.e. pencil beam calculation), MC (BEAMnrc), and the gel measurement in a heterogeneous head phantom Target statistical accuracy was 0.5% with voxel size of 0.5

$\times$ 0.5 $\times$ 0.5 mm^3. Similar monte carlo verification of gel over TPS has been also been observed by Kairn et al. Gamma analysis with stringent acceptance criteria (2%/1mm) reveals that the passing rate is 10% higher for the comparison of the measurement and Monte Carlo results then for that of measurement and TPS results. This result provides valuable confirmation that although there are regions where the dose distribution obtained from the gel differs from the treatment planning prediction, the gel measurement nonetheless provides an accurate measurement of the dose, as calculated via Monte Carlo simulations (Kairn et al., 2012, Yeo et al., 2012).

For the case where a deformed sample was irradiated and allowed to release back to its rest state, a plane through D_{max} is shown in Figure 3-10 (c). Note that this plane is through the point of maximum dose in the irradiated volume, and that this does not occur on the central axis (CAX) as might be expected, nor at the usual expected depth for this energy ($\approx$ 16mm for 6MV) but at 20.5 mm. This demonstrates the complex spatial re-distribution of dose that can occur as a result of a change in shape of a target between irradiations, even for a relatively simple deformation. Dose deposited near the CAX has moved outwards in the direction of the released compression. The net result is a re-distribution of dose in all 3 dimensions.

To illustrate the complexity of trying to calculate such a re-distribution, Figure 3-12 shows depth-dose profiles through each of the points B and C indicated, overlaid with a "normal" DD curve through the CAX of the undeformed sample (A). One can see the foreshortening of the DD curve on the CAX (C) and the re-shaping of the DD distribution off axis through (B). In Figure 3-10 (d), the capacity for integrative dosimetry is illustrated. In this scenario (3), the sample has been irradiated twice with the same 1 x 1 cm beam – once in each state of deformation. The plane through the point of maximum dose is shown, which in this case is at a depth of 16.2 mm as in the undeformed case. This situation arises because the maximum dose points from the deformed irradiation actually move beyond the boundaries of the nominal field. In the general case, the summation will be difficult to predict without a direct 3-D measurement such as that made possible with the DEFGEL.

For the adapted patient plan, Figure 3-13 depicts a comparison between the treatment delivered with and without deformation. For calculating dose difference maps, the pairs of distributions are registered to sub-mm accuracy using the latex container boundaries as shown in Figure 3-8. In this case, the deformation consisting of compression and release in the y-direction can be seen to elongate the field in the y-direction coupled with contraction of the distribution in the x- and z-directions. Substantial dosimetric discrepancies are seen in all 3 planes up to approximately 3 Gy, or ~30 % of the maximum dose delivered.

The use of DEFGEL for studying the effects of deformation on absorbed dose distributions is valid for mass and density conserving deformations. Obvious anatomical examples would include prostate, breast, liver etc. The relevant anatomical deformations would be those related to organ shifts induced by filling and emptying of bladder, rectum, stomach etc as well as respiratory and cardiac motion. The method and results presented here may not be applicable to the case of target organ atrophy for example over the course of treatment, where the notion of dose as a surrogate for biological response becomes complicated by changing target mass and volume.

The effect of deformation on absorbed dose is of significant clinical relevance. Consider, for example, the prostate – which deforms up to half a centimetre in the anterior-posterior direction, with a 10-20 % variation in rectal volume (Kerkhof et al., 2008b, van der Wielen et al., 2008). From the results presented in this work, it is clear that under such circumstances (where the volume is compressed) one would expect the target volume to receive a *lower* dose than that calculated for the undeformed volume, with the adjacent tissues receiving a *higher* dose than otherwise expected. The general consequence is thus that organ deformation may influence the target coverage and organ-at-risk sparing. The DEFGEL phantom has the potential to quantify such issues of under/over-dosage.

The deformable gel model is reasonably adaptable. The cost of this model is relatively low: approximately AUD$7 for each DEFGEL sample. Furthermore they are highly reproducible and it is possible to fabricate many of them with the same batch of gel.

3.6 Conclusion of this work

This chapter has introduced 4D deformable dosimetry using a 3D volumetric deformable polymer gel, 'DEFGEL', as the first inherently coupled deformable dosimeter and phantom. In summary, this work has:

- Developed the first three-dimensional, tissue-equivalent deformable integrating dosimeter.

- Demonstrated robust structural integrity and reproducibility of deformation even after hundreds of deformations.

- Demonstrated experimentally that a change of geometry due to deformation can induce a significant change in the absorbed dose distribution and that such a change can be measured.

- Shown that consecutive irradiations delivered in different states of deformation can be integrated and read out as a single distribution.

- Verified that multiple CT-scanning does not impact on sensitivity.

This work has obvious potential for a number of applications, such as verification of deformable image registration, validation of dose warping strategies based on DIR, and the evaluation of motion compensation strategies in radiotherapy.

The following chapter assesses mathematical tools used to register two images of a deforming object in different deformed states. Specifically, the performance of such algorithms when employed to calculate deformed dose distribution is systematically investigated.

CHAPTER FOUR

: Deformable Image Registration

Calculation of geometrical change and dose-warping

"The Physics is real…you just have to explain it."

Rick Franich's 2nd Law, the author's primary supervisor

4.1 Overview of chapter

For adaptive radiotherapy it is common to collect images of the patient throughout the course of therapy. Because of temporal variations, images from different modalities (e.g. CT/CBCT, PET, MR) are overlaid to create a correlation map between pixels in the images. Deformable image registration (DIR) can be used to correctly account for temporal variations. Such image registration methods exist and their calculations are, in general, driven by high-contrast regions such as bony anatomy or landmarks and interpolations between them. Hence, the analysis of registration accuracy in low-contrast regions is somewhat questionable, as image computation algorithms rely on high-contrast marks, i.e. the analysis can be circular. Knowing the registration accuracy in low-contrast regions is necessary for implementation of this tool in dose deformation algorithms in adaptive radiotherapy.

The present work is an investigation of the spatial accuracy of deformable image registration (DIR) algorithms in low-contrast regions, aiming to establish the efficacy of using DIR as dose deformation algorithms (*Mathematical Model)*, i.e. a means of dose-warping. To achieve this requires an understanding of the principles and mathematics underlying the various DIR methods and algorithms. This knowledge is required to ascertain which methods are likely to be most effective for dose-warping using our deformable dosimeter/phantom and form a shortlist of the vast number of algorithms to investigate. This chapter outlines theoretical aspects of developing a DIR algorithm in the first half (Section 4.2). Subsequent sections illustrate experimental results detailing the validation of DIR algorithms. In both sections, work by other authors is discussed to contextualise the present work.

The following is a list of major terminologies for DIR used in this chapter:

DIR = Deformable image registration
Moving image = source image = data image = secondary image,
Fixed image = target image = reference image = primary image,
Deformed image = calculated image = predicted image = registered image,
VOI = volumes of interest,
DVF = Deformation vector field.

4.2 A review of DIR: Non-rigid image matching

This section outlines principles of deformable image registration and work by other authors on validation of DIR algorithms, illustrating the broad range of approaches and the difficulty in determining a robust method for the quantitative analysis of DIR accuracy.

4.2.1 Why DIR?: Choosing the right type of algorithm

Organ motion is being dealt with *via* a number of strategies in contemporary radiothrapy (Keall et al., 2006, Langen and Jones, 2001, Keall et al., 2005). The clinically-driven requirement of image-matching for dealing with organ *deformation* over the past few decades has resulted in the development of a range of deformable image registration (DIR) algorithms, which are starting to become available as an option in commercial treatment planning systems. It is difficult to determine the number of clinics routinely employing such methodologies, but the growing research interest in deformable image registration within the context of medicine can be qualitatively indicated by the increasing number of publications in recent years i.e. from 70 in 2000-2005 to 244 in 2006-2010 and up to 520 in 2011-2015[†].

Image registration transforms the points in one image to their corresponding points in the other. The transformation can be conducted in several ways such as global or local, rigid or deformable. Rigid registration methods only allow six degrees of freedom (translations and rotations along the x, y, and z axes). When the shapes of target volumes and organs at risk (OARs) change, simple rigid-body correction techniques may not be sufficient for accurate registration. In contrast, deformable image registration (DIR) algorithms enable an alignment of two image sets that are mismatched in a non-linear or non-uniform way. They compute the deformation vector fields (DVFs) that uniquely map each voxel in the deformed anatomy (source image) to a corresponding voxel in the reference anatomy (target image). Such mathematical tools can be particularly useful for a wide variety of applications such as i) image fusion from multi-modality, ii) geometrical change measurements in organs over time, iii) dose warping to map dose distribution corresponding to geometrical deformation that is, in particular, of interest in the present study.

Attempts to contend with organ deformation in image-guided and adaptive radiotherapy dosimetry often involve the implementation of DIR algorithms (Samant et al., 2008, von Siebenthal et al., 2007, Klein and Huesman, 2000, Lu et al., 2006a, Zhong et al., 2008, Davis et al., 2005). Mathematical algorithms which perform 'dose warping' have been described

---

[*] as reflected by a PubMed search of *deformable image registration*, broken into several year periods. There are less than 10 publications prior to 2000.

(Zhong et al., 2008, Janssens et al., 2009b, Nehmeh et al., 2002). Typically, these algorithms apply deformation vector fields (DVFs) derived from non-rigid image registration to a dose distribution calculated by a treatment planning system (TPS). DIR is performed using images of the anatomy in different states of deformation. As DVFs describe the voxel-to-voxel relationship between the "source" and the "target" images, a small discrepancy in this vector can significantly influence the warped dose, particularly at high dose-gradient regions.

DIR algorithms are available for a wide variety of applications. There are several approaches, but most techniques can be broadly categorized as either ''point-based'' or ''intensity-based''(Maintz and Viergever, 1998). Matching is an essential task for many computerised image applications. A clear definition can be given for rigid or articulated bodies: it is to recover rigid displacements of rigid parts. The task is much more complicated for deformable objects with plastic (incompressible) or elastic (compressible) deformations. In this case, there is not a single definition of an ideal optimal match, but as many definitions as practical applications. Each time, one has to define precisely the set of deformations *T* which are explored (rigid, affine, spline, free-form etc), and the type of features which are used (points, curves, surfaces, intensities etc, in which curves and surfaces are an extended concept of point-based, so essentially these can broadly be grouped into two types: point-based or intensity based).

4.2.2 The concept of "attraction" in image registration: an analogy with force and energy in thermodynamic concepts

The energy in Newton's thermodynamics is defined by the integral of force applied for given displacement. A very intuitive way to consider image-to-image matching is based on an analogy with attraction 'force' for measuring the displacement of the two images. One example is gravitation: a point *P* of the deformable model *M* is attracted by all the points *P'* in a static image *S* which are similar. For example, let *K(P, P')* be a similarity criterion, and *D(P, P')* a function of the distance (not necessarily Euclidean),), the force $\vec{f}$ on *P*, induced by the attraction of all the points of *S* can be expressed as:

$$\vec{f}(P) = \sum_{P' \in S} \frac{K(P,P')}{D(P,P')} \overrightarrow{PP'}. \qquad (4\text{-}1)$$

M is deformed according to these forces, and also according to smoothness constraints internal to *M*. Such a method is computationally too expensive [O(n^2)]. A less expensive method is to retain in the computation only one principal attractive point of *S*: a point *P* of *M* is attracted by the point *P'* of *S* which is the 'closest and most similar' to *P*. We perceive in

this definition that a balance between being 'close' (distance criterion) and being 'similar' (similarity criterion) must be determined. For example, in some methods, only contour points are used, and contour points in *S* are equally similar to contour points in *M*, making proximity the most important factor (see below figure).
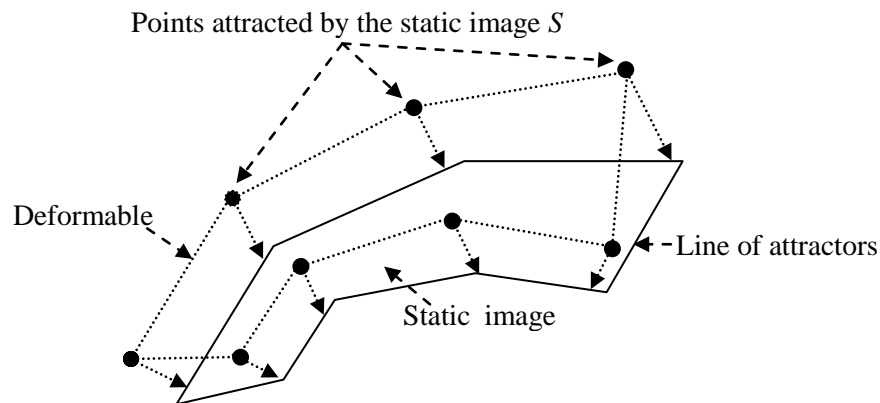
Figure 4-1 A schematic of deformable model with attraction.

Then, calculations of (rigid and/or non-rigid) image registrations aim to minimise the integral of force for given images. This is the case for iterative closest point (ICP) methods; see Besl and McKay (1992) and Zhang (1992) for the rigid case. This is also a basic assumption in the 'snakes' method introduced by Kass *et al*. (1987). This model is a *controlled continuity* spline under the influence of image forces and external constraint forces (high contrast such as bony anatomy and bifurcation or artery). The internal spline forces serve to impose a piecewise smoothness constraint. The image forces push the snake toward salient features like lines, edges, and subjective contours. The external constraint forces are responsible for putting the snake near the desired local minimum. These forces can, for example, come from a user interface, automatic attentional mechanisms, or high-level interpretations; more details are in Kass *et al*.(1987) see also Blake and Yuille (1992) for a review of these techniques.

4.2.3 Point-based techniques

Point-based techniques implement various transformation models including thin-plate splines (Bookstein, 1989), elastic body splines(Kohlrausch et al., 2005, Fornefett et al., 2001), B-splines (Rohlfing et al., 2004b, Rueckert et al., 1999, Schnabel et al., 2003), free form deformations (FFD) (Lu et al., 2004b) and combinations (e.g. B-spline free form deformation) (Rietzel et al., 2005). These techniques, in principle, aim to match the deformed anatomy (source image) with the reference anatomy (target image) by minimizing the distance between features such as points, curves or surfaces of corresponding anatomical structures either manually or automatically. For identifying these features, detection/extraction process for

both images usually requires a certain amount of human interaction and it may result in potential error (Want *et al* 2005), it can be also time consuming. Moreover, point-based methods are based on physical models to follow the changes in anatomy. This requires consideration of the material properties and heavy computation demands. Once the deformation applied to the identified landmarks is known, the movement of the remaining voxels is calculated by interpolation. To be practical for use in radiotherapy it is desirable for DIR methods to be fully automated, able to handle large deformations, fast and, most importantly, accurate. This excludes the point-based methods that require manually selecting a large number of landmarks (Castadot *et al* 2008) although these methods are faster than intensity-based methods when performing image registration because they usually operate on a sparse set of features. However, the time spent on feature extraction can still be significant and error prone as mentioned above.

4.2.4 Intensity-based techniques

Intensity-based algorithms use pixel or voxel data directly, assuming that image intensities alone contain enough information for image registration. These techniques are particularly attractive and time-efficient to solve the problem of intra-modality deformable registration because the attraction force for matching images is based on the gradient of intensity of each voxel (not based on certain interpolation method e.g. affine, b-spline or thin plate spline). Therefore, intensity-based methods do not require feature detection/extraction and instead use similarity measures such as the root mean square error or mutual information between the images or it uses apparent motion of brightness patterns (optical flow)- and hence can be fully automatic.

The well-known Horn and Schunck (Horn and Schunck, 1981a) (HS) algorithm, Lucas and Kanade (Lucas and Kanade, 1981) (LK) algorithm, combined HS-LK algorithm (Bruhn et al., 2005a) and variations of the iterative optical flow algorithm (Barron et al., 1997, Lu et al., 2004a) all fall into the intensity-based category along with the demons algorithm method. The latter incorporates the Thirion (Thirion, 1998a) algorithm, accelerated demons (Wang et al., 2005b) algorithm, symmetric force demons (Rogelj and Kovacic, 2006) algorithm and several variations. It is worthy to note that these algorithms are widely available as Matlab (MathWorks, Natick USA) scripts and also conveniently accessible using the DIRART code developed by Yang *et al* (Yang et al., 2011b) for various applications such as image registration, auto-segmentation of anatomical structure contours, dose warping and dose accumulation.

Similarity measures for template (image) matching

Intensity-based similarity measures work by optimising similarity functions based only on voxel values (not landmarks) with one of the simplest methods being the sum of squared differences (SoSD) between the source image, *S,* and the target image, *T.* The use of SoSD was motivated by the distance measure (the squared Euclidean distance=*d*)

$$d^2 = \| S(i-j) - T(i) \|^2 = \sum_{i,j \in N} [S(i-j) - T(i)]^2 \qquad (4\text{-}2)$$

where *N* is all pixels of 2D image or voxels of 3D in the region/volume of overlap between the source image S and the target image T which is shifted by *j* relative to image S. *S(i)* is the intensity (gray value) of the *i*th voxel in the source image and *T(i)* is the intensity of the corresponding voxel in the target image. In this context, we assume similarity is measured after a rigid registration i.e., the amount of shift (*j*) is zero. In expansion of *d²*,

$$d^2 = \sum_{i \in N} [S^2(i) - 2 \cdot S(i) \cdot T(i) + T^2(i)] \qquad (4\text{-}3)$$

the term $\sum T^2(i)$ is constant as it is the target (reference) image. If the term $\sum S^2(i)$ is approximately constant then the remaining cross-correlation term $c = \sum_{i \in N} S(i) \cdot T(i)$ is a measure of the similarity between the image S and T. SoSD is only suitable for single modality registration as it is highly sensitive to large differences in brightness at the corresponding voxels. SoSD is an appealing choice as it allows for fast optimisation schemes making it computationally very efficient.

However, there are several disadvantages to using cross-correlation term for template matching:

- In case of examining some part of a whole image, if the image energy $\sum S^2(i)$ varies with position, then matching using cross-correlation (= *c*), is dependent on the absolute value of intensity i.e., similarity measurement can fail. For example, the correlation of exactly matching region between the images S and T may be less than the correlation of bright spot between the two images.
- The range of *c* is dependent on the size of the feature.
- Cross-correlation term, *c* is not invariant to changes in image amplitude such as those caused by changing background signal (or intensity) across the image sequence.

Pearson's *correlation coefficient* (CC) overcomes these difficulties by normalizing the image and feature vectors to unit length, yielding a cosine-like correlation coefficient, which is defined as

$$CC = \frac{\sum_{i \in N} \left(S(i) - \overline{S}\right) \cdot \left(T(i) - \overline{T}\right)}{\sqrt{\sum_{i \in N} \left(S(i) - \overline{S}\right)^2} \cdot \sqrt{\sum_{i \in N} \left(T(i) - \overline{T}\right)^2}}, \ where \ \overline{S} = \frac{1}{|N|} \sum_{i \in N} S(i) \ and \ \overline{T} = \frac{1}{|N|} \sum_{i \in N} T(i) \ . \ (4\text{-}4)$$

$\overline{S}$ and $\overline{T}$ are the voxel intensity averaged in the considered volume N; $|N|$ denotes the total number of pixels/voxels of the set N. The cross-correlation (CC) can be applied as a measure of similarity if there is a linear relationship between the brightness levels of the two images. CC allows the same optimisation techniques as SoSD and is therefore computationally fast however, again, cannot be used for multi-modality registration as a global linear transformation of the brightness levels in the two images cannot be assumed (Kaus and Brock, 2007).

The Dice similarity index (DSI) can be also used to compare volumes of interest (VOI) in the reference (=target) image to the corresponding volumes in the moving (source) image after deformation. The DSI indicates the overlapping ratio between the two VOIs. It is defined as

$$DSI = \frac{2 \cdot |A \cap B|}{|A| + |B|} \tag{4-5}$$

where A and B are the two sets of voxels (Dice LR, 1945). The perfect match between the volumes of interest gives a DSI of unity, whereas two disjoint volumes lead to a DSI of zero.

4.2.5 Apparent motion of brightness (intensity) patterns

4.2.5.1 The Optical flow method

Optical flow is the distribution of apparent velocities of brightness pattern movements within an image (tracking the movement of high brightness gradients). The Optical flow method (OFM) was originally developed and studied for use in computer vision to perform video processing, object tracking and motion estimation between two successive frames in time. It has been adapted for use in three-dimensional image registration where the two images are not successive frames in time. This means that the velocities of the individual voxels actually have no time component and can be considered displacements. It is more general to consider $\vec{v}$ as being simply a displacement. In the last two decades the quality of optical flow estimation methods has increased dramatically. Starting from the original approaches of Horn

and Schunck (Horn and Schunck, 1981) as well as Lucas and Kanade (Lucas and Kanade , 1982), research developed many new concepts for dealing with shortcomings of previous models. In order to handle discontinuities in the flow field, the quadratic regulariser in the Horn and Schunck model was replaced by smoothness constraints that permit piecewise smooth results (Deriche et al 1996, Schnorr 1994 and Weichert 2001). Some of these ideas are close in spirit to methods for joint motion estimation and motion segmentation (Farneback 2001 and Mémin 2002), and to optical flow methods motivated from robust statistics where outliers are penalised less severely (Black 1991, Black 1996). Coarse-to-fine strategies (Anandan 1989, Black 1996, Mémin 1998) as well as non-linearised models (Nagel 1986 and Alvarez 2000) have been used to tackle large displacements. Finally, approaches to include temporal changes into spatial information have improved the results simply by using the information of an additional dimension (Nagel 1990, Black 1991, Weichert 2001 and Farneback 2001).

However, not only new ideas have improved the quality of optical flow estimation techniques. Efforts to obtain a better understanding of what the methods do in detail, and which effects are caused by changing their parameters, gave an insight into how several models could work together. Furthermore, various derivative formulations of models gave access to the long experience of numerical mathematics in solving partly difficult optimisation problems. Finding the optimal solution to a certain model is often not trivial, and often the full potential of a model is not used because concessions to implementation aspects have to be made.

In the context of medical physics, optical flow became a name given to a broad category of deformable image registration algorithms (Zhang *et al,* 2008) in which the intensity gradient based approach is the most commonly applied. A mathematical formulation for the optical flow method, including its constraints and associated fundamental assumptions, is derived in Appendix I.

4.2.5.2 Demons method

The demons method uses optical flow as an intermediate step to attraction based techniques by analogy with Maxwell's demons. In this implementation, each image is viewed as a set of iso-intensity contours. Having two images to match, the main idea is that a regular grid of forces deforms an image by pushing the contours in the normal direction. The orientation and magnitude of the displacement is derived from the instantaneous optical flow equation. The main idea is to consider the object boundaries in one image as semi-permeable membranes and to let the other image, considered as a deformable grid model, diffuse through these interfaces, by the action of effectors situated within the membranes.
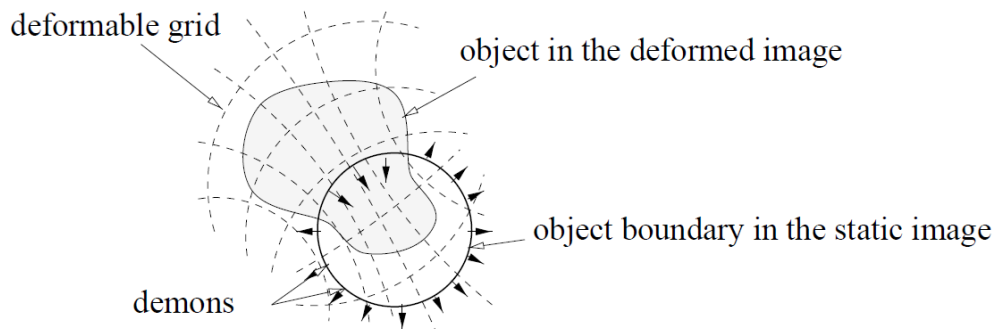
Figure 4-2 Diffusing models: a deformed image, considered as a deformable grid, is diffusing through the contours of the objects in the static image, by the action of effectors, called demons, situated in these interfaces (image reproduced from Thirion, 1998).

There are two approaches to using the demons algorithm: The first approach is to consider the contour of the object in the reference (target) image, *R,* to be a membrane with demons placed along the contour (where the boundary of the object is determined from the gradient of the brightness pattern). The demons will pull (attract) points on the object in the moving (source) image, *M* inside the contour in *R* using optical flow to estimate the "demons forces" (Thirion, 1998b). The second approach is to put a demon at every voxel location and calculate the "demons force" (again, estimated using optical flow) required to push the voxels in *M* to match *R* (Wang et al., 2005e).

A mathematical expression of Thirion's demons method is provided in Appendix I. For more details, the interested reader is referred to numerous studies of the demons algorithm for use in medical image registration (Guimond et al., 2001, Wang et al., 2005e, Xie et al., 2003). In these studies the demons algorithm is assessed using mathematically altered images or patient images.

4.3 Assessment of DIR algorithms performance: Intro

When DIR is used for radiotherapy purposes, validation of the accuracy of a given DIR algorithm is necessary to make sure there is no misinterpretation in imaging analysis (e.g. image fusion or image shift). There are different ways of trying to validate DIR algorithms, each with its own challenges. Such options include i) physical phantoms and ii) patient CT images relying on high-contrast landmarks (bony anatomy or bifurcations). The first option can be criticised in that its results may not be directly related to actual scenarios (i.e. patient images); in contrast, the latter may have absence of knowledge of the ground truth, particularly in between landmarks used for validation (i.e. low-contrast region).

4.3.1 Validation using physical phantoms

A number of studies have demonstrated quantitative evaluation of the DIR accuracy using different strategies, including contour conditions, surface interfaces and implanted landmarks (Wang et al., 2005d, Coselmon et al., 2004, Rietzel and Chen, 2006, Lu et al., 2006b). Some other works also include biomechanical properties for multi-organ deformations (Schnabel et al., 2003, Zhong et al., 2007). Various deformable lung phantoms with known physical deformation have also been used (Cherpak et al., 2011, Seco et al., 2010, Nioutsikou et al., 2006, Kashani et al., 2007c, Walimbe and Shekhar, 2006, Chang et al., 2009), in which the phantom motion can be accurately measured with identifiable land marks.

Wang *et al.* (2005) validated the original demons algorithm (as proposed by Thirion (1998)) by registering CT images of a pelvic phantom with and without an endorectal balloon inflated. 23 fiducial markers were implanted and used to assess spatial disparity. The demons algorithm was found to track the fiducial markers to an accuracy of ~0.8 mm. This result is consistent with the case they tested on pelvic CT images of a patient obtained on two separate days.

A novel method for verifying DIR algorithms in two dimensions was developed by Kirby *et al.* (2011), whereby a phantom representing a single plane of anatomy in a head and neck patient was used. A balloon catheter inside the phantom could simulate tumour growth while CT and camera images were taken before and after the deformation. Non-radiopaque fiducial markers on the surface of the deformable anatomy were visible through an acrylic plate, which enabled an optical camera to measure their positions; thus, establishing the ground truth of deformation. This measured deformation is directly compared to the predictions of DIR algorithms, using several similarity metrics. The ratio of the number of points with more than a 3 mm deformation error over the number that are deformed by more than 3 mm was

used for an error metric to evaluate algorithm accuracy. Different deformation errors resulted from the different similarity metrics. The most accurate deformation predictions had an error of 75 %.

4.3.2 Validation using patient CT

Various studies directly applied DIR to patient CT image sets or digital phantoms generated by Monte Carlo simulation then investigated the accuracy of DIR based on high-contrast features such as bony anatomy and bifurcations (Lu et al., 2004b, Coselmon et al., 2004). Castadot *et al.* (2008) conducted a study into 12 different DIR strategies based on intensity-based measures including the demons algorithm, level-set and fast free-form. The strategies were assessed using five patient CT data sets (imaged once before and once during treatment). Registrations were performed in both directions (chronological and anti-chronological) and were evaluated using a volume-based criterion (Dice similarity index) and an intensity-based criterion (cross-correlation) on manually contoured volumes. It was found that for both evaluation methods the strategies utilising the demons algorithm performed best.

4.3.3 Using DIR for calculation of accumulated dose in a deforming object

Calculation of dose deformation using DIR – dose-warping, which is the topic of the next chapter – is of particular interest in adaptive radiotherapy (ART). This results in attempts to embed a dosimeter within physical phantoms for validation of such calculations, which can provide an additional point comparison between source and target images for validation of DIR algorithms (i.e. the location of an embedded detector and its dose measurement readings).

Several studies have made use of deformable phantoms with one and two-dimensional dosimeters (ion chambers, radiosensitive film, diodes and MOSFET). The demons DIR algorithms were evaluated by Janssens *et al.* (2009) in order to apply it to dose accumulation. A deformable cubic silicon phantom with implanted markers and a cylindrical silicon phantom with MOSFET detectors were used. The phantoms were deformed and images were acquired using a cone-beam CT imager. Dose calculations were performed on the CT scans using the treatment planning system and DIR was performed using the two different phantoms. The resulting DVF was applied to the dose distribution. For both phantoms, resultant warped dose distributions were compared to the original plan in order to investigate how much change could occur. For the cylindrical phantom, measured dose values in the deformed conditions were compared with the dose values of the registered dose distributions. Finally, interfraction dose accumulation for two treatment fractions of a patient with primary

rectal cancer was performed and evaluated using isodose lines and the dose volume histograms of the target volume and normal tissue. A significant decrease in the difference in marker or MOSFET position was observed after registration (p < 0.001) for both phantoms and with both methods, as well as a significant decrease in the dose estimation error (p < 0.01 for the cubic phantom and p < 0.001 for the cylindrical) with both methods.

A number of different approaches to using deformable image registration as a method of calculating accumulated dose distributions in deforming anatomy have been proposed that utilise Monte Carlo simulations. Heath and Seuntjens (2006) and Peterhans *et al* (2011) proposed direct voxel tracking methods for lung tumours. This method tracked the position and shape of each dose voxel as the anatomy changed resulting in irregular (non-rectilinear) voxels. The DOSXYZnrc Monte Carlo code was modified by the authors to calculate dose in voxels that are deformed according to DVFs obtained from DIR. The def-DOSXYZ code was validated by comparing calculations using DOSXYZnrc performed with no deformation of the phantom. These results agreed to within 1%, on average, indicating that the modifications made to the DOSXYZnrc code do not introduce any statistically significant errors; however the computation times were greatly increased due to the handling of irregular voxels. The method proposed by Peterhans *et al.* is essentially the same as that by Heath and Seuntjens however it is a modification of the Swiss Monte Carlo Plan framework rather than DOSXYZnrc.

Calculations in deforming phantoms were compared with the dose remapping method employing trilinear interpolation described by Rosu *et al.* (2005). The trilinear method underestimated the dose by up to 25% within the field for a phantom consisting of 1 mm voxels and a 2 x 2 cm^2 incident beam. Larger discrepancies occurred in the penumbra region. Dose differences within the field were increased to up to 29%, for the same voxel size, for beam incidence perpendicular to the direction of deformation. The discrepancies reduced with decreasing voxel size and deformation magnitude.

4.3.4 Concluding thoughts and a summary of method used in the present study

Assessment of DIR algorithms used for a wide variety of applications, in practice, cannot rely on a single metric. A review of published literature reveals that although a great amount of work has been put into assessing the accuracy of DIR algorithms, the use of DIR for dose-warping has never been validated by comparison to measured high resolution 3D dose distributions. This study delves into several DIR algorithms that are available in the public domain for research purposes and were determined to most likely yield accurate deformation

vector fields (DVFs) from images of our deformable phantom. Note that in this context the image registration is in three dimensions, which is the extended version of 2D method that it historically originated from.

Studies developing DIR algorithms and/or validating these algorithms have used one or more of the aforementioned strategies and usually rely on identifiable markers, such as bony anatomy or implanted fiducial markers (FMs). However, these markers are high contrast features and hence positively influence the DIR result. This implies that analysis of these points may not be representative of the global DIR accuracy. They are nonetheless important to the field, as the accuracy of dose warping will be highly dependent on the accuracy of the DIR used to effect it.

Different operational parameters, used with the same algorithm, can also affect the registration accuracy (Samant et al., 2008, Klein and Huesman, 2000, Lu et al., 2006b). This implies that using automated, standard or default settings may not give estimates with the greatest accuracy, suggesting a need for parameter optimisation. Several popular tool-kits such as Computational Environment for Radiotherapy Research (CERR) (Deasy et al., 2003), Insight Tool Kit (ITK) (Shelton et al., 2005) and Deformable Image Registration and Adaptive Radiotherapy (DIRART) (Yang et al., 2011c) include the capability of adjusting various parameters. DIRART with the associated published technical note has attracted a great deal of attention – the code has been downloaded more than 1400 times over the last few years[‡]. DIRART implements three main classes of intensity based DIR algorithms: Optical flow methods (Horn and Schunck, 1981b, Bruhn et al., 2005b, Barron et al., 1994, Lu et al., 2004b, Yang et al., 2008), demons algorithms (Thirion, 1998b, Wang et al., 2005d), and level-set motion algorithms. There exist multiple variations for each class. Available software applications for clinical use do not necessarily facilitate such flexibility in algorithm selection or parameter optimisation while DIRART allows parameters setting to be adjusted so that each algorithm can be optimised for its best performance.

Previous studies pertaining to anatomic change have focused on tumour motion in the *lung*, as this leads to major discrepancies between daily images and treatment plans (Nehmeh et al., 2002, Jenkins et al., 2005a). Phantom studies have thus involved lung-like models with compressible elements, e.g. sponge (Cherpak et al., 2011, Seco et al., 2010, Nioutsikou et al., 2006, Kashani et al., 2007c, Chang et al., 2009). In contrast, only a few studies have been

---

[‡] **The number of source code downloads was obtained from:**
http://code.google.com/p/dirart/ in May 2015.

undertaken with involving *incompressible* deformable phantoms which could give insight into deformation of organs such as pancreas, prostate, liver, breast etc.

Through the work described in the previous chapter (Chapter 3), a tissue equivalent, mass and density preserving deformable gel dosimetric phantom – dubbed DEFGEL was developed. This previous work enables the measurement of dose in deforming geometries. The next primary interest, as a natural logic, is to use the measurement of dose in deforming geometries for the validation of dose-deformation operations, whereby doses are morphed based on deformation matrices generated by DIR algorithms. However, clearly the accuracy of such an approach is critically dependent upon the accuracy with which DIR algorithms are able to morph the geometry of interest. Consequently, it is important to investigate the accuracy of available algorithms. The remainder of this chapter demonstrates a qualitative and quantitative evaluation process to systematically investigate a range of DIR algorithms in terms of their capacity to generate accurate DVFs for representative examples of deformation of DEFGEL phantoms.

4.4 Assessment of DIR algorithms performance: Materials and Method

This section describes a qualitative and quantitative evaluation process to systematically examine a range of DIR algorithms in terms of their capacity to generate accurate DVFs, particularly in low-contrast regions. CT images of DEFGEL phantoms with 16 implanted fiducial markers (FMs) implanted were acquired in deformed and undeformed states for three different representative deformation geometries. Non-rigid image registration was performed using 12 common algorithms already in the public domain. The optimum parameter setup was identified for each algorithm and each was tested for deformation accuracy in three scenarios: (I) the original images of the DEFGEL with all FMs; (II) images with half of the FMs mathematically erased; and (III) images with all FMs mathematically erased. The deformation vector fields (DVFs) obtained for all scenarios were then applied to the original images containing all 16 FMs. The locations of the FMs estimated by the algorithms were then compared to the actual locations as determined by CT imaging. The accuracy of the algorithms was assessed by evaluation of 3D vectors between true marker locations and predicted marker locations. The influence of the amount of visible information was assessed by interpretation of markers that had been erased and therefore did not contribute to driving the calculation.

4.4.1 DEFGEL phantom and deformation

Chapter 3 describes a deformable, tissue-equivalent, dose-sensitive gel phantom dubbed 'DEFGEL' for use in deformable dosimetry. In this work, it is the first two properties that we exploit to assess the accuracy of a number of common deformation algorithms. The phantom consists of DI water of 88 wt% (w/w) and a hydrogel matrix of 6 wt% (w/w) gelatin in which 3 wt% (w/w) N,N'-methylene-bis-acrylamide (Bis) cross-linking monomer and 3 wt% (w/w) acrylamide (AAm) monomer are dissolved. This formulation is identical to that used for the previous work. The tissue equivalence of DEFGEL was confirmed by two properties: (i) its mechanical properties: physical density of ~1 g/cm^3 and Young's modulus of ~2 kPa (Mahaffy et al., 2000), and (ii) its fundamental radiological properties (based on energy-dependent effective atomic number) (Taylor et al., 2012) which match tissue up to a maximum discrepancy of ~1.5 % (see Figure 3-5) for a very broad range of photon and electron energies.

To investigate displacement of the internal structure after deformation, sixteen Aluminium (Al) fiducial markers (FMs) approximately 1-2 mm in diameter were implanted into the DEFGEL during the gel setting phase. Some markers were made slightly larger than others to aid in distinguishing them from each other. The gel was poured into a thin latex membrane

and a cellulose-acetate film cast was used to mould the DEFGEL into a cylindrical shape of 46 mm diameter. It was then refrigerated at 4 °C for 12 hours before being scanned with x-ray CT.

CT images of the DEFGEL phantom used in this study feature a similar degree of contrast/uniformity and HU intensity as several relevant organs. Figure 4-3 below shows profiles taken from images of DEFGEL and patient organs of relevance. Table 4-1 characterises these *via* their mean HU and standard deviation over a 60 mm profile.
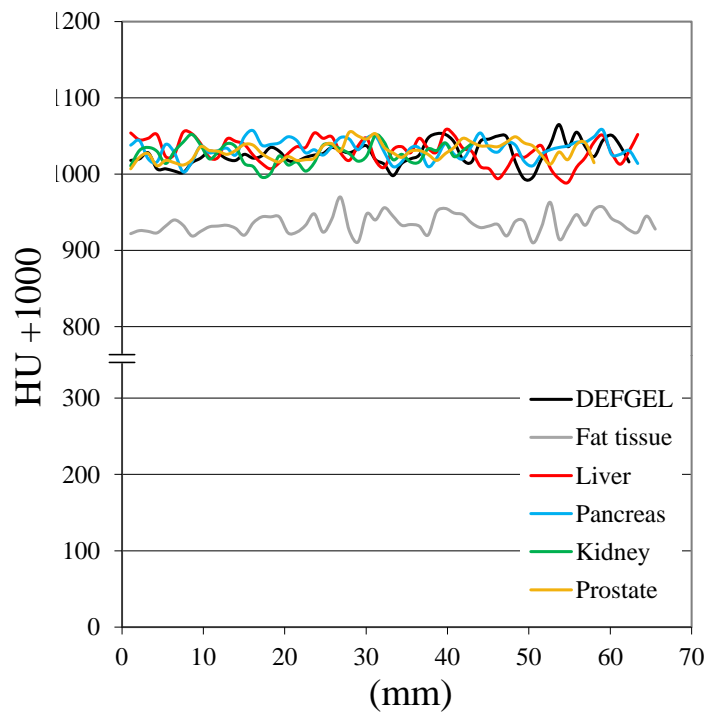
Figure 4-3. Profiles taken through low contrast interior regions of DEFGEL and several organs/tissues illustrating comparable levels of HU (offset at zero to air, as used in treatment planning system) in terms of both mean value and noise. Fat tissue is also shown for comparison, exhibiting similar noise at a different HU level.

Table 4-1 Mean CT number (HU) and standard deviation from CT images of DEFGEL and several organs/tissues which would be considered 'low contrast' within their visible boundaries. Mean and Std Dev are taken over a 60 mm linear profile selected to be interior to the organ/tissue/DEFGEL boundary.

Organs: HU	DEFGEL	Fat tissue	Liver	Pancreas	Kidney	Prostate	Stomach	Small bowel	Diaphragm
Mean:	1027	935	1030	1033	1026	1030	1026	1026	1027
Std Dev:	15.6	12.5	17.0	12.4	13.2	11.5	16.7	20.1	16.0

We applied a series of deformations representative of those observed in anatomical images, i.e. the encroachment on target volumes by adjacent anatomy featuring a displacement or expansion by a convex curved surface (such as in the case of a filling organ). We have considered three variations that describe a range of possibilities:

(i) a bilateral compression of equal displacement from both sides;

(ii) an asymmetric bilateral compression where the convex indentation from one side causes a larger displacement; and

(iii) the combination of a symmetric bilateral compression with an asymmetric indentation of the type described in (ii).

These configurations cover geometric deformations featuring two, one, and zero axes of symmetry in the deformed volumes respectively as well as a range of displacements and directions of marker movement. Each of the deformations was applied by purpose-built acrylic rigs and the compressions were applied principally in a direction perpendicular to the central axis of the cylindrical phantom as indicated in Figure 4-4.

The reproducibility of the deformation and the return to the rest state are important for applications involving DIR and dose integration. The previous chapter shows reproducibility of deformation for hundreds of deformations of a single DEFGEL to the order of ~100 μm, which is the same level of accuracy in the absence of any deformations (see Figure 3-9 and Table 3-1).
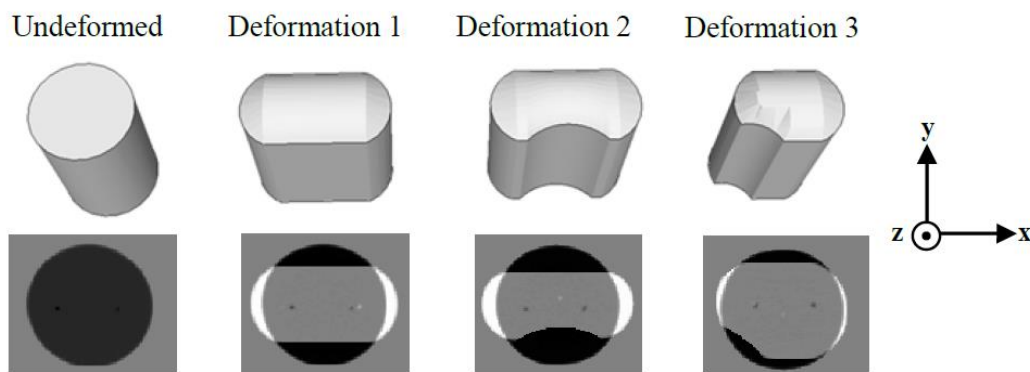
Figure 4-4. The reference (undeformed cylinder) and three geometric deformations employed in this study. The maximum deformation displacements (3D vector) are 11.3, 19.9 and 9.4 mm for Deformations 1, 2 and 3 respectively. The coordinate system associated with the phantom is such that the z-axis is parallel to the axis of the cylinder (out of the plane in bottom row). The deformations were applied principally in the y-direction.

4.4.2 Data collection and processing

The DEFGEL phantom (with 16 implanted FMs) was scanned coaxially in deformed and undeformed states for each deformation type using a GE LightSpeed RT, wide-bore CT scanner (GE Medical Systems, USA). The slice thickness and spacing were both 1.25 mm and a 150 mA/100 kV source was used. The voxel resolution was 0.488 x 0.488 x 1.25 mm^3. To obtain a finer resolution in the third dimension the phantom was rotated 90° and scanned a second time orthogonally. This effectively gave a resolution of 0.488 mm in all three directions, where the x- and y-coordinates of markers were obtained from the coaxial scan and the z-coordinate from the orthogonal scan.

The DICOM image files were converted to .mat files for use in DIRART via CERR (Deasy et al., 2003); an open-source toolkit developed using Matlab. Right-Left (RL), Anterior-Posterior (AP) and Superior-Inferior (SI) were associated with x, y and z directions respectively (see Figure 1) as per DIRART convention. The FM locations were evaluated for both image sets – deformed and undeformed – by identifying the position of local maximum intensity (HU), using DoseLab version 4 (Childress and Rosen, University of Texas, M.D. Anderson Cancer Center, Houston, TX) and Image J (National Institute of Health, Bethesda, Maryland, USA).

4.4.3 Assessment of DIR algorithms

This study investigates twelve of the most commonly used algorithms in current clinical practice. Of these, most are intensity based, and can be grouped into four types: a free form deformation algorithm (Lu et al., 2004b), two variants of the level-set motion algorithm (Vemuri et al., 2000), four variants of the optical flow algorithm (Horn and Schunck, 1981b, Bruhn et al., 2005b, Barron et al., 1994, Yang et al., 2008), and four variants of the demons algorithm (Thirion, 1998b, Wang et al., 2005d, Yeo et al., 2008, Rogelj and Kovačič, 2006). We have deliberately used the DIRART implementations of these algorithms as these are freely available in the public domain. In addition to these 11, the point-based b-spline algorithm employed in the commercial software package VelocityAI (Velocity Medical Systems, Atlanta USA) has also been evaluated.

Several of the algorithms investigated (as described later in Results) failed to adequately register even the boundary shape of the phantom. This paper focuses on the seven highest performing algorithms: original Horn and Schunck (Horn and Schunck, 1981b), combined Horn-Schunck and Lucas- Kanade (Bruhn et al., 2005b), inverse consistent Horn and Schunck

(Yang et al., 2008), iterative optical flow (Barron et al., 1994), Thirion's original demons (Thirion, 1998b), accelerated demons (Wang et al., 2005d) and modified demons (Yeo et al., 2008). Notably, these are all classed as either optical flow or demons algorithms.

To establish the optimum DIR performance for each algorithm, various parameters were systematically adjusted: four multi-grid stages were used (n = 1, 2, 3 and 4) with 10n iterations per pass, while the number of passes for each stage was systematically varied. Coarser stages were typically run with a greater number of passes to improve the agreement with the target image prior to resampling at finer resolutions (Yang et al., 2009). Ultimately, this corresponded to up to 72 pass criteria combinations per algorithm. Agreement was assessed in terms of the minimum difference from the target image for each calculation. Beyond an optimum number of passes, the difference tends to increase, with the observed effect generally being a 'smearing' of the image. Smoothing during a given iteration (α^2 in the optical flow equation (Horn and Schunck, 1981b) or low-pass filter window size of the Gaussian filter for the demons algorithm (Thirion, 1998b) along with smoothing after each pass, multi-grid stage and final stage (σ of the Gaussian low-pass filter applied to the DVF) were also systematically adjusted. The influence of these parameters was assessed using 3D vector errors associated with the calculated FM positions relative to the actual positions known from direct measurement (Section 4.3.2). The optimum parameter set for each algorithm was tested against small perturbations to verify that the change in mean error remained within < 0.24 mm implying absolute convergence within the intrinsic uncertainty resulting from the voxel size (~0.49 mm).

After establishing the optimum parameters for each algorithm, the effect of the presence of high contrast FMs on deformation accuracy was investigated. This was accomplished for each algorithm by performing registrations for each deformation type in three scenarios: I) The original images of the DEFGEL with all 16 FMs. II) Images with eight of the FMs mathematically erased. III) Images with all of the FMs mathematically erased. The FMs were "erased" by replacing the relevant volumes with an array of nearby voxels so as to give a similar intensity distribution and noise level to regions of the DEFGEL where no FMs were present. Line profiles through the region of erased markers were inspected to ensure that no contrast feature remained, nor was introduced, which might influence the outcome of the algorithm in that region. As the required number of passes to achieve convergence may be image content dependent, convergence for the images with erased markers was explicitly confirmed via the method above. The parameters determined using the original images were

then used consistently in each scenario, to quantitatively assess the effect of high contrast features (rather than parameter setting changes).

The DVFs obtained for scenarios II and III were applied to the scenario I data (which contains all 16 FMs). The purpose of this is to assess the accuracy of the calculated deformation in regions of low-contrast, where the DVF was generated without the influence of fiducial markers. The spatial accuracy of the algorithms was assessed by calculating the magnitude of the 3D vectors between the calculated FM positions and their corresponding measured positions. This process is outlined in Figure 4-5.
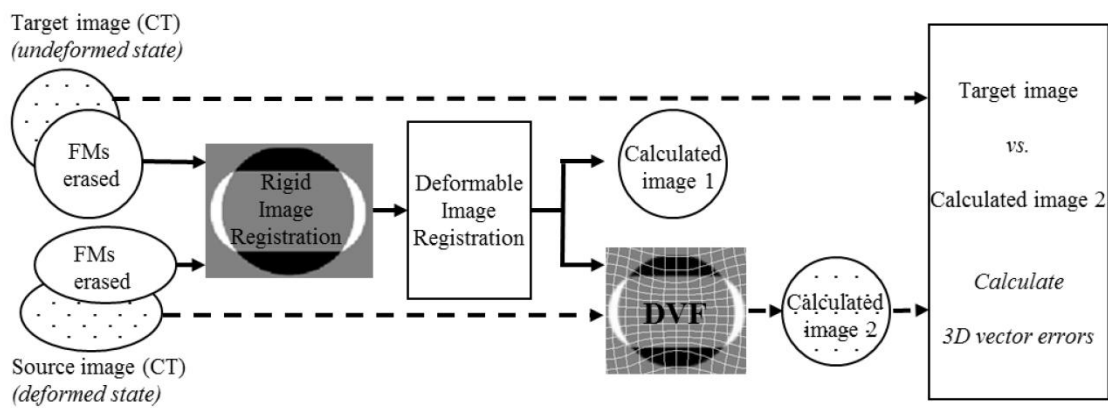
Figure 4-5 An example of the typical workflow for quantitative comparison of calculated and reference image sets in deformed geometries. In this case, the effect of deformation into an oblate shape is investigated (Deformation 1). Before performing registrations, 8 FMs and 16 FMs are erased from both source and target image sets for scenario II and scenario III, respectively. Raw image sets which have all 16 FMs are used for scenario I. Once DIR is performed, the source image is morphed from the oblate shape to the cylindrical shape to match the target image (calculated image 1). Another output of the DIR is a deformation vector field (DVF). This DVF is applied to the raw source image (rather than the image where FMs were erased) to generate calculated image 2. We compare all FM positions of this calculated image to those of the reference image. The mean and standard deviation of the displacement errors are used to evaluate the level of accuracy.

4.5 Assessment of DIR algorithms performance: Results

4.5.1 Determination of optimal parameters

The first assessment of the DIR algorithms was to test whether the general shape of the boundary or contour of the DEFGEL phantom could reasonably be calculated. As shown in Figure 4-6, the *original level-set motion*, *double force demons*, *free form* and *affine approximation of level-set motion* algorithms were unable to replicate the DEFGEL contour. With the exception of the *double force demons*, it was observed that the *optical flow* category and *demons* category algorithms performed reasonably well, matching surface contours between the target image (*undeformed state*) and calculated image very well. This can be seen in the difference maps in which the target image was subtracted from each of the calculated images after DIR respectively (see Figure 4-6). Algorithms A-H are represented by a single difference map in which essentially no features are visible. The *b-spline* algorithm also matched the surface contour very well (which is to be expected as it is a point-based algorithm).

For seven of the eight algorithms able to accurately match the surface of the phantom (Algorithms A to G in Figure 4-6), systematic analysis of algorithm arguments was performed to identify the optimum parameter sets for convergence. That is, the DIR calculation has been performed with four stages ($n = 1, 2, 3, 4$), each with $2n$ passes and each pass having $10n$

A: Original Horn and Schunck
B: Combined Lucas Kanade and Horn and Schunck
C: Inverse consistent Horn and Schunck
D: Iterative Optical Flow Method
E: Fast Demons
F: Modified Demons
G: Original Demons
H: Multipass B-spline
I: Original Level set motion
J: Double Force Demons
K: Free form deformation method
L: Affine approximation of level set motion
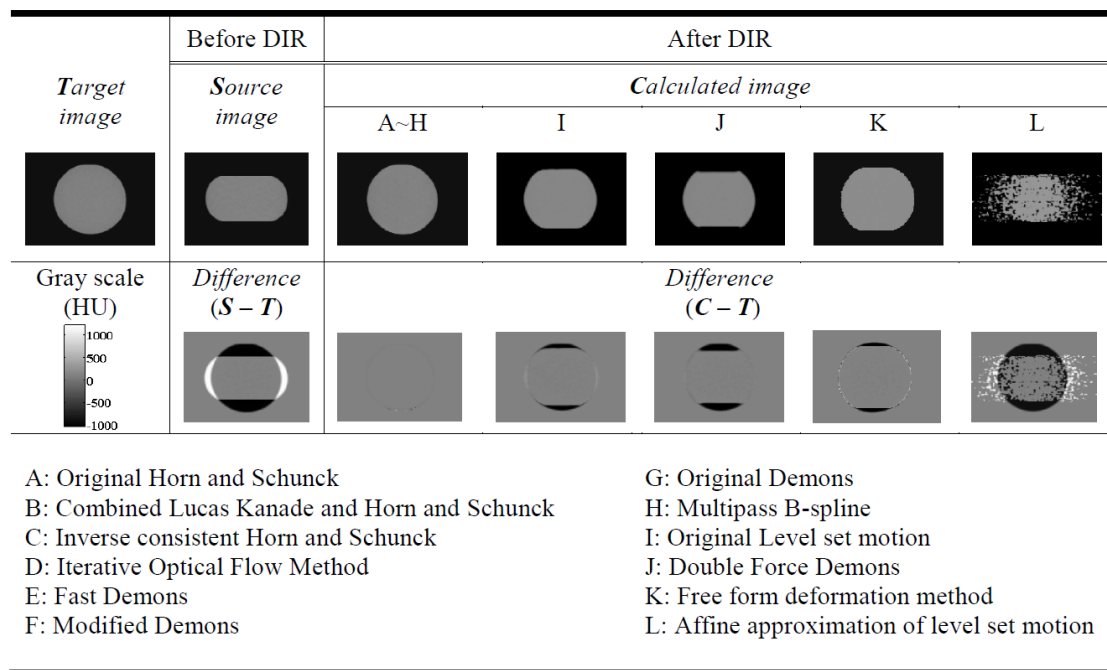
Figure 4-6 Example of initial evaluation of DIR algorithms for Deformation type 1. DIR is performed to match the source image (the oblate shape) to the target image (the cylindrical shape). The upper row shows the Target, Source and each of the *calculated* approximations to the Target image. Difference maps between Calculated images and the Target image are shown in the second row. A single image represents the eight algorithms (A – H) that successfully matched the boundary. The remainder can be seen to have not satisfactorily rendered the phantom boundary.

iterations. This was assessed in terms of the mean displacement error of the 3D vectors between calculated and measured marker positions. The fully optimised parameter combination for all three types of deformations is provided in Table 4-2. Optimal parameters are not shown for the algorithms unable to adequately register the phantom boundary.

Table 4-2 The 11 algorithms investigated in this study together with their corresponding optimal parameters (not shown for the algorithms unable to adequately register the phantom boundary). The parameters examined were smoothing during iterations (α^2 in the optical flow algorithms or Gaussian low-pass filter window size, σ, for demons algorithms), the number of passes at the first multi-grid stage (finest resolution), a, the increment that the number of passes increases for subsequent multi-grid stages, b, and the total number of iterations, N, run over the four multi-grid stages ($n = 1, 2, 3, 4$), where

$$N = \sum_{n=1}^{4} 10n \cdot \{a + (n-1) \cdot b\} \cdot$$

Algorithm Name	Optimum parameters			
	Smoothing (during iteration)	Total number of iteration N (*a,b*)		
		Def1	Def 2	Def 3
A: Original Horn and Schunck	$\alpha^2 = 0.05$	1100 (3, 4)	1000 (4, 3)	600 (4, 1)
B: Combined Lucas Kanade and Horn and Schunck	$\alpha^2 = 0.05$	1200 (4, 4)	500 (3, 1)	600 (4, 1)
C: Inverse consistent Horn and Schunck	$\alpha^2 = 0.05$	2400 (4, 10)	1400 (4, 5)	3200 (4, 14)
D: Iterative Optical Flow Method	$\alpha^2 = 0.05$	400 (2, 1)	600 (2, 2)	400 (2, 1)
E: Fast Demons	$\sigma = 1$	400 (2, 1)	500 (3, 1)	400 (2, 1)
F: Modified Demons	$\sigma = 1$	800 (4, 2)	500 (3, 1)	400 (2, 1)
G: Original Demons	$\sigma = 1$	600 (2, 2)	500 (3, 1)	400 (2, 1)
H: Double Force Demons				
I: Original Level set motion method				
J: Free form deformation method				
K: Affine approximation of level set motion				

The b-spline algorithm (Algorithm H) could not be evaluated as the FMs were not identifiable i.e. the marker locations in the calculated image were so different from those measured, it was not possible to tell which predicted marker was associated with which reference marker. This clearly indicates that despite predicting the surface contour of the phantom very well, a significant error exists inside the target volume of interest. The remaining seven algorithms were assessed for their ability to match points in regions of low contrast. The results for the three different deformations and three scenarios (described in Sections 4.3.1 and 4.3.3 respectively) are presented in the next section (Section 4.5.2).

4.5.2 Three dimensional vector error

Figure 4-7 shows line profiles through selected FMs and the region of an erased marker. This demonstrates that intensity and noise level in the erasure region is indistinguishable from a marker-free region. Coordinates of marker locations were determined from the peaks in these profiles.

A 3D vector was calculated between each measured marker location and its calculated position, the mean, spread and maximum displacement (i.e. magnitude of 3D vectors), of which were used as quality indicators of the performance of each algorithm. Table 4-3 summarises the mean displacement error ($\overline{\Delta}$), standard deviation (σ_Δ), and maximum error (Δ_{max}) for each algorithm applied to each deformation and each FM scenario.
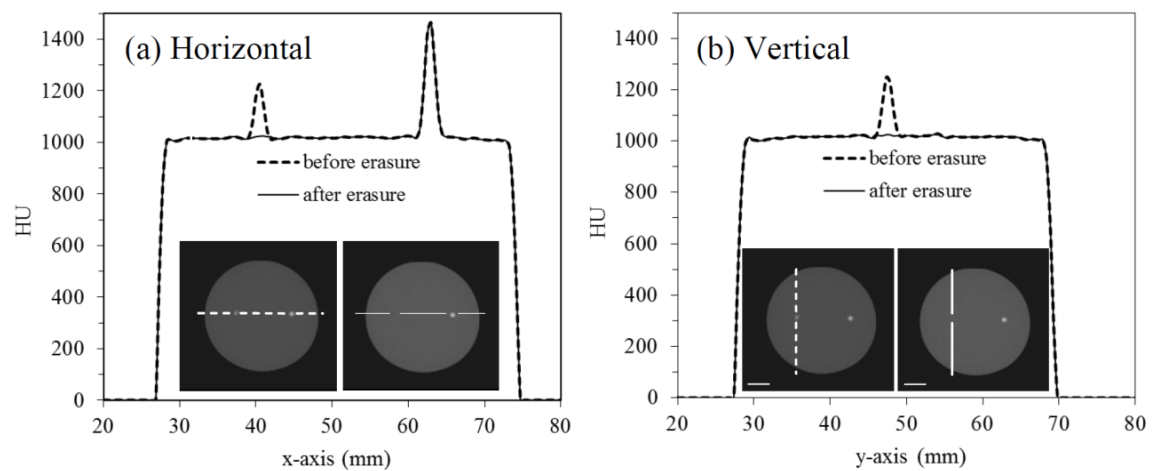
Figure 4-7. (a) Horizontal and (b) vertical line profiles through the marker locations of the inset images (inset images not to scale). The solid and dashed lines indicate the line profile before and after erasing one of the FMs, respectively. The maximum of each peak was used to identify the location of each marker.

A substantial difference can be observed between algorithms. For the first deformation geometry, the mean position error ($\overline{\Delta}$) of 16 markers, varied from 0.3 mm for the best performing algorithm (A) to 2.7 mm for the worst (F). This increased to 1.9-3.9 mm when all of the markers were erased and therefore did not contribute to driving the DVF calculation in the low contrast interior of the sample (Scenario III). The mean position errors for Deformation 3 were similar. However the errors were greater for Deformation 2 which featured the larger displacement of markers from their initial positions. The magnitudes of the errors observed are comparable to previous studies (Kashani et al., 2008b, Janssens et al., 2009c, Wen et al., 2012, Wang et al., 2005a).

Table 4-3. The mean, standard deviation and maximum displacement errors ($\overline{\Delta}$, σ_Δ, Δ_{max}) of the 3D error vectors between calculated and measured marker locations. These are given for seven algorithms (A-G identified in Figure 3), three deformation geometries (1-3), and three different calculation scenarios (I-III) described in text.

(a) Deformation 1	Magnitude of 3D error vector, Δ (mm)								
	Scenario I (all FMs)			Scenario II (half FMs)			Scenario III (no FMs)		
Algorithm	$\overline{\Delta}$	σ_Δ	Δ_{Max}	$\overline{\Delta}$	σ_Δ	Δ_{Max}	$\overline{\Delta}$	σ_Δ	Δ_{Max}
A	0.3	0.4	1.5	1.2	1.3	4.4	1.9	0.9	4.3
B	1.5	0.8	3.1	2.2	1.3	4.6	2.3	1.0	3.6
C	2.2	0.7	3.0	2.4	0.6	3.1	2.5	0.6	3.1
D	1.9	1.1	4.3	2.4	1.3	5.1	3.0	0.8	4.9
E	1.9	0.9	3.8	2.3	1.1	4.9	3.1	1.0	4.9
F	2.7	1.4	5.2	3.5	1.4	5.7	3.9	1.1	5.6
G	2.1	1.0	3.5	2.6	1.2	4.7	3.3	0.9	5.1

(b) Deformation 2	Magnitude of 3D error vector, Δ (mm)								
	Scenario I (all FMs)			Scenario II (half FMs)			Scenario III (no FMs)		
Algorithm	$\overline{\Delta}$	σ_Δ	Δ_{Max}	$\overline{\Delta}$	σ_Δ	Δ_{Max}	$\overline{\Delta}$	σ_Δ	Δ_{Max}
A	1.3	1.1	3.7	3.0	1.6	5.7	3.7	1.6	6.4
B	3.3	1.8	6.6	3.7	1.7	6.6	4.9	1.5	7.2
C	3.5	1.0	4.8	3.6	1.1	5.3	3.7	1.2	5.8
D	3.7	3.3	10.6	5.3	2.8	10.4	5.4	2.2	9.8
E	2.0	1.6	5.4	3.9	2.4	10.4	4.9	2.0	8.3
F	6.1	4.1	11.8	6.3	3.8	12.2	7.5	4.5	13.8
G	2.0	1.5	4.9	3.2	1.8	6.1	3.7	1.7	6.7

(c) Deformation 3	Magnitude of 3D error vector, Δ (mm)								
	Scenario I (all FMs)			Scenario II (half FMs)			Scenario III (no FMs)		
Algorithm	$\overline{\Delta}$	σ_Δ	Δ_{max}	$\overline{\Delta}$	σ_Δ	Δ_{max}	$\overline{\Delta}$	σ_Δ	Δ_{max}
A	0.3	0.3	0.7	1.0	0.8	2.5	1.3	0.6	2.5
B	1.6	0.7	2.5	2.0	0.6	3.1	2.1	0.6	3.1
C	1.3	0.7	2.5	1.6	0.8	3.2	1.8	0.7	3.2
D	2.0	1.2	3.8	2.8	1.6	5.7	3.0	1.4	5.6
E	2.3	1.0	4.6	3.1	0.9	4.5	3.3	0.9	5.1
F	2.5	1.3	5.0	2.9	1.2	5.5	3.2	1.1	5.3
G	2.6	1.2	6.0	2.8	1.1	4.9	3.0	1.0	5.1

The maximum error for a marker in each sample, Δ_{max}, was typically in the order of 1.5-2 times $\overline{\Delta}$ for all algorithms, except for A where the smallest mean error actually makes this ratio larger. This algorithm also featured the smallest Δ_{max} in almost all cases. The largest errors were in the order of 30 % of the phantom diameter. It was noted that the largest component of the 3D vector errors was usually in the longitudinal direction, orthogonal to the direction of the applied compression, however, for some algorithms, the components in the remaining directions were also quite large. This confirms that mass re-distribution is sufficiently complex that DIR must be performed and assessed in three dimensions. Two dimensional calculations are likely to be inadequate.

Comparing deformations 1, 2 and 3, there is a trend across all algorithms of increasing $\overline{\Delta}$ with increasing magnitude of displacement of the markers during deformation. This was the largest for Deformation 2 and a little smaller for Deformation 3 than for Deformation 1 (see Figure 4-4). The mean errors for deformations 1 and 3 were similar, despite the extra complexity of the latter having less symmetry and multiple directions of intrusion. This indicates that the magnitude of deformation has a much larger effect on the accuracy of registration than the complexity of deformation (see Section 2.3.1). This trend also becomes more pronounced as the number of FMs present during registration is decreased.

To achieve a better understanding of the impact of the number of high contrast features, a comparison of $\overline{\Delta}$ across the three scenarios is illustrated in Figure 4-8. For all deformation types, $\overline{\Delta}$ becomes significantly larger when less FMs are present during registration. This is true for all algorithms except *inverse consistent Horn and Schunck* (Algorithm C), which shows relatively little difference ($\overline{\Delta}_{Diff}$ ~10 %) for deformation type 1 and 2. Interestingly, the algorithm yielding the smallest mean error (*original Horn and Schunck*) exhibited a large difference between scenarios ($\overline{\Delta}_{Diff}$ up to 550 %), while the algorithm with the largest mean error (*modified demons*) had a relatively small difference between scenarios ($\overline{\Delta}_{Diff}$ up to 45 %) (See Figure 4-8). Ultimately, the greatest accuracy was exhibited by the *original Horn and Schunck optical flow* algorithm. This featured errors in the order of half of those exhibited by most other algorithms for scenario III, where there were no high-contrast fiducial markers assisting the registration in the low contrast regions. The *modified demons* algorithm showed the largest errors.
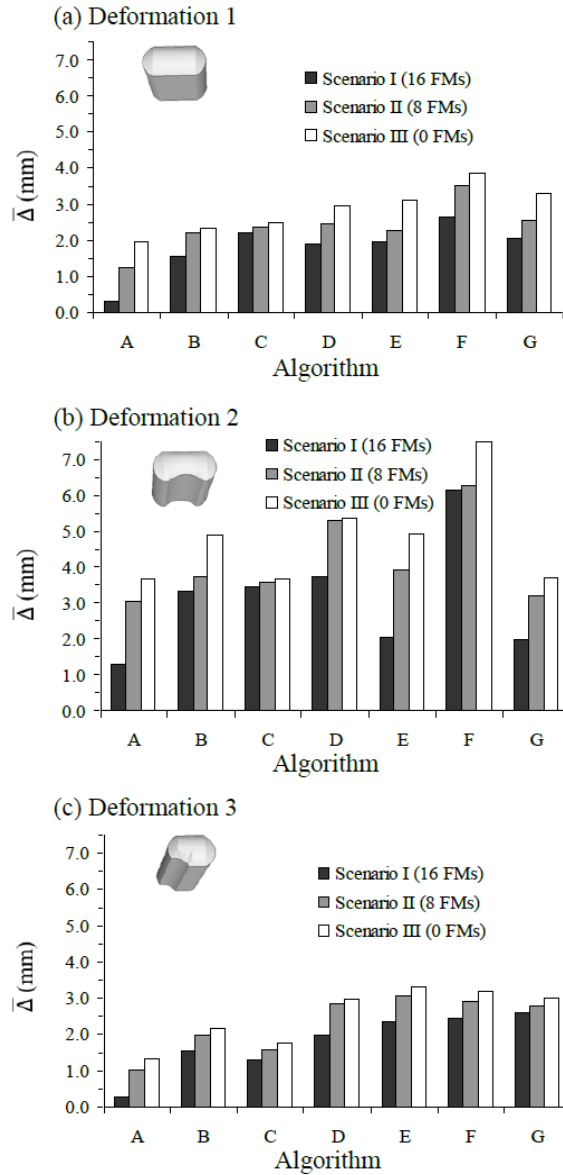
Figure 4-8. Comparison of mean displacement errors across three different scenarios for each registration algorithm: (a) Deformation type 1, (b) Deformation type 2, and (c) Deformation type 3. Inset pictures show representations of DEFGEL phantom in deformed states for each deformation.

4.6 Assessment of DIR algorithms performance: Discussion

Optimisation prior to evaluation of algorithms was necessary because it was found that without this step, some algorithms produced a good match for the boundary contour, but performed poorly for the interior markers. This is important to note, since commercial applications for clinical use do not necessarily incorporate this flexibility, as was the case with the VelocityAI (*b-spline*) implementation. Properly establishing the best parameters may offer as much improvement as algorithm selection. This is likely to be important when using DIR to facilitate dose-warping, as the largest improvements (from optimisation) are found in areas of low contrast rather than at the surface contours. It was found that a greater number of passes was needed for the coarser resolution stages before re-sampling at a finer resolution, and that this helped to increase the convergence speed, the motion capture range and the registration accuracy (Yang et al., 2009). The optimised parameter set was determined using the scenario I images (all markers present) with convergence evaluated via marker position analysis, (i.e. the optimisation process required fiducials to be present). Convergence was also explicitly tested for using the perturbation method and confirmed to be stable. This implied that the optimal parameter set was not a strong function of the number of markers visible inside the phantom boundary. Some algorithms could not even reasonably register the shape of the phantom boundary. This demonstrates that not all algorithms can cope with all DIR tasks, and that a qualitative check of results from multiple algorithms should form part of the algorithm selection and QA process for a given application. The poor performance of some algorithms may be mathematical limitations inherent to the algorithm or due to poor implementation of the algorithm. The developers of DIRART acknowledge in the software documentation that certain implementations may be "buggy" or need "minor changes" and that this may be attributable to insufficient maintenance of original source codes. It is beyond the scope of this study to investigate the reasons for an algorithm's poor performance, with the focus being on the methodology used to quantitatively analyse DIR accuracy. The need for proper assessment of algorithm performance is, however, abundantly clear.

Figure 4-9 shows the range of displacements undergone by markers (1-26 mm) and the calculated position error for the best (Algorithm A) and worst (Algorithm F) performing algorithms. This shows that for the *original Horn and Schunck* (Algorithm A) the errors are reasonably well correlated with the displacements and, from the gradient of the linear fit, errors can be expected to be in the order of 20% of the displacement (R^2=0.76). For the *modified demons* (Algorithm F), the actual displacement is a poor indicator of the errors to be expected for individual locations. In several points, the errors in the calculated positions actually exceeded the displacement from the original position.
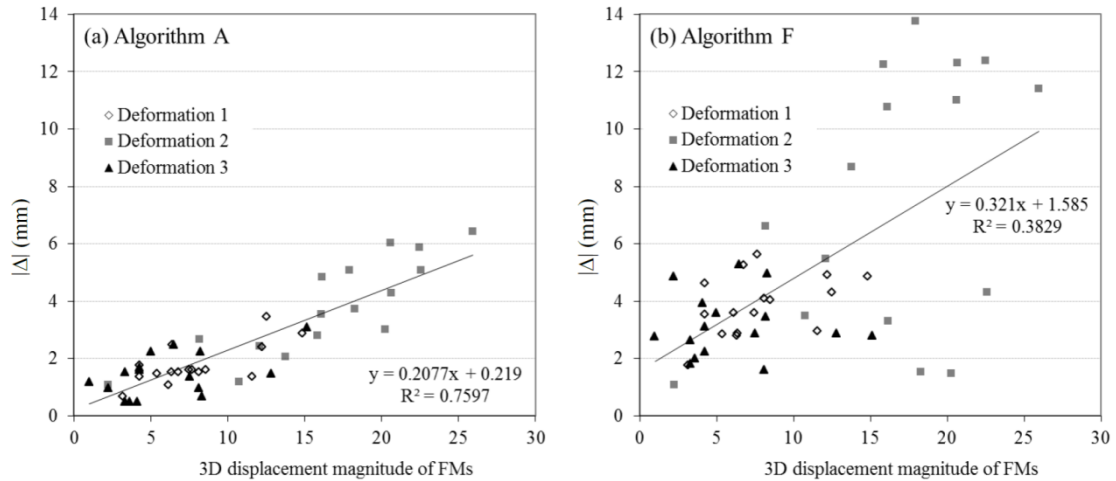
Figure 4-9 Magnitude of 3D error vector (|Δ|) for each marker as a function of its original displacement caused by the deformation, for Algorithms (a) A and (b) F. The individual errors of the *original Horn and Schunck optical flow* are quite well correlated to the markers' magnitudes of true displacement. For the poorer performing *modified demons*, the errors are not well correlated.

The above discussion relates to the performance of algorithms with no markers present (i.e. all markers erased, Scenario III). A comparison of scenarios I, II and III (16, 8 and 0 markers *present* during registration and DVF calculation) clearly shows that a greater number of high contrast features per volume increases registration accuracy. While not surprising, this demonstrates two important issues. Firstly, if the performance of deformable image registration algorithms is evaluated by analysis of features that are present during the calculations, then the outcome will be biased and the results will not be representative of the true performance in low contrast regions. These are precisely the regions we require a quantitative assessment for, as they are not apparent from visual inspection of image matching. It is worth noting that the preferred DIR algorithm is the fastest out of all studied algorithms with respective optimum parameters for each of studied algorithm as shown in Table 4–2.

Secondly, these results permit an evaluation of the benefit achievable by using fiducial markers clinically to improve DIR. This is common practice, for example, in prostate radiotherapy where FMs may be implanted to compensate for the absence of organ contrast when aligning a patient with the treatment beam. Scenario II (half of the markers erased and half present during registration) is of interest in this case. The volume of a prostate is typically ~ 40 mL and up to three fiducial markers are implanted to improve daily patient setup (~14 mL per marker) (Nichol et al., 2007b). Daily patient setup using FMs reduces interfraction setup variation, thereby improving the therapeutic ratio of dose-escalated prostate RT. The use

of FMs assumes that they serve as an accurate surrogate for the position of not only the centroid (centre of mass) of the prostate, but also the surface of the prostate. The volume per marker in scenario II (15 mL per marker) is comparable and gives insight into the accuracy throughout areas of uniform intensity as well as points of high contrast, giving an indication of the overall accuracy obtainable. Maximum deformations of the prostate have been measured to be 6 mm, 13 mm and 7 mm for the three orthogonal directions e.g. (Left-Right, Anterior-Posterior, Superior-Inferior respectively) (Nichol et al., 2007b) which is comparable to Deformation 1 in this study. As the accuracy of registration depends only on the extent and not complexity of deformation, one could expect mean overall registration accuracy in the prostate as good as 1.2 mm using three markers. A comparison to the results for scenario I (16 markers present, 7.5 mL per marker) implies the mean accuracy could be improved to 0.3 mm if six markers were used.

Despite the simplicity of the phantom and deformation model, this system could represent typical deformations of organs such as pancreas, prostate, liver, breast etc. (see Figure 4-3 and Table 5-3 which exhibit similar radiological (Taylor et al., 2009c, Taylor et al., 2012) and physical properties, such as electron density and physical density. The method and results presented here are not necessarily applicable to either the case of deforming targets in lung or tissue atrophy over the course of treatment, where mass and/or density are not conserved. This is not to say that the DIR approach will not work, only that we have not validated those cases here. In any case, in these situations the notion of dose as a surrogate for biological response becomes complicated by changing target masses and volumes. Thus the relationship between the original plan and the mathematical integration of dose over multiple fractions will not be simple. Moreover, the homogeneity of the phantom may not be representative of organs which have other sub-structure such as vasculature, density inhomogeneities or, for example, the urethral architecture in the case of the prostate. The algorithms investigated here were compared to each other in the context of understanding the implications for deformable dosimetry and dose-warping calculations associated with DEFGEL. Implanted substructures such as Nylon wires and Lucite beads (Serban et al., 2008) are under consideration to investigate the effects of sub-structure on DEFGEL modelling of deformable targets.

4.7 Assessment of DIR algorithms performance: Conclusion

Using a tissue equivalent, mass and density preserving deformable gel (DEFGEL) phantom implanted with high contrast fiducial markers, we were able to demonstrate a quantitative evaluation process to systematically investigate the accuracy of DIR algorithms. The results of this study represent DIR performance for analogous mass and density conserving anatomical deformations (rather than lung case) where low contrast image regions are common. Using a method of mathematically erasing the markers prior to registration, we were able to assess the accuracy of algorithms within areas of near-uniform intensity, rather than only at known landmarks. This eliminates bias introduced when using intensity-based algorithms.

Algorithm performance varied substantially. Some were unable even to register the phantom boundary contour satisfactorily. Of those that could, there was a wide range of errors between calculated marker positions and the measured locations. The best performing algorithm – *original Horn and Schunck* – yielded positional errors in the order of ~1 mm up to about 20% of the magnitude of displacement of individual markers. For the worst of the results – *modified demons* algorithm – larger errors were observed and were poorly correlated with the magnitude of displacement, indeed sometimes exceeding the latter.

For most algorithms, larger deformation induced displacements generally resulted in larger errors while there was no trend with respect to the complexity of deformation. The distribution of individual errors was generally characterised by a standard deviation of about ½ to ⅔ of the mean error. The sensitivity of the performance metrics to the number of fiducial markers present shows that if deformable registration is evaluated by analysis of features that are present during the calculations, then the outcome will be biased and the results will not be representative of the true performance in low contrast regions.

A greater number of high contrast features per volume increases registration accuracy, and the technique presented here enables quantification of improvements achievable using fiducial markers for DIR. For example, introducing one marker per 15 mL volume reduced errors typically by up to ~ 30%. Raising the marker density to one per 7.5 mL reduced errors by up to 84% for the best performing algorithm (the *original Horn and Schunck*). As an example of clinical relevance, for treatment of a typical prostate (with volume ~40 mL and three FMs) the achievable accuracy of deformation would be of the order of ~1-2 mm, however this could be improved with the addition of more markers. This information could provide insight for 4D treatment planning strategies including dose warping and deformable dose accumulation.

The next chapter (Chapter 5) discusses the implementation of validated DIR methods from this chapter as dose deformation algorithms, and therefore, the validity of dose deformation.

CHAPTER FIVE

: Validation of dose-warping: Is it sensible to deform doses?

The calculation of complex re-distribution of dose in deforming and moving targets

"Fire is the test of gold; adversity, of strong men."

Lucius Annaeus Seneca

5.1 Overview of chapter

Algorithms exist for the deformation of dose based on patient image sets, though these are sometimes contentious because not all such image calculations are constrained by physical laws (i.e. a perceived 'lack of physics'). What is *not* well known is the degree to which this approach is acceptable. Before it can be adopted, it needs, therefore, to be validated – ideally by direct experiment.

This chapter aims to demonstrate a full 3D experimental validation of results from dose deformation using the evaluated DIR algorithms from the previous chapter (Chapter 4). Complex and re-distributed dose distributions in deforming objects are measured with DEFGEL (*i.e. an experimental model*) followed by irradiation and dose readout using OCT; the corresponding deformed dose distributions are also calculated by DIR and dose-warping using CT image sets of DEFGEL (*i.e. a mathematical model*). The quantitative comparison thereof is performed via 3D γ-analysis to investigate the validity of dose-warping.

5.2 Validation of the dose-warping technique: Background

A variation in anatomic structures due to organ motion and deformation is recognised as a major challenge in contemporary RT. Over the past decade, motion has been a 'big issue' in radiotherapy; as technology to contend with motion improves one might suggest that deformation could be the focus of the coming decade (See Figure 5-1).
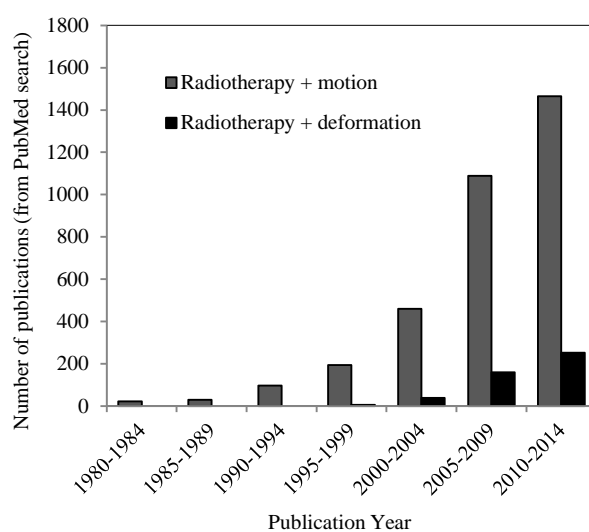
Figure 5-1 Deformation: the next big issue? This figure shows number of publications over the last few decades relating to motion and deformation in radiotherapy (from a simple PubMed search), illustrating that clinical interest in deformation within the context of radiotherapy is on the rise and is perhaps poised to be the next 'big issue' in the coming decade.

Dose accumulation requires that moving and deforming tissues be accurately tracked between images. Hence, understanding the cumulative dose distribution necessitates deformable registration of the two images and corresponding dose distributions. This may be effected by 'dose deformation', whereby an initially planned dose distribution is morphed according to the geometric changes of anatomy evident in the new patient image set. The warped distribution can then be added to previous fractions in order to interpret the accumulated dose. The deformation of dose distribution via the resultant vector map associated with deformable image registration (DIR) calculation is so called 'dose-warping *via* DIR'. This technique is an existing process, proposed to accumulate doses from multiple image sets taken in different time frames. It is sometimes contentious because it is not inherently evident that dose-warping *via* DIR reflects the underlying physical and anatomical processes accurately. Inaccurate dose accumulation could be hazardous in the presence of temporal/spatial anatomy change, as it may lead to treatment decisions being based on incorrect dose distributions.

This contentious (but investigation worthy) topic is reflected by the recent Point-Counterpoint article in *Medical Physics* (Schultheiss and Tomé, 2012) by Drs Schultheiss and Tomé entitled '*It is not appropriate to "deform" dose along with deformable image registration in adaptive radiotherapy'*. The authors presented two opposite viewpoints on this very interesting topic. Dr Tomé – who is against the proposition – provides fascinating case examples of when there is a need of implementing deformable dose accumulation in adaptive radiotherapy:

> "For example, target cold-spots may overlap in reality. Lack of this knowledge could be detrimental to the treatment outcomes, since a significant dose deficit to even a very small portion of a high-risk area within the GTV can have a detrimental effect on the achievable tumor control probability. The same also holds for organs at risk, which by treatment plan design see a highly nonuniform dose distribution. Hence, if accurate estimation of expected normal tissue complication probability for organs at risk is desired for plan adaptation then it is necessary to warp the dose."

The above statements can be applicable to dose warping of both cases i) over multiple fractions (inter-fraction effect) and ii) during a single fraction (intra-fraction effect). The potential advantages of dose-warping for the purpose of accurate dose accumulation may seem self-evident, but one quote from Dr Schultheiss – who is for the proposition – summarises quite succinctly the cause for concern regarding dose deformation effected *via* DIR:

"The ultimate problem with deformed dose is our inability to measure it. Comparison with measurement is always the standard in the mathematical modelling of physical phenomena. Until we can deform dose with algorithms that have been validated against measurement, rather than being merely based on image manipulation, we should withhold all commercial use of this misleading process."

This article relates, of course, very closely to the study of this chapter - a methodology for experimental validation of dose warping – reported in Medical Physics just several issues prior to the article of discussion, entitled '*Is it sensible to deform dose? 3D experimental validation of dose-warping*' (Yeo et al., 2012). Following these articles, our group has responded to the above Point-Counterpoint article, contributing to discussions on the issue – 'the validity of dose-warping'.

There have been a number of groups that have developed deformable phantoms (Chang et al., 2010, Kashani et al., 2008a, Kashani et al., 2007b, Wang et al., 2005b) and attempts to glean dosimetric information through measurements have previously been facilitated by implanting point detectors such as TLD, MOSFET (Cherpak et al., 2010, Janssens et al., 2009a) and two-dimensional detectors (e.g. film) (Nioutsikou et al., 2006, Serban et al., 2008). The ideal approach would be to use a three-dimensional, deformable tissue surrogate that *also* acts as the dosimeter. Published studies evaluating the efficacy of dose-warping using experimental methods are summarised in a table below:

Table 5-1 Published studies evaluating the efficacy of dose-warping using experimental methods.

Dosimeter	DIR algorithm	Phantom	Target	Reference
TLD (0D) and film (2D)	Surface landmark based method	(i) Sponge with acrylic disk	(i) Deform & move	(Vinogradskiy et al., 2009)
Film (2D)	Optical flow method	Lung surrogate	Move only	(Zhang et al., 2008)
Ion chamber (0D)	Optical flow method	Cork and acrylic rod	Move only	(Huang et al., 2010a)
MOSFET (0D)	Demons and Morphons	Silicon with elastic foam	Deform & Move	(Janssens et al., 2009a)
Polymer Gel (3D)	MORFEUS (finite element)	Gel (dosimeter = phantom)	Deform & Move	(Niu et al., 2012)
DEFGEL (3D)	12 different algorithms	Gel (dosimeter = phantom)	Deform & Move	(Yeo et al., 2012)

Ultimately, from a clinical perspective, what is perhaps most of interest is an answer to the question: 'is it sensible to warp doses *via* deformable image registration (DIR)?' Although the answer is not likely to be without complexity, the present work attempts to answer this question by direct three-dimensional experimental evaluation of mathematical dose deformation calculation (i.e. dose-warping technique). The present work subjects the DEFGEL to different deformations and stereotactic beam irradiations, in order to compare warped doses to the corresponding measured doses obtained by DEFGEL. This study has trialled 11 DIR algorithms of which accuracies have been evaluated in the previous chapter.

A novel approach to experimentally validate the calculation of dose deformation via DIR methods is concisely summarised here:

i) DEFGELs are scanned via x-ray CT, in both deformed and undeformed states;

ii) Dose deliveries are planned on the CT images of deformed states using TPS;

iii) For experimental measurements as a ground truth of deformed dose distributions, planned doses are delivered to DEFGELs in deformed states;

iv) Measured dose distributions are readout via OCT scanner (see Chapter 3), in which DEFGELs delivered with deformed states were released to undeformed state before its read-out[4];

v) For mathematical calculations of deformed dose distributions, DIR is performed to match the image in deformed state to the other image in undeformed state;

vi) The planned dose on the deformed state is morphed based on deformation matrices obtained *via* DIR – called deformation vector fields (DVFs); and

vii) The warped dose distribution is then compared to the corresponding measured dose distribution via 3D $\gamma-$analysis in order to validate the dose-warping technique.

viii) CT imaging, subsequent planning and its irradiation of DEFGEL are performed in an undeformed state as *a control case* to quantify the level of agreement expected between plan and measurement in the absence of deformation influence.

The approach is described in more detail in the next section. Through this procedure, this work identifies the best performing of the algorithms studied in the previous chapter and presents a detailed evaluation of the results achievable.

---

[4] In the context of ART, 'deformation' is normally thought of as a change occurring after the original planning CT imaging. Because OCT requires the DEFGEL sample to be reproducibly mounted in its regular cylindrical shape, here we hold the sample in a rig for imaging and irradiation, then the deformation consists of releasing it, allowing it to return to its original cylindrical shape.

5.3 Validation of dose-warping technique: Material and Method

5.3.1 Deformation and beam geometries: For both measurements and calculations of deformed dose distributions using DEFGEL

The previous study described in Chapter 3 reported on a deformable volumetric gel dosimeter/phantom – DEFGEL – that can integrate dose in the presence of temporal/spatial changes in a non-rigid 3D object. This study implemented the same deformations described in Chapter 4 for which the algorithm performance has already been evaluated. The three deformations of the cylindrical phantom are illustrated in Figure 5-2 (which is the upper panel of Figure 4-4, depicted here again for clarity). The maximum deformations (3D vector) in millimetres are 11.3, 19.9 and 9.4 mm for Deformations 1, 2 and 3 respectively.
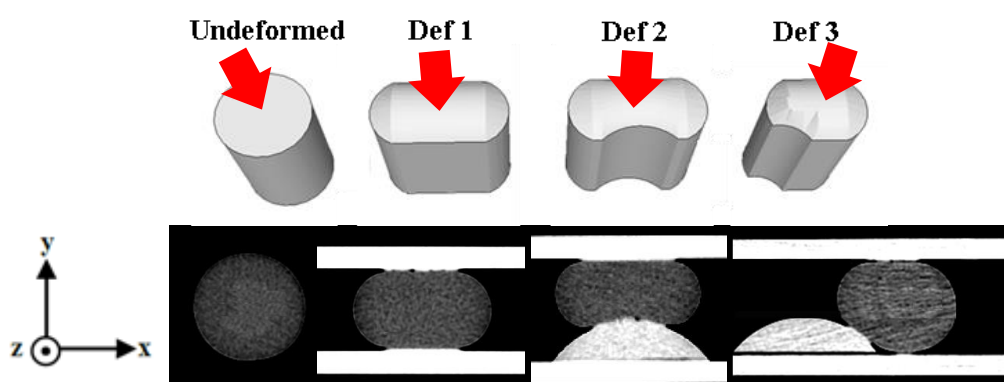
Figure 5-2 Illustrationof the DEFGEL phantom in the Undeformed state and the three different states of deformation. Beam directions (indicated as red-coloured arrows parallel to z-axis) were aligned with the long axis of dosimeter for all cases. The lower panel shows CT images of cross cut of the DEFGEL without deformation and with deformations applied by purpose-built acrylic rigs.

This study evaluates the results for three stereotactic fields (shown in Figure 5-3), possessing different degrees of complexities, which are combined with Def 1 only:

i)   A 10 x 10 mm^2 field;

ii) A cross shaped 20 x 20 mm^2 field (each spoke 10 mm wide); and

iii) A four dynamic-arc stereotactic treatment adapted from a patient plan (a brain metastasis) and recalculated on the DEFGEL (PTV volume of 0.413 cm^3).
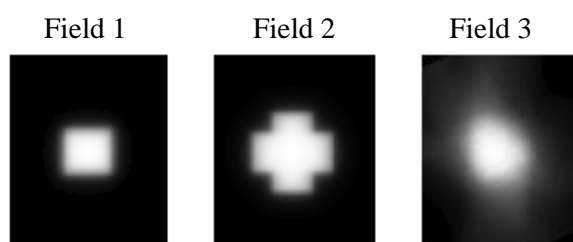
Figure 5-3 Illustration of three planned fields. Transverse cut of D_{max} plane was chosen for illustration of each field. These plans were delivered with their beam direction aligned with the long axis of the dosimeter in both deformed and undeformed state.

CT scanning of DEFGEL was conducted with the absence of deformation and with each of three deformations applied by purpose-built acrylic rigs (see Figure 5-2 as well as Figure 3–3(c) and Figure 3–7(b)). In each case the DEFGEL was submersed in a water phantom. The arc plan was calculated with the iPlan pencil beam algorithm, while the other fields were calculated with Eclipse (pencil beam) – all fields planned with 6 MV and 6.0 Gy to isocentre. Transverse cut of D_{max} planes of these three plans are shown in Figure 5-3. The treatment plans incorporated the tank and deformation rig. The first two fields (the square and the cross shaped) were shaped with the BrainLAB m3 micro-multileaf collimator.

5.3.2 Experimental measurements of deformed dose distributions: irradiation and dose readout

DEFGEL was used to measure dose distributions in both undeformed and deformed states. The arc plan calculated with the iPlan was delivered with a Novalis (BrainLAB, Feldkirchen Germany) dedicated stereotactic unit, while the other fields calculated with Eclipse were delivered with a Varian 21-EX as planned. In each case of irradiation the DEFGEL was set up as scanned and planned with the absence or the presence of deformation as shown in Figure 5-2. Procedures for manufacture of DEFGEL and dose read-out using a cone beam optical CT system are described in Chapter 3 (Section 3.3). In deformed scenarios, DEFGELs delivered with deformed states were released to undeformed state before their read-out. This is because OCT requires the DEFGEL sample to be reproducibly mounted in its regular cylindrical shape. In the context of ART, 'deformation' is normally thought of as a change occurring after the original planning CT imaging). Hence, the deformation, in this case, consists of releasing it, allowing it to return to its original cylindrical shape

5.3.3 Mathematical calculations of deformed dose distributions: DIR algorithms and assessment

The study in Chapter 4 has evaluated 11 DIR algorithms. The major findings are that the Modified Demons algorithm delivered the poorest results and the Original Horn and Schunck algorithm was found to be the most appropriate – yielding the best estimates of deformation of low-contrast regions which are typically less accurately deformed than the high-contrast features that drive the vector field. In this study, these evaluated DIR methods are applied to the mathematical calculation of deformed dose distributions, i.e. used as dose deformation algorithms. The optimal parameter set of each DIR (found in Section 4.5.1) was mainly used to investigate the validity of dose-warping. The impact of smoothing parameters on dose-warping accuracy was additionally investigated.

5.3.4 3D gamma-analysis

For the experimental evaluation of mathematical dose-warping calculation, comparisons of experimental measurements vs. mathematical calculations were performed via a full 3D γ-analysis. Before the concept of γ-analysis was introduced by Harms *et al*. (1998), dose distribution comparisons were subdivided into regions of low and high dose gradients as described by Van Dyk *et al*. (1993). In low gradient regions a simple dose-difference distribution was used while in high gradient regions this comparison was relatively unimportant (due to a small spatial discrepancy giving a large dose-difference) and instead distance-to-agreement (DTA) distributions were used to assess the acceptability of the dose calculation. Gamma-analysis is a composite method that utilises a dose-difference comparison and a DTA analysis. The original method proposed by Harms *et al*. (1998) generated binary distributions formed by the points that failed both the dose-difference and DTA criteria. However this did not lend itself to convenient display and so the convention was to display the dose-difference value at every point that failed the composite criteria. This accentuated the impression of failure in high gradient regions and led Low *et al*. (Low et al., 1998) to implement a numerical quality index based on the same criteria where a value less than unity is considered acceptable. This numerical indexing system is what we now know as γ-analysis.

In the present study it was attempted to specify whether or not each point in the *calculated* dose distribution passed the criteria and so the γ-distribution was determined on the coordinate system of the calculated distribution. Hence, the *calculated* dose distribution, $D_c(\vec{r}_c)$, queried for evaluation, is compared to the corresponding *measured* dose distribution, $D_m(\vec{r}_m)$ used as the reference. The dose difference (ΔD) at the position $\vec{r}_c$ relative to the reference dose D_m in $\vec{r}_m$ is $D_c(\vec{r}_c) - D_m(\vec{r}_m)$. The distance ($\Delta r$ in millimetre) between the reference point (from measured dose distributions) and compared point (from calculated dose distributions) is $|\vec{r}_c - \vec{r}_m|$ (Note that the voxels of the TPS calculated dose data are linearly interpolated to match that of the gel measured dose data). The γ-analysis criteria are denoted by ΔD_{cri} and Δd_{cri} for the dose difference criterion and the DTA criterion, respectively, i.e. each criterion is equally weighted. Then these acceptance criteria for γ-analysis are an ellipsoid in 'ΔD vs. Δr domain', that is,

$$1 = \sqrt{\frac{\Delta D^2}{\Delta D_{cri}^2} + \frac{\Delta r^2}{\Delta d_{cri}^2}} \tag{5-1}$$

Hence, Δr is less than or equal to Δd_{cri}. For each voxel in the compared (calculated) distribution to match the reference dose in $\vec{r}_m$, it needs to contain at least one point $(\vec{r}_c, D_c)$

lying within the ellipsoid of acceptance criteria. A quantitative measure of γ-analysis is determined by the point with the smallest deviation from the reference point, i.e. a γ-index for the point $(\vec{r}_c, D_c)$, $\Gamma_m(\vec{r}_c, D_c)$, is minimal. Hence, a γ- index is defined by

$$\Gamma_m(\vec{r}_c, D_c) = \min(\sqrt{\frac{\Delta D^2}{\Delta D_{cri}^2} + \frac{\Delta r^2}{\Delta d_{cri}^2}})$$

(5-2)

Therefore if $\Gamma_m(\vec{r}_c, D_c) \leq 1$, the result of γ-analysis for the point $(\vec{r}_c, D_c)$ is within the specified acceptance criteria (i.e. passed), otherwise, it is not (i.e. failed).

In this study, this analysis is extended to three dimensions for the DTA criterion, and the passing ratio for the treatment field is calculated for all voxels in the volume receiving >10 % of the maximum dose in order to minimize the effects of noise in low dose regions; such a threshold is commonly used in clinical practice and is consistent with other studies (Ezzell et al., 2009, Petoukhova et al., 2011). This work demonstrates this 'full 3D γ-analysis' for stereotactic fields, which are inherently more complex dosimetrically (Taylor et al., 2011c) and so, importantly, this work also compares planned and measured doses delivered in the absence of any deformation to illustrate the γ agreement expected in the control case. In all other cases, irradiations were performed with the DEFGEL in the compressed state. The γ-passing criteria of 3%/3mm were mainly used in this study as it is routinely used in most clinical practice. In addition, the sensitivity of γ-analysis to different passing criteria was investigated (Section 5.5.4).

5.3.5 Dose warping validation

The general approach for validation of dose-warping undertaken in this work is illustrated in Figure 5-4. The DEFGEL is scanned *via* x-ray CT (GE LightSpeed™ RT CT, GE Healthcare UK), in both deformed and undeformed states. These images are then processed and rigidly registered. The deformable image registration algorithm is used to generate a *calculated* image of the cylindrical DEFGEL from the deformed DEFGEL (i.e. the images of the physically deformed DEFGEL are the 'moving' images, which are morphed to approximate the cylindrical DEFGEL). Ultimately, it is not the generated image which is of interest in the context of dose-warping, but the associated deformation vector field (DVF). Dose-warping is effected by morphing the planned dose distribution using the DVF. This is then quantitatively compared *via* γ-analysis to the corresponding measured dose distribution.
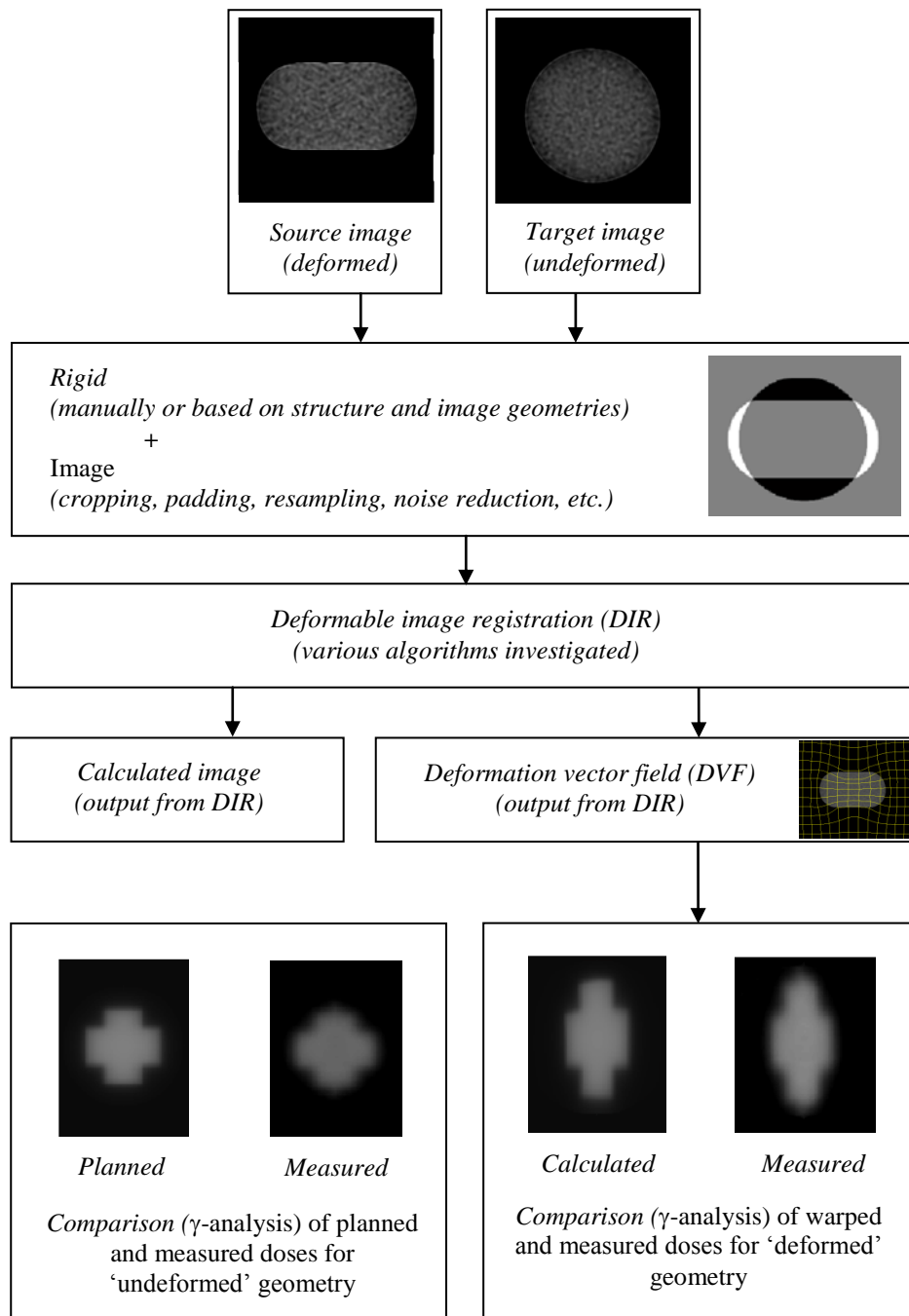
Figure 5-4 An example of the typical workflow for comparison of calculated (dose-warped) and measured fields in deformed geometries. In this case, the effect of deformation into an oblate shape is investigated for a cross-shaped field. The image is warped from the oblate shape to the cylindrical shape. This is done using a DIR algorithm. The output of the DIR includes a deformation vector field (DVF). This DVF can then be applied to the dose distribution (rather than the image), to warp the dose. We first compare (via γ-analysis) the planned and measured distributions without any deformation/dose-warping directly, to evaluate the level of agreement in the absence of deformation (small fields are inherently complex in terms of accurate dosimetry). Subsequently, we compare (via γ-analysis) the measured field in the case of a deformation with the plan that has been dose-warped (using the DVF).

This study first presents a comparison of the results from 11 algorithms in high vs. low contrast regions, using a single deformation and field combination – the cross-shaped field and bilateral symmetric compression (Def2) (Section 5.4.1). As will be shown in the Results section, these results conform to the results of previous chapter that investigated the spatial accuracy of DIR algorithm in low-contrast region. Subsequently, the best-performing algorithm (the Original Horn and Schunck algorithm) was evaluated further to determine the achievable accuracy. Using this algorithm, detailed analysis is performed with all different deformation types combined with a 10 x 10 mm^2 square field (Section 5.4.2). This is followed by detailed analysis with all three different field types combined with a single deformation (Def2) (Section 5.4.3). The following sections evaluated the sensitivity of γ-analysis to different passing criteria (Section 5.4.4), then investigated the impact of the smoothing parameter (i.e. DIR optimisation) on the results of dose warping (Section 5.4.5).

5.4 Validation of dose-warping technique: Results

5.4.1 Comparison of different algorithms in high vs. low contrast regions

Following the assessments of DIR performance (as shown in Chapter 4), this study demonstrates the variability of results from the different algorithms. To do so, dose warping was performed for the cross-shaped field deformed using the bilateral symmetric compression (Def1). The deformation and the field are depicted in Figure 5-2 and Figure 5-3, respectively. Of the 11 algorithms investigated (listed in Table 4-2), 7 of them (A-G) were able to non-rigidly register the oblate source image to the circular target image, as shown in Figure 5-5 and are represented by the single calculated image labelled 'A-G'. The other four algorithms (H-K) failed to register even the circular phantom boundary in the calculated image. The Affine Approximation of LSM algorithm (K) is seen to be particularly dysfunctional. These examples illustrate that not all DIR algorithms will produce DVFs that are usable, and that DIR results should be scrutinised before application to dose warping.

Before DIR		Calculated image After DIR				
Source image	**Target** image	A-G	H	I	J	K
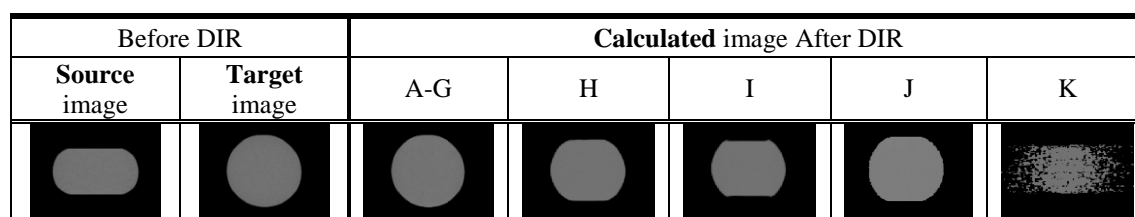
Figure 5-5 The Calculated non-rigid registration of the Source image to the Target image for 11 DIR algorithms. The 7 successful algorithms (A-G) are represented by a single Calculated image that correctly matches the boundary of the Target image. The results for four unsuccessful algorithms are shown individually (H-K). It can be seen that the calculated boundaries are not a good fit to the shape of the Target.

For each of the 11 algorithms, the DVF was applied to the planned dose distribution to generate a calculated approximation of the deformed dose distribution that was directly measured using DEFGEL. These are shown in Figure 5-6 for a dose plane at depth D_{max}. The Horn and Schunck based algorithms, A, B and C can clearly be seen to produce the best results. Note that algorithms D-G, while apparently registering the phantom boundary well, do not necessarily provide good registration of the internal, low contrast regions. Algorithms H-J, derived from registrations where the boundary has not been properly 'expanded' to the circular shape, produced dose maps that more closely resemble the *undeformed* original cross-shaped field as delivered. The result of the dysfunctional algorithm, K, is included for completeness.

An interesting feature of warped dose map K is the surprisingly high γ_{3D} passing ratio (described in detail below) of 53.2 %, which is conspicuously higher than those of maps D to G, despite being heavily fragmented and in no way resembling the expected dose distribution. This arises because of the DTA criterion of gamma comparison. Many of the high dose voxels (red) that can be seen where low dose (blue) is expected are within a very small distance of a low dose voxel that has the appropriate value. A similar argument exists for low dose voxels near the centre of the field where high dose is expected. Thus, it is important, as always, not to accept gamma passing ratios alone as evidence of the quality of dose match. They should be considered only in conjunction with scrutiny of DIR results and inspection of dose difference maps.
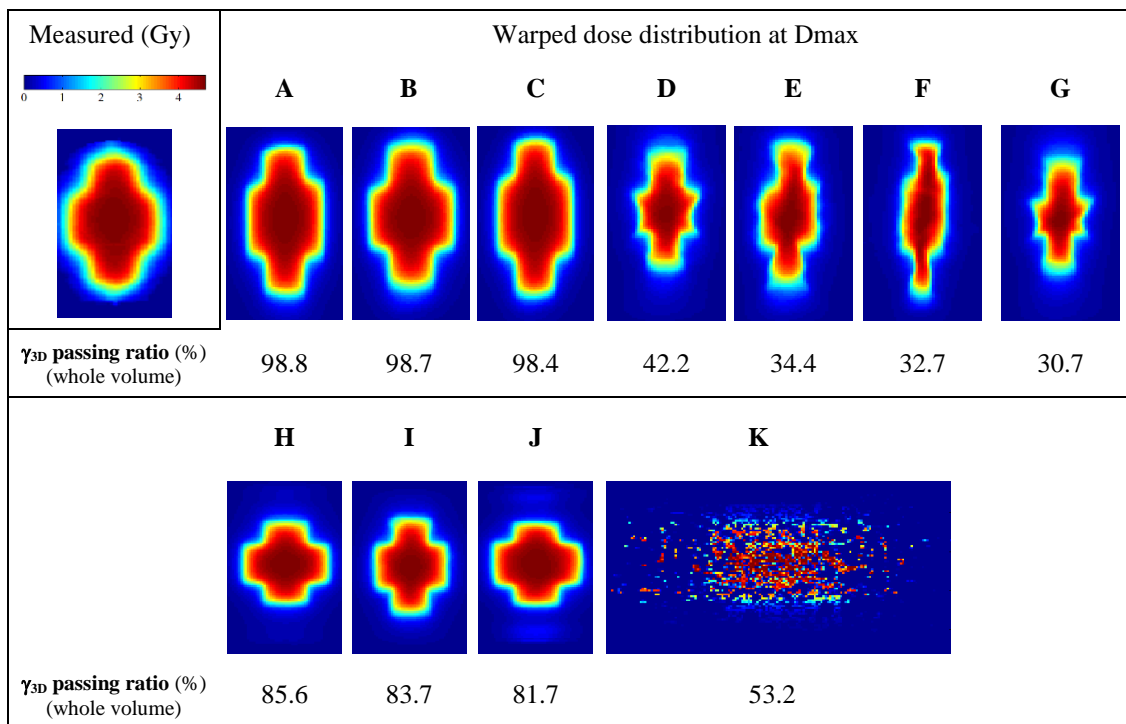
Figure 5-6 The dose-warping estimation of the measured dose distribution shown at top left, for 11 algorithms. Panels A to G are the dose maps derived from algorithms that successfully registered the phantom boundary in the DIR stage, while H to K are for those that did not. The γ_{3D} passing ratio is given for each relative to the measured distribution (3 % / 3 mm criteria).
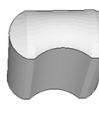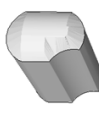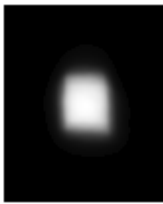
For the Horn and Schunck approach, agreement with experimental data was good (γ_{3D} is over 98 % for all three algorithms A-C); however, it is clear that the internal (low-contrast) regions were far less accurately deformed in the case of the Modified Demons method ($\gamma_{3D} = 32.7$ %). Without this validation process, one might assume that the dose-warping was equivalently accurate in all cases where the algorithms were able to accurately (100 %) reproduce the *contour* of the DEFGEL phantom (i.e. Algorithms A-G).

As the Original Horn and Schunck (OHS) algorithm (Algorithm A) represents the best results that can be obtained from the algorithms tested, it is used for the remaining analysis of performance relative to different deformations and fields.

5.4.2 An evaluation of OHS algorithm (Algorithm A) for different deformations with a small square field

The results of dose-warping a small square field (10 x 10 mm^2) for three different deformations are illustrated in Figure 5-7. The type of deformation is shown, and beneath this the calculated (i.e. dose-warped) and measured dose distributions are presented. To illustrate the level of agreement (for 3 % / 3 mm criteria), γ_{3D} maps are shown at the plane of D_{max} along with the passing fraction for the full volume. In each case the agreement is very good. The 'reference' case – comparison of planned and measured doses in the absence of deformation – demonstrates the baseline level of agreement expected between measurement and calculation; it is important to note this, since one can expect some level of disagreement between pencil-beam calculations and measurements for stereotactic fields (Taylor et al., 2011c).

Consider the data shown in Figure 5-7. For the reference case (i.e. no deformation), the agreement between measurement and planned dose is $\gamma_{3\%/3mm}$ = 99.9 %. Of the deformed cases, Def3 exhibits the least deformation (9.4 mm maximum deformation), and in this case the agreement between measured and warped dose distributions is similarly $\gamma_{3\%/3mm}$ = 99.9 %. Def1 has a maximum deformation of 11.3 mm, and the dose-warped distribution matches measurement such that $\gamma_{3\%/3mm}$ = 99.1 %. Def2 has the largest deformation – about 19.9 mm. Dose-warping calculations for the latter case exhibit the greatest disagreement with measurement: $\gamma_{3\%/3mm}$ = 96.7 %. While probably still acceptable for many applications, it is important to note the obvious trend that the greater the deformation, the less accurate the warped dose distribution. That being said, a ~3 % failure rate in gamma analysis over the whole volume for such a significant deformation is still a confidence-inspiring result, since it is considerably lower than a typical clinical action level (Howell et al., 2008).

Deformation	**Undeformed**	**Def 1**	**Def 2**	**Def 3**
Deformation				
Rigid registration of pre- and post-deformation images				
Calculated:	Planned	Warped	Warped	Warped
Measured:	Undeformed	Deformed	Deformed	Deformed
γ_{3D} **map** (plane at D_{max} shown)				
γ_{3D} **passing ratio** (%) (whole volume)	99.9	99.1	96.7	99.9

Figure 5-7 A comparison of calculated and measured doses in different states of deformation after exposure with a 10×10 mm^2 field. Transverse planes from γ_{3D} matrices are shown with 3 % / 3 mm criteria. The gamma map for the Undeformed case (i.e. comparison of planned and measured dose distributions in the absence of deformation) indicates the achievable agreement.

5.4.3 An evaluation of OHS algorithm (Algorithm A) for different fields' irradiations
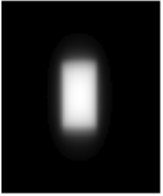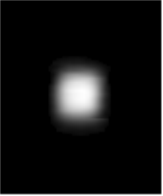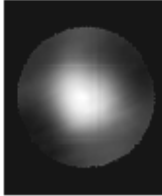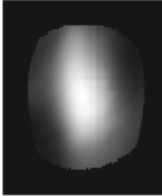
Although the small square field (10×10 mm^2) is dosimetrically interesting (being smaller than the range of secondary electrons and consequently in electronic disequilibrium), it is worth investigating other fields of greater complexity. It is also of interest because larger fields are essentially constructed of small rectilinear beamlets and that this is in many cases how they are calculated. Of three stereotactic fields examined, a four dynamic-arc treatment field the greatest complexity, of which measurements and calculations are shown in Figure

5-8 for both cases – in the absence of deformation and in the presence of deformation (Def1). For deformed cases, a bilateral deformation (Def1) was applied in the y-direction. Complex spatial re-distribution of dose in all three dimensions is observable – i.e. elongated in y-direction and compressed in the other two directions, because the beam was delivered in the deformed state.
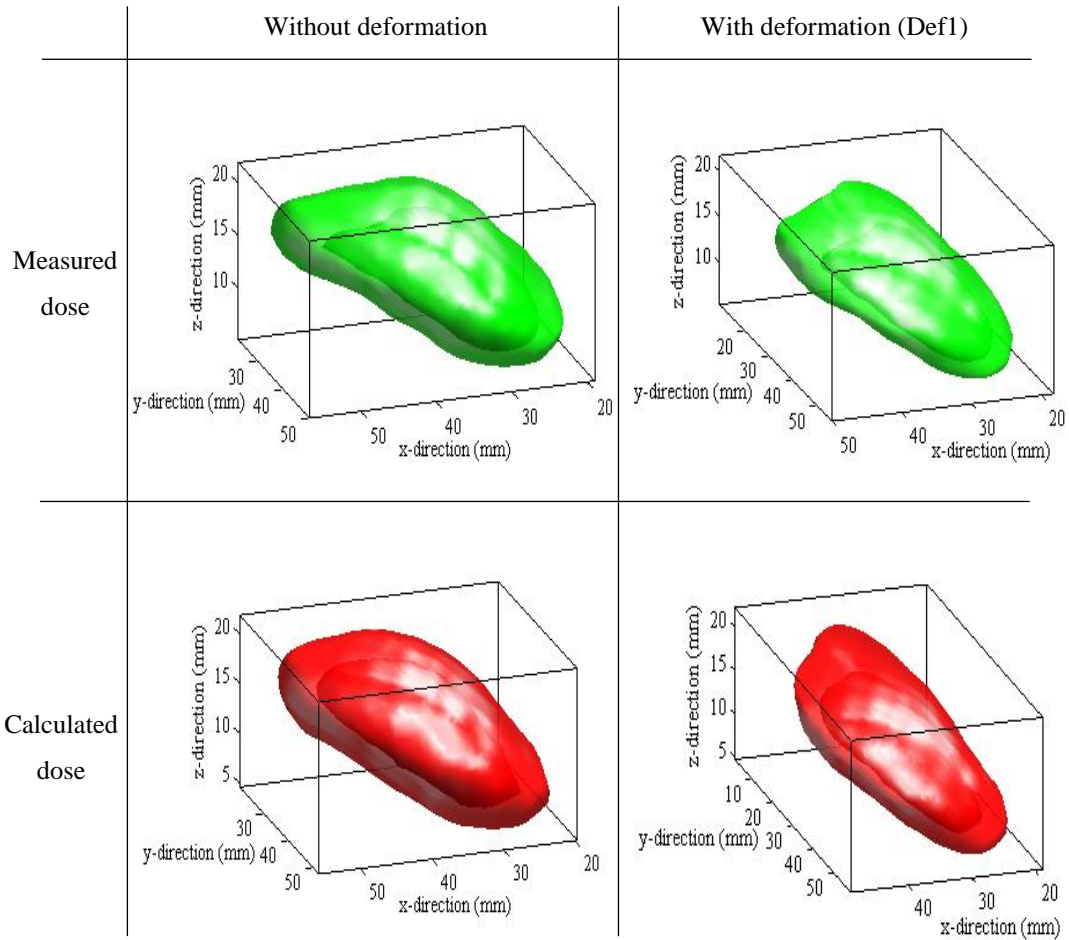
Figure 5-8 70 % and 90 % 3D isosurface doses of a four dynamic-arc treatment field. Upper panels (green colour) are measurements and lower panels (red colour) are calculations of undeformed (left) and deformed (right) scenarios. For deformed cases, a bilateral deformation (Def1) was applied in y-direction. Complex spatial re-distribution of dose in all three dimensions is observable – i.e. elongated in y-direction and compressed in the other two directions, because the beam was delivered in the deformed state.

The results of dose-warping investigation into fields of greater complexity are shown in Figure 5-9. Again, the agreement is good; $\gamma_{3\%/3mz} = 98.8$ % for the cross-field and $\gamma_{3\%/3mm} = 95.8$ % for the complex stereotactic treatment. It is important to note that both these results are within 1 % of the reference (undeformed) cases.

Field Shape	10×10 mm^2		Cross		Dynamic arcs	
	Planned	Warped	Planned	Warped	Planned	Warped
Calculated						
	Undeformed	Deformed	Undeformed	Deformed	Undeformed	Deformed
Measured						
γ_{3D} **map** (plane at D_{max} shown)						
γ_{3D} **passing ratio** (%) (whole volume)	99.9	99.1	99.4	98.8	96.1	95.8

Figure 5-9 A comparison of calculated and measured doses for different irradiations delivered to Undeformed and Deformation 1 DEFGELs. Transverse plane gamma maps (at D_{max}) are shown with 3 % / 3 mm criteria. The gamma map for the Undeformed case (i.e. comparison of planned and measured dose distributions in the absence of deformation) indicates the achievable agreement.

The figure below (Figure 5-10) shows overlaid dose profiles through the elongated (central) axis of the delivered field for the 1x1 cm^2 square field (which were taken from Figure 5.7 and 5.9) for both deformed and undeformed cases.
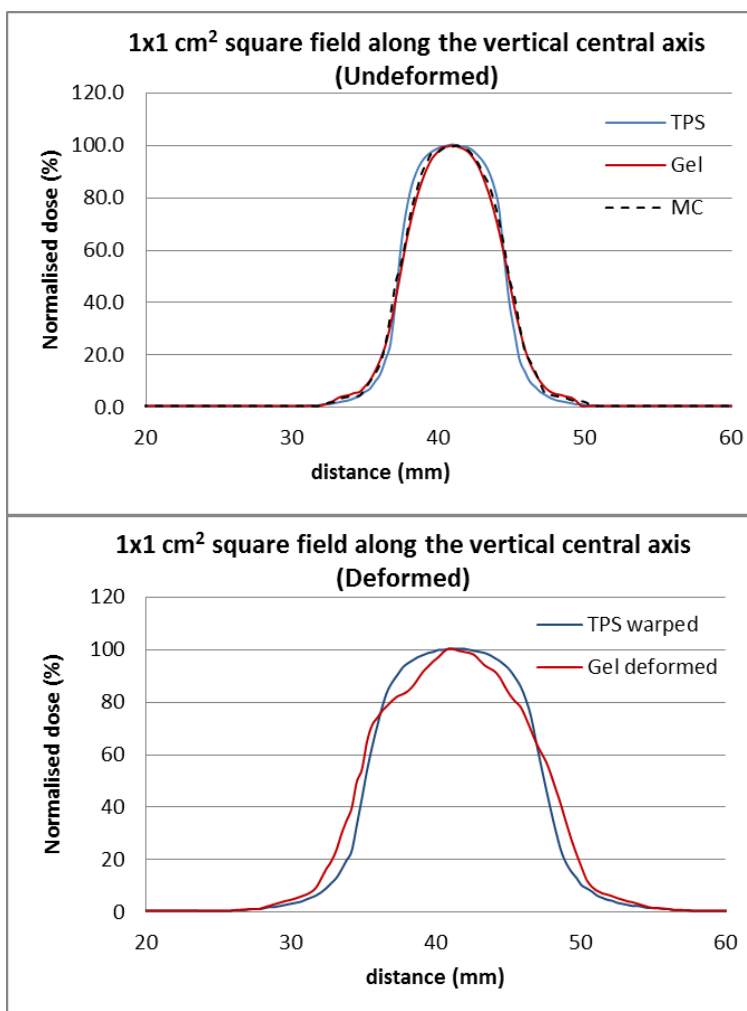
Figure 5-10 A comparison of calculated and measured doses profiles, overlaid through the elongated (central) axis of the delivered field for the 1x1 cm^2 square field (which were taken from Figure 5.7 and 5.9) for both deformed and undeformed cases.

5.4.4 An evaluation of the sensitivity of γ-analysis with different passing criteria

In this study quantitative comparisons have been undertaken primarily using gamma-analysis. It is worth confirming that no disagreement in calculated γ values is being hidden by coarse or 'convenient' criteria. The results for γ-analysis with various criteria are shown in Table 5-2 for Def1 combined with the small square field. For the typical 3 % / 3 mm criterion, the agreement is clearly very good (over 99 %). Expectedly, it is evident that the three dimensional γ-values are more sensitive to distance-to-agreement than dose difference (particularly when dropped to 2 mm). The results indicate that the vast majority of pixels are

warped correctly to < 2 mm, with a smaller fraction (5 – 15 %) accurate to within 2-3 mm, and all voxels correct to within 4 mm. Although the γ passing ratio are consistently lower than those for the 'reference' (undeformed) cases, the agreement between measured and warped dose distributions is generally good.
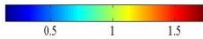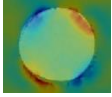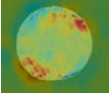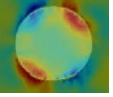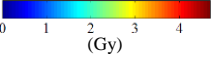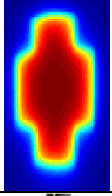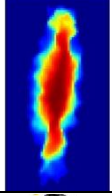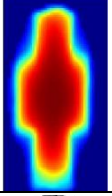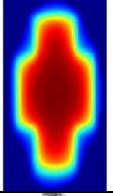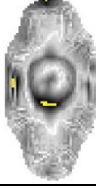
Table 5-2 This table indicates the dependency on criteria specifications for gamma analysis. Gamma analysis undertaken for a range of criteria (2 to 4 % dose difference, Δ, and 2 to 3 mm distance-to-agreement, DTA) for a small (10 mm × 10 mm) square field and deformation type 1. The 'reference' case is shown (agreement between planned and measured in *absence* of deformation) as well as the agreement between dose-warped and measured. The typically quoted 3 % / 3 mm criterion employed clinically is indicated in bold.

3D γ-analysis (% passing criteria)	Reference	Warped	Reference	Warped	Reference	Warped
DTA ＼ Δ (%)	4 %	4 %	3 %	3 %	2 %	2 %
3.0 mm	100	99.9	**99.9**	**99.6**	99.9	98.6
2.5 mm	99.5	98.6	99.2	97.1	98.3	94.4
2.0 mm	95.5	91.7	94.2	88.5	91.2	83.6

5.4.5 An evaluation of the dependency of dose-warping on the smoothing parameters

The smoothing parameter ($=\alpha^2$) was adjusted to investigate the impact of optimisation process on the resulting dose-warping. This optimal value of this parameter was found to be 0.05 for the Original Horn and Schunck algorithm (Algorithm A) – see Section 4.5.1. To investigate the influence of varying this parameters, the level of smoothing was set to half ($\alpha^2=0.025$) or double ($\alpha^2=0.1$) the optimum value as well as to be zero (i.e. no smoothing).

Figure 5-11 illustrates how variation of the smoothing parameter of an algorithm can greatly affect the accuracy of dose-warping, while having very little effect on matching the phantom boundary. For completeness, the Jacobians are also presented (overlaid on the calculated image), which graphically reflect the smoothness of the transformation. Using the optimum smoothing during iterations, ~99 % of voxels passed the gamma test, while using no smoothing at all yielded a passing ratio of ~40 %. Similarly, when the level of smoothing was set to half or double the optimum value the passing ratios were lower. It is interesting to note that, in certain cases, the result of a registration may appear visually to be very good (in terms of boundary matching), while the accuracy of the resulting dose-warping may be poor. This arises from the way in which most algorithms interpolate deformation in low contrast regions.

Smoothing (α^2)	$\alpha^2 = 0.05$ (Optimal)	$\alpha^2 = 0$ (No)	$\alpha^2 = 0.025$ (Half)	$\alpha^2 = 0.1$ (Double)
Jacobian map of DVF (Calculated image)				
Warped dose distribution at D_{max} shown				
γ_{3D} **map** (plane at D_{max} shown)				
γ_{3D} **passing ratio** (%) (whole volume)	98.8	38.8	85.9	92.1

Figure 5-11 A comparison showing the effect of different levels of smoothing. Results of dose-warping the cross-shaped field, in the case of Deformation 1, using the original Horn and Schunck algorithm are shown. Also shown are the transverse plane gamma maps (at D_{max}) from comparison of calculated and measured doses using 3 % / 3 mm criteria. Four different values for smoothing were used: $\alpha^2 = 0.05$ (the optimum value), $\alpha^2 = 0$ (no smoothing), $\alpha^2 = 0.025$ (half of the optimum value) and $\alpha^2 = 0.1$ (double the optimum value). The Jacobian matrix of the DVF is shown in each case.

5.5 Validation of dose-warping technique: Discussion

In this work, it was attempted to answer the question – '*is it sensible to deform doses*?'. The results in Figure 5-7 and Figure 5-9 indicate that it is possible to use dose-warping of planned dose distributions with deformable image registration deformation vector fields to generate accurate predictions of the true absorbed dose. It also demonstrates that the majority of voxels failing the gamma criteria are in areas subject to large deformation, meaning the *complexity* of deformation has far less influence than the *extent* of deformation. The results in Figure 5-10 also indicates that a major contribution to the difference of measurements and calculations were mainly from the limitation of TPS calculation accuracy for small fields (e.g. lateral electron disequilibrium and collimator scatter etc.) as stated in Chapter 3 while stray light perturbation of OCT readout might be a secondary effect (if there is).

Putting the work into a clinical context, typical displacement of the prostate, pancreas and lung lymph node, for instance, are of magnitudes (see Table 5-3) such that one would expect the warped dose predictions to be accurate. This is also the case for typical liver displacement, though these are noted (Rohlfing et al., 2004a) to range up to 34 mm (5-10 mm of mean deformation magnitude) and in this case dose-warping may be less accurate (but can still achieve clinically acceptable accuracy, e.g. above 95% passing rate of gamma analysis with 3%/3mm criteria).

Table 5-3 An illustration of the extent of organ displacement as evident in various published studies.

Site	N patients	Deformation magnitude (mm)		Mode	Reference
		Mean ($\pm \sigma$)	Range		
Liver	16	~4.6 ($\pm$ 3.1)	1.7 -	CBCT	Eccles *et al*(Eccles et al., 2011)
Liver	4	~10	< 34	MRI	Rohlfing *et al*(Rohlfing et al.,
Pancreas	17		< 5	cineMRI	Feng *et al*(Feng et al., 2009)
Prostate	2 (case study)	3.7 ($\pm$ 2.3) and 2.8 ($\pm$		MRI	Kerkhof *et al*(Kerkhof et al.,
Prostate	25		< 5.4	MRI	Nichol *et al*(Nichol et al., 2007a)
Lung tumour	10	0.8 (SI direction)	< 3	4D-CT	Liu *et al*(Liu et al., 2007)
Lymph node	21	7.0 ($\pm$ 4.7)	2 - 23	CT	Jenkins *et al*(Jenkins et al., 2005b)

It is also important to note that the DEFGEL is mass and density conserving and so the results presented here do not necessarily represent the achievable accuracy in anatomy that exhibit significant density changes during deformation. The lung, for instance, would be poorly represented by DEFGEL and one would not expect a meaningful comparison. However, it could be feasible to develop a modified DEFGEL dosimeter using established techniques for lung-equivalent gel dosimetry (DeDeene et al., 2006, Olberg et al., 2000, Gum et al., 2002). The current DEFGEL, as described in this body of work, is more appropriate for anatomy

such as the prostate, liver, pancreas, oesophagus, breast *et cetera*. Furthermore, this study clearly focused on external beam radiotherapy. It is worth noting that the approach also shows promise in brachytherapy (Yeo et al., 2013).

Regardless of dose-warping accuracy, one can consider its clinical need and ask *'is it necessary to deform doses?'* If the paradigm of *uniform* PTV dose coverage is employed, an adequate approach to determine delivered target dose would be to register the GTV with the planning CT to form a composite GTV and check if this composite GTV lies within the uniform 3D PTV dose distribution. Clearly, this approach *does not* necessitate dose deformation but only image deformation. However, in the case of *dose painting* where target dose is intentionally heterogeneous, dose warping is *necessary* to ensure dose to corresponding spatial locations are accurately accumulated. A more typical example *for* the necessity of dose deformation is SBRT case delivered by IMRT/VMAT techniques that yield heterogeneous dose distributions in PTV as well as around the target volume (i.e. OARs). Potential uncertainties on target doses are not only detrimental to estimate local tumour control, but are also critical for risk estimates of organs-at-risk (OARs), such as normal tissue complication probability (NTCP). For the evaluation of such techniques with the presence of anatomy changes it is necessary to appropriately compensate for dose re-distribution in moving/deforming anatomy. Of course, real-time tracking of PTVs with multi-leaf collimators (MLCs) would need somewhat less consideration of dose re-distribution (nonetheless, dose can be still re-distributed due to organ deformation).

As mentioned in the intro section, the recent Point-Counterpoint article (Schultheiss and Tomé, 2012) discusses the proposition: '*It is not appropriate to "deform" dose along with deformable image registration in adaptive radiotherapy'*. Dr Tomé – who is against the proposition – addresses inspiring points in the validity of dose-warping technique in both intra-fraction and inter-fractions:

> "Using image sets acquired just prior to delivery of radiotherapy is, however, only a first order approximation, since things might change during the course of delivery. Before discussing how this point can be addressed, let me just state that the approximation based on a single image set acquired just prior to delivery is still better than assuming that patients are static CT scans and "flying blind." Ultimately, however, we have to go further: ideally one would acquire anatomical image information and record the machine state and dose delivery status at time points during the delivery. This information could then be used, employing deformable dose accumulation across image sets that are highly correlated, to arrive at a more accurate

estimate of dose received for both the target and organs at risk for a given fraction. Dose could then be accumulated over the course of treatment by adding to the record new imaging information along with the dose delivery information from each fraction. The realization of this vision of both dynamically deforming the image and accumulating dose is not too far off into the future and will become clinical reality with the introduction of MR-guided radiation therapy."

The former point, i.e. implementation of intra-fraction dose warping, combined with four-dimensional CT (4DCT) is addressed in the next chapter (Chapter 6) for liver stereotactic body radiotherapy (SBRT).

Another key question in terms of anatomy (also identified in Schultheiss' and Tomé's discussion) is: *what is the accuracy of such methods whereby the mass or density of the tissue in question is not conserved*? This is, in fact, far less well established and is very much a fertile area for research. The complexities of such changes are manifold, including tissue mass changes (e.g. atrophy or oedema), organ content changes (e.g. where the bladder wall needs to be conserved whilst contents depart along with the dose therein) and density changes (e.g. inflation/deflation). To some extent, this could be incorporated into 'algorithm limitations', in as far as the ideal algorithm could handle such complexities. Recent work published by Nithiananthan *et al* in Medical Physics demonstrated the potential for handling missing tissue (e.g. excisions) by modifying the DVF to allow for change beyond the dimensionality of the image (Nithiananthan et al., 2012). There is a pressing need for such methodologies accounting for mass/density changes and such investigations ought to be the focus of future work.

5.6 Validation of dose-warping technique: Conclusion

Using a deformable three dimensional dosimeter (DEFGEL), this work has demonstrated that dose-warping using deformation vector fields obtained *via* deformable image registration can accurately represent the true (measured) dose in a deformed medium. Analysis of a range of DIR algorithms available in the public domain indicate quite variable results, and shows that careful algorithm selection and evaluation is required. For several types and extents of deformation, we have compared measured and 'warped' dose distributions arising from a small (10×10 mm^2) field, cross-shaped (20×20 mm^2) field and a four-dynamic-arc stereotactic field adapted from a patient plan. Achievable gamma analysis shows agreement of $\gamma_{3\%/3mm} \approx 99$ % in each case using the Original Horn and Schunck algorithm after optimisation and algorithm selection process. Rather than the complexity of the treatment delivered, it is the extent of deformation which most greatly affects the accuracy of the warped dose distribution. Considering the square field case, the smallest deformation (~9 mm) yields agreement of $\gamma_{3\%/3mm} = 99.9$ %, whilst the most significant deformation (~20 mm) yields agreement of $\gamma_{3\%/3mm} = 96.7$ %. Typical organ deformations are of the order of 3 to 10 mm. The present study indicates dose-warping may be justified for small deformations in particular, and those that do not involve significant density changes. Dose-warping allows existing patient plans to be morphed according to new/different patient images. Furthermore, it facilitates the calculation of cumulative doses over different states of deformation.

From this work, one may draw the conclusion that dose deformation *can be* accurate and justifiable – within well-defined contexts. In summary, one may state the following regarding the present status of dose-warping and future needs:

- Dose warping has been shown to be quite accurate with comparison to known (measured) data in 3D, within certain contexts.
- Users must be aware that it is possible for algorithms to accurately reproduce the outer contours of structures but inaccurately evaluate internal (low-contrast) volumes.
- Validation of not only algorithm type but also deformation parameters (e.g. smoothing, number of passes, number of iterations per pass etc.) is necessary.
- One must be cautious with 'off-the-shelf' commercial DIR implementations for dose-warping, which may be insufficiently flexible to allow comprehensive validation and optimisation.
- DIR performance when dealing with mass or density changes needs to be validated to make dose-warping confidently applicable to such a case.

The next chapter (Chapter 6) discusses the application of dose-warping methods validated in this chapter into patient cases to retrospectively evaluate 3D planning in a 4D manner.

CHAPTER SIX

: 4D evaluation of conventional 3D treatment plan

Application of the dose-deformation calculation method to a patient treatment plan

"Zwischen die Leber und die Milz past immer noch ein Pils."[**]

Tomas Kron, the author's clinical supervisor.

[**] English translation: Between the liver and the spleen still fits a Pilsner.

This beautiful rhyme had been made during the preparation for the conferences – *IC3DDose and EPSM2012,* where this chapter's work had been presented Dec and Nov 2012 respectively.

6.1 Overview

The final objective of this thesis is to apply the validated dose-warping method to the evaluation of several SBRT liver patient plans (conventional 3D plans). These plans feature steep dose gradients and respiratory movement as well as the associated deformation of the target (liver) and nearby organs-at-risk (OARs) including surrounding healthy liver. 4DCT data exists for these patients, as such, the 4D dose accumulation method was applied to give a better dose estimate, and compare to the 3D plan which assumes no movement or deformation exists, i.e. 4D evaluation of conventional 3D plan via dose-warping technique.

Several studies are presented. The first study is to investigate dosimetric discrepancies between conventional 3D dose calculation and dose-warping based 4D dose accumulation for target as well as OARs. In addition, it aims to investigate how extensive 4D information is required in order to perform accurate enough 4D dose accumulation. This study is to systematically quantify discrepancies of 4D dose accumulation when different numbers of phases from 4DCT are used. The last study is to assess a consequent reduction of healthy tissue sparing at OARs, which may increase risk for surrounding healthy tissues. Estimates for normal tissue complication probabilities (NTCP) based on the two dose calculation schemes are compared.

6.2 4D evaluation of 3D SBRT plans: Introduction

Anatomic changes involving organ deformation due to respiratory motion may introduce discrepancies between planned and delivered doses in radiotherapy (RT). This could result in significant under-dosing of the tumour and overdosing of healthy tissues, particularly for highly conformal techniques applied to thoracic and abdominal malignancy treatments (Nehmeh et al., 2002, Brock et al., 2003, Keall et al., 2005). In order to give a better dose estimate, one approach for calculation of cumulative doses in moving and deforming targets for both inter- and intra-fraction effects is *via* the 'dose-warping' technique using DIR to redistribute dose before summation (Schaly et al., 2004a, Janssens et al., 2009b, Paganetti et al., 2004). The previous chapter (Chapter 5) has demonstrated using 'DEFGEL' (refer to Chapter 3) that this may be performed accurately with certain DIR algorithms (refer to Chapter 4); the original Horn and Schunck (Horn and Schunck, 1981a) optical flow method was found to be suitable when optimised appropriately.

In the past several years, four-dimensional CT (4DCT) scanning techniques have been developed to provide information regarding temporal anatomic changes, in which sequential image datasets are acquired over multiple phases of the respiration cycle (Keall, 2004, Rietzel

et al., 2005). The synergy of these techniques – 'DIR based dose-warping' and '4DCT scanning' – have made possible *4D dose calculation*, which facilitates incorporation of temporal information pertaining to tumour motion and deformation. However, previous studies have, understandably, focused primarily on the case of pulmonary lesions (Starkschall et al., 2009, Zhang et al., 2008, Rosu et al., 2007, Huang et al., 2010b).

Stereotactic body radiotherapy (SBRT), in principle, allows high dose conformity to the tumour with minimal dose to the normal tissue (Dawson et al., 2006, Guckenberger et al., 2007). There is a growing interest in SBRT of the liver (Chang et al., 2011, Sahgal et al., 2012, Lee et al., 2009) and, while there is growing evidence for clinical efficacy, it is vital that the doses actually delivered to tumours and normal tissues are accurately reported (Jackson et al., 2010a, Taylor et al., 2011a). While the impact of respiratory motion is likely to be much reduced with comparison to the lung case, liver SBRT is nonetheless subject to the uncertainties introduced by delivering inherently inhomogeneous dose distributions to deforming and moving organs (Taylor et al., 2011b). As such, SBRT of the liver can offer excellent local control (Rusthoven et al., 2009, Goodman et al., 2010, Guckenberger et al., 2008), but is subject to the difficulties introduced by respiratory motion and associated organ deformation (Taylor et al., 2011a). Consequently, associated discrepancies between planned and delivered doses could result in the potential risk of reduced target coverage and/or increased dose to organs at risk. In this way the correlation between dose and clinical outcome may be better known; this can be particularly relevant when dose prescriptions and resultant treatment plans yield doses to adjacent organs (e.g. the kidney and healthy liver) close to (or over) its dose constraints, thus a clinical decision is required.

In the present work, there are two distinct focuses: firstly for targets (i.e. tumours) and secondly for untargeted normal tissue (i.e. healthy organs). The primary objective of this study is to quantify the extent of dosimetric differences between conventional 3D (static) dose calculation and path-integrated quasi-4D cumulative dose calculation, effected *via* DIR based dose-warping, in the context of liver stereotactic body radiotherapy. 4D plan evaluation of ITV-based 3D plan can provide a more accurate approximation of the actual planned dose than the 3D methodology. Hence, the 4D path-integrated approach will be able to estimate more accurately the delivered dose than ITV-based 3D plan. This is particularly relevant in terms of *accurate* retrospective analysis of outcome-dose correlation, with regards to both tumour control and normal tissue exposure. The 4D approach is inherently more time consuming and we consequently also explore the number of phases required to accurately represent the nominal full 10 phase calculation approach. The secondary objective is to answer to the question – *what is the impact on untargeted healthy organs and corresponding*

risk estimates? For comparison between 3D and 4D calculations, we specifically consider whether organ dose metrics derived from contours defined on the average intensity projection (AIP) or on a single reference phase, provide the better approximation of the 4D dosimetric values. Subsequently, we seek to assess the risk of detriment calculated using conventional 3D and 4D dose-warping approaches in terms of normal tissue complication probabilities (NTCP) (Yorke, 2001, Kong et al., 2007, Miller et al., 2009). Whether for prospective estimation of patient risks or retrospective analysis of plan efficacy, we demonstrate that the quasi-4D dosimetry methodology is important for accurate estimation of doses and corresponding risks.

This chapter has focused on application, in particular, to liver stereotactic body radiotherapy (SBRT) for the reasons described below:

i) The liver often presents the largest degree of anatomic distortion with mass and density conserving deformation, which can cause significant intra- and/or inter-fractional effects throughout fractioned treatment courses;

ii) SBRT is fast increasing as one of the most common advanced modes of radiotherapy for treatment of liver lesions, allowing high dose conformity to the tumour with minimal dose to the normal tissue;

iii) It is nonetheless subject to the uncertainties introduced by delivering inherently inhomogeneous dose distributions to deforming/moving organs;

iv) Comparing, for instance, an alternative advanced mode of radiotherapy such as IMRT, the doses delivered per fraction in SBRT are typically much higher, ranging from approximately 5 – 25 Gy, compared to 1.8 – 3 Gy for IMRT;

v) The consequent number of fractions is fewer, typically 1 – 5 fractions as opposed to 10 – 30;

vi) Furthermore, the margins in conventional radiotherapy may be of the order of centimetres, whilst in SBRT the margins are of the order of millimetres.

These factors emphasise that the liver lesion in conjunction with SBRT treatment modality is the most relevant clinical scenario to perform 4D evaluation of 3D treatment plans by applying the findings presented in previous chapters of this thesis. Liver SBRT involves large mass- and density-conserving deformation with high doses which must necessarily be delivered with high spatial accuracy. Consequently, associated discrepancy between planned and delivered doses is likely to be pronounced, and could result in the risk of reduced dose conformity and tumour control. For these reasons, liver SBRT is likely to gain the most benefit from implementation of 4D dose accumulation. As such, the issues of dosimetry are of critical importance for more effective treatments, and thus improved patient outcomes.

6.3 4D evaluation of 3D SBRT plans: Methods and Materials

Plans were evaluated for four consecutive patients, with five lesions, treated with SBRT for liver metastases and for whom 4DCT imaging had been performed at the time of treatment planning. The datasets exhibited various degrees of tumour motion and shape change, as well as tumour size and location. Table 1 lists the patients' characteristics, including the tumour sizes and motion ranges, where the latter was determined as the distance between the GTV centroids on the two extreme respiratory phases.

6.3.1 Patient data acquisition using 4DCT imaging

Patients were imaged using respiratory correlated x-ray CT (Brilliance CT Big Bore Philips Medical System, Cleveland, OH, USA). Patients were advised to perform free regular breathing, and a respiration signal was acquired via a pressure sensor fixed to the abdominal region by an elastic belt. CT slice thickness and spacing were both 3mm. Respiratory-correlated 4DCT data sets were comprised of a total of 10 phases, acquired at equally-spaced time intervals (0-90% of respiratory period) across the entire breathing cycle. The 0% and 50% phases were confirmed to correspond to end-inspiration and end-expiration, respectively. All acquired 4DCT data sets were imported into the Eclipse treatment planning system (Varian Medical Systems, Palo Alto, CA).

6.3.2 3D treatment planning

i) Tumour definition: Gross tumour volumes (GTVs) were delineated on the two extreme phases (the end-exhalation and the end-inhalation of the breathing cycle). An internal target volume (ITV) was defined as the sum of GTV positions at the extreme phases (0% and 50%) in accordance with an established target volume concept (Rietzel et al., 2006, Wambersie and Landberg, 1999), with no CTV margin applied. A 5 mm margin was isotropically added to the ITV for generation of the planning target volume (PTV) in order to compensate for errors in tumour position.

ii) Anatomical structures contouring process: In clinical practice, our group performs conventional 3D planning using contours derived from the average CT dataset (average intensity projection, AIP) – referred to as $3D_{AIP}$. However, contouring on the reference phase ($3D_{REF}$) is an alternative and equally acceptable workflow practice, as described by others (Jung et al., 2013). In this study, as an additional point of comparison, we assess the implications of contouring with either methodology in terms of 4D dosimetric accuracy. As such, for the $3D_{AIP}$ case, the liver, as well as other normal anatomic structures (specifically the left and right kidney, spinal cord, heart, small bowel, and stomach) were contoured at the AIP image. On the other hand, normal anatomic structures were contoured at the end-exhalation

phase (at 50% of the total breathing cycle) which was chosen as the reference phase where the smallest tumour motion and consequently minimum motion artefacts would be expected (Keall et al., 2006, Keall et al., 2005). The normal liver is defined in the conventional manner (i.e. total liver on AIP image minus ITV for the $3D_{AIP}$ case and total liver on the reference image minus GTV_{+5mm} for the $3D_{REF}$ case). The 'original' dose distribution (the conventional 3D-static plan) was calculated using the average CT dataset.

iii) Equipment and planning parameters:

SBRT treatments were planned on Eclipse v8.9 for treatment on a Varian 21EX (Varian Medical Systems, Palo Alto, CA), equipped with a multi-leaf collimator (5-mm leaf width). Between seven and nine fields (co-planar/non co-planar) were used for stereotactic body radiotherapy (SBRT) delivery via 6 MV photons at 600 MU/min. Dose was calculated using the Eclipse analytical anisotropic algorithm (AAA) with a grid size of 3 mm according to a departmental protocol for liver SBRT (i.e. abdominal lesions). Total doses of 42 Gy in 6 fractions or 50 Gy in 5 fractions were prescribed to a minimum surrounding isodose between 80% − 87%. The resultant prescribed dose, delivered to at least 95% of the volume of interest (VOI) in the PTV, is shown in Table 6-1.

Table 6-1 Patient characteristics (tumour volume and motion range) and D_{95} from dose prescription with fractionation schemes for each patient. GTV_{avg} = gross tumour volume averaged from all 10 phase images; r_{3D} = magnitude of 3D vector; SI = superior-inferior; AP = anterior-posterior; LR = left-right; D_{95} = prescribed dose to at least 95 % of PTV.

Lesion	GTV_{avg} (cm^3)	Motion range (mm)				D_{95} (Gy)	
		r_{3D}	SI	AP	LR		
A (patient 1)	22.7	8.8	7.5	4.6	0.9	43.7	(7.28 Gy × 6)
B (patient 1)	12.4	10.6	10.5	0.5	1.0	41.7	(6.95 Gy × 6)
C (patient 2)	54.5	7.5	7.5	0.0	0.1	46.3	(7.72 Gy × 6)
D (patient 3)	6.7	16.6	16.5	1.8	1.2	54.5	(10.9 Gy × 5)
E (patient 4)	86.2	10.7	10.5	1.6	1.1	44.5	(7.42 Gy × 6)

6.3.3 Deformable image registration

The end-exhalation (50%) phase was defined as the reference (target) image for the treatment plan and the nine remaining phases (0 to 90%, except 50%) were used as the source (moving) images. The latter were morphed to approximate the target image using the optical flow method of deformable image registration (DIR). Selection of the algorithm employed for this study was justified based on our previous study (refer to the two previous chapters, Chapter 4 and Chapter 5) as well as those of other groups (Zhang et al., 2008, Huang et al., 2010b) who

have used it for the lung case. Difference maps (between calculated and 'target' images) were employed to evaluate the accuracy of the calculated deformations generated via DIR. We have used the DIRART implementations (Yang et al., 2011a) of these algorithms as these are freely available in the public domain and thus the present approach may be easily reproduced by interested readers. Furthermore, the calculated deformation vector fields (DVF) are accessible to the user for application to dose-warping, which may not necessarily be the case for commercial software algorithms.

6.3.4 4D-cumulative dose calculations

For each patient, the 3D-static plan was applied individually to each of the ten respiration phases of the CT sets and recalculated. All planning parameters (prescribed monitor units, beam arrangement, leaf positions, isocentre position etc.) remained unchanged. The doses were warped to follow anatomic changes by applying the DVF derived from DIR of each image phase. The resulting dose distributions from all other respiration phases were warped to the reference (end-expiration) phase for summation. The warped doses were equally weighted to estimate the path-integrated 4D-cumulative dose distribution, which constitutes a more accurate approximation of the actual delivered dose than the 3D methodology.

We also explored the number of phases required in the 4D evaluation to obtain an approximately equivalent estimate as the ten-phase approach (with a view to minimising calculation time). Accumulated dose distributions were investigated using fewer phases ($p = 2, 3, 5$). For $p = 5$, two alternative sets of five phases were used (labelled 5_{even} and 5_{odd}). In each scenario, warped doses from the different number of the respiration phases were averaged with equal weighting:

i) $4D_{p=2}$ – two extreme phases (0% and 50 %),

ii) $4D_{p=3}$ – 30%, 60%, and 90% phases,

iii) $4D_{p=5,even}$ – 0%, 20%, 40%, 60%, and 80% phases,

iv) $4D_{p=5,odd}$ – 10%, 30%, 50%, 70%, and 90% phases.

Each of the above four-dimensional cumulative dose calculations were compared to that calculated from the nominal full ten phases ($4D_{p=10}$ dose).

6.3.5 Dosimetric evaluation of 3D-static and 4D-cumulative dose calculations

Dose–volume histogram (DVH) analyses of the target volumes (GTV, CTV, and PTV) and the normal liver were performed. The GTV was defined from the reference phase (50%). The conventional 3D-static and quasi-4D accumulated doses were compared using dose-difference

maps and in terms of dose-homogeneity of target volumes. The latter involves computation of D_x, the absorbed dose delivered to at least x % of the VOI. The dose to 98 % of target volume (D_{98}, or "near-minimum" dose) and the dose to 2 % of the target volume (D_2 or "near-maximum" dose) describe the spectrum of dose that a target volume receives (Grégoire and Mackie, 2011). The resultant ratio of D_2/D_{98} was adopted as a parameter which we henceforth term the homogeneity index (HI) (Guckenberger et al., 2007). This parameter describes dose-homogeneity that is related to the sharpness of the fall-off in the DVH shoulder; an HI value of unity implies *perfect* homogeneity.

The biological effective dose (BED) was also calculated (Fowler, 1989b) using the DVH-based approach:

$$\text{BED} = nd_i \left[1 + \frac{d_i}{(\alpha/\beta)} \right] \ (\text{Gy}) \tag{6-1}$$

where n = the number of fractions, d_i = the dose per fraction in bin i of the DVH, and the value $\alpha/\beta = 2$ Gy was used for late toxicity in the normal liver (Dawson et al., 2002) and the commonly used value $\alpha/\beta = 10$ Gy was applied for the tumour (Wulf et al., 2006).

Organ doses calculated using both the standard contouring on the reference phase ($3D_{\text{REF}}$) and on the AIP ($3D_{\text{AIP}}$) were compared to the 4D method, $4D_{\text{REF}}$ (also contoured on the reference phase). Comparisons were undertaken in terms of the mean dose, D_{mean}, and near-maximum dose, D_2. The former comparison ($3D_{\text{REF}}$ vs. $4D_{\text{REF}}$) is of course the focus of the work, since the organ volumes are then consistent between the two dose calculation schemes. However, $3D_{\text{AIP}}$ is used for organ dose calculation in routine clinical practice. Hence, it is desirable to investigate both cases ($3D_{\text{REF}}$ and $3D_{\text{AIP}}$) for organ doses, in particular when comparing it to $4D_{\text{REF}}$. As such, the latter comparison ($3D_{\text{AIP}}$ vs. $4D_{\text{REF}}$) was also performed; in this way, $3D_{\text{AIP}}$ and $3D_{\text{REF}}$ could be investigated. This also allows identification of the preferred contouring methodology, i.e. whether contours defined on the AIP or reference phase provide the best approximation to the 4D case.

4D evaluation using fewer than 10 phases was performed by comparing DVHs. The ratio of the fractional volumes was considered over the dose sub-range D_{98}-D_{50} for the target (PTV) and normal liver.

6.3.6 Calculation of NTCP for deterministic effects

Calculation of the NTCP in this work follows the Niemierko approach (Niemierko, 1996), and first involves determination of the isoeffective biologically equivalent dose (B). Since the

calculations are based on dose volume histograms (DVH), initially matrices of [B] values are evaluated in terms of the matrix of dose values, [D]. Thus, for each dose element D_i,

$$B_i = D_i \left(\frac{\alpha}{\beta} + \frac{D_i}{f_n} \right) \left(\frac{\alpha}{\beta} + D_f \right)^{-1}$$

(6-2)

in terms of the alpha-beta ratio, α/β, the number of fractions, f_n, and the standard dose per fraction, D_f (2 Gy). The total irradiated volume is then normalised to unity over all N sub-volumes V_j:

$$V_i = V_j \left(\sum_{j=1}^{N} V_j \right)^{-1}, \quad \text{where} \sum_{i=1}^{N} V_i \equiv 1$$

(6-3)

The equivalent uniform dose (EUD) may then be evaluated

$$\text{EUD} = \left(\sum_i \left\{ (V_i)(B_i)^a \right\} \right)^{1/a}$$

(6-4)

where a is a fitting parameter (a is the inverse of the volume dependence parameter n in the Lyman model). In terms of the EUD, the normal tissue complication probability (NTCP) may be defined as:

$$\text{NTCP} = \left(1 + \left(\frac{\text{TD}_{50}}{\text{EUD}} \right)^{4\gamma_{50}} \right)^{-1}$$

(6-5)

where TD_{50} has the usual definition of the 'tolerance dose' corresponding to a 50 % likelihood of a complication and γ_{50} is the slope of the dose response curve (Niemierko, 1996). The parameters of interest are given in Table 6-2. Note that the fractionation scheme employed is 6×7 Gy (42 Gy) and, except where otherwise stated (i.e. comparison with different schemes), all data correspond to this fractionation.

Accurate estimation of normal tissue complication probabilities relies on minimal uncertainties in model parameters. Due to the limited clinical data available in model parameters for hypofractionated treatments, such certainty does not exist for the OARs considered in liver SBRT. In the case of normal liver, Xu et al (Xu et al., 2006) have provided model parameters derived from a dose fractionation scheme of 54 Gy delivered to the isocentre with a median fraction size of 4.6 Gy. We therefore repeated the NTCP calculations using the Lyman/Kutcher-Burman (Kutcher and Burman, 1989) (LKB) model for comparison with the Niemierko estimates that were derived from standard fractionation schemes (Kavanagh et al., 2006, Emami et al., 1991, Fowler, 1989a). The model parameters of Xu et al were also used to demonstrate the differences in NTCP estimates for normal liver with different, commonly used fractionation schemes.

Table 6-2 Organ-specific parameters associated with calculation of the NTCP.

Organ	a	γ_{50}	TD_{50}	α/β	Endpoint and references
Liver (healthy)	1	3	40	3	Liver failure
Kidney	1	3	28	2.5	Nephritis
Spinal cord	13	6.7	66.5	3.3	Myelopathy/necrosis
Heart	2.9	3	49.2	2.5	Pericarditis
Bowel	6	2.6	55	4.3	Perforation/morbidity
Stomach	14	3	65	5	Perforation

6.4 4D evaluation of 3D SBRT plans: Results

6.4.1 4D-CT and 3D-static plan

The tumour displacement (3D vector magnitude) due to breathing motion varied from 7.6 mm (Lesion C, with the largest volume) to 16.6 mm (Lesion D, with the smallest volume); see Table 6-1. As an example of an intermediate magnitude of tumour displacement, Figure 6-1(a) shows sagittal views of Patient 1, generated from ten phases of 4D-CT sets through the same plane. The upper and lower horizontal lines of the figure are placed to guide the eye and help indicate the deformation of the liver and the right kidney. Minor artefacts were observed, especially at the edge of the liver at mid-ventilation phases; however, these did not influence the results as none of the target volumes incorporated regions exhibiting artefacts. Figure 6-1(b) presents dose distributions in three orthogonal planes encompassing the maximum doses for Lesion C and Lesion D, illustrating the dose gradient in the PTV. The existence of the latter dose gradient combined with the impact of deformation and motion is immediate evidence that discrepancies will exist between the 3D and 4D dose calculations. Consequently, this could imply overestimated dose conformity and tumour control for typical planning methodologies.

6.4.2 Deformable image registration

The results of DIR were assessed using difference maps to confirm that the registration was acceptable for all patients. The registration result for two extreme phases (end-inhalation to end-exhalation) is shown in Figure 6-2 as an example (coronal view). In the first row, the upper (red, short dash) and lower (green, long dash) lines show the alignment of the top of the

liver and the kidneys respectively, before and after DIR (simply as a point of reference to aid visual comparison of the images). In the second row, a difference map *before* performing DIR illustrates the difference between the source and target images; the post-DIR difference map compares the target and calculated images. The high level of agreement demonstrates the good performance of the optical flow method.
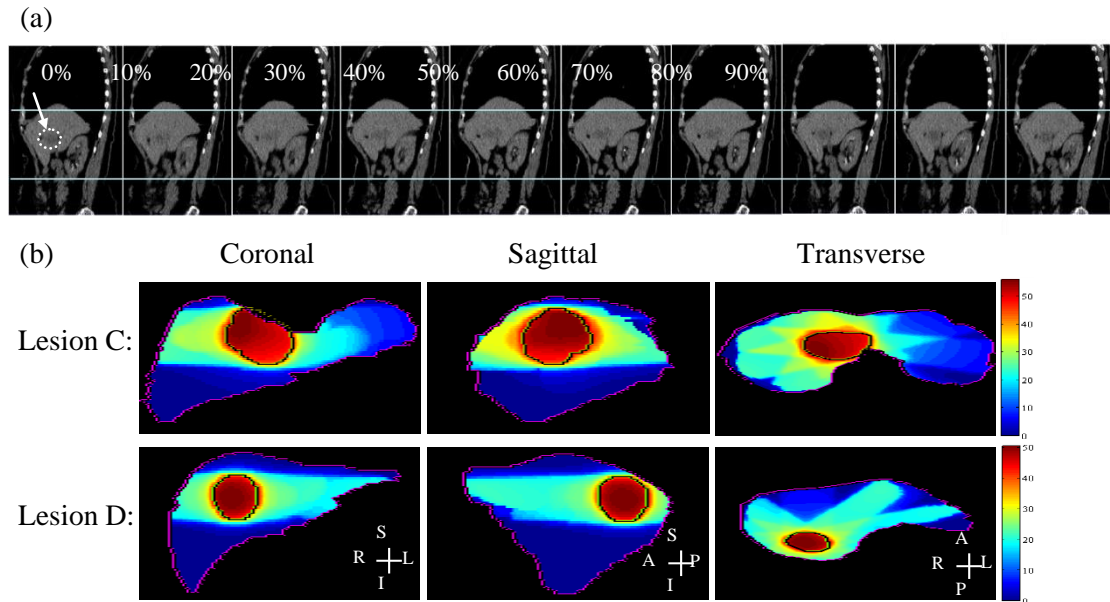
Figure 6-1 **(a)** Example of sagittal planes generated from the 4D-CT sets for Lesion B. The arrow at 0% indicates the target region (indicated with a dotted line). **(b)** Dose distribution in liver; the planning target volumes (PTV) are indicated for Lesion C (the largest volume with the smallest motion) and Lesion D (the smallest volume with the largest motion) in three planes.
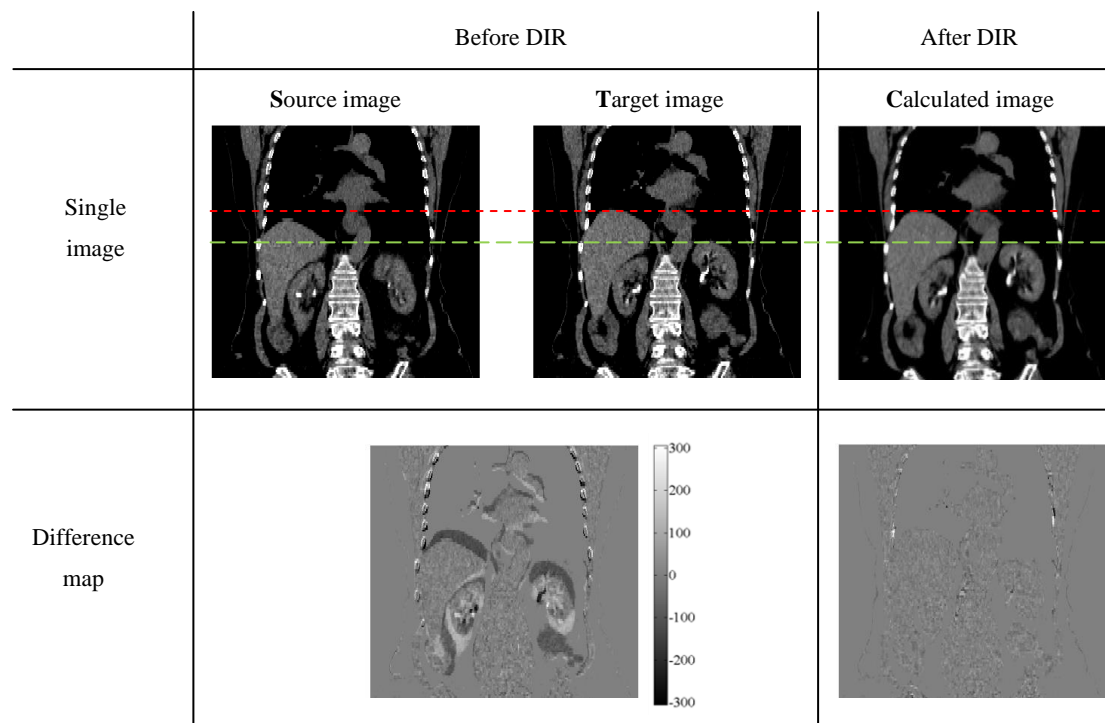
Figure 6-2 Example result of deformable image registration (DIR) using the optical flow method shown in the coronal view (for Patient 1). The scale in the difference map is in HU.

6.4.3 Comparison of 3D and 4D doses

Deformation vector fields resulting from DIR were applied to planned doses at different breathing phases to morph them back to the reference (end-expiration) phase for 4D dose calculations. Difference maps between these warped doses and the reference dose calculated from 3D-static plan were computed. Dose-difference maps of a coronal slice are shown in Figure 6-3 for Lesion D, which exhibited the smallest tumour size with the largest displacement due to breathing motion amongst all five lesions. The value in the bottom-left corner of each figure indicates the maximum point dose difference inside the liver. As expected, dose-differences are greatest for the greatest motion. These maximum differences ranged from ~22% to ~88% with respect to the reference plan.
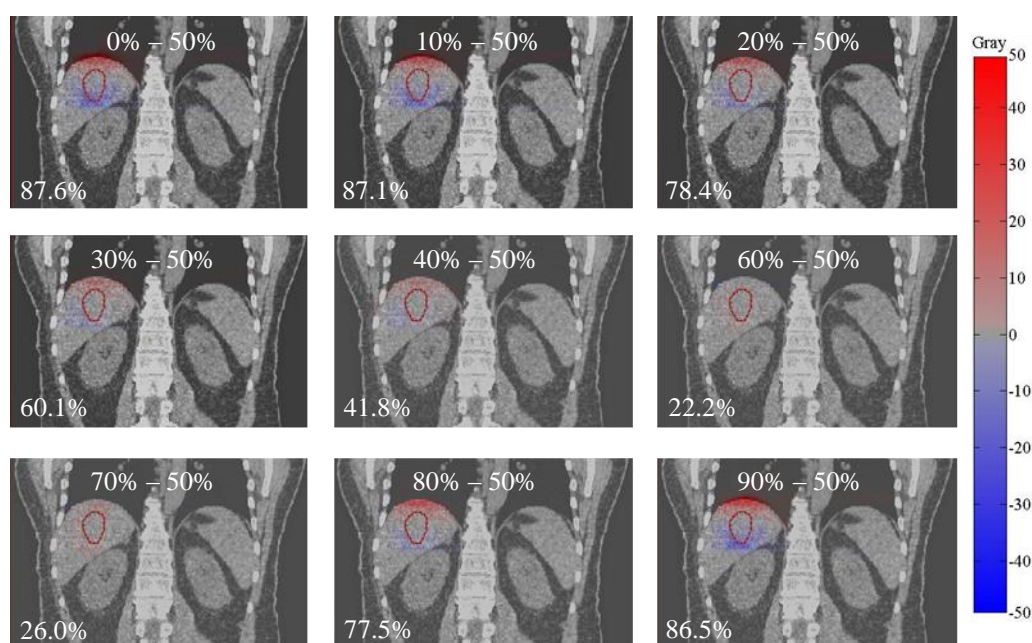
Figure 6-3 An example of dose-difference maps between warped doses from each phase (0% to 90%) and the reference dose (50%) for Lesion D. The percentage in the bottom-left corner of each figure indicates the maximum point dose difference inside the liver. Hot (red) and cold (blue) spots indicate positive and negative differences, respectively.

The warped doses were equally weighted to estimate the path-integrated 4D-cumulative dose distributions. Figure **6-4** (c) depicts dose-volume histograms (DVH) of targets and normal liver for Lesion C and Figure **6-4** (d) shows the DVH ratio of the 3D to 4D calculated doses. In this case, the 3D approach provides a very good estimate of the target doses up to 45 Gy, beyond this the 3D approach overestimates target doses. On the other hand, the normal liver dose is underestimated up to 40 Gy; beyond this the deviation becomes more significant (up

to 50%). These results illustrate that the conventional 3D dose calculation overestimated dose for the targets (particularly PTV), whilst underestimating the dose to the normal liver, compared to the quasi-4D dose calculation. This general trend is observed in all other lesions – detailed DVH results are shown in Figure 6-5.
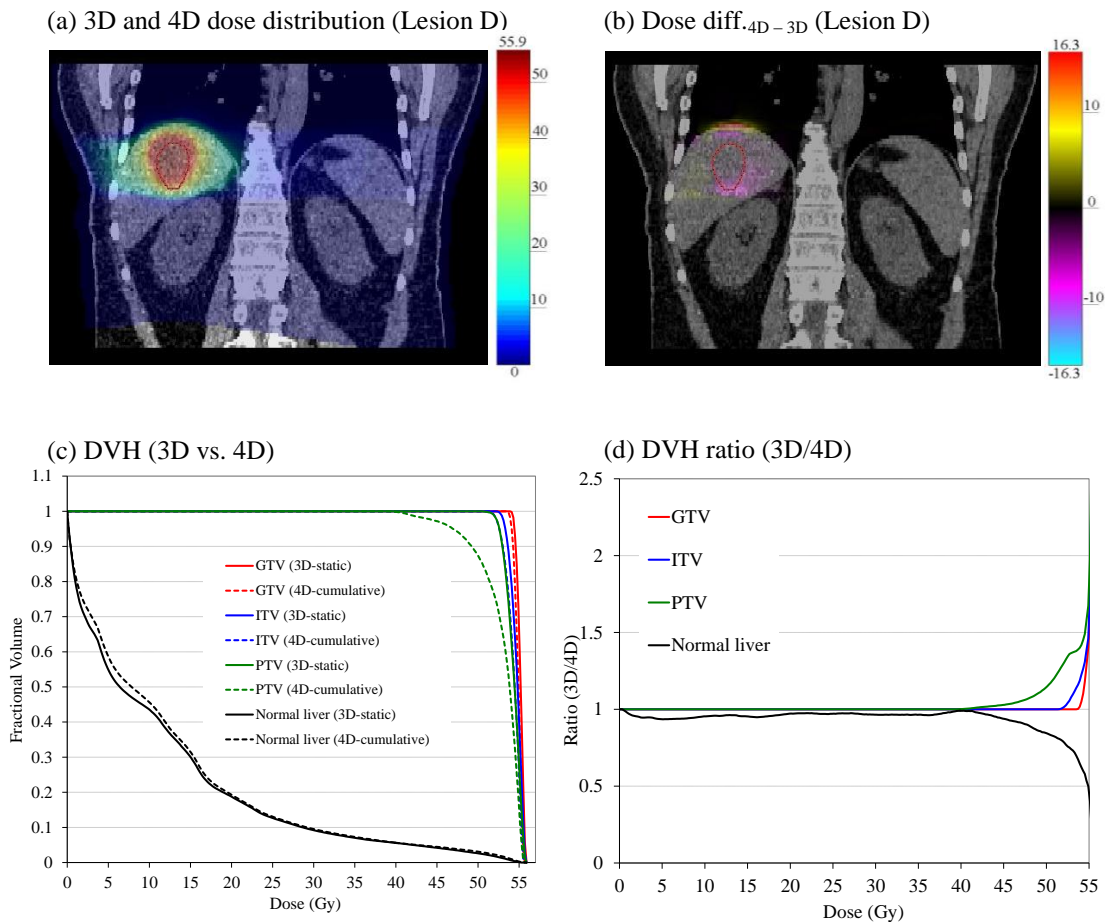
Figure 6-4 Illustration of 4D evaluation of 3D plan. **(a)** 4D calculated dose distribution for Lesion D (coronal plane shown). **(b)** Dose difference between 3D and 4D in the same plane. All units of dose are gray. **(c)** Dose-volume histograms for targets and normal liver. **(d)** The ratio of the 3D to 4D calculated doses up to 55 Gy. In this case, the 3D approach provides a very good estimate of the target doses up to 45 Gy, beyond this the 3D approach overestimates target doses. On the other hand, the normal liver dose is underestimated up to 40 Gy, beyond this the deviation becomes more significant (up to 50%). Straight and dashed lines illustrate 3D and 4D dose calculations respectively (red: GTV, blue: CTV, green: PTV, and black: normal liver).
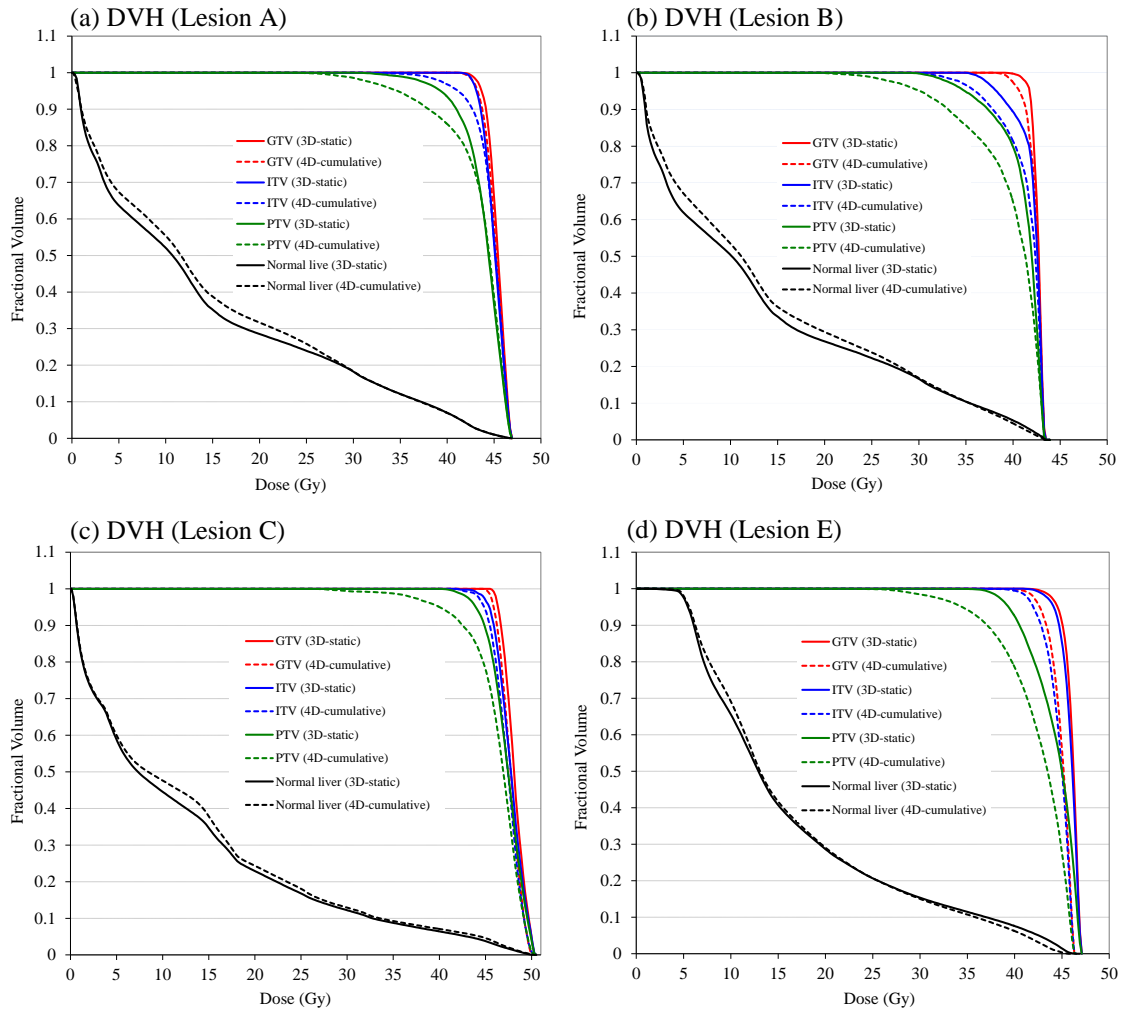
Figure 6-5 DVH comparisons of 3D vs. 4D dose calculation methods **(a)** Lesions A, **(b)** Lesion B, **(c)** Lesion C and **(d)** Lesion E. 3D approach overestimate target doses in particular high dose region (i.e. dose falloff region of DVH shoulder). On the other hand, the normal liver dose is underestimated up to 40 Gy, beyond this the 3D approach overestimate dose received by the normal liver. Straight and dashed lines illustrate 3D and 4D dose calculations respectively (red: GTV, blue: ITV, green: PTV, and black: normal liver).

6.4.4 Target volumes

Table 6-3 summarises the dose-volume relationships for target volumes in the 3D and 4D dose calculations, for all lesions studied. All values in the table are obtained from DVH results shown in Figure 6-4 and Figure 6-5. In order to compare the dosimetric differences between the two calculation schemes, the mean dose (D_{mean}), the 2 % near-maximum dose (D_2) and the 98 % near-minimum dose (D_{98}) are tabulated for GTV, ITV, and PTV. The homogeneity index (HI) was calculated based on the two latter quantities and the ratio of HI of the 3D and 4D calculations (= $HI_{3D/4D}$ %) was also calculated. Expectedly, smaller volumes receive more homogeneous coverage ($HI_{GTV} > HI_{ITV} > HI_{PTV}$).

In the case of the conventional 3D dose calculations, the PTV D_{mean} ranges from 41.1 Gy (BED 68.6 Gy) to 52.7 Gy (BED 105.4 Gy). In the case of the 4D calculation, the BED_{mean} (4D) of the PTV was 1.5 to 8 % lower across all lesions. HI for the 3D dose calculations ranged from 1.02 – 1.08, 1.05 – 1.17, and 1.17 – 1.37 for GTV, ITV, and PTV respectively, across all lesions. HI in the 4D case were higher (less homogeneous), ranging from 1.03 – 1.09, 1.06 – 1.28 and 1.36 – 1.64 for GTV, ITV and PTV, respectively. In other words, the conventional 3D approach *overestimates* the homogeneity by on average over 1 %, 4 % and 17 % for the GTV, ITV and PTV, respectively, relative to the 4D calculation. The volumes GTV_{+5mm} show a similar trend as ITV/PTV results, receiving less dose and poorer homogeneity than predicted by the 3D calculation (see Table 6-4).

Table 6-3 Comparison between conventional 3D dose calculation and path-integrated 4D-cumulative dose calculation in target volumes; dose in Gy, HI is dimensionless.

Lesion	Target (volume in cm³)	D_{mean} (3D / 4D)	BED_{mean} (3D / 4D)	D_2 (3D / 4D)	D_{98} (3D / 4D)	HI (3D / 4D)	HI_{3D}/HI_{4D} (=$HI_{3D/4D}$%)
A	GTV (22.7)	45.0 / 44.8	79.2 / 78.9	46.8 / 46.7	43.1 / 42.7	1.08 / 1.09	99.1
	ITV (31.1)	45.1 / 44.7	79.4 / 78.7	46.7 / 46.7	42.6 / 38.9	1.10 / 1.20	91.7
	PTV (66.4)	44.0 / 43.4	77.4 / 76.4	46.7 / 46.7	36.8 / 30.9	1.27 / 1.51	84.1
B	GTV (12.4)	42.7 / 40.4	71.3 / 67.5	43.4 / 43.2	41.1 / 39.8	1.06 / 1.08	98.2
	ITV (17.9)	42.1 / 39.0	70.3 / 65.1	43.3 / 43.2	36.9 / 33.8	1.17 / 1.28	91.4
	PTV (39.3)	41.1 / 37.8	68.6 / 63.1	43.3 / 43.2	31.7 / 26.4	1.37 / 1.64	83.5
C	GTV (54.5)	48.2 / 47.8	81.9 / 81.3	50.2 / 49.8	46.1 / 45.6	1.08 / 1.09	99.7
	ITV (87.0)	48.0 / 47.4	81.6 / 80.6	50.2 / 49.8	44.7 / 44.1	1.12 / 1.13	99.1
	PTV (168.7)	47.4 / 46.3	80.6 / 78.7	50.1 / 49.8	42.8 / 36.6	1.17 / 1.36	86.0
D	GTV (6.68)	55.3 / 55.0	111.0 / 110.0	55.8 / 55.6	54.3 / 53.9	1.02 / 1.03	99.6
	ITV (21.28)	54.8 / 54.4	109.6 / 108.8	55.7 / 55.5	53.0 / 52.2	1.05 / 1.06	98.8
	PTV (71.36)	52.7 / 50.7	105.4 / 101.4	55.6 / 55.4	46.3 / 35.3	1.20 / 1.57	76.5
E	GTV (86.16)	46.2 / 45.0	82.2 / 80.1	46.7 / 45.9	43.8 / 41.9	1.07 / 1.08	99.1
	ITV (100.5)	46.0 / 44.8	81.9 / 79.7	46.6 / 45.8	43.2 / 41.2	1.08 / 1.11	97.0
	PTV (187.24)	44.3 / 42.4	78.9 / 75.5	46.3 / 45.4	38.2 / 31.0	1.21 / 1.46	82.8

Abbreviation: 3D = three-dimensional dose calculation; 4D = four-dimensional dose calculation; D_{mean} = mean dose; BED_{mean} = biologically effective mean dose, D_2 = 2% near-maximum dose; D_{98} = 98% near-minimum dose; HI = homogeneity index (the ratio of D_2 to D_{98}, D_2/D_{98}), $HI_{3D/4D}$% = the percentage ratio of HI for 3D to 4D (HI_{3D}/HI_{4D}). All doses in Gy.

Quantitatively, the HI ratio ($HI_{3D/4D}$) of the GTV was universally >98 %, indicating good agreement. Physically, this implies that the GTV dose may be well estimated using conventional 3D dose calculation. In contrast, $HI_{3D/4D}$ values were significantly lower for the ITV (ranging from 91.4% to 99.1 %) and PTV (ranging from 76.5% to 86.0 %). These results illustrate that the conventional method of 3D dose calculation overestimates dose homogeneity by up to ~24%, particularly in the high dose gradient region around the PTV margin. Healthy liver tissue adjacent to the PTV could move in and out of the treatment

beam field over the breathing cycle, resulting in undesired dose to healthy liver and a reduction in dose conformity to the PTV. In quantifying such effects, the 4D methodology clearly demonstrates its advantage.

Table 6-4 Comparison between conventional 3D dose calculation and path-integrated 4D cumulative dose calculation in the volume of GTV + 5 mm margin.

GTV_{+5mm} Lesion	Vol (cc)	D_{mean} 3D	D_{mean} 4D	BED_{mean} 3D	BED_{mean} 4D	D_2 3D	D_2 4D	D_{98} 3D	D_{98} 4D	HI 3D	HI 4D	HI_{3D}/HI_{4D} %
A	46.4	44.4	42.8	77.3	73.3	46.6	46.4	40.4	37.6	1.15	1.23	93.5
B	29.2	42.0	39.8	71.4	66.2	43.3	43.2	38.3	34.0	1.13	1.24	90.9
C	100.4	47.8	47.5	85.9	85.0	49.6	49.8	45.3	44.8	1.09	1.11	98.5
D	18.6	54.8	54.5	114.9	113.9	55.6	55.5	53.1	52.3	1.05	1.06	98.7
E	143.3	45.3	43.6	79.5	75.3	46.6	45.9	40.6	35.9	1.15	1.28	89.8

Abbreviation: Vol (cc) = volume in cubic centimetre (cm^3); GTV_{+5mm} = GTV plus 5 mm margin; others are same as those in Table 6–3. All doses in Gy.

Consistent with expectation, it is worth emphasising that the smaller volume with larger motion yielded a greater discrepancy between 3D and 4D dose calculations than the larger volume with smaller motion (see Table 6-4), in agreement with previous findings (Dunn et al., 2012). This highlights that while ITV/PTV concepts ensure GTV coverage, the evaluation of dose coverage and homogeneity in these volumes is not an appropriate indicator of plan quality for 4D evaluation of 3D plans. *4D dose warping explicitly accounts for motion in the treatment field, including ingress of healthy tissue.* These discrepancies arise principally in circumstances whereby the dose gradient is most prominent in the PTV periphery (but well beyond the ITV).

6.4.5 4D approach with <10 phases

Although ten is generally the number of phases required to adequately approximate the motion of a typical tumour due to respiratory motion (Dunn et al., 2012), using fewer phases would reduce calculation time and is consequently worth exploring in terms of accuracy. Figure 6-6 shows, for Lesion E, the coronal view of the dose-difference maps between 4D-cumulative dose calculated from the full ten phases and that calculated from various subsets of phases (p = 2, 3, 5_{even}, and 5_{odd}). Doses in all cases were mapped back onto the reference image set (end-expiration).
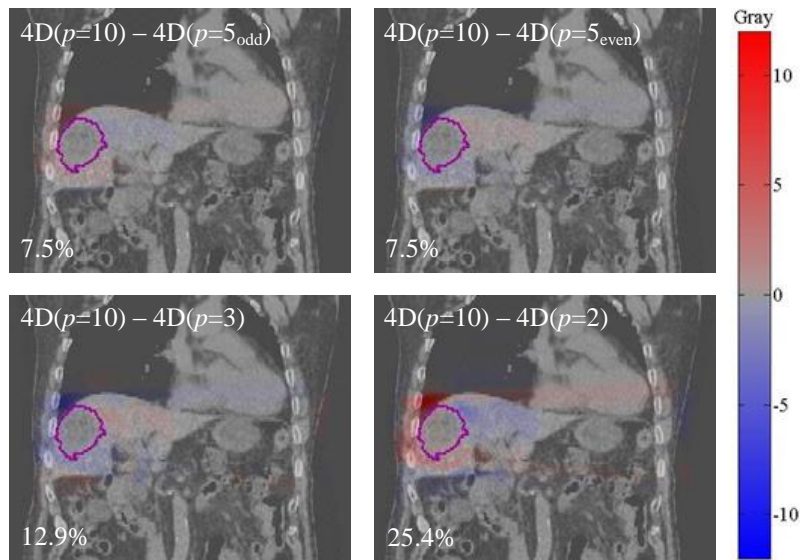
Figure 6-6 Dose-difference maps between 4D doses calculated with different numbers, p, of phases (p = 2, 3, 5_{even} and 5_{odd}) and the standard p = 10 phases. The example is shown for Lesion E, in which the PTV is contoured. The maximum point dose difference is shown as a percentage in the bottom-left of each panel. Hot (red) and cold (blue) spots indicate positive and negative differences, respectively.

The maximum *point* dose difference in PTV, displayed as a percentage in the bottom-left corner of each figure, varied from 7.5% to 25.4%. As expected, this result illustrates that the more phases used for 4D dose calculation, the better the approximation of the delivered dose (p = 10). These point-wise discrepancies, however, do *not* generate a significant difference in DVHs between the two calculation schemes, as shown in Figure 6-7.

Figure 6-7 shows DVH for targets and normal liver in Lesion E. The inset figure panels are ratios of 4D calculations of different numbers of phases (p = 2, 3, 5_{even}, 5_{odd}) relative to the standard number of phases (p = 10). The most striking observation one makes from Figure 6-8 is that even the use of as few as two phases results in a more accurate estimate of the dose than the conventional 3D calculation. In this case (Lesion E), the $4D_{p=3}$ dose or even $4D_{p=2}$ give a good approximation of the full ten-phase dose for the PTV as well as GTV, ITV and normal liver; agreement within 3% is demonstrated over the D_{98} and D_{50} interval.
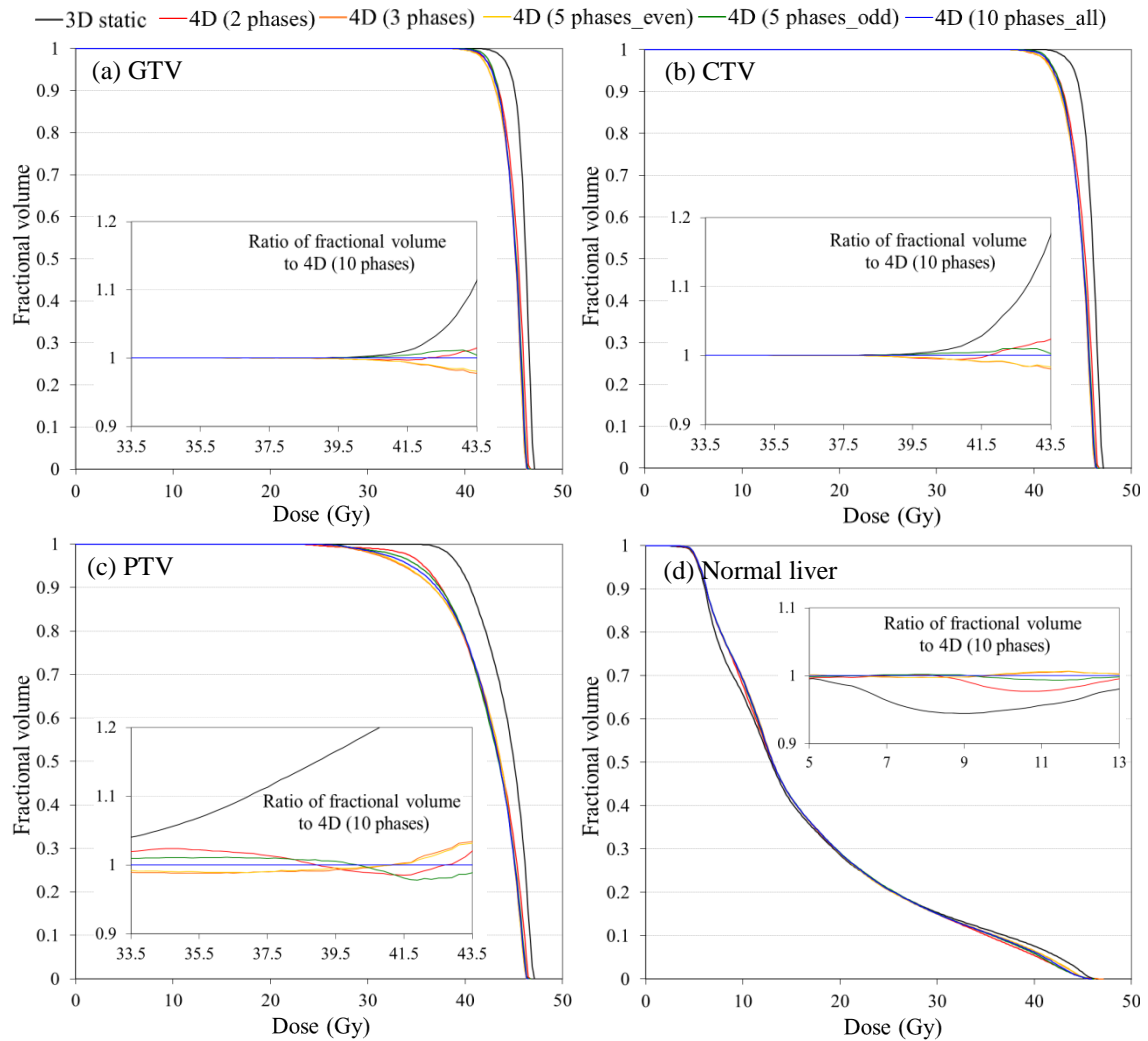
Figure 6-7 DVH for targets and normal liver in Lesion E: (a) GTV, (b) CTV, (c) PTV and (d) Normal liver. Various numbers of phases (p = 2, 3, 5_{even}, 5_{odd}, and 10) were used for the 4D dose calculation. The 3D dose calculation is depicted as a black line and the 4D dose calculation as coloured lines; red: p = 2 phases; orange: p = 3; yellow: p = 5_{even}; green: p = 5_{odd}, and blue: p = 10. The inset figures show the ratio of fractional volume relative to the $4D_{p=10}$ calculation over the D_{98} and D_{50} interval derived from the $4D_{p=2}$ PTV and normal liver histograms..

For the other patients in this study, generally at least three phases are required to achieve a reasonable approximation of the delivered dose as represented by the ten phase set. This is shown in Figure 6-8, which depicts DVH of the PTV for Lesions A – D, respectively; the insets are ratios to the ten phase case. In these cases, 4D dose calculation using two extreme phases yielded differences of up to 10% and 17% for Lesion B and Lesion D, respectively (large motions with small target volumes), compared to the full 10-phase method. In all cases, using three phases was enough to limit differences to less than 5%.
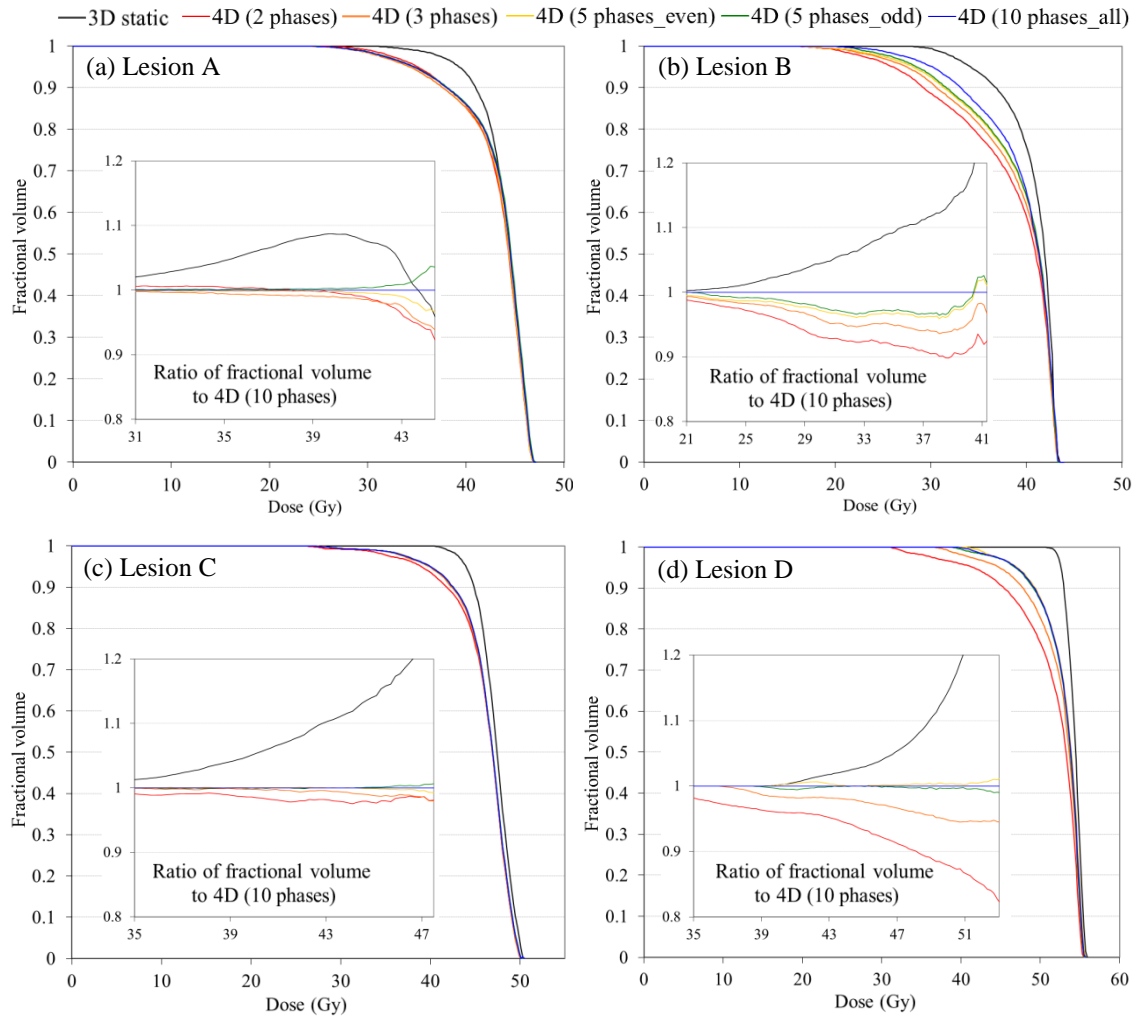
Figure 6-8 DVHs for PTV: a) Lesion A, b) Lesion B, c) Lesion C and d) Lesion D. Inserts show the ratio of fractional volume relative to the $4D_{p=10}$ calculation over the D_{98} and D_{50} interval derived from the $4D_{p=2}$ histogram for each lesion. All lines are as described for Figure 6-7.

6.4.6 Organs at risk: dosimetric comparisons

It is the aim of the current study to highlight the utility of 4D path-integrated dose accumulation (to supplement conventional 3D planned dose calculations) for better estimation of the dose received by both targeted and untargeted volumes in liver SBRT. The foremost objective in planning is to achieve coverage of the primary tumour, as was described in the previous sections, *while* minimising any potential harm to the patient. With this in mind we note that the estimated doses to *healthy* peripheral organs vary dramatically depending on the calculation method (3D or 4D). This is illustrated by the dosimetric comparison shown in Figure 6-9 – examples (e.g. spinal cord) of disparity between 3D and 4D approaches. Motion compensation strategies such as the ITV concept serve to ensure GTV coverage, but the TPS calculation of the dose distribution will not account for the movement of healthy tissue *into* the treatment fields.

134
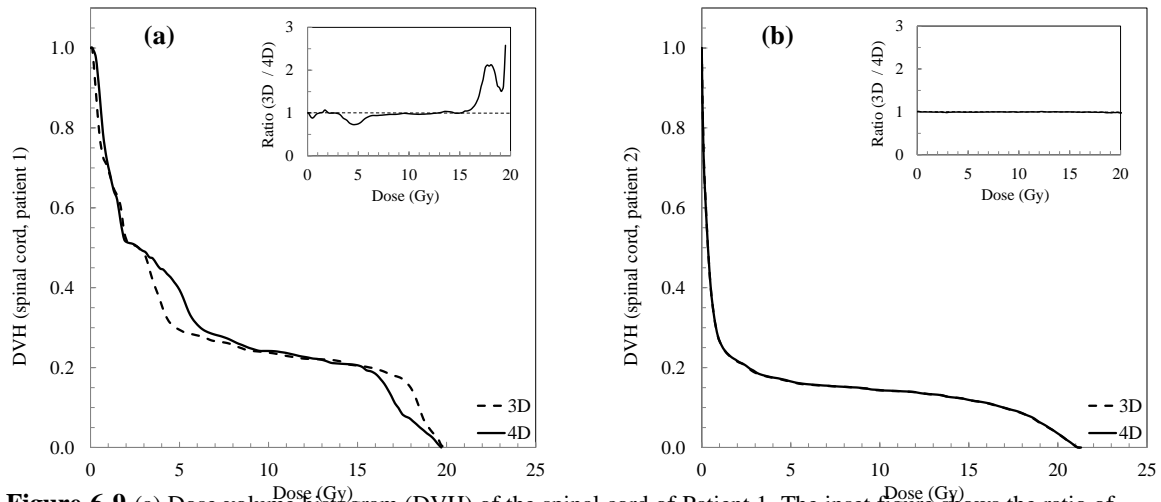
Figure 6-9 (a) Dose volume histogram (DVH) of the spinal cord of Patient 1. The inset figure shows the ratio of the 3D to 4D calculated dose up to 20 Gy. In this case, the 3D approach poorly estimates the dose to the healthy spine. (b) Dose volume histogram (DVH) of the spinal cord of the second patient treated. The inset figure shows the ratio of the 3D to 4D calculated dose up to 20 Gy. In this case, the 3D approach provides a very good estimate of the dose to the healthy spine.

Consider Figure 6-9 (a) and (b), which shows the dose to the same healthy structure for two different patients; in one case, (a), the 3D method is a poor estimate of the dose, while in the other case, (b), it is a very good estimate. Referring Section 6.3.5, although organ doses were calculated using both the standard contouring on the reference phase ($3D_{REF}$) and on the AIP ($3D_{AIP}$), *note that* $3D_{REF}$ and $3D_{AIP}$ are *not differentiated* in Figure 6-9 because the two cases yield essentially same DVH results for the case of spinal cord in Patient 1. In general, it is clear that the doses to healthy tissues calculated using the conventional 3D approach may differ greatly from those determined using the 4D methodology, and this is what has prompted this part of the present study.

Figure 6-10 summarises dosimetric results for critical organs such as normal liver, spinal cord, right/left kidney, stomach, small bowel and heart in both dose calculation schemes. This figure shows two sets of comparison: i) $3D_{REF}$ vs. 4D and ii) $3D_{AIP}$ vs. 4D, which allow illustration of whether contours defined on the AIP or reference phase provide the best approximation to the 4D case. Figure 6-10 (a) and (c) show the mean doses, D_{mean}, and the near-maximum doses, D_2, (maximum dose received by at least 2 % of the volume), respectively, calculated using 4D path-integrated dose accumulation method (i.e. taking into account organ motion/deformation). The error bars indicate maxima and minima observed for the patient cohort studied. The ratio of the conventional 3D calculated doses to the 4D path-integrated cumulative dose are shown in Figure 6-10 (b) D_{mean} and (d) for D_2. Overall, the average difference (between 3D and 4D) in D_{mean} is about 10 % and in D_2 is around 5 %.

135
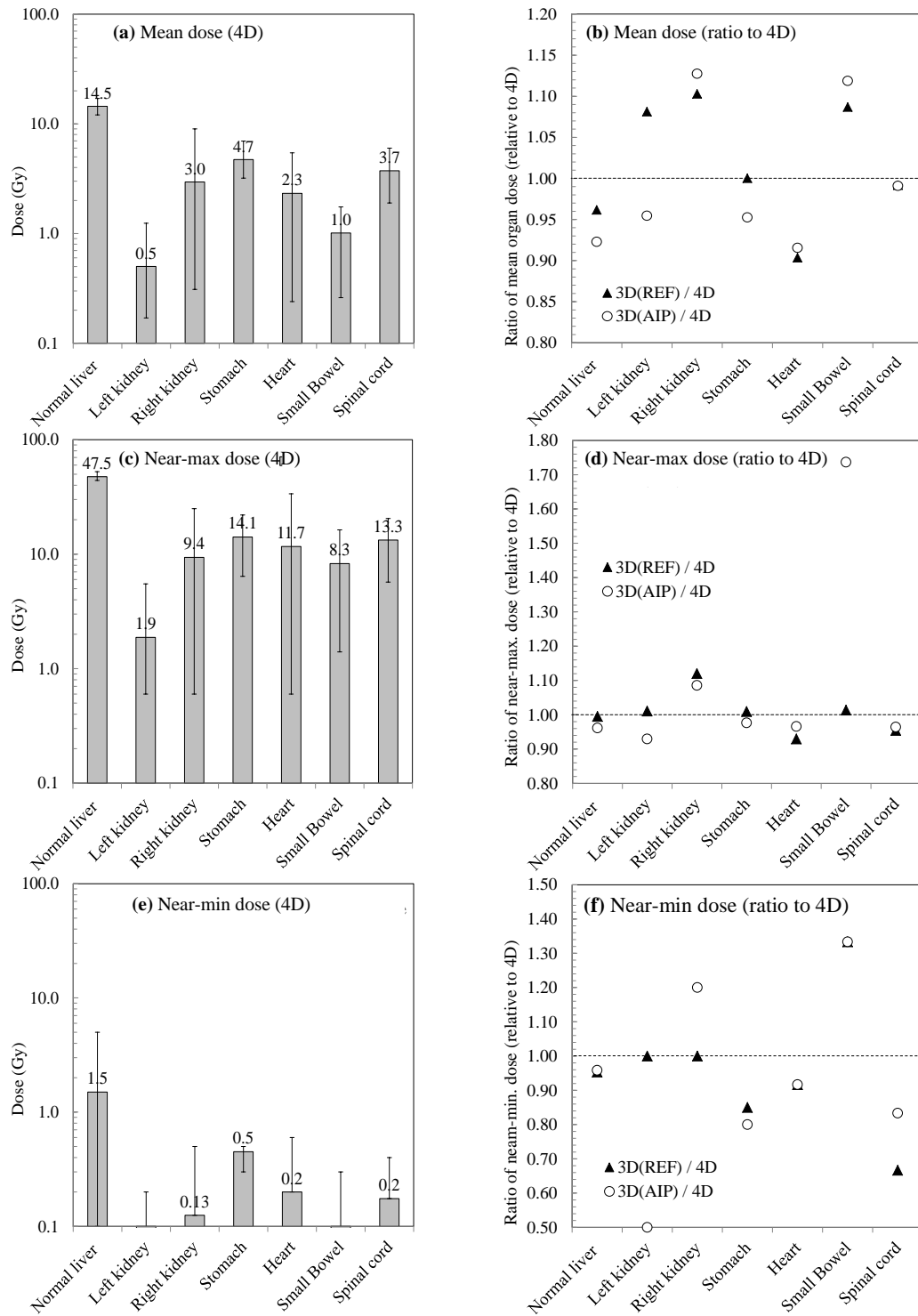
Figure 6-10 Comparison of 3D and 4D dose calculations. The data presented is the average over all patients studied. **(a)** The mean healthy organ doses (D_{mean}). The error bars indicate maximum and minimum observed values. **(b)** The ratio of the mean dose as calculated *via* conventional 3D methods relative to the 4D case; shown for both contouring on the reference phase and on the AIP. **(c)** The near-maximum dose (D_2). The error bars indicate maximum and minimum observed values. **(d)** The ratio of the near-maximum dose as calculated *via* conventional 3D methods relative to the 4D case; shown for both contouring on the reference phase and on the AIP. The average difference (between 3D and 4D) in the mean dose is about 10 % and in D_2 is around 5 %. **(e)** The near-minimum dose (D_{98}). The error bars indicate maximum and minimum observed values. Values less than 0.1 Gy are not shown. **(f)** The ratio of the near-minimum dose as calculated *via* conventional 3D methods relative to the 4D case; shown for both contouring on the reference phase and on the AIP. Labelled values in **(a)**, **(c)** and **(e)** are the average of (D_{mean}), (D_2) and (D_{98}), respectively, from all patients studied.

For normal liver, there is an observable trend such that D_{mean} calculated from the 3D-static dose calculation were up to 8% lower compared to 4D-cumulative dose calculation. On the other hand, for right kidney, the mean doses calculated from the 3D-static dose calculation were up to 21% higher compared to 4D-cumulative dose calculation. Doses to other organs are low and consequently differences between 3D (both $3D_{REF}$ and $3D_{AIP}$) and 4D methods are not as troubling in an absolute sense. This illustrates that reduced doses in tumours due to organ motion/deformation can lead to increased doses to the normal liver (which encompasses the entire tumour volume) as well as the right kidney and/or small bowel (which are adjacent to the normal liver). In particular, such results can be more clearly observed in the case of Patient 1; see Figure 6-11 that shows an example of DVHs comparisons for critical organs (e.g. healthy liver, spinal cord, right kidney, stomach and small bowel).
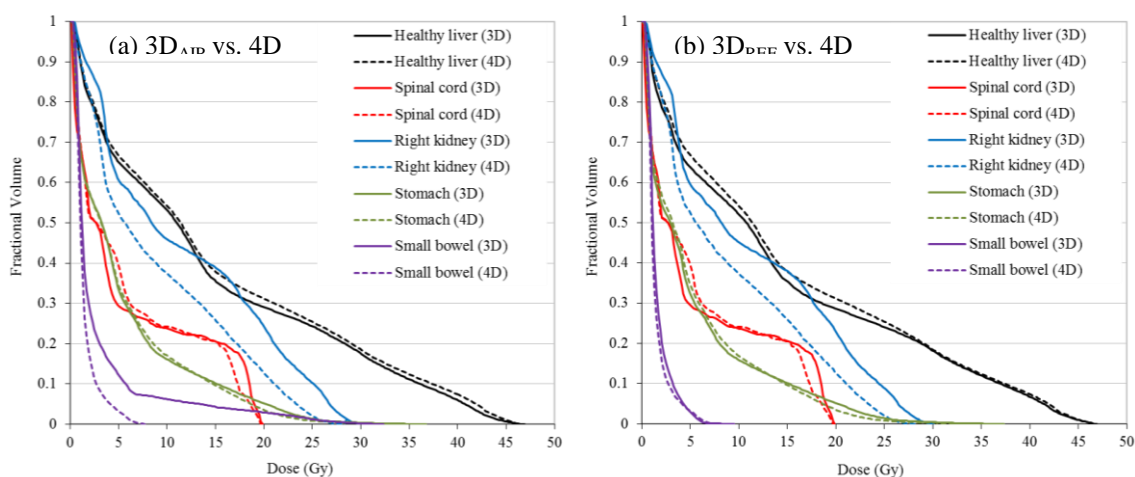
Figure 6-11 An example of dose-volume histograms (DVHs) comparisons for critical organs in Patient 1: (a) 3D AIP vs. 4D, (b) 3D REF vs. 4D. Straight and dashed lines illustrate the results calculated from 3D-static and 4D-cumulative dose calculation, respectively (black: normal liver, red: spinal cord, blue: right kidney, green: stomach, and purple: small bowel).

For more details, Table 6-5 lists D_{mean}, D_2 (=$D_{nearmax}$) and D_{max} of the aforementioned critical organs – which were source data used to plot Figure 6-10. Comparing two 3D contouring methods ($3D_{REF}$ and $3D_{AIP}$) used for the conventional 3D-static dose calculation, there is little differences in the results between $3D_{REF}$ and $3D_{AIP}$ contouring methods for most of organs, such as the left kidney, spinal cord, small bowel and heart. This is expected, as mentioned previously, because of low doses to such organs; consequently no strong trend can be found in the two 3D contouring methods and dose differences relative to 4D methods are negligible in an absolute sense. Nonetheless, exceptions are the normal liver for all patients and the right

kidney and small bowel for Patient 1. Focusing on these organs received relatively high doses, it seems that, in a conservative manner, contouring on the reference phase (the 3D$_{REF}$ case) provides a more accurate estimate of the dose (i.e. reduced disparity between 3D and 4D methods).

Table 6-5 Comparison of 3D and 4D dose calculation in critical organs; dose in Gy. The normal liver is defined as total liver minus GTV. The '3D$_{AIP}$' data refers to that contoured on the AIP.

Patient no.	Organs (AIP / REF volumes in cm^3)	D_{mean} (3D$_{AIP}$/ 3D$_{REF}$ /4D$_{REF}$)	$D_{2\ (nearmax)}$ (3D$_{AIP}$/ 3D$_{REF}$/ 4D$_{REF}$)	D_{max} (3D$_{AIP}$/ 3D$_{REF}$/ 4D$_{REF}$)
1	Normal Liver (1049.2 / 1166.1)	14.5 / 14.5 / 15.4	43.1 / 43.7 / 44.1	46.9 / 46.9 / 46.9
	Spinal Cord (30.7 / 30.7)	6.0 / 5.9 / 6.0	19.5 / 19.5 / 19.3	19.9 / 19.9 / 19.7
	Right Kidney (119.2 / 118.5)	11.6 / 11.4 / 9.6	28.1 / 27.9 / 25.0	30.3 / 30.1 / 28.3
	Left Kidney (131.8 / 113.1)	1.2 / 1.6 / 1.2	5.0 / 6.0 / 5.5	6.7 / 6.7 / 6.5
	Stomach (224.3 / 223.9)	5.4 / 5.3 / 5.3	23.7 / 23.8 / 22.0	36.7 / 37.3 / 36.7
	Small Bowel (49.9 / 35.4)	2.9 / 1.7 / 1.5	23.0 / 5.4 / 5.7	32.1 / 9.5 / 7.7
	Heart (534.3 / 459.3)	1.6 / 1.4 / 1.6	8.9 / 8.4 / 9.5	27.3 / 27.3 / 28.7
2	Normal Liver (2038.0 / 2258.7)	12.3 / 12.7 / 13.3	45.6 / 47.1 / 47.5	49.9 / 49.9 / 50.3
	Spinal Cord (52.4 / 52.4)	3.2 / 3.7 / 3.4	20.5 / 20.5 / 20.5	21.3 / 21.3 / 21.3
	Right Kidney (238.7/ 212.4)	0.4 / 0.4 / 0.3	0.7 / 0.7 / 0.6	0.9 / 0.9 / 0.9
	Left Kidney (232.2 / 201.1)	0.4 / 0.4 / 0.4	0.8 / 0.8 / 0.7	1.1 / 1.1 / 0.9
	Stomach (326.9 / 322.2)	3.4 / 3.7 / 3.4	11.5 / 11.9 / 11.5	16.7 / 16.7 / 16.3
	Small Bowel (447.5 / 426.4)	0.3 / 0.3 / 0.3	1.5 / 1.5 / 1.4	2.5 / 2.9 / 2.3
	Heart (587.5 / 588.0)	4.7 / 4.6 / 5.4	28.9 / 28.1 / 33.7	46.1 / 46.3 / 47.1
3	Normal Liver (1776.6 / 1838.5)	11.3 / 11.6 / 12.1	50.9 / 51.6 / 52.6	55.7 / 55.9 / 55.7
	Spinal Cord (13.4 / 12.3)	3.9 / 3.8 / 3.8	8.0 / 7.7 / 7.7	8.9 / 8.5 / 8.5
	Right Kidney (227.8 / 219.9)	0.5 / 0.5 / 0.4	2.0 / 2.3 / 1.8	6.5 / 7.5 / 5.3
	Left Kidney (191.6 / 194.4)	0.2 / 0.2 / 0.2	0.7 / 0.8 / 0.7	2.9 / 2.9 / 2.3
	Stomach (169.3 / 177.6)	6.8 / 6.9 / 7.0	16.6 / 16.6 / 16.6	17.5 / 17.5 / 17.5
	Small Bowel (245.2 / 206.0)	1.3 / 2.1 /1.8	15.7 / 16.7 / 16.3	18.9 / 18.7 / 18.7
	Heart (768.3 / 757.1)	0.2 / 0.2 / 0.2	0.6 / 0.6 / 0.6	1.7 / 1.7 / 2.3
4	Normal Liver (887.3 / 949.3)	16.6 / 16.9 / 17.0	43.1 / 46.6 / 45.8	46.7 / 46.9 / 46.5
	Spinal Cord (54.9 / 54.3)	1.8 / 1.9 / 1.9	4.6 / 4.6 / 5.7	5.3 / 5.3 / 7.3
	Right Kidney (301.3 / 282.9)	1.8 / 2.0 / 2.1	9.5 / 9.3 / 10.1	13.5 / 12.5 / 13.9
	Left Kidney (98.6 / 93.8)	0.2 / 0.2 / 0.2	0.4 / 0.4 / 0.6	0.9 / 0.7 / 2.1
	Stomach (366.5 / 346.1)	2.8 / 3.0 / 3.2	5.3 / 5.9 / 6.4	8.1 / 13.7 / 14.1
	Small Bowel (662.3 / 507.7)	0.5 / 0.5 / 0.5	8.5 / 9.8 / 9.7	22.3 / 22.3 / 25.5
	Heart (494.2 / 468.3)	1.8 / 1.8 / 2.1	3.1 / 2.9 / 2.9	3.3 / 3.3 / 3.3

6.4.7 Organs at risk: NTCP

It is generally accepted that the expected toxicity associated with radiotherapy cannot be defined by the prescription dose alone (Kong et al., 2006), and it is for this reason that physical models and simple dosimetric descriptors are essential in plan evaluation. One such means of assessing the impact on healthy tissues is *via* normal tissue complication probabilities. We have computed these, using the Niemierko approach, for the healthy liver volume, kidneys, oesophagus, spinal cord, heart, bowel, stomach and duodenum. The equivalent uniform doses (EUD, see Eq. (6.4)) are shown in Figure 6-12. The percentage increase in disparity in EUD when organs are contoured on the average is: liver 3.3%, left kidney 1.7%, right kidney 21%, oesophagus 0%, spinal cord 1.7%, heart 1.1%, bowel 36% and stomach 0.7%.
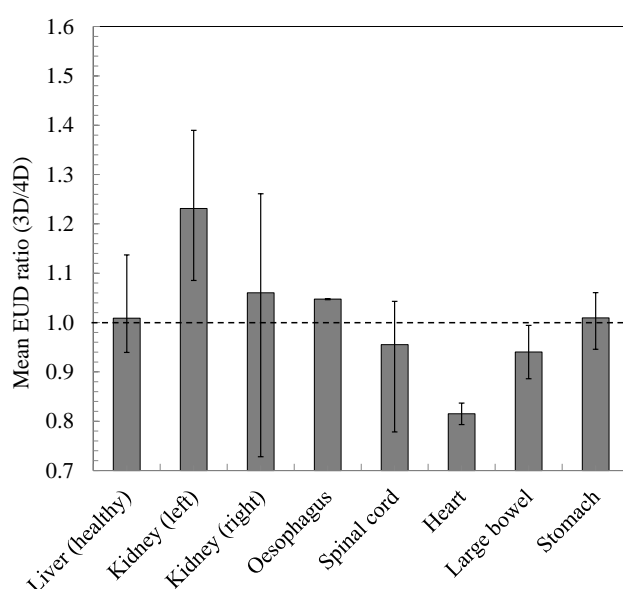
Figure 6-12 The mean ratio of EUD (3D/4D) for various healthy organs; the error bars indicate maxima and minima for the patient cohort studied.

The NTCP for all OARs were found to be very small (<0.2%) for the fractionation scheme used. Repeating the calculations for normal liver using the Lyman/Kutcher-Burman (LKB) approach (Kutcher and Burman, 1989) and model estimates based on Xu *et al* (Xu et al., 2006), results in higher NTCP estimates, but exhibit similar differences in the ratios of NTCP for the 3D and 4D approaches; see Table 6-6. Differences in absolute values of NTCP were expected based on the data and methods used to derive model parameters (including differences in fractionation schemes) and also differences in toxicity endpoints.

Table 6-6 *NTCP (%).* Investigation of the effect of common(Pan et al., 2011) alternative fractionation schemes on the NTCP of healthy liver and comparison of the 3D and 4D dose calculation approaches and comparison of the Niemierko- (2 Gy per fraction) and Xu-based (4.6 Gy per fraction) estimates. The 'reference' fractionation scheme (i.e. that actually delivered and to which the other data in this paper corresponds) is 6×7 Gy. Some cases would have been rejected or replanned but are shown here for completeness. While the dose fractions employed in the Xu work differ from those in this study, this table nonetheless highlights the sensitivity of NTCP estimation to fractionation; the NTCP calculated using the Xu data are in general higher, but exhibit similar differences between 3D and 4D.

Fractionation scheme	Patient 1		Patient 2		Patient 3		Patient 4	
	3D	4D	3D	4D	3D	4D	3D	4D
6×7 Gy (Emami)	0.06	0.11	0.01	0.02	<0.01	<0.01	0.20	0.18
6×7 Gy (Xu)	1.3	1.6	0.7	0.9	0.5	0.6	2.0	1.9
3×15 Gy (Xu)	16.1	20.1	8.2	10.8	5.3	6.1	24.0	23.1
4×12 Gy (Xu)	10.2	12.8	5.2	6.8	3.4	3.9	15.6	15.1

6.5 4D evaluation of 3D SBRT plans: Discussion

The results indicate that the mean dose to the PTV is consistently underestimated by the 3D approach by, on average, 4 %. The minimum dose (received by at least 98 % of the volume) is more notably affected, i.e. with the 3D AIP method resulting (on average) in overestimation of the GTV, ITV and PTV doses of 2 %, 5 % and 22 % respectively, while the near maximum dose in each volume is similar regardless of whether 3D or 4D methods are used. The mean ITV dose is similarly overestimated by 3 %. Unexpected deficiencies in dose coverage at the periphery may result in the risk of inadequate tumour control. In terms of the GTV, the results described in this work are consistent with other work undertaken concurrently with the present study (Jung et al., 2013), which found that the GTV dose is estimated with sufficient accuracy using conventional 3D methods, but when comparing to the 4D approach it is clear that the dose to other regions (particularly healthy organs) is poorly predicted. This study found that, on average, the mean GTV dose is overestimated by 2 % when planning on the average intensity projection.

As one might expect, the greater consequences – in terms of absolute difference between 3D and 4D – occur for untargeted organs at risk (OAR). These include critical organs such as the normal liver, spinal cord, right kidney and duodenum; however, one might argue that these are less concerning because the absolute doses are small. However, inaccurate estimation of healthy organ doses leads to inaccurate outcome correlation, tissue complication estimation and so forth. Expectedly, volumes of contoured organs are consistently higher when contouring on an AIP (compared to reference-phase contouring), with the exception of the healthy liver, the volume of which is underestimated due to its definition as the liver minus the PTV, where the PTV is larger than the GTV in the reference phase. Although the two methods result in significant differences in predicted healthy organ doses (many tens of percent), there was ultimately no strong trend for over- or under-prediction of doses to particular organs. This negates the possibility of applying generic correction factors or similar to doses estimated using AIP-based 3D methods, and implies that – particularly for sensitive patient groups (Suit et al., 2007, Taylor and Kron, 2011, Tubiana, 2009, Xu et al., 2008) – the 4D method ought to be employed. The expectation of a correlation between the magnitude of motion and/or deformation and the magnitude of errors quantifiable by the 4D approach, suggests the possibility for patient selection rather than routine 4D calculations. For instance, a typical clinical workflow might involve:

- Patients exhibiting large tumour excursion to be flagged for additional analysis
- Cross-check using 4D methodology undertaken by physics/RT
- Dose coverage and risk data presented to complement 3D information
- If large differences in dose calculations are noted, it is recommended that the treating clinician be notified to decide whether the initial plan is to be re-optimised or not – more conservative approach to be adapted in estimating clinical risk to critical organs

Relative homogeneity indices, $HI_{3D/4D}$, of as low as 76.5% in the PTV were observed, which illustrates that conventional 3D dose calculation approach overestimates homogeneity by up to ~24%, occurring primarily in the high dose gradient region around the PTV margin. The GTV is of course less affected, though $HI_{3D/4D}$ of 98 % nevertheless reflects an underestimate of homogeneity. There are of course arguments (de Pooter et al., 2007, Nagata et al., 2007, Okunieff et al., 2006, Ruggieri et al., 2010, Taylor et al., 2011b) for and against the 'necessity' of dose homogeneity, or at least the prioritisation thereof, but regardless of the philosophy to which one subscribes there is the unarguable necessity to *know* whether or not the dose is homogeneous. Extending these results to other cases, one would expect even more pronounced effects in the case of, for instance, very small fields, lung tumours, high-energy treatments and so on (Jin et al., 2007, Miller et al., 1998, White et al., 1996). It is worth noting that $HI_{3D/4D}$ of the PTV was well correlated to the motion-volume relationship (see

Table 6-1): a smaller volume with larger motion yields greater $HI_{3D/4D}$ than a larger volume with smaller motion. In other words, *where the volume is small and the motion is large, the 3D approach results in poor homogeneity estimation*, whereas in the converse case it may not be necessary to pursue the 4D method, and the conventional AIP-based calculations may be sufficient.

Since such 4D calculation is relatively resource intensive – increasing proportionally to the number of datasets analysed – we investigated alternative reduced phase binned solutions. The objective of this was to determine whether fewer than the typical ten-phase 4DCT dataset is sufficiently accurate. Together, the magnitude of the 3D motion vector and the GTV volume may be suitable indicators facilitating determination of whether a large number of phases is necessary for the 4D methodology and deserves further investigation. Notably, we found that for our patient cohort 4D dose calculation with *at most* three phases was a reasonable approximation of the standard ten-phase approach. Quantitatively, agreement was found to be within 5 % over the D_{98} and D_{50} intervals in the PTV DVH for all lesions. The authors regard 5% deviation as a borderline for acceptability when accounting for other uncertainties specific to the treatment technique. Nevertheless, the implication of this finding is that a strategy of utilising an abbreviated dose-accumulation process may be adopted, which is potentially useful as resource restrictions are likely to serve as a barrier to clinical implementation of non-adaptive 4D dose calculation.

Differences in absolute values of NTCP were expected based on the data and methods used to derive model parameters (including differences in fractionation schemes) and also differences in toxicity endpoints (Marks et al., 2010, Bentzen et al., 2010). Whilst the absolute values for the NTCPs were different (0.5 – 2.0 % using the parameters of Xu *et al,* compared with < 0.1– 0.2 % using the parameters in Table 6-2), all values in this study were less than 5 %. This result is unsurprising within the context of fractionation schedules at our clinic (PMCC), which are informed by NTCP calculations to provide an estimated risk of radiation induced liver disease (RILD) of < 5%. In this case the dose of 42 Gy in 6 fractions of 7 Gy each was delivered. However, exploration of alternative fractionation schemes does reveal significant differences, as shown in Table 6-6 which shows NTCP data for the (healthy) liver for several of the most common (Pan et al., 2011) liver SBRT fractionation approaches. The results in Table 6-6 demonstrate that significant uncertainties exist in the estimation of NTCP and that substantial differences in these values may exist across the different fractionation schemes. These model parameters are derived from clinical observations and estimates of the doses delivered. Whilst the estimates of NTCP for the OAR appear to be low, considerable uncertainty exists in the modelling parameters. Furthermore, it is likely that this uncertainty

increases when the dose fractionation scheme differs notably from that employed when the parameters were originally derived. As clinical data emerges from this rapidly growing treatment modality, one may believe that realistic estimates of the dose actually delivered to the liver (e.g. through the quasi-4D method presented here) will lead to greater confidence in the model estimates. Such information is vital if treatment prescriptions are to be informed by NTCP estimates.

It is important to note that dose-warping cannot be experimentally validated in density changing media because, to date, there is no measurement tool available for such validation. Hence, it is acknowledged that there it is possible for slight source of uncertainty when dose-warping is implemented near and/or within density changing media, e.g. the superior border of the liver in this study.

6.6 4D evaluation of 3D SBRT plans: Conclusion

This work has investigated the potential limitation of conventional 3D dose calculation methods for liver SBRT by implementing quasi-4D dose-warping based dose-accumulation and comparing it with the former. This study has demonstrated that the use of conventional 3D dose estimates (that do not take into account temporal changes) may be insufficiently accurate for this purpose, and that a quasi-4D dose-warping based dose-accumulation method may yield more suitable data. The key findings are that conventional 3D planning based on an AIP may:

- Overestimate target dose

- Underestimate healthy liver dose

- Poorly predict dose to proximate OAR

- Overestimate target dose homogeneity

- Influence estimates of normal tissue complications (while its risks are low)

This has obvious implications for treatment plan evaluation, retrospective plan analysis and outcome correlation. The quasi-4D methodology described here provides additional information for clinical decision making. Accurate DVH-based plan evaluation and indeed appropriate reporting of doses associated with observed endpoints necessitate accurate dosimetry.

In this study, it is clearly demonstrated that conventional 3D planning on an AIP appears to accurately calculate dose to the GTV and ITV, while significantly overestimating doses to the PTV (by up to 9%) and underestimating dose to the surrounding healthy liver (by up to 8%), compared to the dose-warping based 4D calculation methodology. In 3D calculations, contours defined on the full expiration phase (REF) yield better dose estimates for healthy liver than AIP contours. For most other OARs, AIP and REF contours yield similar estimates. Where differences occurred, REF contours yielded better estimates than AIP contours in most cases indicating that contouring should be performed on a full expiration reference phase image (even if AIP contours are used for plan design). This study has furthermore demonstrated that 4D dose calculation with at most *three* phases is a reasonably accurate approximation of 'full' 4D dose calculation with the nominal ten phases, facilitating more expeditious calculations and reduced overhead burden. While estimates of the NTCP risks are low for the fractionation scheme employed, significant uncertainty exists in model parameters used for hypofractionated treatments. Providing dose estimates that most closely represent the actual dose delivered will provide valuable information to improve our understanding of the dose response for partial volume irradiation using hypofractionated schedules. The 4D approach more accurately informs treatment plan evaluation, retrospective plan analysis and outcome correlation.

CHAPTER SEVEN

: Conclusions and Recommendations

Final comments on the significance of the work and recommendations regarding the adaptation of deformation in both medical imaging and radiation oncology

"One must have a good memory to keep the promises one has made."[††]

Friedrich Nietzsche

[††] The promises the author has made in this thesis?

: Not to conjecture at random but to provide *a concise summary of results and conclusions* of the studies overviewed in the introduction (Chapter 1) of this thesis.

7.1 A major challenge in contemporary radiotherapy

The primary objective of this thesis has been to model and validate delivered doses on deformable moving targets. Specifically, this refers to

i) *measurements* of complex and re-distributed dose distributions by developing a tissue-equivalent deformable dosimetric phantom (*an experimental model*);

ii) *calculations* of the deformed dose distribution following assessment of deformable image registration algorithms' accuracy via the developed phantom (*a mathematical model*);

iii) by comparison thereof, *validation* of the dose-warping technique; and

iv) *application* of the validated method to conventional 3D plan evaluation, in this case liver stereotactic body radiotherapy, as the final objective of this thesis.

The issues of dosimetric discrepancies between initial treatment plans and verification measurements, thereby allowing re-optimisation of original plans, are important for improved patient outcomes. The method developed in this work and consequent results have addressed a major challenge facing physicists and clinicians in contemporary radiotherapy – the inter- and intra-fractional variation in anatomic shape due to organ motions and associated deformations. This issue is related to the entire radiotherapy procedure, from image acquisition for pre-treatment dose calculation to dose delivery verification and risk assessment. The existence of organ deformation accompanying anatomic motion adds a further layer of complexity to the problem. While dosimetric uncertainties arising from the patient *motion* have been dealt with through a number of strategies, conventional dose-calculations by treatment planning systems (TPS) have not accounted for the associated organ *deformation* in current clinical practices.

This thesis has addressed the need to investigate dose distribution/re-distribution in deformable moving targets that can occur during and/or between treatments. Consequently, this work has helped establish a framework that ensures more accurate measurements and calculations for dose accumulation, which can reduce the probability of potential detriment to the patient and thus enhances the positive treatment outcome.
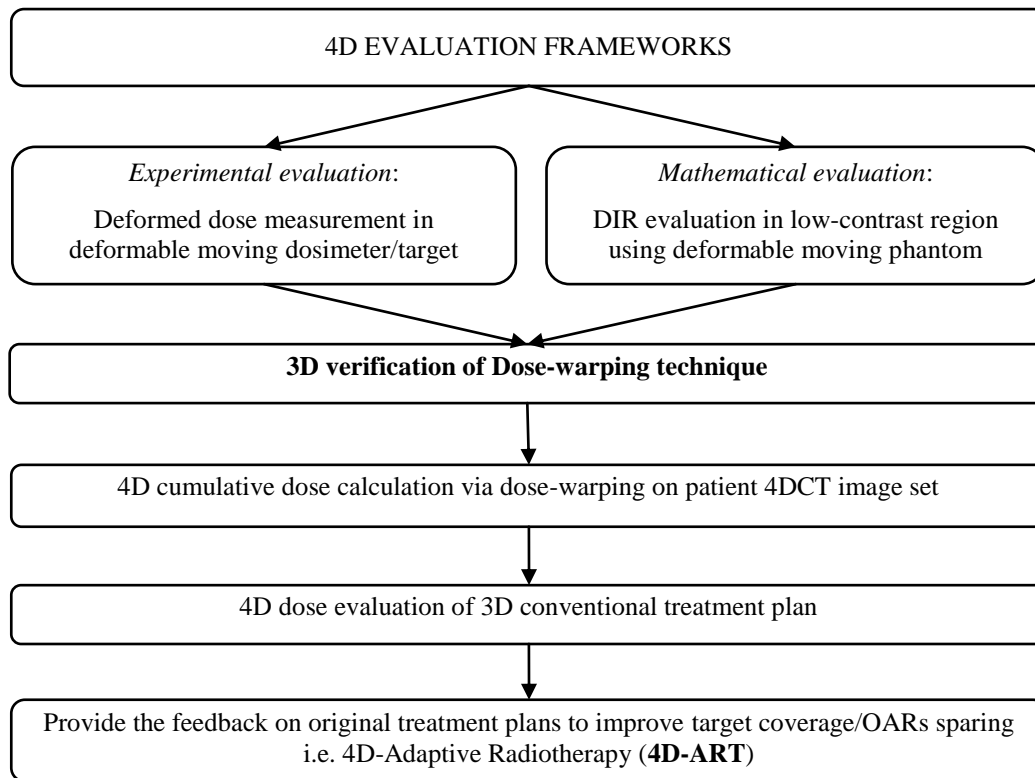
Figure 7–1 The framework developed in this thesis for four-dimensional dose evaluation. This framework consolidates a novel deformable dosimetry, image guidance, deformable image registration (DIR) and dose-mapping; such can be applied to dose reconstruction, accumulative dose calculation and treatment plan evaluation to fully elucidate the dosimetric impact and make corresponding corrections throughout the treatment course, i.e. re-optimisation of the plan.

7.2 The measurement of dose delivered to deformable moving targets

The development of a tool for deformed dose *measurement* corresponds to the first part of this thesis (i.e. *an experimental model*). Dosimetry for highly conformal and small radiation fields has inherent complexities. For instance, issues related to detector volume averaging due to the coarse resolution of a large detector relative to the conformal fields and perturbation of the field due to the difference between detectors and the medium, in terms of radiological and physical properties (i.e. water equivalence). Polymer gel dosimetry is a promising tool for verification of such radiation field delivery. Gel dosimeters are tissue-equivalent and volumetric, yielding three-dimensional dose information, thereby functioning as both the phantom and dosimeter material. A further layer of complexity in addition to the above is the dose measurements on deformable moving targets, which is, in this author's opinion, one of the principle challenges in contemporary RT. In this thesis, this need was addressed by developing a novel system for deformable dosimetry. This refers to a 3D volumetric deformable polymer gel, dubbed DEFGEL, as the first inherently coupled dosimeter and deformable phantom.

In summary, development of the dosimetric measurement system in this study involved the first three-dimensional, tissue-equivalent deformable integrating dosimeter (DEFGEL) by modifying conventional PAG and using latex membrane as a container. DEFGEL was characterised in terms of radiological and physical properties for tissue equivalency, as well as dose sensitivity and stability for calibration (dose vs. change in optical density). This study demonstrated robust structural integrity and reproducibility of deformation even after hundreds of deformations, and also verified that multiple CT-scanning does not impact on sensitivity. Dose delivery to the DEFGEL phantom was performed in three arrangements: (i) without deformation, (ii) with deformation, and (iii) within cumulative exposures with and without deformation, i.e., dose integration. In the *absence* of deformation as a ground truth, results showed high agreement with treatment planning system (pencil beam algorithm) calculations for all fields tested with different degrees of complexities (3D γ-evaluation indicated ~ 97% agreements with criteria of 2%/2mm for even stereotactic small field adapted from a patient plan. Comparison of dose profiles and 2D isodose distributions from the aforementioned three arrangements illustrated complex spatial redistribution of dose in all three dimensions occurring as a result of the change in shape of the target between irradiations, even for a relatively simple deformation (bilateral compression). Discrepancies of up to 30% of the maximum dose were evident from dose difference maps for three orthogonal planes taken through the isocenter of a stereotactic field. This study also demonstrated that consecutive irradiations delivered in different states of deformation can be integrate and read out as a single distribution.

In conclusion, this study has experimentally proven that a change of geometry due to deformation can induce a significant change in the absorbed dose distribution and that such a change can be measured. Therefore, this work has obvious potential for a number of applications for not only external beam radiotherapy and brachytherapy, but also the verification of deformable image registration, validation of dose warping strategies based on DIR, and the evaluation of motion/deformation compensation strategies in radiotherapy. These studies were conducted and the summary of results thereof is provided in the following three sections.

7.3 The validation of deformable image registration

The validation of deformable image registration (DIR) algorithms is a clinically-driven requirement of image-matching for dealing with organ deformation; it is also a necessary component in achieving accuracy in the *mathematical model* for dose deformation. The focus of this thesis was primarily concerned with the calculation of dose in deforming geometries and the

validation of dose-deformation operations, whereby doses are morphed based on deformation matrices generated by DIR algorithms. However, clearly the accuracy of such an approach is critically dependent upon the accuracy with which DIR algorithms are able to morph the geometry of interest. Consequently, it is important to investigate the accuracy of available algorithms.

In summary this work has used a tissue equivalent, mass and density preserving deformable gel (DEFGEL) phantom implanted with high contrast fiducial markers (FMs), to evaluated three different representative types of deformation *via* DEFGEL phantoms. The performance of a set of DIR algorithms has been assessed within areas of near-uniform intensity, rather than only at known landmarks, using a method of mathematically erasing the markers prior to registration. This is in order to eliminate bias introduced from the fact that high contrast features drive the registration, in particular for intensity-based algorithms. This study demonstrated that the performance of all algorithms is critically dependent upon the parameters set, thereby one *cannot* simply use the "default" parameters and must undertake a thorough optimisation process before implementation for clinical use. Subsequently, this work has shown that algorithm performance varied substantially after each algorithm was optimised – up to 72 combinations were undertaken. Some were unable even to register the phantom boundary contour satisfactorily; of those that could, there was a wide range of errors between calculated marker positions and the measured locations.

Using this evaluation process, this work yielded the following key findings:
The best performing algorithm – *original Horn and Schunck* – yielded positional errors in the order of ~1 mm up to about 20% of the magnitude of displacement of individual markers. For the worst of the results – *modified demons* algorithm, larger errors in the order of ~5 to 7 mm were observed and were poorly correlated with the magnitude of displacement, indeed sometimes exceeding the magnitude of actual displacement of individual markers. For most algorithms, larger deformation induced displacements generally resulted in larger errors while there was no trend with respect to the complexity of deformation. The distribution of individual errors was generally characterised by a standard deviation of about ½ to ⅔ of the mean error for all the tested algorithms. The sensitivity of DIR performance to the number of fiducial markers present was quantified. This showed that if deformable registration is evaluated by analysis of features that are present during the calculations, then the outcome will be biased and the results will not be representative of the true performance in low-contrast regions. On the other hand, it should be identified that the technique presented in this study has enabled quantification of improvements achievable using fiducial markers for DIR. For instance, a greater number of high

contrast features per volume increases registration accuracy, by 6 times for the best case. As an example of clinical relevance, the use of three FMs in a 40 ml volume (comparable to a typical prostate volume) halves the mean error from ~2 to ~1 mm in the low-contrast region, compared to reliance on the boundary contour alone.

Overall, this work has facilitated a qualitative and quantitative evaluation process to systematically investigate a range of DIR algorithms in terms of their capacity to generate accurate deformation vector fields. Consequently, the findings in this study have identified the performance of each DIR algorithm, in particular, in *low-contrast* regions. This has also enabled calculation of dose deformation inside the target volume with a known degree of confidence in the spatial accuracy.

7.4 The calculation of dose delivered to deformable moving targets

The verification of methodologies for deformed dose *calculation* corresponds to the second part of the primary objective in this thesis (i.e. *mathematical model and verification*). In this study, the calculation of warped (deformed) dose distribution is directly compared to the corresponding measured dose distribution via DEFGEL, in order to experimentally validate the dose-warping technique.

Several key findings are summarised here:

Analysis of a range of DIR algorithms available in the public domain indicates quite variable results. This showed that careful algorithm evaluation and selection are required before clinical implementation of this technique for 4D dose evaluation or 4D planning purposes. For the comparisons between "warped" dose distributions and the corresponding measured dose distributions using the best DIR algorithm, 3D γ-analysis shows agreement of $\gamma_{3\%/3mm} \approx 99\%$ in each case of several types and extents of deformation. Rather than the complexity of the treatment delivered, it is the extent of deformation which most greatly affects the accuracy of the warped dose distribution. Note that these results are consistent with the results of DIR performance, as described in the preceding chapter. For a square field case, the smallest deformation (~9 mm) yields agreement of $\gamma_{3\%/3mm} = 99.9\%$, whilst the most significant deformation (~20 mm) yields agreement of $\gamma_{3\%/3mm} \approx 96.7\%$. The results indicate *dose-warping* can be justified for even fairly large deformations, relative to both field and target sizes and for those deformations that do not obviously involve significant density changes (e.g. lungs). *Dose-warping* techniques together with proper validation and selection of DIR algorithms/methods allows existing patient plans to be morphed according to new/different patient images.

Furthermore, this technique facilitates the calculation of cumulative doses over different states of deformation.

In summary, this work has demonstrated a full 3D experimental validation of results from a range of dose deformation algorithms available in the public domain. Consequently, this work showed that DIR based *dose-warping* can accurately represent the true (measured) dose in a deformed medium, thereby enabling dose-warping techniques to be implemented for 4D evaluation of conventional patient treatment planning.

The variability of results highlights the need for vendors to perform robust clinical evaluations of their algorithms to ensure the optimal parameter settings are used in DIR software implementations, or provide flexibility in parameter selection to the user so that they can optimise the accuracy for clinical scenarios. It also suggests the need for a range of tools to be available in DIR software implementations which allow individual users to verify DIR performance in quantifiable and clinically relevant ways. These tools are now beginning to emerge on the market; examples of these tools provided by vendors include IMSimQA™ by Oncology Systems, Ltd. (Shropshire, UK), MIM Symphony™ by MIM Software, Inc. (Cleveland, OH, USA), Velocity™ by Varian Medical Systems, Inc. (Palo Alto, CA, USA), and RTx™ by Mirada Medical (Oxford, UK), which utilises DIRs for different RT applications.

7.5 The 4D evaluation of conventional 3D planning

The application of the validated calculation method to a patient treatment planning system is the final objective of this thesis, following the development of both methodologies for deformed dose *measurement* and the corresponding *calculation*. This study has focused on application to liver stereotactic body radiotherapy (SBRT), which is fast increasing as one of the most common advanced modes of radiotherapy for liver lesions. Liver SBRT involves large mass and density conserving deformation with high doses, which must necessarily be delivered with high spatial accuracy. Consequently, associated discrepancies between planned and delivered doses may be pronounced; such uncertainties are not accounted for in current practice, which may result in reduced dose conformity and tumour control.

Such issues underscore the relevance of the findings presented in this thesis. In this context, 4D evaluation of conventional 3D treatment planning in liver SBRT has been performed using dose-warping based dose calculation and subsequent dose accumulation.

This yielded several key findings:

Dose-volume histogram analysis (DVH) clearly indicated that the typical 3D planning approach appears to accurately calculate dose to the GTV while overestimating doses to PTV as well as ITV (= CTV) by up to 9% of D_{mean} and underestimating dose to normal liver by up to 8% of D_{mean}, compared to the 4D evaluation methodology. The homogeneity of the dose distribution is overestimated when using conventional 3D calculations on an AIP by up to 24%. Doses to other organs are low and consequently differences between 3D and 4D methods are not as troubling in an absolute sense, although discrepancies between the two methods in terms of mean doses were up to a factor of two. Hence, dose differences are typically small for untargeted critical organs. Consequently, OAR dose differences between two contouring methods, defined on the AIP or reference phase, are not quantitatively substantial in terms of an absolute dose. A further interesting finding is that we have shown 4D-cumulative dose calculation with at most *three* phases is a reasonably accurate approximation of a 'full' 4D dose calculation with the nominal ten phases for all patients. This indicates that judicious selection of phases may allow representative planning from as few as 3, which is useful from a patient throughput perspective. The general consequence can thus be that reduced doses/dose conformity in ITV/PTV due to organ motion/deformation mainly lead to excessive doses to the healthy liver which encompassed the entire tumour volume, but not to other adjacent organs. This study has quantitatively demonstrated this, which is currently not considered in most treatment planning systems and subsequent plan evaluations.

Overall, the 4D evaluation technique highlights that reduced doses/dose conformity in ITV/PTV due to organ motion/deformation mainly lead to excessive doses to an organ surrounding target(s) and also other organs whose exposed area varies due to breathing motion/deformation, which are not reflected on 3D plans. It is also worth noting that the coverage of a time-resolved target (i.e. GTV) is ensured by additional margins with ITV/PTV approach, although undesired reduction of dose conformity in ITV (=CTV) can also potentially cause reduced tumour control. Resultant 4D accumulated dose distributions reveal excessive organ doses that are not directly reflected on NTCP calculation of the healthy organ surrounding target(s); this is because a part of the surrounding organ receiving excessive doses is not included in the volume of normal tissues but is included in the margin around GTV. In this study, the absolute values for the NTCP to the healthy liver were less than 5%, which is not surprising as 6 x 7 Gy fractionation schedule used in this study at our clinic (PMCC) is informed by NTCP calculations to provide an estimated risk of radiation induced liver disease (RILD) of < 5%. However, the exploration of alternative fractionation schemes does reveal significant differences (see Table 6-5), demonstrating that significant uncertainties exist in the estimation of NTCP across the different

fractionation schemes. Although it is ideal to implement biological parameters as plan quality indicators, there is too little multi-institutional data available for TCP/NTCP to be accurately modelled with correlations of DVH metrics. Until there are data demonstrating outcomes as good or better, it is unlikely that a clinician would accept extremely cold regions in a CTV or hot regions in a PTV, despite having acceptable TCP values which was highlighted by a recent point-counterpoint article in *Medical Physics* (Deasy et al., 2015).

We believe that realistic estimates of the dose actually delivered to the liver (e.g. through the quasi-4D method presented here) will lead to greater confidence in the model estimates. Such information is vital if treatment prescriptions are to be informed by NTCP estimates. Clearly, the more accurately we can estimate the true delivered dose to the patient, the better we can define model parameters to predict clinical outcomes in the era of hypofractionated treatments (Jackson et al., 2010b). Although the deterministic effects appear to be low for the fractionation scheme ultimately employed, one cannot ignore the notable differences in calculated healthy organs dose for the two methods. Ultimately, the most efficacious treatment approach will always be to follow the goal of radiotherapy – delivering a lethal dose of radiation to a tumour whilst minimising damage to surrounding healthy tissues. 4D evaluation methodology described in this work has the potential to quantify such issues of under- and/or over-dosage, so as to allow more accurate dose prediction and consequently enhance the positive treatment outcome.

The expectation of a correlation between the magnitude of motion and/or deformation and the magnitude of errors quantifiable by the 4D approach, suggests the possibility for patient selection rather than routine 4D calculations. For instance, a typical clinical workflow might involve:

- Patients exhibiting large tumour excursion to be flagged for additional analysis
- Cross-check using 4D methodology undertaken by physics/RT
- Dose coverage and risk data presented to complement 3D information
- If large differences in dose calculations are noted, it is recommended that the treating clinician be notified to decide whether the initial plan is to be re-optimised or not – more conservative approach to be adapted in estimating clinical risk to critical organs

As a final note on the topic of dose-warping based 4D plan evaluation and potential re-optimisation of plan, it is important to mention the observation that the 4D dose calculation using as few as three phases followed by judicious selection of phases may allow representative planning of using the full 10 phases (agreement within 3% is demonstrated over the D_{98} and D_{50} interval), despite significant differences of computational time between the two. This may influence decision making, particularly given the relatively laborious nature of 4D planning and associated potential reduction in patient throughput.

7.6 Clinical significance

The outcomes of this thesis have direct clinical impact and utility, summarised as follows. The development of:

(i) *Novel deformable dosimetry with DEFGEL.* This work provides a tool to directly measure deformed dose distributions in 3D. This research has attracted attention because of the absence of such a tool in the past and because of the numerous potential applications which can made utilising this system; such as verification of dose delivery in various cases – breast, prostate, liver, kidney etc. – and anthropomorphic phantom for QA process.

(ii) *A systematic method for DIR assessment*. While there is fast increasing interest in deformable image registration, there is a lack of knowledge in the performance of DIR algorithm in *low-contrast* regions for mass and density conserving deformation. The method described in this study builds upon current research, enabling assessment of the accuracy of DIR algorithms within areas of near-uniform intensity, rather than only through known landmarks. This eliminates bias introduced from the fact that high contrast features drive the registration. This is important because of the clinically-driven requirement that knowledge of the error arising from DIR process is needed for various state-of-the-art techniques such as image-fusion, dose-mapping, auto-contouring, tumour atrophy calculation, 4D planning etc.

(iii) *A methodology to validate dose-warping technique.* This study contributes towards 3D empirical evidence demonstrating the accuracy of dose-warping, which has been a contentious topic because some of such image calculations are not constrained by physical laws. This study has demonstrated the 3D experimental validation of results from a range of dose deformation algorithms available in the public domain. This work has direct clinical relevance, evidenced by the development of dose-warping based 4D treatment planning system (TPS) currently being marketed by vendors, such as RaySearch TPS (RaySearch Laboratories, Stockholm, Sweden).

(iv) *4D evaluation of liver SBRT plan.* This current work highlights the discrepancies between planned dose and actual delivered dose resulting from anatomic variations in the case of conventional 3D treatment planning of SBRT. The application of the framework detailed in this work has quantified such issues of under- and/or over-dosage at the target and the surrounding organs, respectively. The impact of this study is also reflected by further collaboration for kidney VMAT/SBRT study at the Peter MacCallum Cancer Centre (Melbourne, Australia)

In conclusion, the framework designed in this study consolidates a novel deformable dosimetry, , a deformable phantom, deformable image registration (DIR) and dose-mapping. Such tools can be applied to dose reconstruction, accumulative dose calculation and treatment plan evaluation to fully elucidate the dosimetric impact and make corresponding corrections throughout the

treatment course, i.e. plan re-optimisation. It is worth noting that there are several groups that have contributed to each of topics set out above. Of many relevant studies, some examples are that i) Juang et al introduced and characterised a novel deformable plastic dosimeter (PRESAGE-Def) and investigated the accuracy of a b-spline based commercial DIR (Juang et al., 2013); ii) Kirby et al demonstrated an optical method of validating DIR using non-radiopaque markers, optical camera and 2D deformable phantom (Kirby et al., 2011); iii) Brock et al developed a biomechanical DIR algorithm (finite-element-model based) (Brock et al., 2003) and Velec et al validated this DIR using PRESAGE-Def dosimeter (Velec et al., 2015); iv) Jung et al demonstrated 4D dose calculations using an intensity-based DIR for liver cases (Jung et al., 2013). Along with such important studies by other groups, the results shown in this thesis provide practical means (beyond issues of purely academic interest) to efficiently deal with a major challenge in contemporary RT.

7.7 Outlook

In this thesis, the principle focus has been dosimetric discrepancies associated with deformation in both dose measurements and dose calculations. However, there are many challenges in accurately predicting such deviated dose distributions, and the present thesis has therefore some limitations that should be noted.

For instance, there remain a number of challenges associated with gel dosimetry, the recommended method for measurement of deformed dose distribution, which present challenges to routine clinical implementation. This includes the requirement for a toxic/carcinogenic chemical handling (e.g. Acrylamide) and gel preparation laboratory, equipped with acid safe, chemical disposal facilities, fume cupboard and associated circulation system. Other issues include the fact that the dosimeters are single-use per day and readout systems, such as optical CT scanners or MRI, require careful corrections for scatter or noise respectively, and may not always be readily available.

There are also several limitations on the recommended method for calculation of deformed dose distribution – dose-warping technique – which morph doses using deformation matrices obtained *via* deformable image registration. It is important to mention that clinics ought to thoroughly research the suitability of the algorithms they employ, because the algorithm-specific optimisation process is a critical necessity which is not only nontrivial but is also computationally-demanding. It has been our own experience that commercial algorithms may perform very poorly in this regard and are designed with simplicity in mind; consequently the

real limitation is that many computational parameters are unavailable to the end-user. Although there are several attempts in commercial treatment planning systems to implement 4D dose calculations *via* DIR-based dose-warping, the available systems are currently mainly used for research purposes and need to undergo rigorous investigation before clinical usage.

In addition, there are various difficulties associated with the sophisticated nature of tumour behaviour that are beyond the scope of this thesis; in particular, the handling of density changes and atrophies are issues as all tumours change in size, and in some cases do so during and/or between treatment fractions. For example, the method and results presented in this thesis may not be applicable to the cases of organ atrophy and tumour density change over the course of treatment, where the notion of dose (the absorbed energy per mass) as a surrogate for biological response becomes complicated by changing target mass and volume. This is further complicated if the targeted tumour is located in heterogeneous media, such as the lung or any other anatomy incorporating or juxtaposed with, for instance, airways, cavity or bone. This is an arising issue in radiotherapy that physicists and clinicians ought to acquaint themselves with. There are a number of studies being undertaken both internationally and locally at RMIT University, including the 4D experimental method for the assessment of intra-fraction motion and deformation of targeted organs; auto-contouring of atrophy in breast tumour lesions; breathing corrected VMAT for kidney tumours and so on.

While liver SBRT was primarily studied for immediate clinical application, it is hoped that the findings of this thesis can be applicable to other organs with various RT modalities where conformal fields are used in the existence of anatomic motion and associated organ deformation (although it has not been shown/demonstrated in the thesis). It is because most organs are subject to no (or minimal) density changes, e.g. tissue, fat, light bone etc., except the lungs which noticeably exhibit density changes generally in a range of 0.2 to 0.5 g/cc. Despite it has not been experimentally investigated, what is obvious is that GTV plus margin yields excessive dose to surrounding healthy lungs which can be better quantified by a 4D method (although its accuracy is still not exactly known). Ultimately, daily CBCT images could be utilised to account for inter-fraction effect, however, it should be acknowledged that such assessments are outside the scope of the current thesis, while this topic could be a valuable extension of this project as future work. It may be also worth noting that MR-linac could be available in routine clinical practice in near future, so that changes in patient anatomy could be constantly monitored during delivery and then possibly adapted online for both intra- and inter-fraction effects. In such a case there is no doubt that the 4D evaluation data via deformable dose accumulation could be more applicable in order to better correlate planed/delivered doses and clinical outcome. The

framework developed in this thesis also relates to investigating various state-of-the-art radiotherapy tools such as image-fusion, dose-mapping, auto-contouring, and tumour atrophy calculation. Most importantly, however, it is hoped that the outcomes of this thesis will help to improve treatment plan accuracy, and thus to contribute to the impact on patient treatment outcome. By considering both computation and measurement, it is also hoped that this work will open new windows for future work and hence provide the building blocks to contribute to further the enhancement and the benefit of radiotherapy treatment.

Appendix I: Deriving DIR mathematical formulations

I-1. Theory of the Optical flow method

As set out in Section 4.2.5, optical flow is the distribution of apparent velocities of movement of brightness patterns within an image (i.e. tracking the movement of high brightness gradients). Before deriving a mathematical formulation for optical flow method, the fundamental assumptions are described which yield an intuitive idea of constraints that should be included in such a model. These assumptions include:

(1) Brightness constancy– the intensity of a point in an image does not change with the displacement and time,

(2) Gradient constancy – the gradient of the intensity of a point in an image does not vary due to the displacement and time,

(3) Spatial smoothness – the nearby points move in the same manner,

(4) Multistage approach – there is at least one local minimum as well as the global minimum in the similarity measure.

In the human body, the density of most organs does not change notable with time. The first assumption of OFM should apply to those organs, with exceptions such as the lungs. The lungs are slightly denser at the end of expiration than that at the end of inspiration. This slight density change is handled by introducing a non-zero term ε in the equations. The second and third assumptions also hold for the human body. The main example of shearing motion is the interface between the lungs and chest wall. Since this is not a very sharp shearing motion, especially between multi-respiratory phases, it does not present a problem in the image registration (Zhang et al 2008).

The first assumption can be expressed as:

$$I(x, y, z, t) = I(x + dx, y + dy, z + dz, t + dt) \tag{I-1}$$

where $I(x, y, z, t)$ is the intensity (or the brightness) of the image at location (x, y, z) and time t. This assumption has one obvious drawback: it is quite susceptible to slight changes in brightness, which often appear in natural images with different time frames. It is, hence, useful to allow some small variations in the intensity and help to determine the displacement vector by a criterion that is invariant under intensity changes. Such a criterion is the gradient of the image intensity resulting in the second assumption (Uras et al, 1994). This gives $\nabla I(x, y, z, t) = \nabla I(x + dx, y + dy, z + dz, t + dt)$, where ∇ denotes the spatial gradient. This constraint is particularly helpful for translatory motion, while it can be better suited for more complicated motion patterns. The Taylor series expansion of Eq. (I-1) is

$$I(x, y, z, t) = I(x + dx, y + dy, z + dz, t + dt)$$

$$= I(x, y, z, t) + \frac{\partial I(x, y, z, t)}{\partial x} dx + \frac{\partial I(x, y, z, t)}{\partial y} dy + \frac{\partial I(x, y, z, t)}{\partial z} dz + \frac{\partial I(x, y, z, t)}{\partial t} dt + \varepsilon \quad \text{(I-2)}$$

$$= I(x, y, z, t) + I_x dx + I_y dy + I_z dz + I_t dt + \varepsilon$$

where I_x, I_y, I_z and I_t are the partial derivatives of I in respect to x, y, z and t at (x, *y* ,z, *t)* respectively. The notation ε contains the second and higher order terms in *dx, dy, dz* and *dt*. Eliminating ε and combining with Eq. (I-1) as implied in the first assumption, Eq. (I-2) leads to the well-known optical flow constraint (Horn and Schunck, 1981):

$$I_x v_x + I_y v_y + I_z v_z + I_t = 0 \quad \text{or} \quad \vec{\nabla} I \cdot \vec{\mathbf{v}} + I_t = 0 \quad \text{(I-3)}$$

where $v_x = dx/dt$, $v_y = dy/dt$, $v_z = dz/dt$, are the three components of the spatial displacement (= optical flow or motion vector field) for location (*x, y, z*) at time *t* towards time *t* +d*t*. It has been widely used in the literature (Iu and Liu 1999, Zhang *et al* 2008, Horn and Shunck 1981 and Joshep 1987). In order to allow some intensity change between images, a non-zero term ε_g is introduced to Eq. (I-3):

$$(\vec{\nabla} I \cdot \vec{v} + I_t) = \varepsilon_g \ , \quad \text{(I-4)}$$

where ε_g denotes the global smoothness constraint (or data conservation constraint). The validity of ignoring the right hand side of Eq. (I-2) is dependent on the magnitude of the displacement and the spatial frequency content of the intensity pattern relative to the size of VOI, e.g. large displacement or frequent pattern change leads to greater second and higher order terms of Taylor series for the intensity. The first assumption is satisfied only without considering density change or occlusion of features in the images. It is well-known that this constraint by itself is not sufficient to solve $\vec{v}(v_x, v_y, v_z)$ (Brox *et al*, 2004).

Using the first two assumptions the model estimates the displacement of a voxel only locally, without considering any interaction with neighbouring voxels. The differential constraint equation, Eq. (I-3), can be used in motion detection (Fennema and Thompson, 1979). It is a single equation in the two unknown vectors which forms a single constraint line in velocity space. Any velocity on this line satisfies the constraint. This was called the "aperture problem" since it implies that locally the velocity cannot be determined uniquely when the intensity gradient vanishes somewhere, or if only the flow in normal direction to the gradient can be estimated. In addition, some outliers could be expected in the estimates. Hence, it is useful to introduce the third assumption- that the apparent velocity of the brightness pattern is assumed to vary smoothly almost everywhere in the image (Horn & Schunck, 1981). As the optimal displacement field will have discontinuities at the boundaries of objects in the image, it is

sensible to generalise the smoothness assumption by demanding a *piecewise smooth* flow field (Black 1991 and Black 1996). Horn and Schunck (1981) introduced a smoothness constraint in order to solve uniquely for displacement, so as to deal with points within areas of zero brightness gradients by assigning them the averages of the neighbouring velocity estimates. Due to the iterative nature of the Horn and Schunck method with combining the fourth assumption, areas of uniform brightness will be filled from the boundary inwards. This is known as the velocity smoothness constraint (ε_s^2). A number of other authors (Tretiak and Pastor 1984; Nagel 1987; Uras et al. 1988; Verri et al. 1990 and Srinivasan 1990) produced two or more linear equations in $\vec{v}(v_x, v_y, v_z)$ by assuming constancy of partial derivatives and other functions of the intensity. A third approach (Lucas and Kanade 1981 and Campani and Verri 1990) is to assume the velocity field is locally constant and to combine constraint equations from neighboring pixels (note they dealt with 2D *planar* images at that time). A review of these and other similar approaches such as correlation and energy models, can be found in Baron et al. (1993).

In the Horn and Schunck method, which is the most commonly used over the others (Castadot *et al*, 2008), the velocity smoothness constraint was introduced to further constrain the solution for $\vec{v}(v_x, v_y, v_z)$ by combining the second assumption of a smooth flow field in the form of a *smoothness*, or *regulariazation* term (ε_s^2). The most common formulation of the regularizing term is the *first*-order, or membrane, model which is the Laplacians ($= \nabla^2$) of the three components of the derivative of the spatial displacement:

$$\nabla^2 \vec{v}(v_x, v_y, v_z) = \left(\frac{\partial v_x}{\partial x}\right)^2 + \left(\frac{\partial v_x}{\partial y}\right)^2 + \left(\frac{\partial v_x}{\partial z}\right)^2 + \left(\frac{\partial v_y}{\partial x}\right)^2 + \left(\frac{\partial v_y}{\partial y}\right)^2 + \left(\frac{\partial v_y}{\partial z}\right)^2$$
$$+ \left(\frac{\partial v_z}{\partial x}\right)^2 + \left(\frac{\partial v_z}{\partial y}\right)^2 + \left(\frac{\partial v_z}{\partial z}\right)^2 = \varepsilon_s^2 \tag{I-5}$$

, where ε_s^2 denotes the velocity smoothness (constant intensity) constraint.

The problem of determining optical flow (motion vector field) $\vec{v}(v_x, v_y, v_z)$ can be formulated to minimize the objective function 'ε', as *least-squares* estimation, the sum of a combination of E_g and E_s over *VOI* with weighting factor λ ($=\alpha^2$) :

$$\varepsilon = \iiint_{VOI} \left(\varepsilon_g^2 + \alpha^2 \cdot \varepsilon_s^2\right) dxdydz$$
$$= \iiint_{VOI} \varepsilon_g^2 dxdydz + \alpha^2 \cdot \iiint_{VOI} \varepsilon_s^2 dxdydz \quad, \tag{I-6}$$
$$= E_g(\vec{v}) + \lambda \cdot E_s(\vec{v})$$

, where ε denotes the velocity smoothness constraint and the weighting factor λ controls the relative importance of the brightness constancy and the spatial smoothness terms. In computer and vision science the objective function 'ε' and is referred to as 'energy' and so 'energy minimisation' refers to the above process. Applying the Euler-Lagrange equations from variational calculus, it can be derived as below:

$$\alpha^2 \nabla^2 v_x = \varepsilon_g \frac{\partial}{\partial x} I(x+dx, y+dy, z+dz, t+dt)$$

$$\alpha^2 \nabla^2 v_y = \varepsilon_g \frac{\partial}{\partial y} I(x+dx, y+dy, z+dz, t+dt) \qquad \text{(I-7)}$$

$$\alpha^2 \nabla^2 v_z = \varepsilon_g \frac{\partial}{\partial z} I(x+dx, y+dy, z+dz, t+dt)$$

, where $\nabla^2 v_x, \nabla^2 v_y$ and $\nabla^2 v_z$ are the Laplacian of v_x, v_y and v_z, respectively. They can be approximated by $\nabla^2 v_x \approx \kappa(\overline{v_x} - v_x), \nabla^2 v_y \approx \kappa(\overline{v_y} - v_y)$ and $\nabla^2 v_z \approx \kappa(\overline{v_z} - v_z)$, where $\overline{v_x}, \overline{v_y}$ and $\overline{v_z}$ denote the local average of v_x, v_y and v_z, respectively, and $\kappa \approx 3$. The calculation of the local average depends on the decision function as detailed in the later section (Section I-3). Horn and Schunck solves the non-linear differential equation in Eq. (I-7) by a numerical approach with linearization (Horn and Shucnk, 1981). This can be briefly described as:

$$v_x = \overline{v_x} - I_x \frac{\left(\overline{v_x}I_x + \overline{v_x}I_y + \overline{v_x}I_z + I_t\right)}{\alpha^2 + I_x^2 + I_y^2 + I_z^2},$$

$$v_y = \overline{v_y} - I_y \frac{\left(\overline{v_x}I_x + \overline{v_x}I_y + \overline{v_x}I_z + I_t\right)}{\alpha^2 + I_x^2 + I_y^2 + I_z^2}, \qquad \text{(I-8)}$$

$$v_z = \overline{v_z} - I_z \frac{\left(\overline{v_x}I_x + \overline{v_x}I_y + \overline{v_x}I_z + I_t\right)}{\alpha^2 + I_x^2 + I_y^2 + I_z^2}.$$

I-2. Iterative approach

One main drawback of Horn and Schunck's algorithm is that it fails to handle larger motion as so to be trapped to the local (i.e. the lack of the fourth assumption in the previous section). This is because the majority of images where the higher order derivatives of the intensity function are not all zero, so the first-order approximation in Eq.(I-2) and Eq.(I-3) can *no longer* lead to good motion estimates when the motion is large. Iterative approach is based on the following argument:

Assuming each iteration improves the estimates of the flow field (i.e., $|v_x^n - v_x| + |v_y^n - v_y| + |v_z^n - v_z| \rightarrow 0 \, as \, n \rightarrow \infty$), *then we should always compare the predicted*

(calculated) image, I(x+dx^n,y+dy^n,z+dz^n,t+dt), with the target (reference) image I(x, y, z, t), in order to improve the current estimates in the next iteration.

This approach aims to find the adjustment of the velocity v_x, v_y and v_z at each iteration. The solution of the spatial displacement for each voxel in Eq.(I-8), then, is obtained using three Gauss–Seidel iterations (Zhang *et al* 2008) by applying variational calculus:

$$v_x^{(n+1)} = v_x^{(n)} - I_x \frac{\left(v_x^{(n)} I_x + v_y^{(n)} I_y + v_z^{(n)} I_z + I_t\right)}{\alpha^2 + I_x^2 + I_y^2 + I_z^2},$$

$$v_y^{(n+1)} = v_y^{(n)} - I_y \frac{\left(v_x^{(n)} I_x + v_y^{(n)} I_y + v_z^{(n)} I_z + I_t\right)}{\alpha^2 + I_x^2 + I_y^2 + I_z^2}, \qquad \text{(I-9)}$$

$$v_z^{(n+1)} = v_z^{(n)} - I_z \frac{\left(v_x^{(n)} I_x + v_y^{(n)} I_y + v_z^{(n)} I_z + I_t\right)}{\alpha^2 + I_x^2 + I_y^2 + I_z^2}.$$

Many techniques have been implemented to make the OFM accurate and practical for medical physics research and eventually clinical practice, which include:

1. A multi-resolution feature which calculates the deformation matrix from coarse resolution level to fine, which keeps the displacement between two corresponding voxels always small in the calculation. This helps in increasing accuracy as well as in decreasing calculation time.

2. A multi-pass approach (Iu and Liu 1999) in which multi-loop calculation updates the deformation matrix after each loop of calculation. The idea is to perform registration multiple times on the same image resolution stage. Because the result of image registration is often not good enough in one computation, registration can be computed again in a new pass based on the result of the previous pass. As iterations progress in each pass Taylor's series expansion of the intensity function starts from a same reference point (initial moving image in each pass). However, as each pass progresses, the Taylor's series expansion of the intensity function starts from the updated reference point calculated by a previous pass (i.e. the observation point in the Taylor's series expansion moves accordingly with the current motion estimates). We have demonstrated that by doing so, the so-called constant intensity constraint can be better and better satisfied as the iteration process continues. This concept can be readily adapted to many optical flow algorithms where $\varepsilon = 0$ is assumed for performance improvement. Comparing with a traditional method, this new concept can offer faster and better convergence, and the capability to handle larger motion.

I-3. Outlier rejection

A set of assumptions – the brightness constancy and spatial smoothness – for calculating optical flow in the algorithms, by necessity, is a simplication of the real world and hence may be violated in some circumstances. For example, the common assumption that the optical flow varies smoothly is violated when motion boundaries are present. In the medical imaging perspective, part of an organ may not be contained in the target image but it could occur in the source image by moving into the field of view (FOV) and vice versa. The existence of occlusion and multiple motions between image sets in time interval *dt* causes the discontinuity to arise in the motion field (Iu and Liu 1999) (e.g. shearing motions at the interface between the lungs and chest wall or between the lungs and diaphrams). At motion discontinuities, the smoothness constraint is *no longer* valid. Violations such as these result in significant measurement errors referred to as outliers (Black et al 1996). To handle these errors, the sensitivity of the calculated optical flow (i.e. the motion vector field) to violations of the assumptions must be reduced by doing outlier detection/rejection which is used to stop the smoothness constraint from propagating across the motion boundaries. Outlier rejection (OR) refers to the mechanism of excluding data which do not fit into the underlying model and so to play the role of an edge preserving filter. Normally, a decision function, combined with a deterministic optimization scheme, is defined in order to detect and reject the outlier.

Let's recall the velocity smoothness constraint (=ε), Eq.(I-4) can be expressed as below:

$$\varepsilon = E_g(\vec{v}) + \lambda \cdot E_s(\vec{v}) \qquad \text{(I-10)}$$

where ε denotes the velocity smoothness constraint and the weighting factor λ controls the relative importance of the brightness constancy and the spatial smoothness terms. The velocity smoothness constraint ε can be regarded as an error measurement. As the size of VOI tends to zero, the solution for $\vec{v}(v_x, v_y, v_z)$ is under-constrained. A large ROI is needed to sufficiently constrain the solution and provide some insensitivity to noise. The larger the VOI, however, the less likely the assumptions about the motion will be valid over the entire region. For example, the assumption of constant velocity used in E_g above will be violated by affine flow, transparency, motion boundaries, etc. The dilemma surrounding the appropriate size of VOI is referred to as the *generalised aperture problem*. The assumption of spatial smooth flow used in E_s also forces the local flow vector $\vec{v}(v_x, v_y, v_z)$ to be close to the average of its neighbours.

When a motion discontinuity is present, this results in smoothing across the boundary which reduces the accuracy of the flow field and obscures important structural information about the presence of an object boundary.

There are a number of formulations to define the outlier rejection mechanisms. In principle, the outlier rejection mechanism can be naturally carried out by changing the way that the averages of local motion field, $\vec{v}(v_x, v_y, v_z)$, are calculated for each voxel, by discarding the outlier in the neighbourhood. Let $\bar{v}(i) = (\bar{v}_x(i), \bar{v}_y(i), \bar{v}_z(i))$ be the motion of voxel i. Without outlier rejection, the local motion average depends on all the neighbours in the pre-defined neighbourhood.

$$\bar{v}(i) = \frac{\sum_{j \in N(i)} v(j) \cdot w(j)}{\sum_{j \in N(i)} w(j)} \qquad (I\text{-}11)$$

where $N(i)$ denotes the neighbourhood of the current voxel located at i, and $w(j)$ is the weighting factor for neighbour j, $j \in N(i)$, depending on where the j's located relative to the i. For instance, when a 3x3x3 matrix is used (i.e. the size of N is twenty-six), the corresponding weight $w(j) = 3$ for facet sharing six non-diagonal neighbours, $w(j) = 2$ for twelve edge-sharing diagonal ones and $w(j) = 1$ for eight vertex-sharing diagonal ones.

The calculated matrix is closer to the true values after each loop. Multiple passes with small number of iterations in each pass generate better results than one pass with larger number of iterations (Yang *et al*, 2011). This is a major improvement that makes OFM an accurate algorithm.

For detecting outliers, the similarity measure of motion field is defined using the squared Euclidean distance (=d) between two motion vectors, (see Section 4.2.5.1). Eq.(I-11) becomes the distance measure

$$\bar{v}(i) = \frac{\sum_{j \in N(i)} v(j) \cdot w(j) \cdot g(i,j)}{\sum_{j \in N(i)} w(j) \cdot g(i,j)} \qquad (I\text{-}12)$$

where $d(i, j) = \| v(i) - v(j) \|^2$, i and j are two neighbouring voxels, and $g(i, j)$ is the decision weighting function for controlling the local outlier rejection process. $g(i, j) = g(d(i, j))$ is a function of the motion similarity measure (see Section 4.2.5.1) between two neighbouring voxels. In smooth areas of having a low gradient of intensity, all the neighbours will be accepted because their similarity measures are similar there by definition.

Normally, a decision weighting function, combined with a deterministic optimisation scheme, is defined in order to detect and then either accept or reject the outlier. For example, in a

thresholding approach, a decision weighting function can be described with the threshold constant (T)

$$g(i, j) = g(d(i, j)) = \begin{cases} 1 & if \ d(i, j) \le T \\ 0 & else \end{cases}.$$ (I-13)

or g-functions can be also various continuous functions (see below example functions which are depicted on the left Figure I-1 (Black *et al*, 1995). The right column of Figure I-1 shows *influence functions* (ψ), which is the derivative of decision weighting function g, to characterises the behaviour of a decision weighting function g.

1. The quadratic g-function :

$g(x) = x^2$, $\psi(x) = 2x$.

2. The hyperbolic tangent g-function : $g(x) = tanh(x)$, $\psi(x) = 1 - tan^2(x)$.

$g(x) = tanh(x)$, $\psi(x) = 1 - tan^2(x)$.

3. Skipped mean (Truncated quadratic) (Hampel et al., 1986):

$$g(x) = \begin{cases} x^2 & |x| \le \sqrt{\beta} \\ \beta & otherwise \end{cases}, \quad \psi(x) = \begin{cases} 2x & |x| \le \sqrt{\beta} \\ 0 & otherwise \end{cases}.$$

4. Huber's minimax function(Huber, 1981):

$$g(x) = \begin{cases} \dfrac{x^2}{2\varepsilon} + \dfrac{\varepsilon}{2} & |x| \le \varepsilon \\ |x| & otherwise \end{cases}, \quad \psi(x) = \begin{cases} \dfrac{x}{\varepsilon} & |x| \le \varepsilon \\ sign(x) & otherwise \end{cases}.$$

5. Lorentzian function:

$$g(x) = \log\left(1 + \frac{1}{2}\left(\frac{x}{\sigma}\right)^2\right), \quad \psi(x) = \frac{2x}{2\sigma^2 + x^2}.$$

6. Andrew's Sine (Andrew, 1972):

$$g(x) = \begin{cases} 4 \, sin^2(\dfrac{x}{2\sigma}) & |x| \le \pi\sigma \\ 4 & otherwise \end{cases}, \quad \psi(x) = \begin{cases} \dfrac{2}{\sigma} \, sin(\dfrac{x}{\sigma}) & |x| \le \pi\sigma \\ 0 & otherwise \end{cases}.$$

Function	Function formula	g-function	ψ - function
a) Quadratic	$g(x) = x^2$, $\psi(x) = 2x$.		
b) Hyperbolic tangential	$g(x) = tanh(x)$, $\psi(x) = 1 - tan^2(x)$.		
c) Skipped mean (Truncated quadratic)	$g(x) = \begin{cases} x^2 & \lvert x \rvert \le \sqrt{\beta} \ , \\ \beta & otherwise \ , \end{cases}$ $\psi(x) = \begin{cases} 2x & \lvert x \rvert \le \sqrt{\beta} \ , \\ 0 & otherwise \ . \end{cases}$		
d) Huber's minimax	$g(x) = \begin{cases} \dfrac{x^2}{2\varepsilon} + \dfrac{\varepsilon}{2} & \lvert x \rvert \le \varepsilon \ , \\ \lvert x \rvert & otherwise \ , \end{cases}$ $\psi(x) = \begin{cases} \dfrac{x}{\varepsilon} & \lvert x \rvert \le \varepsilon \ , \\ sign(x) & otherwise \ . \end{cases}$		
e) Lorentzian	$g(x) = \log\left(1 + \dfrac{1}{2}\left(\dfrac{x}{\sigma}\right)^2\right)$, $\psi(x) = \dfrac{2x}{2\sigma^2 + x^2}$.		
f) Andrew's sine	$g(x) = \begin{cases} 4\,sin^2(\dfrac{x}{2\sigma}) & \lvert x \rvert \le \pi\sigma \\ 4 & otherwise \ , \end{cases}$ $\psi(x) = \begin{cases} \dfrac{2}{\sigma}\,sin(\dfrac{x}{\sigma}) & \lvert x \rvert \le \pi\sigma \ , \\ 0 & otherwise \ . \end{cases}$		
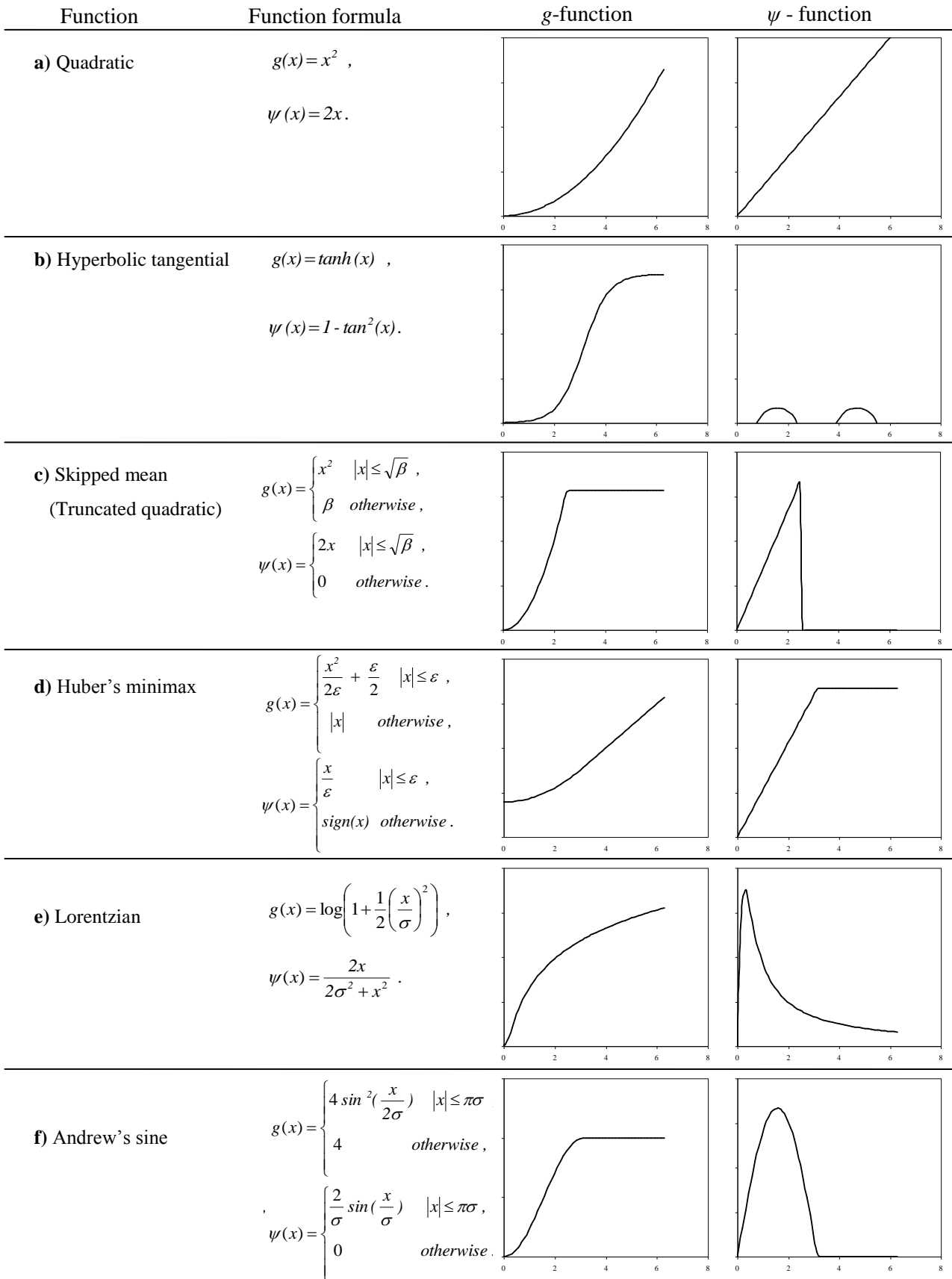
Figure I-1 Six examples of a decision weighting function (estimators).

166

I-4. Demons method

As set out in Section 4.2.5, Thirion's demons method uses a model where the boundary of an object in one image can be thought of as a semi-permeable membrane through which the corresponding object in the other image can diffuse (Thirion, 1998b). For clarity, Figure 4–2 is duplicated here.
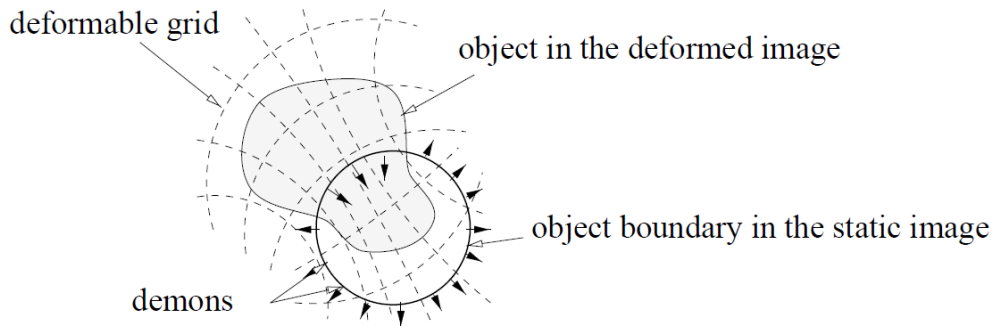
Figure I-2 Diffusing models: a deformed image, considered as a deformable grid, is diffusing through the contours of the objects in the static image, by the action of effectors, called demons, situated in these interfaces (image reproduced from Thirion, 1998).

There are two approaches to using the demons algorithm: The first approach is to consider the contour of the object in the reference (target) image, R to be a membrane with demons placed along the contour (where the boundary of the object is determined from the gradient of the brightness pattern). The demons will pull (attract) points on the object in the moving (source) image, M inside the contour in R using optical flow to estimate the "demons forces" (Thirion, 1998b). The second approach is to put a demon at every voxel location and calculate the "demons force" (again, estimated using optical flow) required to push the voxels in M to match R (Wang et al., 2005e).

Consider a mathematical expression briefly for the "demons force". For a given point, P, in an object, let r be the intensity in R, and m be the intensity function in M. The object in the image M has to be deformed to match that in the image R. In this notation, the optical flow constraint of Eq. (I-4) can be rephrased:

$$\vec{v} \cdot \vec{\nabla} r = m - r. \qquad \text{(I-14)}$$

As this constraint is not sufficient to define the velocity $\vec{v}$, one solution is to regularize the problem to obtain the local values of $\vec{v}$ as shown in Section 4.2.5.1. Another solution is to consider that the end point of $\vec{v}$ is the closest point of the hypersurface m, with respect to

spatial (x, y, z) translation, in other words, multiply both sides of Eq.(I-14) by the spatial gradient ($\vec{\nabla} r$), which leads to:

$$\vec{v} = \frac{(m-r)\vec{\nabla} r}{(\vec{\nabla} r)^2}.$$

(I-15)

This equation is unstable for small values of the spatial gradient $\vec{\nabla} r$. Ideally, the expression should be close to zero for small $\vec{\nabla} r$. A solution is to multiply Eq. (I-15) by the estimated displacement required, $\vec{v}$, for point P to match the corresponding point in M is given by $\{(\vec{\nabla} r)^2 / [(\vec{\nabla} r)^2 + (m-r)^2]\}$, which gives:

$$\vec{v} = \frac{(m-r)\vec{\nabla} r}{(\vec{\nabla} r)^2 + (m-r)^2} \text{ or } \vec{v} = \vec{0}, \text{ if } (\vec{\nabla} r)^2 + (m-r)^2 < \varepsilon$$

(I-16)

, where $\vec{v} = (v_x, v_y, v_z)$ and $\vec{\nabla} r$ is the spatial gradient of the reference image. With this expression for the "demons force", the optical flow can be calculated in two steps: first compute the instantaneous optical flow for every point in R, and then regularize the deformation field. As explained in Section 4.2.5.1, in optical flow, $\vec{v}$ is considered to be a velocity because the images are two successive time frames: $\vec{v}$ is the displacement during the time interval between the two image frames. In fact, when comparing images of two different patients, there is no such temporal consideration and it is more general to consider $\vec{v}$ as being simply a displacement.

There is a need for smoothness to balance the "demons forces" with physical constraints and maintain geometric continuity, which is a corresponding consideration with a process of Eq. (I-5) and Eq. (I-6) for the original optical flow algorithm. This is handled by passing a Gaussian filter with variance of σ^2 over the deformation field following each iteration (Weiguo et al., 2004). For more details, the interested reader is referred to numerous studies of the demons algorithm for use in medical image registration (Guimond et al., 2001, Wang et al., 2005e, Xie et al., 2003).

REFERENCES

AIHW 2010. Australia's health 2010. *Australia's health series no.12. Cat. no. AUS 122.* Canberra: AIHW.

AIHW 2012. Australia's health 2012. *Australia's health series no.13. Cat. no. AUS 156.* Canberra: AIHW.

ADAMOVICS, J. & MARYANSKI, M. A new approach to radiochromic three-dimensional dosimetry-polyurethane. Journal of Physics: Conference Series, 2004. IOP Publishing, 172.

ADAMOVICS, J. & MARYANSKI, M. 2006. Characterisation of PRESAGE™: A new 3-D radiochromic solid polymer dosemeter for ionising radiation. *Radiation Protection Dosimetry,* 120**,** 107-112.

ALPEN, E. L. 1997. *Radiation biophysics*, Academic Press.

ALQATHAMI, M., BLENCOWE, A., QIAO, G., BUTLER, D. & GESO, M. 2012a. Optimization of the sensitivity and stability of the PRESAGE™ dosimeter using trihalomethane radical initiators. *Radiation Physics and Chemistry*.

ALQATHAMI, M., BLENCOWE, A., YEO, U. J., DORAN, S. J., QIAO, G. & GESO, M. 2012b. Novel Multicompartment 3-Dimensional Radiochromic Radiation Dosimeters for Nanoparticle-Enhanced Radiation Therapy Dosimetry. *International Journal of Radiation Oncology* Biology* Physics*.

ARCANGELI, G., MAURO, F., MORELLI, D. & NERVI, C. 1979. Multiple daily fractionation in radiotherapy: Biological rationale and preliminary clinical experiences. *European Journal of Cancer (1965),* 15**,** 1077-1083.

ATTIX, F. 1986. Introduction on radiological physics and radiological dosimetry. *Wiley, New York*.

BAILEY, D., KUMARASWAMY, L. & PODGORSAK, M. 2010. A fully electronic intensity-modulated radiation therapy quality assurance (IMRT QA) process implemented in a network comprised of independent treatment planning, record and verify, and delivery systems. *Radiology and oncology,* 44**,** 124-130.

BALDOCK, C., BURFORD, R., BILLINGHAM, N., WAGNER, G., PATVAL, S., BADAWI, R. & KEEVIL, S. 1999. Experimental procedure for the manufacture and calibration of polyacrylamide gel (PAG) for magnetic resonance imaging (MRI) radiation dosimetry. *Physics in medicine and biology,* 43**,** 695.

BALDOCK, C., DEENE, Y. D., DORAN, S., IBBOTT, G., JIRASEK, A., LEPAGE, M., MCAULEY, K. B., OLDHAM, M. & SCHREINER, L. J. 2010. Polymer gel dosimetry. *Physics in Medicine and Biology,* 55**,** R1-R63.

BARENDSEN, G. 1982. Dose fractionation, dose rate and iso-effect relationships for normal tissue responses. *International Journal of Radiation Oncology* Biology* Physics,* 8**,** 1981-1997.

BARRON, J., FLEET, D. & BEAUCHEMIN, S. 1997. Performance of optical flow techniques. *Int J Computer Vision,* 12**,** 43-77.

BARRON, J. L., FLEET, D. J. & BEAUCHEMIN, S. 1994. Performance of optical flow techniques. *International Journal of Computer Vision,* 12**,** 43-77.

BENTZEN, S., CONSTINE, L., DEASY, J. O., EISBRUCH, A., JACKSON, A., MARKS, L., TEN HAKEN, R. & YORKE, E. 2010. Quantitative analyses of normal tissue effects in the clinic (QUANTEC): An introduction to the scientific issues. *Int. J. Radiat. Oncol. Biol. Phys.,* 76**,** S3-9.

BERSON, A. M., EMERY, R., RODRIGUEZ, L., RICHARDS, G. M., NG, T., SANGHAVI, S. & BARSA, J. 2004. Clinical experience using respiratory gated radiation therapy: comparison of free-breathing and breath-hold techniques. *International Journal of Radiation Oncology* Biology* Physics,* 60**,** 419-426.

BLACKWELL, C. R., COURSEY, B. M., GALL, K. P., GALVIN, J. M., MCLAUGHLIN, W. L., MEIGOONI, A. S., NATH, R., RODGERS, J. E. & SOARES, C. G. 1998.

Radiochromic film dosimetry: recommendations of AAPM radiation therapy committee task group 55. *Medical Physics,* 25**,** 2093.

BLEEHEN, N. & STENNING, S. 1991. A Medical Research Council trial of two radiotherapy doses in the treatment of grades 3 and 4 astrocytoma. The Medical Research Council Brain Tumour Working Party. *British journal of cancer,* 64**,** 769.

BLOMGREN, H., LAX, I., NÄSLUND, I. & SVANSTRÖM, R. 1995. Stereotactic high dose fraction radiation therapy of extracranial tumors using an accelerator: clinical experience of the first thirty-one patients. *Acta Oncologica,* 34**,** 861-870.

BOGUCKI, T., MURPHY, W., BAKER, C., PIAZZA, S. & HAUS, A. 1997. Processor quality control in laser imaging systems. *Medical Physics,* 24**,** 581.

BOMFORD, C. & KUNKLER, I. 2003. Walter and Miller's Textbook of Radiotherapy, Radiation Physics, Therapy and Oncology. Churchill Livingstone. Elsevier Science Limited.

BOOKSTEIN, F. L. 1989. Principal Warps: Thin-Plate Splines and the Decomposition of Deformations. *IEEE Transactions on Pattern Analysis and Machine Intelligence,* 11**,** 567-585.

BOSI, S., NASERI, P., PURAN, A., DAVIES, J. & BALDOCK, C. 2007. Initial investigation of a novel light-scattering gel phantom for evaluation of optical CT scanners for radiotherapy gel dosimetry. *Physics in Medicine and Biology,* 52**,** 2893-2903.

BOSI, S. G., BROWN, S., SARABIPOUR, S., DE DEENE, Y. & BALDOCK, C. 2009. Modelling optical scattering artefacts for varying pathlength in a gel dosimeter phantom. *Physics in Medicine and Biology,* 54**,** 275-283.

BRINDHA, S., VENNING, A., HILL, B. & BALDOCK, C. 2004. Experimental study of attenuation properties of normoxic polymer gel dosimeters. *Physics in medicine and biology,* 49**,** N353.

BROCK, K., MCSHAN, D., TEN HAKEN, R., HOLLISTER, S., DAWSON, L. & BALTER, J. 2003. Inclusion of organ deformation in dose calculations. *Medical Physics,* 30**,** 290-295.

BRUHN, A., WEICKERT, J. & SCHNORR, C. 2005a. Lucas/Kanade meets Horn/Schunck: Combining local and global optic flow methods. *Int J Computer Vision,* 61**,** 211-231.

BRUHN, A., WEICKERT, J. & SCHNÖRR, C. 2005b. Lucas/Kanade meets Horn/Schunck: Combining local and global optic flow methods. *International Journal of Computer Vision,* 61**,** 211-231.

BRYAN, P., CUSTAR, S., HAAGA, J. & BALSARA, V. 1984. Respiratory movement of the pancreas: an ultrasonic study. *Journal of Ultrasound in Medicine,* 3**,** 317-320.

BUCCIOLINI, M., BUONAMICI, F. B., MAZZOCCHI, S., DE ANGELIS, C., ONORI, S. & CIRRONE, G. A. P. 2003. Diamond detector versus silicon diode and ion chamber in photon beams of different energy and field size. *Medical Physics,* 30**,** 2149.

BUCHALI, A., KOSWIG, S., DINGES, S., ROSENTHAL, P., SALK, J., LACKNER, G., BÖHMER, D., SCHLENGER, L. & BUDACH, V. 1999. Impact of the filling status of the bladder and rectum on their integral dose distribution and the movement of the uterus in the treatment planning of gynaecological cancer. *Radiotherapy and Oncology,* 52**,** 29-34.

CEBERG, S., KARLSSON, A., GUSTAVSSON, H., WITTGREN, L. & BÄCK, S. Å. J. 2008. Verification of dynamic radiotherapy: the potential for 3D dosimetry under respiratory-like motion using polymer gel. *Physics in Medicine and Biology,* 53**,** N387-N396.

CHANG, D., SWAMINATH, A., KOZAK, M., WEINTRAUB, J., KOONG, A., KIM, J., DINNIWELL, R., BRIERLEY, J., KAVANAGH, B., DAWSON, L. & SCHEFTER, T. 2011. Stereotactic body radiotherapy for colorectal liver metastases: A pooled analysis. *Cancer,* 117**,** 4060-4069.

CHANG, J., LEE, D. & SUH, T. 2009. Development of a Deformable Lung Phantom for the Evaluation of Deformable Registration. *Journal of Applied Clinical Medical Physics,* 11**,** 281-286.

CHANG, J., SUH, T. & LEE, D. 2010. Development of a deformable lung phantom for the evaluation of deformable registration. *J. Appl. Clin. Med. Phys.,* 11**,** 281-286.

CHENG, C. W. & DAS, I. J. 1996. Dosimetry of high energy photon and electron beams with CEA films. *Medical Physics,* 23**,** 1225.

CHERPAK, A., SERBAN, M., SEUNTJENS, J. & CYGLER, J. 2010. 4D dose-position verification in radiation therapy using the RADPOS system in a deformable lung phantom. *Med Phys,* 38**,** 179-187.

CHERPAK, A., SERBAN, M., SEUNTJENS, J. & CYGLER, J. E. 2011. 4D dose-position verification in radiation therapy using the RADPOS system in a deformable lung phantom. *Medical physics,* 38**,** 179-187.

COLVILL, E., POULSEN, P. R., BOOTH, J., O'BRIEN, R., NG, J. & KEALL, P. 2014. DMLC tracking and gating can improve dose coverage for prostate VMAT. *Medical physics,* 41**,** 091705.

COSELMON, M. M., BALTER, J. M., MCSHAN, D. L. & KESSLER, M. L. 2004. Mutual information based CT registration of the lung at exhale and inhale breathing states using thin-plate splines. *Medical physics,* 31**,** 2942-2948.

DAVIS, B., FOSKEY, M., ROSENMAN, J., GOYAL, L., CHANG, S. & JOSHI, S. 2005. Automatic segmentation of intra-treatment CT images for adaptive radiation therapy of the prostate. *Medical Image Computing and Computer-Assisted Intervention***,** 442-450.

DAWSON, L. A., ECCLES, C. & CRAIG, T. 2006. Individualized image guided iso-NTCP based liver cancer SBRT. *Acta Oncologica,* 45**,** 856-864.

DAWSON, L. A., NORMOLLE, D., BALTER, J. M., MCGINN, C. J., LAWRENCE, T. S. & TEN HAKEN, R. K. 2002. Analysis of radiation-induced liver disease using the Lyman NTCP model. *International Journal of Radiation Oncology* Biology* Physics,* 53**,** 810-821.

DE DEENE, Y. Fundamentals of MRI measurements for gel dosimetry. Journal of Physics: Conference Series, 2004. IOP Publishing, 87.

DE DEENE, Y., HANSELAER, P., DE WAGTER, C., ACHTEN, E. & DE NEVE, W. 2000. An investigation of the chemical stability of a monomer/polymer gel dosimeter. *Physics in Medicine and Biology,* 45**,** 859.

DE DEENE, Y., HURLEY, C., VENNING, A., VERGOTE, K., MATHER, M., HEALY, B. & BALDOCK, C. 2002. A basic study of some normoxic polymer gel dosimeters. *Physics in medicine and biology,* 47**,** 3441.

DE DEENE, Y., VERGOTE, K., CLAEYS, C. & DE WAGTER, C. 2006. The fundamental radiation properties of normoxic polymer gel dosimeters: a comparison between a methacrylic acid based gel and acrylamide based gels. *Physics in medicine and biology,* 51**,** 653.

DE POOTER, J. A., WUNDERINK, W., MÉNDEZ ROMERO, A., STORCHI, P. R. & HEIJMEN, B. J. 2007. PTV dose prescription strategies for SBRT of metastatic liver tumours. *Radiotherapy and Oncology,* 85**,** 260-266.

DEASY, J. O., BLANCO, A. I. & CLARK, V. H. 2003. CERR: a computational environment for radiotherapy research. *Medical physics,* 30**,** 979-985.

DEASY, J. O., MAYO, C. S. & ORTON, C. G. 2015. Treatment planning evaluation and optimization should be biologically and not dose/volume based. *Medical physics,* 42**,** 2753.

DEDEENE, Y., VERGOTE, K., CLAEYS, C. & DEWAGTER, C. 2006. Three dimensional radiation dosimetry in lung-equivalent regions by use of a radiation sensitive gel foam: Proof of principle. *Med Phys,* 33**,** 2586-2597.

DEENE, Y. D., VERGOTE, K., CLAEYS, C. & WAGTER, C. D. 2006. The fundamental radiation properties of normoxic polymer gel dosimeters: a comparison between a methacrylic acid based gel and acrylamide based gels. *Physics in medicine and biology,* 51**,** 653-673.

DORAN, S. J. & KRSTAJI, N. The history and principles of optical computed tomography for scanning 3-D radiation dosimeters. 2006. IOP Publishing, 45-57.

DUAN, J., SHEN, S., FIVEASH, J. B., BREZOVICH, I. A., POPPLE, R. A. & PAREEK, P. N. 2003. Dosimetric effect of respiration-gated beam on IMRT delivery. *Medical Physics,* 30**,** 2241.

DUAN, J., SHEN, S., FIVEASH, J. B., POPPLE, R. A. & BREZOVICH, I. A. 2006. Dosimetric and radiobiological impact of dose fractionation on respiratory motion induced IMRT delivery errors: A volumetric dose measurement study. *Medical physics,* 33**,** 1380-1387.

DUGGAN, D. M., DING, G. X., COFFEY, C. W., KIRBY, W., HALLAHAN, D. E., MALCOLM, A. & LU, B. 2007. Deep-inspiration breath-hold kilovoltage cone-beam CT for setup of stereotactic body radiation therapy for lung tumors: initial experience. *Lung Cancer,* 56**,** 77-88.

DUNN, L., KRON, T., TAYLOR, M. L. & FRANICH, R. D. 2012. A phantom for testing of 4D-CT for radiotherapy of small lesions. *Medical Physics,* Accepted.

ECCLES, C., DAWSON, L., MOSELEY, J. & BROCK, K. 2011. Interfraction liver shape variability and impact on GTV position during liver stereotactic radiotherapy using abdominal compression. *Int. J. Radiat. Oncol. Biol. Phys.,* 80**,** 938-946.

EMAMI, B., LYMAN, J., BROWN, A., COIA, L., GOITEIN, M., MUNZENRIDER, J., SHANK, B., SOLIN, L. & WESSON, M. 1991. Tolerance of normal tissue to therapeutic irradiation. *Int. J. Radiat. Oncol. Biol. Phys.,* 21**,** 109-122.

EZZELL, G. A., BURMEISTER, J. W., DOGAN, N., LOSASSO, T. J., MECHALAKOS, J. G., MIHAILIDIS, D., MOLINEU, A., PALTA, J. R., RAMSEY, C. R. & SALTER, B. J. 2009. IMRT commissioning: multiple institution planning and dosimetry comparisons, a report from AAPM Task Group 119. *Medical physics,* 36**,** 5359-5373.

FENG, M., BALTER, J., NORMOLLE, D., ADUSUMILLI, S., CAO, Y., CHENEVERT, T. & BEN-JOSEF, E. 2009. Characterisation of pancreatic tumour motion using cine-MRI: Surrogates for tumour position should be used with caution. *Int. J. Radiat. Oncol. Biol. Phys.,* 74**,** 885-891.

FLAMPOURI, S., JIANG, S. B., SHARP, G. C., WOLFGANG, J., PATEL, A. A. & CHOI, N. C. 2006. Estimation of the delivered patient dose in lung IMRT treatment based on deformable registration of 4D-CT data and Monte Carlo simulations. *Physics in medicine and biology,* 51**,** 2763.

FONG, P. M., KEIL, D. C., DOES, M. D. & GORE, J. C. 2001. Polymer gels for magnetic resonance imaging of radiation dose distributions at normal room atmosphere. *Physics in medicine and biology,* 46**,** 3105.

FORNEFETT, M., ROHR, K. & STIEHL, H. S. 2001. Radial basis functions with compact support for elastic registration of medical images. *Image and Vision Computing,* 19**,** 87-96.

FOWLER, J. 1989a. The linear-quadratic formula and progress in fractionated radiotherapy: A review. *Br J Radiol,* 62**,** 679-694.

FOWLER, J. F. 1989b. The linear-quadratic formula and progress in fractionated radiotherapy. *British Journal of Radiology,* 62**,** 679-694.

GONZÁLEZ, D., MENTEN, J., BOSCH, D., VAN DER SCHUEREN, E., TROOST, D., HULSHOF, M. & BERNIER, J. 1994. Accelerated radiotherapy in glioblastoma multiforme: a dose searching prospective study. *Radiotherapy and Oncology,* 32**,** 98-105.

GOODHEAD, D. 1994. Initial events in the cellular effects of ionizing radiations: clustered damage in DNA. *International Journal of Radiation Biology,* 65**,** 7-17.

GOODMAN, K., KAVANAGH, B., MATUREN, K., ZHANG, Z., MO, Q. & YANG, G. 2010. Dose-escalation study of single-fraction stereotactic body radiotherapy for liver malignancies. *International Journal of Radiation Oncology* Biology* Physics,* 78**,** 486-493.

GORDON, S. A. 1957. I. The effects of ionizing radiation on plants: biochemical and physiological aspects. *Quarterly Review of Biology*, 3-14.

GORE, J. & KANG, Y. 1984. Measurement of radiation dose distributions by nuclear magnetic resonance (NMR) imaging. *Physics in medicine and biology,* 29**,** 1189.

GORE, J., RANADE, M., MARYANSKI, M. & SCHULZ, R. 1999. Radiation dose distributions in three dimensions from tomographic optical density scanning of polymer gels: I. Development of an optical scanner. *Physics in Medicine and Biology,* 41**,** 2695.

GORJIARA, T., HILL, R., KIM, J. H., KUNCIC, Z., ADAMOVICS, J. & BALDOCK, C. Study of dosimetric water equivalency of PRESAGE® for megavoltage and kilovoltage x-ray beams. Journal of Physics: Conference Series, 2010. IOP Publishing, 012053.

GOWDA, R. V., HENK, J. M., MAIS, K. L., SYKES, A. J., SWINDELL, R. & SLEVIN, N. J. 2003. Three weeks radiotherapy for T1 glottic cancer: the Christie and Royal Marsden Hospital Experience. *Radiotherapy and oncology,* 68**,** 105-111.

GREER, P. B. 2007. Off-axis dose response characteristics of an amorphous silicon electronic portal imaging device. *Medical Physics,* 34**,** 3815-3824.

GREER, P. B. & POPESCU, C. C. 2003. Dosimetric properties of an amorphous silicon electronic portal imaging device for verification of dynamic intensity modulated radiation therapy. *Medical Physics,* 30**,** 1618-1627.

GRÉGOIRE, V. & MACKIE, T. 2011. State of the art on dose prescription, reporting and recording in Intensity-Modulated Radiation Therapy (ICRU report No. 83). *Cancer/Radiothérapie*.

GRUSELL, E. & RIKNER, G. 2000. Evaluation of temperature effects in p-type silicon detectors. *Physics in Medicine and Biology,* 31**,** 527.

GUCKENBERGER, M., SWEENEY, R., WILBERT, J., KRIEGER, T., RICHTER, A. & BAIER, K. 2008. Image-guided radiotherapy for liver cancer using respiratory-correlated computed tomography and cone-beam computed tomography. *Int. J. Radiat. Oncol. Biol. Phys.,* 71**,** 297-304.

GUCKENBERGER, M., WILBERT, J., KRIEGER, T., RICHTER, A., BAIER, K., MEYER, J. & FLENTJE, M. 2007. Four-dimensional treatment planning for stereotactic body radiotherapy. *International Journal of Radiation Oncology* Biology* Physics,* 69**,** 276-285.

GUERRERO, T., ZHANG, G., SEGARS, W., HUANG, T. C., BILTON, S., IBBOTT, G., DONG, L., FORSTER, K. & LIN, K. P. 2005. Elastic image mapping for 4-D dose estimation in thoracic radiotherapy. *Radiation protection dosimetry,* 115**,** 497.

GUIMOND, A., ROCHE, A., AYACHE, N. & MEUNIER, J. 2001. Three-dimensional multimodal brain warping using the Demons algorithm and adaptive intensity corrections. *IEEE Transactions on Medical Imaging,* 20**,** 58-69.

GUM, F., SCHERER, J., BOGNER, L., SOLLEDER, M., RHEIN, B. & BOCK, M. 2002. Preliminary study on the use of an inhomogeneous anthropomorphic Fricke gel phantom and 3D magnetic resonance dosimetry for verification of IMRT treatment plans. *Physics in Medicine and Biology,* 47**,** N67.

GUO, P., ADAMOVICS, J. & OLDHAM, M. 2006. A practical three-dimensional dosimetry system for radiation therapy. *Medical Physics,* 33**,** 3962.

GUPTA, B. & NILEKANI, S. 1998. Ferrous ion oxidations by H, OH and H_2O_2 in aerated FBX dosimetry system. *Radiation Physics and Chemistry,* 53**,** 643-650.

HAGEN, U. 1989. Biochemical aspects of radiation biology. *Cellular and Molecular Life Sciences,* 45**,** 7-12.

HIGGINS, P., ALAEI, P., GERBI, B. & DUSENBERY, K. 2003. In vivo diode dosimetry for routine quality assurance in IMRT. *Medical Physics,* 30**,** 3118.

HIGGINS, P. D., SIBATA, C. H., SISKIND, L. & SOHN, J. W. 1995. Deconvolution of detector size effect for small field measurement. *Medical Physics,* 22**,** 1663.

HILTS, M., AUDET, C., DUZENLI, C. & JIRASEK, A. 2000. Polymer gel dosimetry using x-ray computed tomography: a feasibility study. *Physics in Medicine and Biology,* 45**,** 2559-2571.

HILTS, M. & DUZENLI, C. 2004. Image filtering for improved dose resolution in CT polymer gel dosimetry. *Medical physics,* 31**,** 39.

HOBAN, P., HEYDARIAN, M., BECKHAM, W. & BEDDOE, A. 1999. Dose rate dependence of a PTW diamond detector in the dosimetry of a 6 MV photon beam. *Physics in Medicine and Biology,* 39**,** 1219.

HORN, B. & SCHUNCK, B. 1981a. Determining optical flow. *Artif. Intell.,* 17**,** 186-203.

HORN, B. K. P. & SCHUNCK, B. G. 1981b. Determining optical flow. *Artificial intelligence,* 17**,** 185-203.

HOWELL, R. M., SMITH, I. & JARRIO, C. S. 2008. Establishing action levels for EPID-based QA for IMRT. *J. Appl. Clin. Med. Phys,* 9**,** 16-25.

HUANG, T., LIANG, J., DILLING, T., WU, T. & ZHANG, G. 2010a. Four-dimensional dosimetry validation and study in lung radiotherapy using deformable image registration and Monte Carlo techniques. *Radiat. Oncol.,* 5**,** 45.

HUANG, T. C., LIANG, J. A., DILLING, T., WU, T. H. & ZHANG, G. 2010b. Four-dimensional dosimetry validation and study in lung radiotherapy using deformable image registration and Monte Carlo techniques. *Radiation Oncology,* 5**,** 45.

HUGO, G. D., AGAZARYAN, N. & SOLBERG, T. D. 2002. An evaluation of gating window size, delivery method, and composite field dosimetry of respiratory-gated IMRT. *Medical Physics,* 29**,** 2517.

HÜTTERMANN, J., KOEHNLEIN, W. & TEOULE, R. 1978. Effects of ionizing radiation of DNA: physical, chemical, and biological aspects.

ICRP 2007. ICRP Publication 103. *Ann. ICRP,* 37**,** 2.

ICRU 1978. ICRU Report 29: Dose Specification for Reporting External Beam Therapy with Photons and Electrons. Washington, DC: International Commission on Radiation Units and Measurements.

ICRU 1993. ICRU Report 50: Prescribing, Recording and Reporting Photon Beam Therapy. Bethesda, MD: International Commission on Radiation Units and Measurements.

ICRU 1999. ICRU Report 62: Prescribing, Recording and Reporting Photon Beam Therapy (Supplement to ICRU Report 50). Bethesda, MD: International Commission on Radiation Units and Measurements.

ISLAM, K., DEMPSEY, J. F., RANADE, M. K., MARYANSKI, M. J. & LOW, D. A. 2003. Initial evaluation of commercial optical CT-based 3D gel dosimeter. *Medical Physics,* 30**,** 2159.

JACKSON, A., MARKS, L., BENTZEN, S., EISBRUCH, A., YORKE, E., TEN HAKEN, R., CONSTINE, L. & DEASY, J. 2010a. The lessons of QUANTEC: Recommendations for the reporting and gathering data on dose-volume dependencies of treatment outcome. *Int. J. Radiat. Oncol. Biol. Phys.,* 76**,** S155-160.

JACKSON, A., MARKS, L. B., BENTZEN, S. M., EISBRUCH, A., YORKE, E. D., TEN HAKEN, R. K., CONSTINE, L. S. & DEASY, J. O. 2010b. The lessons of QUANTEC: recommendations for reporting and gathering data on dose–volume dependencies of treatment outcome. *International Journal of Radiation Oncology* Biology* Physics,* 76**,** S155-S160.

JANSSENS, G., DE XIVRY, J., FEKKES, S., DEKKER, A., MACQ, B., LAMBIN, P. & VAN ELMPT, W. 2009a. Evaluation of nonrigid registration models for interfraction dose accumulation in radiotherapy. *Med Phys,* 36**,** 4268-4276.

JANSSENS, G., DE XIVRY, J. O., FEKKES, S., DEKKER, A., MACQ, B., LAMBIN, P. & VAN ELMPT, W. 2009b. Evaluation of nonrigid registration models for interfraction dose accumulation in radiotherapy. *Medical Physics,* 36**,** 4268-4276.

JANSSENS, G., ORBAN DE XIVRY, J., FEKKES, S., DEKKER, A., MACQ, B., LAMBIN, P. & VAN ELMPT, W. 2009c. Evaluation of nonrigid registration models for interfraction dose accumulation in radiotherapy. *Medical Physics,* 36**,** 4268-76.

JENKINS, P., SALMON, C. & MANNION, C. 2005a. Analysis of the movement of calcified lymph nodes during breathing. *International Journal of Radiation Oncology* Biology* Physics,* 61**,** 329-334.

JENKINS, P., SALMON, C. & MANNION, C. 2005b. Analysis of the movement of calcified lymph nodes during breathing. *Int. J. Radiat. Oncol. Biol. Phys.,* 61**,** 329-334.

JIN, L., WANG, L., LI, J., LUO, W., FEIGENBERG, S. & MA, C. 2007. Investigation of optimal beam margins for stereotactic radiotherapy of lung-cancer using Monte Carlo dose calculations. *Physics in Medicine and Biology,* 52**,** 3549-3561.

JIRASEK, A., HILTS, M., SHAW, C. & BAXTER, P. 2006. Investigation of tetrakis hydroxymethyl phosphonium chloride as an antioxidant for use in x-ray computed tomography polyacrylamide gel dosimetry. *Physics in medicine and biology,* 51**,** 1891.

JUANG, T., DAS, S., ADAMOVICS, J., BENNING, R. & OLDHAM, M. 2013. On the need for comprehensive validation of deformable image registration, investigated with a novel 3-dimensional deformable dosimeter. *International Journal of Radiation Oncology* Biology* Physics,* 87**,** 414-421.

JUNG, S. H., YOON, S. M., PARK, S. H., CHO, B., PARK, J. W., JUNG, J., PARK, J.-H., KIM, J. H. & DO AHN, S. 2013. Four-dimensional dose evaluation using deformable image registration in radiotherapy for liver cancer. *Medical physics,* 40**,** 011706.

JURSINIC, P. A. & NELMS, B. E. 2003. A 2-D diode array and analysis software for verification of intensity modulated radiation therapy delivery. *Medical Physics,* 30**,** 870.

KAIRN, T., TAYLOR, M., CROWE, S., DUNN, L., FRANICH, R., KENNY, J., KNIGHT, R. & TRAPP, J. 2012. Monte Carlo verification of gel dosimetry measurements for stereotactic radiotherapy. *Physics in Medicine and Biology*.

KARIM, A. B., MAAT, B., HATLEVOLL, R., MENTEN, J., RUTTEN, E. H., THOMAS, D. G., MASCARENHAS, F., HORIOT, J. C., PARVINEN, L. M. & VAN REIJN, M. 1996. A randomized trial on dose-response in radiation therapy of low-grade cerebral glioma: European Organization for Research and Treatment of Cancer (EORTC) Study 22844. *International Journal of Radiation Oncology* Biology* Physics,* 36**,** 549-556.

KASHANI, R., HUB, M., BALTER, J., KESSLER, M., DONG, L., ZHANG, L., XING, L., XIE, Y., HAWKES, D., SCHNABEL, J., MCCLELLAND, J., JOSHI, S., CHEN, Q. & LU, W. 2008a. Objective assessment of deformable image registration in radiotherapy: A multi institution study. *Med Phys,* 35**,** 5944-5953.

KASHANI, R., HUB, M., BALTER, J. M., KESSLER, M. L., DONG, L., ZHANG, L., XING, L., XIE, Y., HAWKES, D. & SCHNABEL, J. A. 2008b. Objective assessment of deformable image registration in radiotherapy: A multi-institution study. *Medical Physics,* 35**,** 5944-5953.

KASHANI, R., HUB, M., BALTER, J. M., KESSLER, M. L., DONG, L., ZHANG, L., XING, L., XIE, Y., HAWKES, D. & SCHNABEL, J. A. 2008c. Objective assessment of deformable image registration in radiotherapy: A multi-institution study. *Medical physics,* 35**,** 5944.

KASHANI, R., HUB, M., KESSLER, M. L. & BALTER, J. M. 2007a. Technical note: a physical phantom for assessment of accuracy of deformable alignment algorithms. *Medical physics,* 34**,** 2785-2788.

KASHANI, R., LAM, K., LITZENBERG, D. & BALTER, J. 2007b. Technical note: A deformable phantom for dynamic modeling in radiation therapy. *Med Phys,* 34**,** 199-201.

KASHANI, R., LAM, K., LITZENBERG, D. & BALTER, J. 2007c. Technical note: A deformable phantom for dynamic modeling in radiation therapy. *Medical physics,* 34**,** 199-201.

KAUS, M. & BROCK, K. 2007. Deformable Image Registration for Radiation Therapy Planning: Algorithms and Applications. *Biomechanical Systems Technololgy.* Cornelius T Leondes: World Scientific Publishing Co. Pte. Ltd.

KAVANAGH, B., SCHEFTER, T., CARDENES, H., STIEBER, V., RABEN, D., TIMMERMAN, R., MCCARTER, M., BURRI, S., NEDZI, L., SAWYER, T. & GASPAR, L. 2006. Interim analysis of a prospective phase I/II trial of SBRT for liver metastases. *Acta Oncologica,* 45**,** 848-855.

KEALL, P. 2004. 4-dimensional computed tomography imaging and treatment planning. *Seminars in Radiation Oncology,* 14**,** 81-90.

KEALL, P. & BALDOCK, C. 1999. A theoretical study of the radiological properties and water equivalence of Fricke and polymer gels used for radiation dosimetry. *Australasian physical & engineering sciences in medicine/supported by the Australasian College of Physical Scientists in Medicine and the Australasian Association of Physical Sciences in Medicine,* 22**,** 85-91.

KEALL, P. J., JOSHI, S., VEDAM, S. S., SIEBERS, J. V., KINI, V. R. & MOHAN, R. 2005. Four-dimensional radiotherapy planning for DMLC-based respiratory motion tracking. *Medical Physics,* 32**,** 942-951.

KEALL, P. J., MAGERAS, G. S., BALTER, J. M., EMERY, R. S., FORSTER, K. M., JIANG, S. B., KAPATOES, J. M., LOW, D. A., MURPHY, M. J. & MURRAY, B. R. 2006. The management of respiratory motion in radiation oncology report of AAPM Task Group 76. *Medical Physics,* 33**,** 3874-3900.

KEALL, P. J., NG, J. A., O'BRIEN, R., COLVILL, E., HUANG, C.-Y., POULSEN, P. R., FLEDELIUS, W., JUNEJA, P., SIMPSON, E. & BELL, L. 2015. The first clinical treatment with kilovoltage intrafraction monitoring (KIM): A real-time image guidance method. *Medical physics,* 42**,** 354-358.

KERKHOF, E., VAN DER PUT, R., RAAYMAKERS, B., VAN DER HEIDE, U., VAN VULPEN, M. & LAGENDIJK, J. 2008a. Variation in target and rectum dose due to prostate deformation: An assessment by repeated MR imaging and treatment planning. *Physics in Medicine and Biology,* 53**,** 5623-5634.

KERKHOF, E., VAN DER PUT, R., RAAYMAKERS, B., VAN DER HEIDE, U., VAN VULPEN, M. & LAGENDIJK, J. 2008b. Variation in target and rectum doses due to prostate deformation: An assessment by repeated MR imaging and treatment planning. *Physics in Medicine and Biology,* 53**,** 5623-5634.

KIRBY, N., CHUANG, C. & POULIOT, J. 2011. A two-dimensional deformable phantom for quantitatively verifying deformation algorithms. *Medical physics,* 38**,** 4583-4586.

KIRBY, N., CHUANG, C., UEDA, U. & POULIOT, J. 2013. The need for application-based adaptation of deformable image registration. *Medical Physics,* 40**,** 011702.

KLEIN, G. & HUESMAN, R. 2000. Elastic material model mismatch effects in deformable motion estimation. *IEEE Transactions on Nuclear Science,* 47**,** 1000-1005.

KOHLRAUSCH, J., ROHR, K. & STIEHL, S. 2005. A New Class of Elastic Body Splines for Nonrigid Registration of Medical Images. *Journal of Mathematical Imaging and Vision,* 19**,** 253–280.

KONG, F., HAYMAN, J., GRIFFITH, K., KALEMKERIAN, G., ARENBERG, D., LYONS, S., TURRISI, A., LICHTER, A., FRAASS, B., LAWRENCE, T. & TEN HAKEN, R. 2006. Final toxicity results of a radiation-dose escalation study in patients with non-small-cell lunc cancer (NSCLC): Predictors for radiation pneumonitis and fibrosis. *Int. J. Radiat. Oncol. Biol. Phys.,* 65**,** 1075-1086.

KONG, F., PAN, C., EISBRUCH, A. & TEN HAKEN, R. 2007. Physical models and simpler dosimetric descriptors of radiation late toxicity. *Semin. Rad. Onc.,* 11**,** 108-120.

KORREMAN, S. S., PEDERSEN, A. N., NØTTRUP, T. J., SPECHT, L. & NYSTRÖM, H. 2005. Breathing adapted radiotherapy for breast cancer: comparison of free breathing gating with the breath-hold technique. *Radiotherapy and oncology: journal of the European Society for Therapeutic Radiology and Oncology,* 76**,** 311.

KRON, T. 1994. Thermoluminescence dosimetry and its applications in medicine--Part 1: Physics, materials and equipment. *Australasian physical & engineering sciences in medicine/supported by the Australasian College of Physical Scientists in Medicine and the Australasian Association of Physical Sciences in Medicine,* 17**,** 175.

KRON, T., WONG, J., ROLFO, A., PHAM, D., CRAMB, J. & FOROUDI, F. 2010. Adaptive radiotherapy for bladder cancer reduces integral dose despite daily volumetric imaging. *Radiotherapy and Oncology,* 97**,** 485-487.

KUBO, H. D. & WANG, L. 2000. Compatibility of Varian 2100C gated operations with enhanced dynamic wedge and IMRT dose delivery. *Medical Physics,* 27**,** 1732.

KUPELIAN, P. A., CIEZKI, J., REDDY, C. A., KLEIN, E. A. & MAHADEVAN, A. 2008. Effect of increasing radiation doses on local and distant failures in patients with localized prostate cancer. *International Journal of Radiation Oncology* Biology* Physics,* 71**,** 16-22.

KUTCHER, G. & BURMAN, C. 1989. Calculation of complication probability factors for non-uniform normal tissue irradiation: the effective volume method. *Int. J. Radiat. Oncol. Biol. Phys.,* 16**,** 1623-1630.

LAGERWAARD, F. J., VAN SORNSEN, K. J. R., NIJSSEN-VISSER, M., SCHUCHHARD-SCHIPPER, R. H., OEI, S. S., MUNNE, A. & SENAN, S. 2001. Multiple" slow" CT scans for incorporating lung tumor mobility in radiotherapy planning. *International Journal of Radiation Oncology, Biology, Physics,* 51**,** 932.

LANGEN, K. & JONES, D. 2001. Organ motion and its management. *International Journal of Radiation Oncology* Biology* Physics,* 50**,** 265-278.

LANGEN, K., MEEKS, S., POOLE, D., WAGNER, T., WILLOUGHBY, T., ZEIDAN, O., KUPELIAN, P., RUCHALA, K. & OLIVERA, G. 2005. Evaluation of a diode array for QA measurements on a helical tomotherapy unit. *Medical Physics,* 32**,** 3424.

LAUB, W. U., KAULICH, T. W. & NÜSSLIN, F. 1999. A diamond detector in the dosimetry of high-energy electron and photon beams. *Physics in Medicine and Biology,* 44**,** 2183.

LAUB, W. U. & WONG, T. 2003. The volume effect of detectors in the dosimetry of small fields used in IMRT. *Medical Physics,* 30**,** 341.

LAX, I., BLOMGREN, H., NÄSLUND, I. & SVANSTRÖM, R. 1994. Stereotactic radiotherapy of malignancies in the abdomen: methodological aspects. *Acta Oncologica,* 33**,** 677-683.

LEE, M., KIM, J., DINNIWELL, R., BRIERLEY, J., LOCKWOOD, G., WONG, R., CUMMINGS, B., RINGASH, J., TSE, R., KNOX, J. & DAWSON, L. 2009. Phase I study of individualised stereotactic body radiotherapy of liver metastases. *J Clin Oncol,* 27**,** 1585-1591.

LEE, S. P., LEU, M. Y., SMATHERS, J. B., MCBRIDE, W. H., PARKER, R. G. & WITHERS, H. R. 1995. Biologically effective dose distribution based on the linear quadratic model and its clinical relevance. *International Journal of Radiation Oncology* Biology* Physics,* 33**,** 375-389.

LEPAGE, M., JAYASAKERA, P., BÄCK, S. Å. J. & BALDOCK, C. 2001a. Dose resolution optimization of polymer gel dosimeters using different monomers. *Physics in medicine and biology,* 46**,** 2665.

LEPAGE, M. & JORDAN, K. 3D dosimetry fundamentals: gels and plastics. Journal of Physics: Conference Series, 2010. IOP Publishing, 012055.

LEPAGE, M., WHITTAKER, A., RINTOUL, L. & BALDOCK, C. 2000. 13C-NMR, 1H-NMR, and FT-Raman study of radiation-induced modifications in radiation dosimetry polymer gels. *Journal of applied polymer science,* 79**,** 1572-1581.

LEPAGE, M., WHITTAKER, A. K., RINTOUL, L., BÄCK, S. Å. J. & BALDOCK, C. 2001b. The relationship between radiation-induced chemical processes and transverse relaxation times in polymer gel dosimeters. *Physics in medicine and biology,* 46**,** 1061.

LIU, H., BALTER, P., TUTT, T., CHOI, B., ZHANG, J., WANG, C., CHI, W., LUO, D., PAN, T., HUNJAN, S., STARKSCHALL, G., ROSEN, I., PRADO, K., LIAO, Z., CHANG, J., KOMAKI, R., COX, J., MOHAN, R. & DONG, L. 2007. Assessing respiratory-induced tumour motion and internal target volume using four-dimensional computed tomography for radiotherapy of lung cancer. *Int. J. Radiat. Oncol. Biol. Phys.,* 68**,** 531-540.

LOHR, F., DEBUS, J., FRANK, C., HERFARTH, K., PASTYR, O., RHEIN, B., BAHNER, M. L., SCHLEGEL, W. & WANNENMACHER, M. 1999. Noninvasive patient fixation for extracranial stereotactic radiotherapy. *International Journal of Radiation Oncology* Biology* Physics,* 45**,** 521-527.

LOPATIUK-TIRPAK, O., LANGEN, K., MEEKS, S., KUPELIAN, P., ZEIDAN, O. & MARYANSKI, M. 2008a. Performance evaluation of an improved optical computed tomography polymer gel dosimeter system for 3D dose verification of static and dynamic phantom deliveries. *Medical physics,* 35**,** 3847-3859.

LOPATIUK-TIRPAK, O., LANGEN, K., MEEKS, S., KUPELIAN, P., ZEIDAN, O. & MARYANSKI, M. 2008b. Performance evaluation of an improved optical computed tomography polymer gel dosimeter system for 3D dose verification of static and dynamic phantom deliveries. *Medical physics,* 35**,** 3847.

LOW, D., HARMS, W., MUTIC, S. & PURDY, J. 1998. A technique for the quantitative evaluation of dose distributions. *Med Phys,* 25**,** 656.

LOW, D. A., MORAN, J. M., DEMPSEY, J. F., DONG, L. & OLDHAM, M. 2011. Dosimetry tools and techniques for IMRT. *Medical Physics,* 38**,** 1313-38.

LOW, D. A., PARIKH, P., DEMPSEY, J. F., WAHAB, S. & HUQ, S. 2003. Ionization chamber volume averaging effects in dynamic intensity modulated radiation therapy beams. *Medical Physics,* 30**,** 1706.

LU, W., CHEN, M., OLIVERA, G., RUCHALA, K. & MACKIE, T. 2004a. Fast free-form deformable registration via calculus of variations. *Physics in Medicine and Biology,* 49.

LU, W., CHEN, M. L., OLIVERA, G. H., RUCHALA, K. J. & MACKIE, T. R. 2004b. Fast free-form deformable registration via calculus of variations. *Physics in Medicine and Biology,* 49**,** 3067-3087.

LU, W., CHEN, M. L., OLIVERA, G. H., RUCHALA, K. J. & MACKIE, T. R. 2004c. Fast free-form deformable registration via calculus of variations. *Physics in Medicine and Biology,* 49**,** 3067-3087.

LU, W., OLIVERA, G. H., CHEN, Q., CHEN, M. L. & RUCHALA, K. J. 2006a. Automatic re-contouring in 4D radiotherapy. *Physics in medicine and biology,* 51**,** 1077-1099.

LU, W., OLIVERA, G. H., CHEN, Q., RUCHALA, K. J., HAIMERL, J., MEEKS, S. L., LANGEN, K. M. & KUPELIAN, P. A. 2006b. Deformable registration of the planning image (kVCT) and the daily images (MVCT) for adaptive radiation therapy. *Physics in medicine and biology,* 51**,** 4357-4374.

LUCAS, B. & KANADE, T. 1981. An iterative image registration technique with an application to stereo vision. *Proceedings of imaging understanding workshop***,** 121-130.

LUCHKA, K. & PISTORIUS, S. 2001. Dosimetric investigation and portal dose image prediction using an amorphous silicon electronic portal imaging device. *Medical Physics,* 28**,** 911-924.

LYMAN, J. T. 1985. Complication probability as assessed from dose-volume histograms. *Radiation Research,* 104**,** 13-19.

MAGERAS, G. S. & YORKE, E. Deep inspiration breath hold and respiratory gating strategies for reducing organ motion in radiation treatment. Seminars in Radiation Oncology, 2004. 65.

MAHAFFY, R. E., SHIH, C. K., MACKINTOSH, F. C. & KÄS, J. 2000. Scanning Probe-Based Frequency-Dependent Microrheology of Polymer Gels and Biological Cells. *Physical Review Letters,* 85**,** 880-883.

MAINTZ, J. & VIERGEVER, M. A. 1998. A survey of medical image registration. *Medical image analysis,* 2**,** 1-36.

MARKS, L., YORKE, E., JACKSON, A., TEN HAKEN, R., CONSTINE, L., EISBRUCH, A., BENTZEN, S., NAM, J. & DEASY, J. 2010. Use of normal tissue complication models in the clinic. *Int. J. Radiat. Oncol. Biol. Phys.,* 76**,** S10-19.

MARYANSKI, M., GORE, J. & SCHULZ, R. 1994. Three-dimensional detection, dosimetry and imaging of an energy field by formation of a polymer in a gel. Google Patents.

MATHER, M. L. & BALDOCK, C. 2003. Ultrasound tomography imaging of radiation dose distributions in polymer gel dosimeters: Preliminary study. *Medical physics,* 30**,** 2140.

MATHER, M. L., WHITTAKER, A. K. & BALDOCK, C. 2002. Ultrasound evaluation of polymer gel dosimeters. *Physics in Medicine and Biology,* 47**,** 1449.

MCALEESE, J., STENNING, S., ASHLEY, S., TRAISH, D., HINES, F., SARDELL, S., GUERRERO, D. & BRADA, M. 2003. Hypofractionated radiotherapy for poor prognosis malignant glioma: matched pair survival analysis with MRC controls. *Radiotherapy and oncology,* 67**,** 177-182.

MCAULEY, K. B. Fundamentals of polymer gel dosimeters. Journal of Physics: Conference Series, 2007. IOP Publishing, 35.

METCALFE, P., HOBAN, P. & KRON, T. 1997. *The physics of radiotherapy X-rays from linear accelerators*, Medical Physics Pub.

MI, F. L., SUNG, H. W., SHYU, S. S., SU, C. C. & PENG, C. K. 2003. Synthesis and characterization of biodegradable TPP/genipin co-crosslinked chitosan gel beads. *Polymer,* 44**,** 6521-6530.

MILLER, J., FULLER, M., VINOD, S., SUCHOWERSKA, N. & HOLLOWAY, L. 2009. The significance of the choice of radiobiological (NTCP) models in treatment plan objective functions. *Aust. Phys. Eng. Sci. Med.,* 32**,** 81-87.

MILLER, R. C., BONNER, J. A. & KLINE, R. W. 1998. Impact of beam energy and field margin on penumbra at lung tumor-lung parenchyma interfaces. *International Journal of Radiation Oncology* Biology* Physics,* 41**,** 707-713.

MOERLAND, M., VAN DEN BERGH, A., BHAGWANDIEN, R., JANSSEN, W., BAKKER, C., LAGENDIJK, J. & BATTERMANN, J. 1994. The influence of respiration induced motion of the kidneys on the accuracy of radiotherapy treatment planning, a magnetic resonance imaging study. *Radiotherapy and Oncology,* 30**,** 150-154.

MOSTAAR, A., HASHEMI, B., ZAHMATKESH, M., AGHAMIRI, S. & MAHDAVI, S. 2010. A basic dosimetric study of PRESAGE: the effect of different amounts of fabricating components on the sensitivity and stability of the dosimeter. *Physics in Medicine and Biology,* 55**,** 903.

MUENCH, P. J., MEIGOONI, A. S., NATH, R. & MCLAUGHLIN, W. L. 1991. Photon energy dependence of the sensitivity of radiochromic film and comparison with silver halide film and LiF TLDs used for brachytherapy dosimetry. *Medical Physics,* 18**,** 769.

NAGATA, Y., MATSUO, Y., TAKAYAMA, K., NORIHISA, Y., MIZOWAKI, T., MITSUMORI, M., SHIBUYA, K., YANO, S., NARITA, Y. & HIRAOKA, M. 2007. Current status of stereotactic body radiotherapy for lung cancer. *International Journal of Clinical Oncology,* 12**,** 3-7.

NEHMEH, S., ERDI, Y., LING, C., ROSENZWEIG, K., SQUIRE, O., BRABAN, L., FORD, E., SIDHU, K., MAGERAS, G. & LARSON, S. 2002. Effect of respiratory gating on reducing lung motion artifacts in PET imaging of lung cancer. *Medical physics,* 29**,** 366-371.

NICHOL, A., BROCK, K., LOCKWOOD, G., MOSELEY, D., ROSEWALL, T., WARDE, P., CATTON, C. & JAFFRAY, D. 2007a. A magnetic resonance imaging study of prostate deformation relative to implanted gold fiducial markers. *Int. J. Radiat. Oncol. Biol. Phys.,* 67**,** 48-56.

NICHOL, A. M., BROCK, K. K., LOCKWOOD, G. A., MOSELEY, D. J., ROSEWALL, T., WARDE, P. R., CATTON, C. N. & JAFFRAY, D. A. 2007b. A magnetic resonance imaging study of prostate deformation relative to implanted gold fiducial markers. *International Journal of Radiation Oncology* Biology* Physics,* 67**,** 48-56.

NIEMIERKO, A. 1996. Reporting and analyzing dose distributions: A concept of equivalent uniform dose. *Med Phys,* 24**,** 103-110.

NILSSON, S., NORLÉN, B. J. & WIDMARK, A. 2004. A systematic overview of radiation therapy effects in prostate cancer. *Acta Oncologica,* 43**,** 316-381.

NIOUTSIKOU, E., SYMONDS-TAYLER, J. R. N., BEDFORD, J. L. & WEBB, S. 2006. Quantifying the effect of respiratory motion on lung tumour dosimetry with the aid of

a breathing phantom with deforming lungs. *Physics in Medicine and Biology,* 51**,** 3359-3474.

NITHIANANTHAN, S., SCHAFER, S., MIROTA, D., STAYMAN, J., ZBIJEWSKI, W., REH, D., GALLIA, G. & SIEWERDSEN, J. 2012. Extra-dimensional Demons: A method for incorporating missing tissue in deformable image registration. *Med Phys,* 39**,** 5718-5731.

NIU, C., FOLTZ, W., VELEC, M., MOSELEY, J., AL-MAYAH, A. & BROCK, K. 2012. A novel technique to enable experimental validation of deformable dose accumulation. *Med Phys,* 39**,** 765.

OKUNIEFF, P., PETERSEN, A. L., PHILIP, A., MILANO, M. T., KATZ, A. W., BOROS, L. & SCHELL, M. C. 2006. Stereotactic body radiation therapy (SBRT) for lung metastases. *Acta Oncologica,* 45**,** 808-817.

OLBERG, S., SKRETTING, A., BRULAND, O. & OLSEN, D. 2000. Dose distribution measurements by MRI of a phantom containing lung tissue equivalent compartments made of ferrous sulphate. *Physics in Medicine and Biology,* 45**,** 2761.

OLDHAM, M. 3D dosimetry by optical-CT scanning. Journal of Physics: Conference Series, 2007. IOP Publishing, 58.

OLDHAM, M., SIEWERDSEN, J. H., SHETTY, A. & JAFFRAY, D. A. 2001. High resolution gel-dosimetry by optical-CT and MR scanning. *Medical Physics,* 28**,** 1436.

OLDING, T., HOLMES, O. & SCHREINER, L. J. 2010. Cone beam optical computed tomography for gel dosimetry I: scanner characterization. *Physics in Medicine and Biology,* 55**,** 2819-2840.

OLDING, T. & SCHREINER, L. J. 2011. Cone-beam optical computed tomography for gel dosimetry II: imaging protocols. *Physics in Medicine and Biology,* 56**,** 1259-1279.

OLIVE, P. L. 1998. The Role of DNA Single- and Double-Strand Breaks in Cell Killing by Ionizing Radiation. *Radiation Research,* 150**,** S42-S51.

PAGANETTI, H., JIANG, H., ADAMS, J. A., CHEN, G. T. & RIETZEL, E. 2004. Monte Carlo simulations with time-dependent geometries to investigate effects of organ motion with high temporal resolution. *International Journal of Radiation Oncology* Biology* Physics,* 60**,** 942-950.

PAN, H., SIMPSON, D., MELL, L., MUNDT, A. & LAWSON, J. 2011. A survey of stereotactic body radiotherapy use in the United States. *Cancer,* 117**,** 4566-4572.

PEDERSEN, A. N., KORREMAN, S., NYSTRÖM, H. & SPECHT, L. 2004. Breathing adapted radiotherapy of breast cancer: reduction of cardiac and pulmonary doses using voluntary inspiration breath-hold. *Radiotherapy and Oncology,* 72**,** 53-60.

PEETERS, S. T. H., HEEMSBERGEN, W. D., VAN PUTTEN, W. L. J., SLOT, A., TABAK, H., MENS, J. W., LEBESQUE, J. V. & KOPER, P. C. M. 2005. Acute and late complications after radiotherapy for prostate cancer: results of a multicenter randomized trial comparing 68 Gy to 78 Gy. *International Journal of Radiation Oncology Biology Physics,* 61**,** 1019-1034.

PERACCHIA, G. & SALTI, C. 1981. Radiotherapy with thrice-a-day fractionation in a short overall time: clinical experiences. *International Journal of Radiation Oncology* Biology* Physics,* 7**,** 99-104.

PETOUKHOVA, A., VAN EGMOND, J., EENINK, M., WIGGENRAAD, R. & VAN SANTVOORT, J. 2011. The ArcCHECK diode array for dosimetric verification of HybridArc. *Physics in medicine and biology,* 56**,** 5411.

POLLACK, A., ZAGARS, G. K., SMITH, L. G., LEE, J. J., VON ESCHENBACH, A. C., ANTOLAK, J. A., STARKSCHALL, G. & ROSEN, I. 2000. Preliminary results of a randomized radiotherapy dose-escalation study comparing 70 Gy with 78 Gy for prostate cancer. *Journal of clinical oncology,* 18**,** 3904-3911.

REMOUCHAMPS, V. M., LETTS, N., VICINI, F. A., SHARPE, M. B., KESTIN, L. L., CHEN, P. Y., MARTINEZ, A. A. & WONG, J. W. 2003a. Initial clinical experience with moderate deep-inspiration breath hold using an active breathing control device in the treatment of patients with left-sided breast cancer using external beam radiation therapy. *International Journal of Radiation Oncology, Biology, Physics,* 56**,** 704.

REMOUCHAMPS, V. M., VICINI, F. A., SHARPE, M. B., KESTIN, L. L., MARTINEZ, A. A. & WONG, J. W. 2003b. Significant reductions in heart and lung doses using deep inspiration breath hold with active breathing control and intensity-modulated radiation therapy for patients treated with locoregional breast irradiation. *International Journal of Radiation Oncology* Biology* Physics,* 55**,** 392-406.

RICE, R., HANSEN, J., SVENSSON, G. & SIDDON, R. 2000. Measurements of dose distributions in small beams of 6 MV x-rays. *Physics in Medicine and Biology,* 32**,** 1087.

RIETZEL, E. & CHEN, G. T. Y. 2006. Deformable registration of 4D computed tomography data. *Medical Physics,* 33**,** 4423-4430.

RIETZEL, E., LIU, A. K., DOPPKE, K. P., WOLFGANG, J. A., CHEN, A. B., CHEN, G. T. Y. & CHOI, N. C. 2006. Design of 4D treatment planning target volumes. *International Journal of Radiation Oncology* Biology* Physics,* 66**,** 287-295.

RIETZEL, E., PAN, T. & CHEN, G. T. Y. 2005. Four-dimensional computed tomography: image formation and clinical protocol. *Medical physics,* 32**,** 874-889.

ROGELJ, P. & KOVACIC, S. 2006. Symmetric image registration. *Med. Image Anal.,* 10**,** 484-493.

ROGELJ, P. & KOVAČIČ, S. 2006. Symmetric image registration. *Medical image analysis,* 10**,** 484-493.

ROHLFING, T., MAURER, C., O'DELL, W. & ZHONG, J. 2004a. Modeling liver motion and deformation during the respiratory cycle using intensity-based nonrigid registration of gated MR images. *Med Phys,* 31**,** 427-432.

ROHLFING, T., MAURER JR, C. R., O'DELL, W. G. & ZHONG, J. 2004b. Modeling liver motion and deformation during the respiratory cycle using intensity-based nonrigid registration of gated MR images. *Medical physics,* 31**,** 427-432.

ROSU, M., BALTER, J. M., CHETTY, I. J., KESSLER, M. L., MCSHAN, D. L., BALTER, P. & TEN HAKEN, R. K. 2007. How extensive of a 4D dataset is needed to estimate cumulative dose distribution plan evaluation metrics in conformal lung therapy? *Medical Physics,* 34**,** 233-245.

ROSU, M., CHETTY, I. J., BALTER, J. M., KESSLER, M. L., MCSHAN, D. L. & TEN HAKEN, R. K. 2005. Dose reconstruction in deforming lung anatomy: dose grid size effects and clinical implications. *Medical physics,* 32**,** 2487.

RUECKERT, D., SONODA, L., HAYES, C., HILL, D., LEACH, M. & HAWKES, D. 1999. Nonrigid registration using free-form deformations: application to breast MR images. *IEEE Trans Med Imaging,* 18**,** 712-721.

RUGGIERI, R., NACCARATO, S. & NAHUM, A. E. 2010. Severe hypofractionation: Non-homogeneous tumour dose delivery can counteract tumour hypoxia. *Acta Oncologica,* 49**,** 1304-1314.

RUSTHOVEN, K., KAVANAGH, B., CARDENES, H., STIEBER, V., BURRI, S. & FEIGENBERG, S. 2009. Multi-institutional phase I/II trial of stereotactic body radiotherapy for liver malignancies. *J Clin Oncol,* 27**,** 1572.

RUTQVIST, L. E., ROSE, C. & CAVALLIN-STÅHL, E. 2003. A systematic overview of radiation therapy effects in breast cancer. *Acta Oncologica,* 42**,** 532-545.

SAHGAL, A., ROBERGE, D., SCHELLENBERG, D., PURDIE, T., SWAMINATH, A., PANTAROTTO, J., FILION, E., GABOS, Z., BUTLER, J., LETOURNEAU, D., MASUCCI, G., MULROY, L., BEZJAK, A., DAWSON, L. & PARLIAMENT, M. 2012. The Canadian Association of Radiation Oncology Scope of Practice Guidelines for Lung, Liver and Spine Stereotactic Body Radiotherapy. *Clinical Oncology,* 24**,** 629-639.

SAKHALKAR, H., ADAMOVICS, J., IBBOTT, G. & OLDHAM, M. 2009. A comprehensive evaluation of the PRESAGE⁄ optical-CT 3D dosimetry system. *Medical Physics,* 36**,** 71.

SALAZAR, O. M., RUBIN, P., FELDSTEIN, M. L. & PIZZUTIELLO, R. 1979. High dose radiation therapy in the treatment of malignant gliomas: final report. *International Journal of Radiation Oncology* Biology* Physics,* 5**,** 1733-1740.

SAMANT, S. S., XIA, J., MUYAN-ÖZÇELIK, P. & OWENS, J. D. 2008. High performance computing for deformable image registration: Towards a new paradigm in adaptive radiotherapy. *Medical physics,* 35**,** 3546-3553.

SCHALY, B., KEMPE, J., BAUMAN, G., BATTISTA, J. & DYK, J. V. 2004a. Tracking the dose distribution in radiation therapy by accounting for variable anatomy. *Physics in Medicine and Biology,* 49**,** 791-805.

SCHALY, B., KEMPE, J., BAUMAN, G., BATTISTA, J. & DYK, J. V. 2004b. Tracking the dose distribution in radiation therapy by accounting for variable anatomy. *Physics in Medicine and Biology,* 49**,** 791-805.

SCHNABEL, J. A., TANNER, C., CASTELLANO-SMITH, A. D., DEGENHARD, A., LEACH, M. O., HOSE, D. R., HILL, D. L. G. & HAWKES, D. J. 2003. Validation of nonrigid image registration using finite-element methods: application to breast MR images. *IEEE Trans Med Imaging,* 22**,** 238-247.

SCHREINER, L. Review of Fricke gel dosimeters. Journal of Physics: Conference Series, 2004. IOP Publishing, 9.

SCHULTHEISS, T. & TOMÉ, W. 2012. It is not appropriate to "deform" dose along with deformable image registration in adaptive radiotherapy. *Med Phys,* 39**,** 6531-6533.

SCHULTHEISS, T. E. & TOME, W. A. 2013. Response to "Comment on 'It is not appropriate to"deform" dose along with deformable image registration in adaptive radiotherapy-[Med. Phys. 39, 6531-6533 (2012)]'". *Medical physics,* 40**,** 017102.

SCHULTHEISS, T. E., TOME, W. A. & ORTON, C. G. 2012. Point/counterpoint: it is not appropriate to" deform" dose along with deformable image registration in adaptive radiotherapy. *Medical physics,* 39**,** 6531-6533.

SECO, J., LU, X. Q., EBE, K., MAYO, C., IONASCU, D., WINEY, B., GIAKOUMAKIS, N., ARISTOPHANOUS, M., BERBECO, R. & ROTTMAN, J. 2010. Use of a realistic breathing lung phantom to evaluate dose delivery errors. *Medical physics,* 37**,** 5850-5857.

SENDEN, R., DE JEAN, P., MCAULEY, K. & SCHREINER, L. 2006. Polymer gel dosimeters with reduced toxicity: a preliminary investigation of the NMR and optical dose–response using different monomers. *Physics in medicine and biology,* 51**,** 3301.

SEPPENWOOLDE, Y., SHIRATO, H., KITAMURA, K., SHIMIZU, S., VAN HERK, M., LEBESQUE, J. V. & MIYASAKA, K. 2002. Precise and real-time measurement of 3D tumor motion in lung due to breathing and heartbeat, measured during radiotherapy. *International Journal of Radiation Oncology* Biology* Physics,* 53**,** 822-834.

SERBAN, M., HEATH, E., STROIAN, G., COLLINS, D. L. & SEUNTJENS, J. 2008. A deformable phantom for 4D radiotherapy verification: Design and image registration evaluation. *Medical physics,* 35**,** 1094-1102.

SHELTON, D., STETTEN, G., AYLWARD, S., IBÁÑEZ, L., COIS, A. & STEWART, C. 2005. Teaching medical image analysis with the Insight Toolkit. *Medical Image Analysis,* 9**,** 605-611.

SHIRATO, H., HARADA, T., HARABAYASHI, T., HIDA, K., ENDO, H., KITAMURA, K., ONIMARU, R., YAMAZAKI, K., KURAUCHI, N. & SHIMIZU, T. 2003. Feasibility of insertion/implantation of 2.0-mm-diameter gold internal fiducial markers for precise setup and real-time tumor tracking in radiotherapy. *International Journal of Radiation Oncology* Biology* Physics,* 56**,** 240-247.

SHIRATO, H., SHIMIZU, S., KUNIEDA, T., KITAMURA, K., VAN HERK, M., KAGEI, K., NISHIOKA, T., HASHIMOTO, S., FUJITA, K. & AOYAMA, H. 2000. Physical aspects of a real-time tumor-tracking system for gated radiotherapy. *International Journal of Radiation Oncology* Biology* Physics,* 48**,** 1187-1195.

SIXEL, K. E., AZNAR, M. C. & UNG, Y. C. Deep inspiration breath hold to reduce irradiated heart volume in breast cancer patients. Engineering in Medicine and Biology Society, 2000. Proceedings of the 22nd Annual International Conference of the IEEE, 2000. IEEE, 2728-2731.

STARKSCHALL, G., BRITTON, K., MCALEER, M. F., JETER, M. D., KAUS, M. R., BZDUSEK, K., MOHAN, R. & COX, J. D. 2009. Potential dosimetric benefits of four-dimensional radiation treatment planning. *International Journal of Radiation Oncology* Biology* Physics,* 73**,** 1560-1565.

STRAUSS, A., DRITSCHILO, A., NATHANSON, L. & PIRO, A. J. 1981. Radiation therapy of malignant melanomas: an evaluation of clinically used fractionation schemes. *Cancer,* 47**,** 1262-1266.

SUIT, H., GOLDBERG, S., NIEMIERKO, A., ANCUKIEWICZ, M., HALL, E., GOITEIN, M., WONG, W. & PAGANETTI, H. 2007. Secondary carcinogenesis in patients treated with radiation: a review of data on radiation-induced cancers in human, non-human primate, canine and rodent subjects. *Radiation Research,* 167**,** 12-42.

SURAMO, I., PÄIVÄNSALO, M. & MYLLYLÄ, V. 1984. Cranio-caudal movements of the liver, pancreas and kidneys in respiration. *Acta Radiologica: Diagnosis,* 25**,** 129.

TAYLOR, M. 2011. Robust determination of effective atomic numbers for electron interactions with TLD-100 and TLD-100H thermoluminescent dosimeters. *Nuclear Instruments and Methods in Physics Research Section B: Beam Interactions with Materials and Atoms,* 269**,** 770-773.

TAYLOR, M., KRON, T. & FRANICH, R. 2011a. A contemporary review of stereotactic radiotherapy: Inherent dosimetric complexities and the potential for detriment. *Acta Oncol,* 50**,** 483-508.

TAYLOR, M., SMITH, R., DOSSING, F. & FRANICH, R. 2012. Robust calculation of effective atomic numbers: The Auto-Zeff software. *Medical Physics,* 39**,** 1769-1778.

TAYLOR, M. L., FRANICH, R. D., JOHNSTON, P. N., MILLAR, R. M. & TRAPP, J. V. 2007a. Systematic variations in polymer gel dosimeter calibration due to container influence and deviations from water equivalence. *Physics in Medicine and Biology,* 52**,** 3991.

TAYLOR, M. L., FRANICH, R. D., JOHNSTON, P. N., MILLAR, R. M. & TRAPP, J. V. 2007b. Systematic variations in polymer gel dosimeter calibration due to container influence and deviations from water equivalence. *Physics in Medicine and Biology,* 52**,** 3991-4005.

TAYLOR, M. L., FRANICH, R. D., TRAPP, J. V. & JOHNSTON, P. N. 2008. The effective atomic number of dosimetric gels. *Australas. Phys. Eng. Sci. Med.,* 31**,** 131-138.

TAYLOR, M. L., FRANICH, R. D., TRAPP, J. V. & JOHNSTON, P. N. 2009a. A comparative study on the effect of calibration conditions on the water equivalence of a range of gel dosimeters. *IEEE Trans. Nucl. Sci.,* 56**,** 429-436.

TAYLOR, M. L., FRANICH, R. D., TRAPP, J. V. & JOHNSTON, P. N. 2009b. Electron interaction with gel dosimeters: Effective atomic numbers for collisional, radiative and total interaction processes. *Radiat. Res.,* 171**,** 123-126.

TAYLOR, M. L., FRANICH, R. D., TRAPP, J. V. & JOHNSTON, P. N. 2009c. Electron interaction with gel dosimeters: Effective atomic numbers for collisional, radiative and total interaction processes. *Radiation research,* 171**,** 123-126.

TAYLOR, M. L. & KRON, T. 2011. Consideration of the radiation dose delivered away from the treatment field to patients in radiotherapy. *Journal of medical physics/Association of Medical Physicists of India,* 36**,** 59-71.

TAYLOR, M. L., KRON, T. & FRANICH, R. D. 2011b. A contemporary review of stereotactic radiotherapy: Inherent dosimetric complexities and the potential for detriment. *Acta Oncologica,* 50**,** 483-508.

TAYLOR, M. L., KRON, T. & FRANICH, R. D. 2011c. A contemporary review of stereotactic radiotherapy: Inherent dosimetric complexities and the potential for detriment. *Acta Oncol*.

TEN HAKEN, R., FORMAN, J., HEIMBURGER, D., GERHARDSSON, A., MCSHAN, D., PEREZ-TAMAYO, C., SCHOEPPEL, S. & LICHTER, A. 1991. Treatment planning issues related to prostate movement in response to differential filling of the rectum and bladder. *International Journal of Radiation Oncology* Biology* Physics,* 20**,** 1317-1324.

THAMES, H. D., PETERS, L. T., WITHERS, H. R. & FLETCHER, G. H. 1983. Accelerated fractionation vs hyperfractionation: rationales for several treatments per day. *International Journal of Radiation Oncology* Biology* Physics,* 9**,** 127-138.

THIRION, J. 1998a. Image matching as a diffusion process: An analogy with Maxwell's demons. *Med. Image Anal.,* 2**,** 243-260.

THIRION, J. P. 1998b. Image matching as a diffusion process: an analogy with Maxwell's demons. *Medical Image Analysis,* 2**,** 243-260.

TIMMERMAN, R. D., FORSTER, K. M. & CHINSOO CHO, L. Extracranial stereotactic radiation delivery. Seminars in Radiation Oncology, 2005. Elsevier, 202-207.

TODD, P. 1983. Unique biological aspects of radiation hazards—an overview. *Advances in Space Research,* 3**,** 187-194.

TRAPP, J., MICHAEL, G., DE DEENE, Y. & BALDOCK, C. 2002. Attenuation of diagnostic energy photons by polymer gel dosimeters. *Physics in medicine and biology,* 47**,** 4247.

TRCR 2006. Radiotherapy Dose-Fractionation. *The Royal College of Radiologists*.

TREVERT, E. 1896. *Something about X Rays for Everybody*, Medical Physics Publishing Corporation.

TRONCALLI, A. J. & CHAPMAN, J. 2003. TLD linearity vs. beam energy and modality. *Medical Dosimetry,* 27**,** 295-296.

TUBIANA, M. 2009. Can we reduce the incidence of second primary malignancies occurring after radiotherapy? A critical review. *Radiotherapy and Oncology,* 91**,** 4-15.

TURNER, S. L., SWINDELL, R., BOWL, N., MARRS, J., BROOKES, B., READ, G. & COWAN, R. A. 1997. Bladder movement during radiation therapy for bladder cancer: implications for treatment planning. *International Journal of Radiation Oncology, Biology, Physics,* 39**,** 355.

VAN DER WIELEN, G. J., MUTANGA, T. F., INCROCCI, L., KIRKELS, W. J., VASQUEZ OSORIO, E. M., HOOGEMAN, M. S., HEIJMEN, B. J. M. & DE BOER, H. C. J. 2008. Deformation of prostate and seminal vesicles relative to intraprostatic fiducial markers. *International Journal of Radiation Oncology* Biology* Physics,* 72**,** 1604-1611.

VAN SÖRNSEN, K. J. R., LAGERWAARD, F. J., SCHUCHHARD-SCHIPPER, R. H., NIJSSEN-VISSER, M., VOET, P., OEI, S. S. & SENAN, S. 2001. Dosimetric consequences of tumor mobility in radiotherapy of stage I non-small cell lung cancer--an analysis of data generated using'slow'CT scans. *Radiotherapy and oncology: journal of the European Society for Therapeutic Radiology and Oncology,* 61**,** 93.

VEDAM, S., KEALL, P., KINI, V., MOSTAFAVI, H., SHUKLA, H. & MOHAN, R. 2002. Acquiring a four-dimensional computed tomography dataset using an external respiratory signal. *Physics in Medicine and Biology,* 48**,** 45.

VELEC, M., JUANG, T., MOSELEY, J. L., OLDHAM, M. & BROCK, K. K. 2015. Utility and validation of biomechanical deformable image registration in low-contrast images. *Practical radiation oncology*.

VEMURI, B., YE, J., CHEN, Y. & LEONARD, C. 2000. A level-set based approach to image registration. *Proceedings of IEEE Workshop on Mathematical Methods in Biomedical Image Analysis***,** 86-93.

VENNING, A., NITSCHKE, K., KEALL, P. & BALDOCK, C. 2005a. Radiological properties of normoxic polymer gel dosimeters. *Medical physics,* 32**,** 1047.

VENNING, A. J., HILL, B., BRINDHA, S., HEALY, B. J. & BALDOCK, C. 2005b. Investigation of the PAGAT polymer gel dosimeter using magnetic resonance imaging. *Physics in Medicine and Biology,* 50**,** 3875-3888.

VENNING, A. J., NITSCHKE, K. N., KEALL, P. J. & BALDOCK, C. 2005c. Radiological properties of normoxic polymer gel dosimeters. *Medical physics,* 32**,** 1047-1053.

VINOGRADSKIY, Y., BALTER, P., FOLLOWILL, D., ALVAREZ, L., WHITE, R. & STARKSCHALL, G. 2009. Verification of four-dimensional photon dose calculations. *Med Phys,* 36**,** 3438.

VON SIEBENTHAL, M., SZÉKELY, G., LOMAX, A. J. & CATTIN, P. C. 2007. Systematic errors in respiratory gating due to intrafraction deformations of the liver. *Medical physics,* 34**,** 3620-3629.

WALIMBE, V. & SHEKHAR, R. 2006. Automatic elastic image registration by interpolation of 3D rotations and translations from discrete rigid-body transformations. *Medical Image Analysis,* 10**,** 899-914.

WAMBERSIE, A. & LANDBERG, T. 1999. ICRU 62: Prescribing, Recording and Reporting Photon Beam Therapy (Supplement to ICRU Report 50). *International Commission on Radiation Units and Measurements.*

WANG, H., DONG, L., LII, M. F., LEE, A. L., DE CREVOISIER, R., MOHAN, R., COX, J. D., KUBAN, D. A. & CHEUNG, R. 2005a. Implementation and validation of a three-dimensional deformable registration algorithm for targeted prostate cancer radiotherapy. *International Journal of Radiation Oncology* Biology* Physics,* 61**,** 725-735.

WANG, H., DONG, L., O'DANIEL, J., MOHAN, R., GARDEN, A., ANG, K., KUBAN, D., BONNEN, M., CHANG, J. & CHEUNG, R. 2005b. Validation of an accelerated demons algorithm for deformable image registration in radiation therapy. *Physics in Medicine and Biology,* 50**,** 2887-2905.

WANG, H., DONG, L., O'DANIEL, J., MOHAN, R., GARDEN, A. S., ANG, K. K., KUBAN, D. A., BONNEN, M., CHANG, J. Y. & CHEUNG, R. 2005c. Validation of an accelerated'demons' algorithm for deformable image registration in radiation therapy. *Physics in medicine and biology,* 50**,** 2887.

WANG, H., DONG, L., O'DANIEL, J., MOHAN, R., GARDEN, A. S., ANG, K. K., KUBAN, D. A., BONNEN, M., CHANG, J. Y. & CHEUNG, R. 2005d. Validation of an accelerated 'demons' algorithm for deformable image registration in radiation therapy. *Physics in medicine and biology,* 50**,** 2887-2905.

WANG, H., DONG, L., O'DANIEL, J., MOHAN, R., GARDEN, A. S., KIAN ANG, K., KUBAN, D. A., BONNEN, M., CHANG, J. Y. & CHEUNG, R. 2005e. Validation of an accelerated `demons' algorithm for deformable image registration in radiation therapy. *Physics in Medicine and Biology,* 50**,** 2887-905.

WEIGUO, L., MING-LI, C., OLIVERA, G. H., RUCHALA, K. J. & MACKIE, T. R. 2004. Fast free-form deformable registration via calculus of variations. *Physics in Medicine and Biology,* 49**,** 3067-87.

WEISS, P. H., BAKER, J. M. & POTCHEN, E. J. 1972. Assessment of hepatic respiratory excursion. *Journal of Nuclear Medicine,* 13**,** 758-759.

WEN, N., GLIDE-HURST, C., NURUSHEV, T., XING, L., KIM, J., ZHONG, H., LIU, D., LIU, M., BURMEISTER, J. & MOVSAS, B. 2012. Evaluation of the deformation and corresponding dosimetric implications in prostate cancer treatment. *Physics in Medicine and Biology,* 57**,** 5361-5379.

WESTERMARK, M., ARNDT, J., NILSSON, B. & BRAHME, A. 2000. Comparative dosimetry in narrow high-energy photon beams. *Physics in Medicine and Biology,* 45**,** 685.

WHITE, P. J., ZWICKER, R. D. & HUANG, D. T. 1996. Comparison of dose homogeneity effects due to electron equilibrium loss in lung for 6 MV and 18 MV photons. *International Journal of Radiation Oncology, Biology, Physics,* 34**,** 1141-1146.

WILKINS, D., LI, X. A., CYGLER, J. & GERIG, L. 1997. The effect of dose rate dependence of p-type silicon detectors on linac relative dosimetry. *Medical Physics,* 24**,** 879.

WOLFSON, A. H. Conventional radiation therapy of cervical cancer. 1999. Wiley Online Library, 242-246.

WU, C., JERAJ, R., OLIVERA, G. H. & MACKIE, T. R. 2002a. Re-optimization in adaptive radiotherapy. *Physics in Medicine and Biology,* 47**,** 3181-3195.

WU, C., JERAJ, R., OLIVERA, G. H. & MACKIE, T. R. 2002b. Re-optimization in adaptive radiotherapy. *Physics in medicine and biology,* 47**,** 3181.

WULF, J., GUCKENBERGER, M., HAEDINGER, U., OPPITZ, U., MUELLER, G., BAIER, K. & FLENTJE, M. 2006. Stereotactic radiotherapy of primary liver cancer and hepatic metastases. *Acta Oncologica,* 45**,** 838-847.

WUU, C. S. & XU, Y. 2006. Three-dimensional dose verification for intensity modulated radiation therapy using optical CT based polymer gel dosimetry. *Medical physics,* 33**,** 1412.

WYSOCKA, B., KASSAM, Z., LOCKWOOD, G., BRIERLEY, J., DAWSON, L. A., BUCKLEY, C. A., JAFFRAY, D., CUMMINGS, B., KIM, J. & WONG, R. 2010. Interfraction and respiratory organ motion during conformal radiotherapy in gastric cancer. *International Journal of Radiation Oncology, Biology and Physics,* 77.

XIE, Z. Y., NG, L. & GEE, J. 2003. Two algorithms for non-rigid image registration and their evaluation. *In:* SONKA, M. & FITZPATRICK, J. M. (eds.) *Medical Imaging 2003: Image Processing, Pts 1-3.*

XU, X. G., BEDNARZ, B. & PAGANETTI, H. 2008. A review of dosimetry studies on external-beam radiation treatment with respect to second cancer induction. *Physics in Medicine and Biology,* 53**,** R193-R241.

XU, Y., WUU, C. S. & MARYANSKI, M. J. 2003. Determining optimal gel sensitivity in optical CT scanning of gel dosimeters. *Medical Physics,* 30**,** 2257.

XU, Y., WUU, C. S. & MARYANSKI, M. J. 2004. Performance of a commercial optical CT scanner and polymer gel dosimeters for 3-D dose verification. *Medical physics,* 31**,** 3024.

XU, Z., LIANG, S., ZHU, J., ZHU, X., ZHAO, J., LU, H., YANG, Y., CHEN, L., WANG, A., FU, X. & JIANG, G. 2006. Prediction of radiation-induced liver disease by Lyman normal-tissue complication probability model in three-dimensional conformal radiation therapy for primary liver carcinoma. *Int. J. Radiat. Oncol. Biol. Phys.,* 65**,** 189-195.

YAMADA, Y., ACKERMAN, I., FRANSSEN, E., MACKENZIE, R. G. & THOMAS, G. 1999. Does the dose fractionation schedule influence local control of adjuvant radiotherapy for early stage breast cancer? *International Journal of Radiation Oncology* Biology* Physics,* 44**,** 99-104.

YAN, G., FOX, C., LIU, C. & LI, J. G. 2008. The extraction of true profiles for TPS commissioning and its impact on IMRT patient-specific QA. *Medical Physics,* 35**,** 3661.

YANG, D., BRAME, S., EL NAQA, I., ADITYA, A., WU, Y., GODDU, S. M., MUTIC, S., DEASY, J. O. & LOW, D. A. 2011a. Technical Note: DIRART–A software suite for deformable image registration and adaptive radiotherapy research. *Medical physics,* 38**,** 67.

YANG, D., BRAME, S., EL NAQA, I., ADITYA, A., WU, Y., GODDU, S. M., MUTIC, S., DEASY, J. O. & LOW, D. A. 2011b. Technical Note: DIRART–A software suite for deformable image registration and adaptive radiotherapy research. *Med Phys,* 38**,** 67.

YANG, D., BRAME, S., NAQA, I. E., ADITYA, A., WU, Y., GODDU, S. M., MUTIC, S., DEASY, J. O. & LOW, D. A. 2011c. Technical Note: DIRART -- A software suite for deformable image registration and adaptive radiotherapy research. *Medical Physics,* 38**,** 67-77.

YANG, D., CHAUDHARI, S. R., GODDU, S. M., PRATT, D., KHULLAR, D., DEASY, J. O. & EL NAQA, I. 2009. Deformable registration of abdominal kilovoltage treatment planning CT and tomotherapy daily megavoltage CT for treatment adaptation. *Medical Physics,* 36**,** 329-338.

YANG, D., LI, H., LOW, D. A., DEASY, J. O. & NAQA, I. E. 2008. A fast inverse consistent deformable image registration method based on symmetric optical flow computation. *Physics in medicine and biology,* 53**,** 6143-6165.

YEO, B., SABUNCU, M., VERCAUTEREN, T., AYACHE, N., FISCHL, B. & GOLLAND, P. 2008. Spherical demons: Fast surface registration. *Medical Image Computing and Computer-Assisted Intervention***,** 745-753.

YEO, U., TAYLOR, M., SUPPLE, J., SMITH, R., KRON, T. & FRANICH, R. Deformable gel dosimetry I: application to external beam radiotherapy and brachytherapy. Journal of Physics: Conference Series, 2013. IOP Publishing, 012032.

YEO, U. J., TAYLOR, M. L., SUPPLE, J. R., SMITH, R. L., DUNN, L., KRON, T. & FRANICH, R. D. 2012. Is it sensible to 'deform' dose? 3D experimental validation of dose-warping. *Medical physics,* 39**,** 5065-5072.

YORKE, E. 2001. Modeling the effects of inhomogeneous dose distributions in normal tissues. *Semin. Rad. Onc.,* 11**,** 198-209.

ZACKRISSON, B., MERCKE, C., STRANDER, H., WENNERBERG, J. & CAVALLIN-STÅHL, E. 2003. A systematic overview of radiation therapy effects in head and neck cancer. *Acta Oncologica,* 42**,** 443-461.

ZHANG, G. G., HUANG, T. C., FORSTER, K. M., LIN, K. P., STEVENS, C., HARRIS, E. & GUERRERO, T. 2008. Dose mapping: validation in 4D dosimetry with measurements and application in radiotherapy follow-up evaluation. *Computer methods and programs in biomedicine,* 90**,** 25-37.

ZHONG, H., KIM, J. & CHETTY, I. J. 2010. Analysis of deformable image registration accuracy using computational modeling. *Medical physics,* 37**,** 970.

ZHONG, H., KIM, J., LI, H., NURUSHEV, T., MOVSAS, B. & CHETTY, I. J. 2012. A finite element method to correct deformable image registration errors in low-contrast regions. *Physics in Medicine and Biology,* 57**,** 3499.

ZHONG, H., PETERS, T. & SIEBERS, J. V. 2007. FEM-based evaluation of deformable image registration for radiation therapy. *Physics in medicine and biology,* 52**,** 4721-4738.

ZHONG, H., WEISS, E. & SIEBERS, J. V. 2008. Assessment of dose reconstruction errors in image-guided radiation therapy. *Physics in Medicine and Biology,* 53**,** 719-745.